The Local Galaxy Density Field and its Effects on the Cosmic Microwave Background

CAROLINE FRANCIS

Institute for Astronomy

School of Physics

University of Edinburgh

Doctor of Philosophy

April 2008

Abstract

This thesis presents a reconstruction of the local galaxy density field to a maximum redshift of $z = 0.3$ from a photometric galaxy catalogue based on the Two Micron All-Sky Survey (2MASS) Extended Source Catalogue (XSC). A Wiener filter approach is adopted for the reconstruction, which is carried out using a basis of spherical harmonics to describe angular variations and spherical Bessel functions to describe the radial part of the field. The angular resolution is fixed at $\ell_{\rm max} = 30$ and the radial resolution is set to match this at the characteristic redshift of the survey, $z \sim 0.1$, resulting in $\Delta r \simeq 30\,h^{-1}$Mpc. A novel technique for replacing missing information from the galactic plane is developed and tested using simulation data, before being applied to the reconstruction of the local density field.

This reconstruction is used to predict the contribution to the Cosmic Microwave Background (CMB) of the local Integrated Sachs-Wolfe (ISW) effect and large-scale thermal Sunyaev-Zel'dovich (tSZ) effect. The impact of the predicted local ISW effect on the observed CMB signal is investigated, particularly with regard to reported anomalies on large angular scales. It is found that removal of the predicted local ISW signal to $z_{\rm max} = 0.3$ from the CMB data can alleviate many of these anomalies.

A technique is developed for predicting the large-scale thermal and kinetic Sunyaev-Zel'dovich signals arising from a baryon distribution, when only the corresponding dark matter density and velocity fields are known. This is used in conjunction with the reconstruction of the local density field to predict the large-scale tSZ signal in the Universe. The effect of this signal on the CMB is also analysed, including a discussion of its impact on cosmological parameter estimation and its influence, together with the predicted local ISW signal, on an anomalous cold spot observed in the CMB. Using the predicted large-scale tSZ signal, the prospects for *Planck* detecting this CMB foreground are examined. It is found that the sensitivity of *Planck* and its broad frequency range should enable the detection of this signal which is an important

test of our preferred cosmological model.

A cross-correlation of the photometric redshift 2MASS galaxy data with year-3 WMAP CMB data is performed to attempt to detect the local ISW signal and to investigate whether the addition of photometric redshifts to the 2MASS dataset improves its detection prospects. There is no significant ISW signal found in this analysis, and the expected cross-correlation signal in a ΛCDM universe is only weakly preferred over no correlation, with likelihood ratio 1.5:1. In this case, the addition of photometric redshifts resulted in no improvement in the detection. The ISW detection prospects of hypothetical future large-scale structure surveys are assessed in conjunction with a 'best possible' ISW experiment where one imagines measuring the ISW temperature fluctuations across the whole sky to some $z_{\rm max}$. A photometric redshift large-scale structure survey with characteristic redshift $z = 0.3$ observing ~ 10 million galaxies out to $z_{\rm max} = 0.7$ has reasonable detection prospects, strongly preferring the ΛCDM hypothesis over a 'no ISW' hypothesis in the majority of cases, and with a small (less than 10%) chance of a Type I error at this threshold. The 'best possible' experiment with $z_{\rm max} = 0.7$ is found to strongly prefer a ΛCDM hypothesis only 85% of the time, with a 1% chance of such data strongly preferring a 'no ISW' hypothesis.

Declaration

I declare that this thesis is not substantially the same as any that I have submitted for a degree or diploma or other qualification at any other University. I further state that no part of my thesis has already been or is being concurrently submitted for any such degree, diploma or other qualification.

This thesis is the outcome of my own work except where specifically indicated in the text.

Caroline Francis

Edinburgh,

April 2008.

Acknowledgements

Now the time has finally come to write my acknowledgements, I find that it is an experience entirely in keeping with the rest of my PhD: not as straightforward as I had anticipated.

Firstly, thank you to my family, who have supported my desire to cling to student life for as long as possible and provided encouragement when things got tough. Thank you particularly for not asking how it was going any more than strictly necessary. Special thanks to my parents, to Paul and to Grandma.

Thanks to John, for being an excellent supervisor, for generating motivation when it was sorely needed and for bearing with all the stupid mistakes. Thanks also to Andy T, Bob Mann, Maria Rosa, Ross McLure and Alan Heavens for all their suggestions and insightful questions which have improved this thesis. Special mentions should also go to Will for wrestling with GADGET for me, to Eric for explaining the mysteries of hydrodynamic codes and to Mark for writing Paperscope just when I needed it. Thanks to Scott Kay and Frazer Pearce for their help with obtaining and understanding Millennium simulation gas data and to Kate Land, for providing both data and helpful advice.

To Anita, Barney, Matt, Rachel and Rita: I couldn't have asked for a better bunch of people to experience doing a PhD with - you've been great. I'll fondly remember all the coffee times, nights at the pub, conferences, the skiing trip (sorry, winter school...) and other entertainments.

To Emma, Niall, the Toms, Matt and especially Rita: thank you for being wonderful office mates, for putting up with the bad days and my attempts at distraction. To Stuart, thanks for all the computing help and to Simon, Michael, Jess, Liv, Jenny, Rachel, Sarah, Gila and others that I have forgotten, thank you for all the great days/nights out.

To Anna, Em, Jade, Lisa, Sara, Tam, Anne, Beccy, Clare, Hannah, Lou and Naomi, thank you for being there when needed. Thanks also to Jorge Cham for his PhD comic strip which

often raised a smile and was bizarrely encouraging.

Finally, to Miller, I don't have words to adequately thank you for all your love and support over the last three and a half years. You've been a star. Thank you.

Contents

List of Figures

List of Tables

CHAPTER 1

Introduction

1.1 Background Cosmology

Within the currently favoured cosmological model, at early times, the Universe was incredibly hot and dense. As it evolved, the Universe expanded and cooled and when the temperature dropped below a threshold of $T \sim 0.3$eV (Kolb and Turner, 1990, pp78-80), protons and electrons began to combine to form atoms and the Universe became transparent. Radiation, which was previously coupled to the electron-proton gas, was able to free-stream for the first time – we observe this radiation today as the Cosmic Microwave Background (CMB). Further cooling saw the attractive gravitational forces between particles overcome the pressure which resists this attraction. In this way, small fluctuations in density in the early Universe gradually led to the formation of structures in overdense regions.

We believe that the Universe which we observe today can be described as a perturbation to a simpler model that characterizes a smooth universe with no structures in it. This smooth background universe is outlined in the remainder of Section 1.1; structure formation in the perturbed universe model is described in Section 1.2 and details of the CMB are given in Section 1.3. Finally, the contents of this thesis are outlined in Section 1.4.

1.1.1 Cosmological Principle

The Cosmological Principle states that on sufficiently large scales the Universe is *homogeneous* and *isotropic*, where homogeneous means independent of position and isotropic means independent of direction. This implies that the density in the Universe is the same everywhere – there are no special positions or directions.

The Cosmological Principle is an assumption on which our model for the large scale Universe rests; however, we are now in a position to test some aspects of this assumption. The high degree of isotropy observed in the CMB data (see Section 1.3) together with the uniformity of the observed galaxy distribution when averaged on sufficiently large scales, provides evidence for large scale isotropy in the Universe.

Assumptions about the nature of the Universe such as homogeneity and isotropy are necessary to reduce the number of possible cosmological models which could describe our Universe. The motivation for this particular form of the Cosmological Principle is twofold: firstly, this is the simplest mass distribution that we could consider; secondly, if we accept the *Copernican Principle*, which states that we do not inhabit a special place in the Universe, and assume isotropy about our position (which looks likely observationally), then we are led to the Cosmological Principle.

1.1.2 General Relativity and the Friedmann Robertson Walker Metric

We believe that the large-scale Universe should be described by General Relativity and the Cosmological Principle. From these two assumptions we can formulate a cosmological model. General Relativity tells us that we need a metric to describe spacetime, and the symmetry considerations introduced by the Cosmological Principle lead us to adopt the Robertson-Walker spacetime metric

$$-ds^2 = c^2 d\tau^2 = g_{ab}\, dx^a dx^b = c^2 dt^2 - R^2(t)\left[dr^2 + S_k^2(r)\left(d\theta^2 + \sin^2\theta\, d\phi^2\right)\right], \quad (1.1)$$

where $R(t)$ is the scale factor, r is a comoving coordinate (see Section 1.1.3) and k is the curvature constant. The function $S_k(r)$ is determined by the value of k (discussed further below), taking the form

$$S_k(r) = \begin{cases} \sin(r) & \text{if } k = 1 \\ r & \text{if } k = 0 \\ \sinh(r) & \text{if } k = -1 \end{cases} .$$

At this point, it is useful to define a dimensionless scale factor $a(t)$ given by

$$a(t) = \frac{R(t)}{R_0},$$

with R_0 the value of the scale factor today. In equation (1.1) the comoving coordinate r is dimensionless. For the remainder of this thesis, we will take $k = 0$ as indicated by observations, and whenever comoving distances r_{com} are discussed, this actually refers to the quantity $r_{\text{com}} = R_0 r$ with r dimensionless and defined above. The *conformal time*, η, is sometimes used as an alternative time coordinate, this is defined by

$$\frac{d\eta}{dt} = \frac{1}{a} \tag{1.2}$$

and hence with these definitions the Robertson-Walker metric in a $k = 0$ universe can be written

$$c^2 d\tau^2 = g_{ab} dx^a dx^b = a^2 \left[c^2 d\eta^2 - dr_{\text{com}}^2 - r_{\text{com}}^2 (d\theta^2 + \sin^2\theta d\phi^2) \right] . \tag{1.3}$$

We are also led to introduce a *stress-energy* or *energy-momentum* tensor, $T^{\mu\nu}$, to describe the components that make up the Universe. The symmetry considerations of the Cosmological Principle imply that we should use the perfect fluid form for this. The Einstein equations relate the contents of the Universe (matter, radiation etc.) to spacetime itself via the Einstein tensor, $G^{\mu\nu}$ which is a combination of metric components and their derivatives

$$G^{\mu\nu} = \frac{8\pi G}{c^4} T^{\mu\nu}. \tag{1.4}$$

A cosmological constant term may also feature in this equation,

$$G^{\mu\nu} + \Lambda g^{\mu\nu} = \frac{8\pi G}{c^4} T^{\mu\nu}. \tag{1.5}$$

This term was originally introduced by Einstein to allow a non-expanding universe to satisfy the equations, but has gained popularity more recently due to the observed accelerating expansion of the Universe (see Section 1.1.5).

This elegant model is however fundamentally flawed in that it fails to match the Universe that we observe. Such a model universe will not give rise to any structures: there would be no galaxies, clusters or superclusters and indeed, we would not exist. This is a result of the constraints imposed by the Cosmological Principle which tells us that *on large scales*, statistically, the Universe should be at a constant density throughout space. Hence we need a modification to our present model to describe the observed small scale Universe. The currently favoured model postulates that the Universe can be described as a perturbation to a smooth background universe that satisfies General Relativity and the Cosmological Principle. This picture states that small perturbations in the density field present in the early universe will be amplified under gravitational instability to become the structures that we see around us today. This is an assumption, but there is a wealth of evidence to support such a model, including the existence of small temperature fluctuations in the CMB. The implications of this perturbation model of the Universe are explored in Sections (1.2) and (1.3), whilst here we continue to describe the smooth background universe.

The curvature constant that appears in the Robertson-Walker metric encodes information about the geometry of the universe. There are 3 possible values for k, allowable by the symmetry considerations imposed in formulating the Robertson-Walker metric: $k = 1, 0$ or -1. The $k = 1$ case describes a closed Universe of finite extent; in such a Universe two geodesics initially parallel to one another will eventually converge. The $k = 0$ case describes an infinite, flat Universe where two initially parallel geodesics remain so, and the $k = -1$ case describes an infinite open Universe where the two geodesics will eventually diverge. As mentioned above, observations favour a flat, $k = 0$ universe (Spergel et al., 2006).

1.1.3 The Expanding Universe

Observations of nearby galaxies show that the overwhelming majority are receding from us and that the speed of recession is larger for more distant galaxies (see figure 1.1). This observation forms the basis of what is usually known as the *Hubble Law* which states that there is a relationship between the speed of recession and the distance to a galaxy

$$v = H_0 d, \tag{1.6}$$

where v is the recession velocity, d is the distance and H_0 is the *Hubble constant*. This obser-

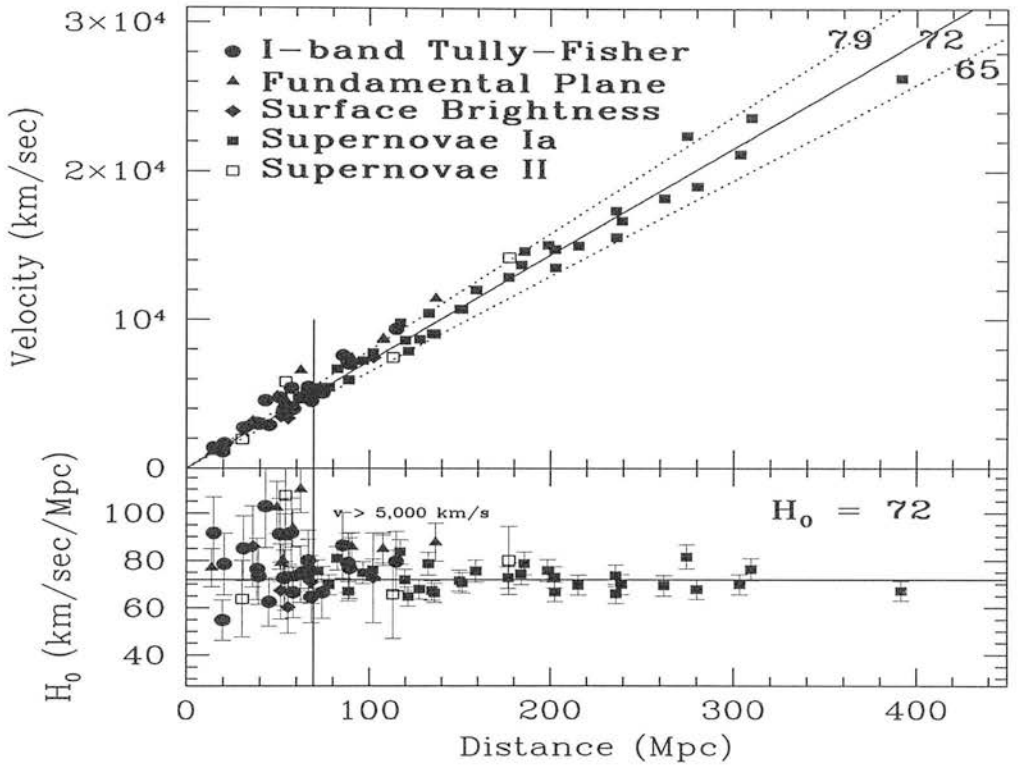

Figure 1.1: *From Freedman et al. (2001)*: Distance and recession velocity measurements for nearby galaxies measured by the Hubble Space Telescope Key Project. The linear relationship between galaxy distance and recession velocity is clearly visible, with $H_0 \simeq 0.72$.

vation provided the first indication that our Universe is expanding.

H_0 is the current value of the Hubble parameter, H, where

$$H = \frac{\dot{a}}{a}. \tag{1.7}$$

H_0 is commonly expressed in the form

$$H_0 = 100h\text{kms}^{-1}\text{Mpc}^{-1},$$

current observational limits place $h = 0.73^{+0.03}_{-0.03}$ (Spergel et al., 2006). The dimensionless scale factor, a, which appears in the Robertson-Walker metric (1.1) and the definition of the Hubble parameter (1.7) is a useful tool for expressing this expansion. Normalised to $a = 1$ today, the scale factor tells us how *comoving* distances are related to *proper* distances. Comoving

distances are defined so as to be independent of the background expansion of the Universe. This means that important scales at different epochs of the universe can all be compared in comoving units since they are normalised to the size that they would have today. This is not possible with proper units which tell us how large a physical scale was at the particular epoch in question. Comoving and proper distances are related via

$$r_{\text{proper}} = a r_{\text{com}},$$

and we can see then that equation (1.6) follows from considering the coordinate separation between two observers. If this separation is δr in comoving coordinates, then we see a proper separation of $\delta l = a\delta r$. The velocity attributed to the other observer in each case is then (Padmanabhan, 1993, p54)

$$\delta v = \frac{d}{dt}\delta l = \dot{a}\delta r = \frac{\dot{a}}{a}\delta l. \tag{1.8}$$

Distances in cosmology are often given in terms of a *redshift*, this is defined in terms of the frequency shift induced in a signal as it travels through an expanding spacetime

$$1 + z = \frac{\nu_{emitted}}{\nu_{observed}} = \frac{1}{a},$$

where ν denotes frequency and z denotes redshift. We can in fact see that $\nu \propto a^{-1}$ from equation (1.8).

Considering the propagation of a radial light signal enables us to obtain from the metric (1.1) the following important relationship between redshift and comoving distance:

$$R_0 r(z) = \int_0^z \frac{c}{H(z')}\, dz', \tag{1.9}$$

where r is comoving distance, z is redshift, c is the speed of light and H is the Hubble parameter.

1.1.4 Friedmann Equations

Expanding the Einstein equations (1.4) into time and spatial components leads us to the Friedmann equations that describe the evolution of the smooth background Universe given by our model.

$$\frac{\dot{a}^2}{a^2} = \frac{8\pi G}{3}\rho - \frac{kc^2}{a^2} \tag{1.10}$$

$$\frac{\ddot{a}}{a} = -\frac{4\pi G}{3}\left(\rho + 3\frac{p}{c^2}\right), \tag{1.11}$$

where ρ is energy density, p is pressure, k is the curvature constant and a is the dimensionless scale factor. Taking the derivative of equation (1.10) with respect to time and eliminating $\ddot{a}$ between the two equations leads to an equation of energy conservation

$$\dot{\rho} = -3\frac{\dot{a}}{a}\left(\rho + \frac{p}{c^2}\right).$$

This equation holds for all the components of the Universe individually and hence tells us about the evolution of their energy densities.

Using the value of the Hubble constant today, H_0, we can establish a *critical density* – the density that the Universe would have today if it were flat i.e. if $k = 0$,

$$\rho_{crit} = \frac{3H_0^2}{8\pi G}.$$

Then the densities of other components can then be expressed in dimensionless form relative to this critical density

$$\Omega_i = \frac{\rho_i}{\rho_{crit}},$$

where i denotes any component of the Universe e.g. dark matter, radiation (see Section 1.1.5). Evaluating equation (1.10) at the present day gives an expression for k

$$H_0^2 = \frac{8\pi G}{3}\rho_0 - kc^2 \Rightarrow k = \frac{H_0^2(\Omega_0 - 1)}{c^2},$$

where Ω_0 is the current dimensionless energy density in all components in the universe. Now we can recast the first Friedmann equation (1.10) in a different form:

$$H^2 = H_0^2\left(\Omega_{m,0}(1+z)^3 + \Omega_{r,0}(1+z)^4 + \Omega_{v,0} + (1-\Omega_0)(1+z)^2\right), \tag{1.12}$$

where $\Omega_{i,0}$ refers to the current value of Ω_i and $i = r$ (radiation), $i = m$ (matter) and $i = v$ (vacuum energy or the cosmological constant). This reveals the relationship between density

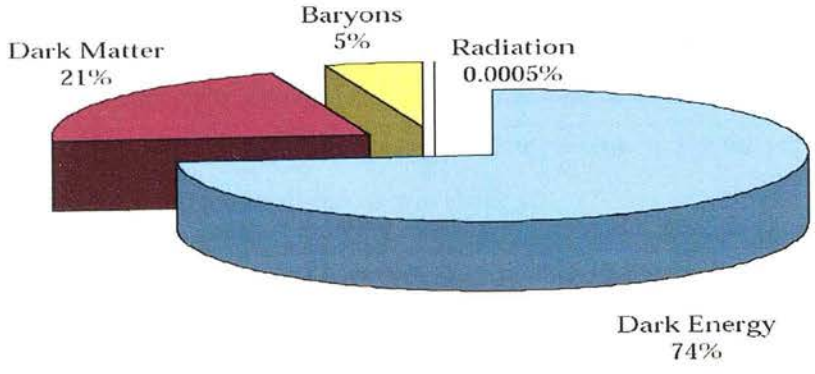

Figure 1.2: The energy budget of the Universe.

and the geometry of the universe. A universe with $\rho_{tot} < \rho_{crit}$ will have $\Omega_0 < 1$ and therefore a negative k, i.e. it is open; a universe with $\rho_{tot} = \rho_{crit}$ has $\Omega_0 = 1$ and is flat; finally, a universe with $\rho_{tot} > \rho_{crit}$ has $\Omega_0 > 1$ and is closed.

1.1.5 Components of the Universe

The matter that we see all around us and observe in stars and galaxies is baryonic matter, this only comprises around 5% of the total energy density in the Universe. Within current popular cosmological models, the remainder is almost completely accounted for by *dark matter* ($\sim 21\%$) and *dark energy* ($\sim 74\%$). At earlier times in its history, radiation accounted for a significant fraction of the total energy density, but today radiation makes up only $\sim 0.0005\%$ of the total energy density (see figure 1.2).

Baryons

Light elements are believed to form via *primordial nucleosynthesis* which took place at early times. Elements heavier than Lithium have been created since this time in stars. It is usually assumed that the conditions of the early universe are close to thermal equilibrium since the density was very high. The fluids of interest at this time are simple enough to be treated as perfect gases. Using thermodynamic arguments, the behaviour of different component species can be investigated as the universe expands and cools. Once the interaction timescale for a given species becomes much greater than the expansion timescale, the component in question 'decouples' or 'freezes out' from the rest of the Universe. The freeze out of such species creates

a set of relics from different stages of the expansion and cooling of which the CMB photons are one (see Section 1.3).

Once the temperature drops below $\sim 10^{10}$K, the weak interaction can no longer keep the abundances of protons and neutrons in equilibrium (e.g. Peacock, 1999, p294). After the loss of equilibrium, the temperature initially remains too high for protons and neutrons to combine to form nuclei; during the time taken for the universe to cool enough for this to happen, some fraction of the neutrons will decay. The first nuclei to form are Deuterium which in turn build up to form Helium. Since Deuterium is weakly bound, it forms late, and the temperature soon falls too low for further nuclear burning, thus very few elements beyond Helium form. The abundances of Deuterium and Helium which should be observed today as a result of this primordial nucleosynthesis can be calculated for different values of the baryon-to-photon ratio η, which in turn leads to a prediction for Ω_b. Current light element abundance measurements favour $0.017 \leq \Omega_b h^2 \leq 0.024$ (Yao et al., 2006), in good agreement with independent estimates from the CMB, measurements of gas in galaxy groups and line of sight observations of quasars.

Having a value for the baryon density Ω_b, we can compare this to estimates of the stellar density Ω_* obtained from observations of galaxies. It is found that $\Omega_* \sim 0.05\Omega_b - 0.1\Omega_b$ (e.g. Cole et al., 2001; Bell et al., 2003) and therefore that most of the baryons in the universe are not in the form of stars. Galaxy clusters contain vast reservoirs of shock-heated gas which is visible in the X-ray and a huge amount of gas also makes up the Intergalactic Medium (IGM).

Dark Matter

Dark matter interacts only through gravity and the weak interaction, which has important implications for its detection. There is a body of evidence that supports the existence of dark matter, mainly by inferring its presence gravitationally. First proposed by Zwicky in the 1930s to explain "missing mass" in the Coma cluster, dark matter came to the fore once again in the late 1960s when further evidence for its existence was found in the flattened rotation curves of many spiral galaxies. From a purely Keplerian description of galaxy rotation velocities, we would expect a decline $\propto r^{-1/2}$ in the velocities at large radii since the total (visible) mass within this radius could be expected to have reached a constant value. However, there is no decline observed for the majority of galaxies and instead the rotation curve is flat out to large

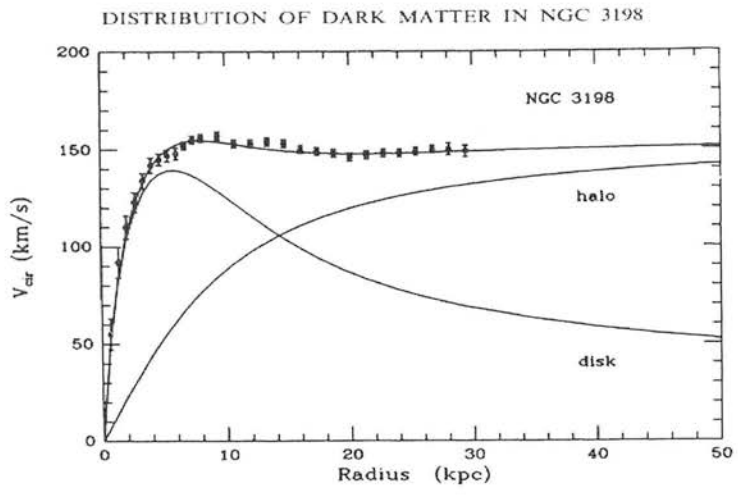

Figure 1.3: *From van Albada et al. (1985)*: Observations of the rotation curve of NGC 3198 (points with error bars) and best fit models for an exponential disk and spherical dark matter halo. The disk model clearly does not reproduce the observed flat rotation curve, yet the addition of a spherical halo can rectify this.

radii. The explanation is that there is additional (invisible) mass which is included within the radius of the orbit as r increases (see figure 1.3). This evidence has now been augmented by gravitational lensing, large scale structure, galaxy cluster and CMB observations. These are more difficult to explain in a universe without dark matter than galaxy or cluster dynamics.

Gravitational lensing exploits the gravitational deflection of light predicted by General Relativity and therefore provides a direct measure of *all* the matter in a region of space, not just the visible, baryonic matter. Recently, observations of 1E0657-56, the 'Bullet Cluster', using gravitational lensing have revealed that peaks in the mass distribution are not coincident with the locations of the visible mass in the cluster as indicated by *Chandra* X-ray observations of the hot intracluster gas (Clowe et al., 2006). The discrepancy has been attributed to the lensing observations revealing the dark matter distribution which differs from the gas distribution due to the gas lagging behind the dark matter as interactions slow it down. Further evidence is provided in the CMB angular power spectrum which contains a series of peaks whose heights constrain the amounts of baryonic and total matter; in models of structure formation which require the majority of the matter in the universe to be dark to reproduce observations, and in the galaxy power spectrum which constrains the amounts of baryonic and total matter. A further implication of this is that dark matter cannot be entirely baryonic.

Experiments are also being performed to attempt direct detection of dark matter particles as they pass through the Earth. The main technique involves the use of cryogenic detectors and searching for evidence of the interaction of dark matter particles with the detector material. The detectors are housed in deep mine shafts to shield them from cosmic rays. So far, no conclusive detections have been made, but detectors are now becoming sensitive to interesting regimes of parameter space (e.g. Araújo et al., 2006). Detection of dark matter in this manner would be completely independent from cosmological evidence for its existence.

Despite the evidence outlined here, dark matter remains a contentious issue, with alternative gravity theories also providing explanations for some of the observations cited as evidence for the existence of dark matter. Such theories alleviate the need for an additional invisible matter component in the Universe by altering the way in which gravity acts on large scales. This causes solar system dynamics to be unaffected but changes for example the behaviour of gravity on the scales needed to explain galaxy rotation curves without dark matter. The original alternative gravity theory was MOND (MOdified Newtonian Dynamics, Milgrom, 1983) , although it is generally accepted that this theory is not sufficient to explain, for example, cluster dynamics. This has now been joined by a plethora of other, often complex models e.g. TeVeS (Bekenstein, 2004); it remains to be seen whether any of these can explain all the observational evidence in support of dark matter.

Dark Energy

The existence of Dark Energy is arguably more controversial than dark matter. A universe component with a negative pressure, acting against the tendency for gravitational collapse that would exist in its absence, has been a recurring idea since Einstein first formulated his theory of Relativity. More recently, the idea of a Dark Energy component in the Universe has re-emerged with observations of supernovae (Riess et al., 1998; Perlmutter et al., 1999) showing that the Universe is not only expanding but that the expansion is occurring at an increasing rate (see figure 1.4).

A general Dark Energy model allows the equation of state, $w_{\rm DE}$, of the Dark Energy fluid to vary with time

$$p_{\rm DE}(z) = w_{\rm DE}(z)\rho_{\rm DE}(z)c^2.$$

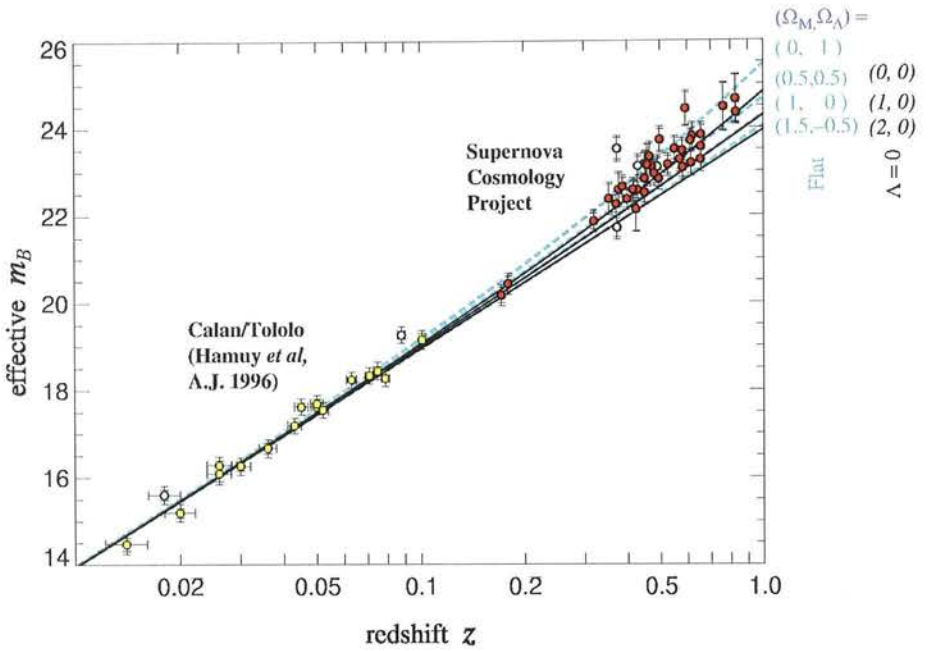

Figure 1.4: *From Perlmutter et al. (1999)*: Observations of supernovae give a Hubble diagram that is strongly inconsistent with a flat matter-dominated Universe. The high redshift supernovae are observed to lie further from us than would be expected in this case, providing evidence for a Dark Energy component in the Universe.

Assuming for the moment a Dark Energy dominated universe allows us to place an upper limit on the value of $w_{\rm DE}$ necessary for accelerated expansion from equation (1.11)

$$\begin{aligned} \ddot{a} &> 0 \Rightarrow -\frac{4\pi G}{3}\left(\rho + 3\frac{p}{c^2}\right) = -\frac{4\pi G}{3}\rho(1+3w_{\rm DE}) > 0 \\ \Rightarrow w_{\rm DE} &< -\frac{1}{3} \end{aligned}$$

A specific form for Dark Energy is the *cosmological constant*, which has a constant equation of state $w_{\rm DE} = -1$. This actually dates back to Einstein who introduced such a component to allow the Universe to be static – the accepted viewpoint at the time. If we assume that the equation of state for Dark Energy is constant and that the Universe is flat, then current constraints on the value of $w_{\rm DE}$ are $w_{\rm DE} = -0.97^{+0.07}_{-0.09}$ (Spergel et al., 2006), consistent with a cosmological constant.

The time evolution of the equation of state is often modelled via the following parametrisation of Dark Energy

$$w_{\rm DE}(a) = w_0 + (1-a)w_a,$$

at present, w_a cannot be well constrained by data.

1.2 Structure Formation in the Universe

As mentioned in Section 1.1.2, a smooth universe cannot form any structures. To modify the smooth universe model so that it describes the Universe that we actually inhabit, a perturbation to the smooth background description is made. This perturbed universe has small fluctuations in the density, pressure, velocity and potential fields present in the early universe. Fluctuations in the density field grow under gravitational instability, eventually forming the structures that we observe today. An inflationary model is often assumed to be the mechanism by which these small fluctuations are introduced.

1.2.1 Inflation

The basic idea of an inflationary universe is a period of expansion which then launches the Hubble expansion. Some of the simplest models for inflation suggest an energy scale of around 10^{14}GeV, corresponding to a duration t = 10^{-34}s (Kolb and Turner, 1990, p269). Inflation solves a number of problems that exist in the current cosmological paradigm.

The first of these is that the Cosmic Microwave Background (relic radiation from a time shortly after the Big Bang, see Section 1.3) is remarkably uniform across the entire sky, despite the fact that regions of space where we observe radiation with the same mean temperature today were not causally connected at the time of its emission. Inflation solves this *horizon problem* by rapidly expanding the Universe early in its history so that the entire region observed in the CMB is causally connected before this super-luminal expansion.

The *flatness problem* is also solved by inflation. This stems from the fact that the Universe is observed to be very close to flat today and must therefore also have been very close to flat in the past, which seems like fine-tuning. An inflation model can make this more natural given a long enough period of expansion because the curvature term can quite naturally be made a factor of at least 10^{60} times smaller than the density term in the Friedmann equation, thus solving the fine tuning issue.

Finally, in inflationary models, quantum fluctuations in the very early universe can provide seeds for the small fluctuations from which structures will evolve. The simplest models of inflation predict that these early fluctuations will have a Gaussian distribution and the focus of much research at present is determining whether or not this is the case e.g. Cabella et al. (2006); Rubiño-Martín et al. (2006).

The perturbations present in the density field can have one of two forms: *isocurvature* or *adiabatic*. Adiabatic perturbations are genuine perturbations in the energy density ($\delta\rho \neq 0$) and all components in the universe have the same form of perturbation

$$\delta \equiv \frac{\delta n_i}{n_i},$$

where i refers to any component and n is the local number density. It is usual to assume that the perturbations are adiabatic since scale invariant isocurvature perturbations lead to a source of anisotropy on large scales which is inconsistent with observations of galaxies and the CMB (Efstathiou and Bond, 1986). It is however possible that a small isocurvature component to the perturbations could exist (Trotta, 2007), but observations suggest that they are predominantly adiabatic.

1.2.2 Linear Structure Formation

How do we move from the existence of small fluctuations in a density field in the early universe to the complex structures that we observe today? On certain scales, the answer to this question can be demonstrated using relatively simple analytic arguments; it is these scales that are considered here. We deal only with *linear* structure formation, which means that only small perturbations to the density, velocity, potential and pressure fields are considered. Once these perturbations grow large, they enter the non-linear regime and a full analysis of their behaviour requires numerical simulation. Some analytic arguments can be applied in the quasi-linear regime to give an indication of the behaviour of perturbations that have passed beyond the linear regime, but exact arguments are not possible here. This Section outlines the evolution of perturbations in the linear regime and gives an insight into the process of structure formation in the universe.

Dynamics of structure formation

A full treatment of the perturbations introduced into the density, pressure, velocity and potential fields would require General Relativity. One would proceed by perturbing the background metric and the energy-momentum tensor (Padmanabhan, 1993), and following through the results of these perturbations to finish with equations expressing the evolution of the perturbations. We consider here a Newtonian approximation rather than the full General Relativistic treatment. This is sufficient for small enough perturbations because small perturbations imply that we are considering weak fields and in such cases the Newtonian approximation is valid. In general, this analysis holds for perturbations on scales much smaller than the Hubble radius c/H. Perturbations on larger scales require a full General Relativistic treatment to deal with gauge issues. The results that we would obtain from a full treatment are formally similar to those obtained from a Newtonian approximation (on the scales where this is valid).

We will work in a proper coordinate system with position given by $\mathbf{x}$ and velocity $\mathbf{v}$. In this coordinate system, the homogeneous background has velocities given by the Hubble law $\mathbf{v}_0 = H\mathbf{x}$. All smooth background quantities are labelled with the subscript 0 and small perturbations to the background are $\delta\rho, \delta p$ etc. Growth of inhomogeneities in the density field can begin as soon as the universe becomes matter dominated (although baryonic inhomogeneities cannot grow until after decoupling). We consider below a single fluid model for collisional matter since it is then an easy matter of ignoring the pressure terms to convert this to a model for collisionless matter.

Equations of fluid motion

We begin with the equations of motion for a non-relativistic fluid (since the Cosmological Principle tells us that the smooth background universe can be described as a perfect fluid)

$$\frac{D\rho}{Dt} = -\rho\nabla.\mathbf{v} \qquad \text{Continuity Equation} \tag{1.13}$$

$$\frac{D\mathbf{v}}{Dt} = -\frac{\nabla p}{\rho} - \nabla\Phi \qquad \text{Euler Equation} \tag{1.14}$$

$$\nabla^2\Phi = 4\pi G\rho \qquad \text{Poisson equation} \tag{1.15}$$

where

$$\frac{D}{Dt} = \frac{\partial}{\partial t} + (\mathbf{v}.\nabla),$$

is the *convective derivative* i.e. the derivative with respect to the fluid motion, ρ is the density, v the velocity, p the pressure and Φ the potential field.

- The continuity equation is simply an expression of conservation of mass. It states that the change in the mass inside an element of the fluid is equal to the difference between the mass convected into the element and the mass convected out of the element.

- The Euler equation states that the acceleration of a small fluid element (per unit volume) $\rho D\mathbf{v}/Dt$, is due to the difference in pressure acting on opposite sides of the element (per unit volume), $-\nabla p$, and the gravitational force (per unit volume) acting on the element, $-\rho\nabla\Phi$.

- The Poisson equation tells us about the relationship between the potential fluctuations and the density perturbations that cause them.

As $\mathbf{v}_0 = H\mathbf{x}$ and ρ_0 is homogeneous, we find that for the smooth background

$$\begin{aligned} \frac{\partial \rho_0}{\partial t} &= -3H\rho_0 \\ \frac{\partial \mathbf{v}_0}{\partial t} + H\mathbf{v}_0 &= -\frac{\nabla p_0}{\rho_0} - \nabla\Phi_0 \\ \nabla^2\Phi_0 &= 4\pi G\rho_0. \end{aligned}$$

First order solutions

Consider small perturbations to the background density, velocity, pressure and potential fields i.e. $\delta\rho \ll 1$ etc

$$\begin{aligned} \rho &= \rho_0 + \delta\rho \\ \mathbf{v} &= \mathbf{v}_0 + \delta\mathbf{v} \\ p &= p_0 + \delta p \\ \Phi &= \Phi_0 + \delta\Phi. \end{aligned}$$

Substituting the above into equations (1.13), (1.14) and (1.15) and ignoring terms higher than first order in the perturbations, we can deduce

$$\begin{aligned} \frac{\partial \delta\rho}{\partial t} + (\mathbf{v}_0.\nabla)\delta\rho &= -\rho_0 \nabla.\delta\mathbf{v} - \delta\rho \nabla.\mathbf{v}_0 \\ \frac{\partial \delta\mathbf{v}}{\partial t} + (\mathbf{v}_0.\nabla)\delta\mathbf{v} + (\delta\mathbf{v}.\nabla)\mathbf{v}_0 &= -\frac{\nabla\delta p}{\rho_0} - \nabla\delta\Phi \\ \nabla^2\delta\Phi &= 4\pi G\delta\rho, \end{aligned}$$

recalling the homogeneity of ρ_0 and assuming an equation of state for the smooth background $p_0 = w\rho_0$ where w is independent of position (a condition of adiabatic perturbations).

Using the smooth background equations to re-express $\partial\rho_0/\partial t$ and defining $\delta = \delta\rho/\rho_0$, the *overdensity*, gives the new form for the continuity equation

$$\frac{\partial \delta}{\partial t} + (\mathbf{v}_0.\nabla)\delta = -\nabla.\delta\mathbf{v}. \tag{1.16}$$

The first order form of the Euler equation can be deduced by noting

$$\begin{aligned} [(\delta\mathbf{v}.\nabla)\mathbf{v}_0]_k &= \delta v_j \, \nabla_j \, (\mathbf{v}_0)_k \\ &= \delta v_j \, \nabla_j \, H \, x_k = H \, \delta v_j \, \delta^j_k = H \, \delta v_k \\ &= [H \, \delta\mathbf{v}]_k \, , \end{aligned}$$

so that

$$\frac{\partial \delta\mathbf{v}}{\partial t} + (\mathbf{v}_0.\nabla) \, \delta\mathbf{v} = -H\delta\mathbf{v} - \frac{\nabla\delta p}{\rho_0} - \nabla\delta\Phi. \tag{1.17}$$

The Poisson equation is easily seen to reduce to

$$\nabla^2\delta\Phi = 4\pi G\delta\rho = 4\pi G\rho_0\delta. \tag{1.18}$$

We now have a set of 3 equations for 4 unknowns so one final equation is needed to complete the set. This is the equation relating density and pressure

$$c_s^2 = \frac{\delta p}{\delta\rho},$$

where c_s is the sound speed.

These equations hold as long as the perturbations remain small. Once they become large, linear theory fails and the above becomes invalid. In general, the full non-linear problem needs to be analysed numerically, which is where cosmological N-body simulations come into their own.

Comoving coordinates

The above equations have been formulated in *Eulerian* coordinates, using proper lengths. Often in fluid dynamics we choose to use *Lagrangian* coordinates that move with the fluid. This means that the Lagrangian position of a particle in the fluid is fixed in time.

As with many situations in cosmology the analysis above becomes simpler if we switch to a coordinate system that incorporates the background expansion i.e. comoving coordinates, see Section 1.1.3. In a smooth universe, comoving coordinates are an example of a Lagrangian coordinate system. However, when we consider a perturbed version of this universe comoving coordinates are no longer Lagrangian as they do not completely move with the fluid. Although the background expansion is incorporated, peculiar velocities (components of the velocity of an object *not* due to the background expansion) are not.

To put the above equations into comoving coordinates we need the position coordinates to change to incorporate the expansion factor given by $a(t)$

$$\mathbf{x} = a\mathbf{r},$$

where $\mathbf{x}$ is the Eulerian position and $\mathbf{r}$ is the comoving position. Similarly, the peculiar velocity will change to

$$\delta\mathbf{v} = a\mathbf{u},$$

where $\mathbf{u}$ is the comoving peculiar velocity. Now

$$\nabla_p = \frac{\partial}{\partial \mathbf{x}} = \frac{\partial}{a\partial \mathbf{r}} = \frac{\nabla_c}{a},$$

where the p and c subscripts refer to proper (Eulerian) and comoving coordinates respectively.

The time coordinates are also altered so that time derivatives are with respect to the expansion of the smooth background

$$\frac{d}{dt} = \frac{\partial}{\partial t} + (\mathbf{v}_0.\nabla).$$

If $\mathbf{g} = -\nabla_p \delta\Phi$ then rewriting equations (1.16), (1.17) and (1.18) in comoving coordinates gives

$$\dot{\delta} = -\nabla_c.\mathbf{u} \tag{1.19}$$

$$\dot{\mathbf{u}} + 2H\mathbf{u} = \frac{\mathbf{g}}{a} - \frac{\nabla_c \delta p}{a^2 \rho_0} \tag{1.20}$$

$$\nabla_c^2\, \delta\Phi = 4\pi G \rho_0\, \delta\, a^2, \tag{1.21}$$

where $\dot{} = d/dt$. We now drop the c subscript and take $\nabla = \nabla_c$ in what follows.

1.2.3 Growing Modes

The above equations describe the evolution of the density, velocity, potential and pressure fields. In order to learn about the formation of structures it is necessary to study the evolution of the density field. Beginning with the continuity equation and eliminating the velocity field using the Euler equation gives a second order differential equation for the density field, often known as the *growth equation*,

$$\begin{aligned}
\dot{\delta} &= -\nabla.\mathbf{u} \\
\Rightarrow \ddot{\delta} &= -\nabla.\dot{\mathbf{u}} = -\nabla.\left(-2H\mathbf{u} + \frac{\mathbf{g}}{a} - \frac{\nabla\delta p}{a^2\rho_0}\right) \\
\Rightarrow \ddot{\delta} + 2H\dot{\delta} &= 4\pi G\rho_0\delta + \frac{c_s^2\nabla^2\delta}{a^2}.
\end{aligned}$$

If we move to Fourier space, expanding the density perturbation in Fourier modes $\delta \propto e^{-i\mathbf{k}.\mathbf{r}}$, then each k mode evolves independently and hence

$$\begin{aligned}
\ddot{\delta}_k + 2H\dot{\delta}_k &= 4\pi G\rho_0\delta_k - \frac{c_s^2 k^2 \delta_k}{a^2} \\
\Rightarrow \ddot{\delta}_k + 2H\dot{\delta}_k &= \left(4\pi G\rho_0 - \frac{c_s^2 k^2}{a^2}\right)\delta_k.
\end{aligned} \tag{1.22}$$

The sign of the term in brackets on the right hand side of equation (1.22) determines the behaviour of the density perturbations. In the absence of the damping term $2H\dot{\delta}$ (equivalent to considering this equation in a non-expanding universe), the behaviour of the solutions may be simply analysed: if the term in brackets were positive $4\pi G\rho_0 > c_s^2 k^2/a^2$ then we would have growing and decaying solutions given by the exponentials e^{At}, e^{-At} where $A = \sqrt{4\pi G\rho_0 - c_s^2 k^2/a^2}$; if the term in brackets were negative, we would have oscillatory solutions. The damping term makes such an analysis more complex but it remains true that when $4\pi G\rho_0 \gg c_s^2 k^2/a^2$ we will have growing and decaying solutions (although due to the damping, power law solutions are more likely than exponentials) and when $4\pi G\rho_0 \ll c_s^2 k^2/a^2$ we will have oscillatory solutions.

Physically, this different behaviour is due to whether or not pressure in the fluid can be neglected. If this is the case, the solutions are growing and decaying modes; if pressure cannot be neglected, we have oscillatory solutions. This arises because gravity acts to make structures collapse and pressure acts to oppose it, thus setting up an oscillation. The physical scale at which the gravitational ($4\pi G\rho_0$) and pressure ($c_s^2 k^2/a^2$) terms balance is called the *Jeans length*, $\lambda_J = c_s\sqrt{\pi/G\rho}$. Long wavelength modes ($\lambda \gg \lambda_J$) can grow and short wavelength modes ($\lambda \ll \lambda_J$) oscillate. As λ_J is time dependent in an expanding Universe, a given mode λ can have periods of growth and oscillation governed by the evolution of λ_J

For cold collisionless matter, there is no pressure term and the equation for the growth of density perturbations simplifies to

$$\ddot{\delta} + 2H\dot{\delta} = 4\pi G\rho_0\delta. \tag{1.23}$$

This equation can be solved analytically in certain special cases, otherwise it must be solved numerically or a numerical approximation to the solution must be employed.

In the case of a universe containing dark matter and dark energy with a constant equation of state w we can see that the Hubble constant is a solution to equation (1.23) for certain values of w

$$\ddot{H} + 2H\dot{H} = 4\pi GH\left(\rho_m + \rho_\Lambda\left[-2(1+w) + 3(1+w)^2\right]\right).$$

Hence, $\delta = H$ solves equation (1.23) if $1 + 4w + 3w^2 = 0$ or if $\rho_\Lambda = 0$ i.e. if $w = -1/3$ or $w = -1$ or $\rho_\Lambda = 0$.

In these cases (assuming now a flat universe) H is a decaying mode as we can see from $\dot{H} = -4\pi G(\rho_m + \rho_\Lambda(1+w)) \leq 0$ with $\rho_m, \rho_\Lambda \geq 0$ and $w = -1/3, -1$. In the case of structure formation, the growing mode is of most interest since, as its name suggests, the decaying mode decreases to become negligible over time. This decaying mode corresponds to a situation where a perturbation with initial overdensity and velocity are arranged such that the initial velocity perturbation eventually 'undoes' the density perturbation (Kolb and Turner, 1990, p347). To find the growing mode in any of the cases described above ($w = -1, w = -1/3$ etc), we use the reduction of order method.

Assume that the second solution has the form $\delta_2(t) = f(t)\delta_1(t) = f(t)H(t)$. Then,

$$\begin{aligned} \ddot{\delta_2} &= \ddot{f}\delta_1 + 2\dot{f}\dot{\delta}_1 + f\ddot{\delta}_1 \\ \Rightarrow \frac{\ddot{f}}{\dot{f}} &= -\frac{2\dot{\delta}_1 + 2H\delta_1}{\delta_1} \\ \Rightarrow f(t) &= B\int \frac{1}{\delta_1^2 a^2}dt = B\int \frac{1}{\dot{a}^2}dt, \end{aligned}$$

where B is a constant and a is the scale factor. Usually the value of the B is found by requiring that $\delta_2 = a$ in the matter-dominated era, then the growing mode solution is

$$\delta_2 = \frac{5}{2}H_0^2\Omega_{m,0}H\int \frac{1}{\dot{a}^2}dt. \tag{1.24}$$

A popular numerical approximation for the growing mode solution to equation (1.23) in a flat universe with a cosmological constant is (Carroll et al., 1992)

$$\delta_2 = \frac{5}{2}\frac{\Omega_m(a)\,a}{\Omega_m^{4/7}(a) - \Omega_\Lambda(a) + \left(1 + \frac{\Omega_\Lambda(a)}{70}\right)\left(1 + \frac{\Omega_m(a)}{2}\right)}.$$

More recently, a fit to the growing mode in a flat Universe with dark energy that has a constant equation of state (not necessarily $w = -1$) has been found (Percival, 2005).

1.2.4 Peculiar Velocity Fields

Inhomogeneities in the matter distribution imply the existence of small fluctuations in the CMB as discussed in Section 1.3, but they also imply that galaxies should have peculiar velocities i.e. velocities that are not due to the Hubble flow. The comoving peculiar velocity field $\mathbf{u}$ is

related to the density field δ in the manner given by equations (1.19) and (1.20). Moving to Fourier space allows us to re-express the velocity field in terms of the density field.

Before we begin, it is useful to decompose the velocity field into rotational and irrotational terms

$$\mathbf{u} = \mathbf{u}_{rot} + \mathbf{u}_{irrot},$$

where

$$\nabla.\mathbf{u}_{rot} = 0 \Rightarrow \mathbf{k}.\mathbf{u}_{rot} = 0 \qquad \nabla \wedge \mathbf{u}_{irrot} = 0 \Rightarrow \mathbf{k}.\mathbf{u}_{irrot} = |\mathbf{k}||\mathbf{u}_{irrot}|.$$

Now from equations (1.19) and (1.20) we find

$$\dot{\delta}_k - \frac{i\mathbf{k}.\mathbf{u}_{irrot}}{a} = \dot{\delta}_k - \frac{iku}{a} = 0,$$

where $k = |\mathbf{k}|$ and $u = |\mathbf{u}_{irrot}|$. Then

$$u = \frac{a\,\dot{\delta}_k}{ik} \Rightarrow \mathbf{u}_{irrot} = \frac{a\,\dot{\delta}_k}{ik}\hat{\mathbf{k}}.$$

From the Euler equation (1.20),

$$\begin{aligned}
&\frac{d(a\mathbf{u}_{rot} + a\mathbf{u}_{irrot})}{dt} - i\,\mathbf{k}\,c_s^2\,\delta_k - i\,\mathbf{k}\,\delta\Phi = 0 \\
&\Rightarrow \hat{\mathbf{k}}_\perp \left\{ \frac{d(a|\mathbf{u}_{rot}|)}{dt} \right\} + \hat{\mathbf{k}} \left\{ \frac{d}{dt}\left(\frac{a^2\dot{\delta}_k}{ik} \right) - i\,k\,c_s^2\,\delta_k - i\,k\,\delta\Phi \right\} = 0 \\
&\Rightarrow \frac{d\mathbf{u}_{rot}}{dt} = 0 \\
&\Rightarrow \mathbf{u}_{rot} = \frac{const}{a}.
\end{aligned}$$

Hence we see that $\mathbf{u}_{rot}$ decays and if we consider a late enough epoch, this mode will be negligible. The peculiar velocity field can therefore be expressed entirely in terms of the irrotational mode which is proportional to $\mathbf{k}$. We therefore drop the *irrot* subscript in the following. From the continuity equation (1.19) once again

$$\begin{aligned}
\dot{\delta}_k &= \frac{i}{a}\mathbf{k}.\mathbf{u}_k \\
\mathbf{u}_k &= -\frac{ia}{k}\,\hat{\mathbf{k}}\,\dot{\delta}_k.
\end{aligned}$$

The time derivative of the growing mode can be expressed

$$\dot{\delta} = \dot{a}\frac{d\delta}{da} = H\,\delta\,f(\Omega) \text{ where } f = \frac{a}{\delta}\frac{d\delta}{da}. \tag{1.25}$$

and hence,

$$\begin{aligned} \mathbf{u}_k &= -\frac{ia}{k^2} H\, f\, \mathbf{k}\, \delta_k \\ \frac{-k^2}{a^2}\delta\Phi_k &= \frac{i}{a}\mathbf{k}.\mathbf{g}_k = 4\pi G\rho_0\delta_k \text{ (Poisson)}, \end{aligned} \tag{1.26}$$

but by definition $\mathbf{g}_k$ is parallel to $\mathbf{k}$ so

$$\begin{aligned} \Rightarrow \mathbf{u}_k &= \frac{Hf}{4\pi G\rho_0}\mathbf{g}_k \\ \Rightarrow \mathbf{u}_k &= \frac{2f}{3H\Omega_m}\mathbf{g}_k. \end{aligned}$$

Therefore, in real space,

$$\mathbf{u} = \frac{2f}{3H\Omega_m}\mathbf{g}. \tag{1.27}$$

Linear perturbation theory therefore implies that peculiar velocities are proportional to gravitational acceleration.

1.2.5 Power Spectra

The overdensity field δ evolves from some initial state to the end state that we observe today. The evolution is most simply described in Fourier space, in terms of the Fourier modes of the overdensity field δ_k. For each value of k, δ_k describes the overdensity field on a particular physical scale. The evolution of a particular mode in the early Universe is dependent on its scale. There are 3 basic stages of evolution characterised by the order in which two events affect a single mode: the time of matter-radiation equality and the time at which the mode enters the horizon (Dodelson, 2003, p182). The time of horizon entry describes when the physical scale of the mode in question becomes smaller than the radius of the causally connected universe at that time.

A transfer function $T(k)$ can be defined that encodes information about the evolution of the different modes through the epochs of matter-radiation equality and horizon crossing. After this

stage and outwith the non-linear regime, the evolution of modes on all scales is the same and can be encoded using the growth function defined in Section 1.2.3. The transfer function can be calculated theoretically using the Boltzmann equations which describe the evolution of each species in the universe (Eisenstein and Hu, 1998).

The evolution of the gravitational potential Φ (which is easily related to the overdensity δ via Poisson's equation) can be expressed in terms of the same transfer function, its value today is related to a primordial potential set up during inflation via (Dodelson, 2003, p183)

$$\Phi(\mathbf{k}, a) = \Phi_p(\mathbf{k}) \times \{T(k)\} \times \{\text{Growth Function}(a)\}\,,$$

where Φ_p is the primordial potential set up during inflation – theory can tell us the form of Φ_p.

The power spectrum of the density field is defined by

$$\left\langle \delta(\mathbf{k})\delta^*(\mathbf{k}')\right\rangle = (2\pi)^3 P(k)\delta^3(\mathbf{k}-\mathbf{k}'),$$

where the angular brackets denote an ensemble average. The power spectrum encodes a wealth of useful information and its form is predictable from theory once a cosmological model is fixed. The form of the matter power spectrum can be expressed as (Dodelson, 2003, p184)

$$P(k,a) = 2\pi^2 \delta_{\mathrm{H}}^2 \frac{k^n}{H_0^{n+3}} T^2(k) \left(\frac{D_1(a)}{D_1(a=1)}\right),$$

where δ_{H} is the amplitude at horizon crossing predicted by inflation, n is the spectral index (an inflationary parameter) and D_1 is the growth function. Here the transfer function has been normalised so that $T(k) = 1$ for the largest scale modes.

Figure 1.5 shows the total matter power spectrum calculated using the fitting formula of (Eisenstein and Hu, 1998). There is an obvious turnover in the power spectrum at around $k = 0.02h\mathrm{Mpc}^{-1}$ which corresponds to the scale of a mode that enters the horizon at matter-radiation equality. Modes that enter the horizon before this time (those corresponding to smaller physical scales) have their growth retarded. This can be explained physically by considering a universe containing only dark matter and radiation. Before matter-radiation equality, most of the energy in the Universe is in the radiation. Consider a small scale dark matter perturbation. Photons will be able to stream out of a perturbation of this size before matter-radiation equality and will take most of the energy in the perturbation with them. This loss of energy retards the growth of the dark matter perturbation. On larger scales, photons will not have

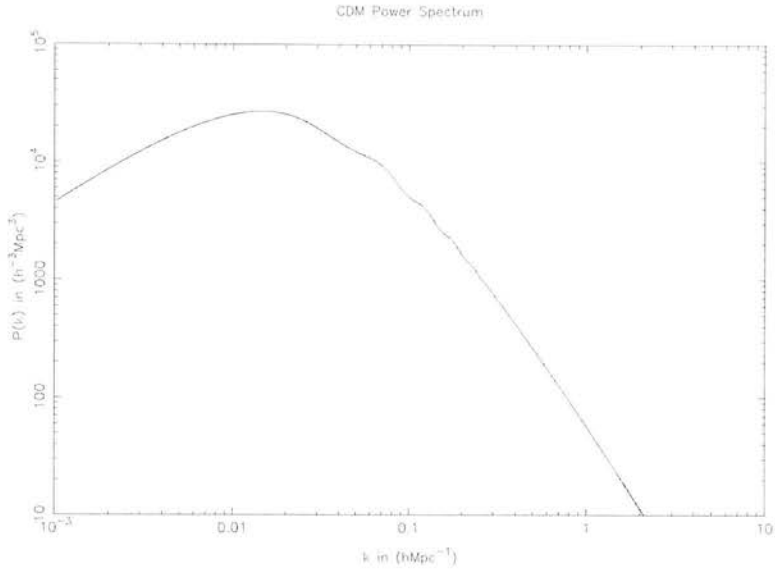

Figure 1.5: The matter power spectrum for a flat cosmological model with $h = 0.74$, $\Omega_m = 0.24$ and $\Omega_b = 0.04$.

time to stream out of the perturbation and there is no energy loss. In this case the growth is not retarded. Including baryons in this picture does not significantly change the results. Using this picture, we can also understand that the earlier a mode enters the horizon (the smaller the physical scale we are considering), the greater the suppression of its growth. Hence the power spectrum shows a turnover and is a decreasing function of k on small scales. On large scales $T(k) = 1$ and the spectral index n is usually taken as $n \simeq 1$ so we see $P(k) \propto k$ on large scales.

Oscillations are visible in the spectrum for $k \gtrsim 0.04h\text{Mpc}^{-1}$, these are due to the presence of baryons in the universe. As is explained in more detail in Section 1.3, photons and baryons were tightly coupled in the early universe and undergoing a harmonic motion with decaying amplitude since at this time, the amplitude of photon-baryon oscillations could not grow. When the photons and baryons decoupled slightly after recombination, the oscillations were imprinted in the baryon distribution and thus appear in a weak form in the total matter power spectrum. These oscillations are generated by the same mechanism that leads to the peaks in the angular power spectrum of the CMB.

The overall normalization of the power spectrum is not fixed by theory. The parameter δ_{H} refers to the amplitude of scalar perturbations to Φ at horizon crossing but different inflationary scenarios will lead to different values of δ_{H}. Instead, the amplitude of the matter power

spectrum is fixed by observation using the parameter $\sigma_8 = \sigma(8\,h^{-1}\mathrm{Mpc})$ which describes the strength of matter clustering on a scale of $8\,h^{-1}$Mpc and is defined by

$$\sigma^2(R) = 4\pi \int \frac{dk}{k} k^3 P(k) W^2(k = R), \tag{1.28}$$

where $W(k)$ is the Fourier transform of the spherical top hat window function which defines the scale at which we fix the normalisation and $P(k)$ is the linear extrapolation of the matter power spectrum. Current observations place reasonable constraints on its value $\sigma_8 = 0.75^{+0.05}_{-0.06}$ (Spergel et al., 2006). Also useful is the dimensionless form of the power spectrum $\Delta^2(k)$

$$\Delta^2(k) = \frac{k^3 P(k)}{2\pi^2}.$$

which is then related to σ by

$$\frac{d\sigma^2}{d\ln k} = \Delta^2(k)$$

1.2.6 Galaxy Bias

At this point, it is necessary to consider carefully exactly what it is that we measure. When we observe galaxies, we see light not mass, and the light that we observe comes from only the baryonic material in the Universe. In order to measure the matter power spectrum or any other indicator of the strength of matter clustering, it is necessary to make some assumptions about the extent to which the light that is observed relates to the underlying matter distribution. The simplest relationship that could be imagined between some tracer of the matter distribution and the distribution itself is the *linear bias relation* (Peacock, 1999, p526)

$$\Delta^2_{tracer} = b^2 \Delta^2_{mass},$$

where b is the bias parameter. Different surveys are sensitive to light from different types of galaxies. For example, surveys that select galaxies in red light will be more likely to observe elliptical galaxies which have been shown to inhabit the denser regions of the Universe. We would therefore expect to recover a stronger clustering signal from this type of survey than one which selected galaxies in blue light since bluer galaxies inhabit less dense regions of the Universe (Norberg et al., 2002). Biases of $b = 1.10 \pm 0.08$ (Lahav et al., 2002) and

$b = 1.04 \pm 0.11$ (Verde et al., 2002) have been measured for the 2dF survey using different techniques. The SDSS survey contains more strongly clustered red galaxies, and as a result shows more small scale power if the normalization is chosen to match 2dF on large scales (Cole et al., 2006).

By considering the power spectrum on the largest linear scales, the different measures of clustering can all be rescaled to agree with one fixed measure and the relative bias between these can be calculated. The fact that this is possible and that the agreement between the rescaled datasets is so good suggests that there is a genuine underlying relationship between what we measure from large scale galaxy clustering and the underlying mass fluctuations (Peacock and Dodds, 1994). If this were not the case, then it would require some unusual physics to allow this degree of agreement in the rescaled clustering data which is obtained from different tracers.

In addressing the question of why the galaxy distribution may be biased with respect to the matter distribution, it is necessary to consider the manner in which structures form. We believe that galaxies form within the potential wells defined by the collapse of dark matter haloes (White and Rees, 1978). On large scales, bias in the galaxy distribution is therefore directly related to the bias in the distribution of dark matter haloes. Cole and Kaiser (1989) analysed the latter using Press-Schechter theory (Press and Schechter, 1974) together with the idea that an object of a given mass will collapse sooner if it lies in a region which is overdense on large scales (White et al., 1987). One finds from this (Mo and White, 1996)

$$b = 1 + \frac{\nu^2 - 1}{\delta_c}$$

where b is the bias in the distribution of dark matter haloes, δ_c is the density threshold for collapse and $\nu = \delta_c/\sigma(M)$ with σ defined in equation (1.28) i.e. this is a measure of the threshold density relative to the rms density fluctuation.

1.3 Cosmic Microwave Background

1.3.1 The Cosmic Microwave Background

In the hot, dense early Universe, hydrogen and helium are fully ionised and photons scatter off free electrons. The time between successive Thomson scatterings of photons and electrons is

much shorter than the expansion timescale of the Universe, which is given by the Hubble time $1/H$. This means that the photon-baryon fluid is *tightly coupled* as the interaction rate of the two species is so high. As a result, small fluctuations in the baryon distribution are matched by fluctuations in the distribution of photons.

As the Universe cools, electrons and protons begin to recombine as hydrogen atoms and the time between successive Thomson scatterings increases as the number of free electrons falls. For temperatures lower than 0.3eV (Kolb and Turner, 1990, pp78-80) the Thomson scattering interaction rate is able to drop below the expansion rate. At this point, the photons decouple from the baryons and thermal equilibrium between these two species is lost. The photons are now able to *free stream* across the Universe, and it is these photons that we observe today as the CMB. The time of decoupling of the photons is called *last scattering*, which occurred roughly 300,000 years after the Big Bang. Since last scattering occurs at a redshift of approximately $z \sim 1100$, when the photon temperature was $T \sim 3000$K, the temperature scaling relation gives

$$T(z=0) = \frac{T(z)}{1+z} \simeq 2.7\text{K}.$$

The radiation has also been redshifted to peak at microwave wavelengths. Such background radiation with a blackbody spectrum, an average temperature of around 3K and small temperature fluctuations about this mean is a prediction of the Big Bang model.

The microwave background was first observed in 1965 by Arno Penzias and Robert Wilson (Penzias and Wilson, 1965) and its discovery made the Big Bang cosmology the most plausible of the cosmological models of the time and provided evidence against other previously popular models such as the steady state theory. It took a further 28 years before technology advanced enough to enable us to observe the tiny temperature fluctuations in this radiation. These fluctuations, of the order of 1 part in 10^5, must be present for any structures to have developed in the Universe under our current models of structure formation. The first detection of these was made in 1992 by the COBE satellite (Smoot et al., 1992). The most recent CMB temperature data has been taken by the Wilkinson Microwave Anisotropy Probe (WMAP, Hinshaw et al., 2006), a satellite mission that has been observing the microwave sky since 2001. The WMAP data has enabled us to find cosmological parameters to unprecedented accuracy.

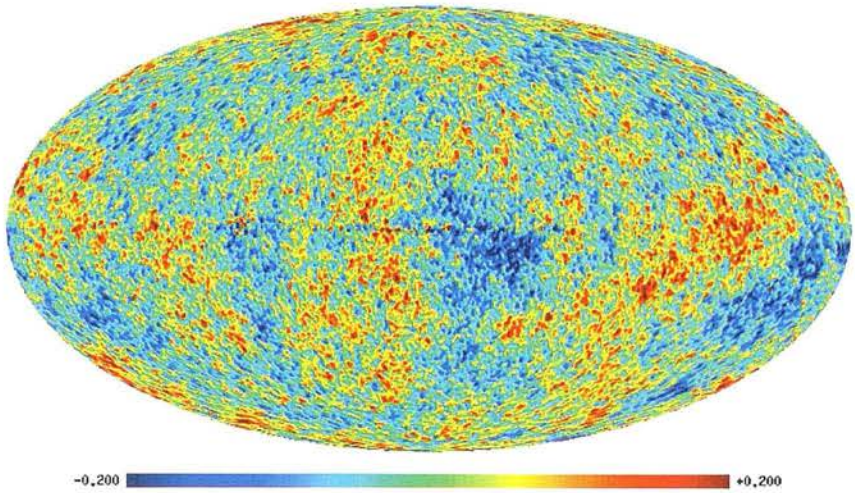

Figure 1.6: The CMB temperature fluctuations around the mean in mK as observed by WMAP (Hinshaw et al., 2006). The temperature fluctuations shown above are due to inhomogeneities in the photon distribution at the time when photons decoupled from baryons around 300,000 years after the Big Bang.

1.3.2 Temperature Anisotropies

Once the photons enter the free streaming epoch, their distribution carries information about the spatial distribution that they had at last scattering and therefore about the spatial distribution of the baryons at that time. We see variations in the spatial distribution of the photons at last scattering as angular variations in their temperature distribution across the sky (see figure 1.6).

In order to study the temperature fluctuations, it is convenient to expand them in terms of spherical harmonics and then to study their angular power spectrum (see also Appendix A)

$$\frac{T(\mathbf{x},\hat{\mathbf{n}},\eta)-T_0}{T_0} = \Theta(\mathbf{x},\hat{\mathbf{n}},\eta) = \sum_{\ell}\sum_{m} a_{\ell m}(\mathbf{x},\eta)\, Y_{\ell m}(\hat{\mathbf{n}}), \tag{1.29}$$

where $Y_{\ell m}(\hat{\mathbf{n}})$ are spherical harmonics, $\hat{\mathbf{n}}$ is a unit direction vector, η is conformal time and T_0 is the average temperature of the CMB (Dodelson, 2003, p240). From this definition,

$$a^T_{\ell m} = \int \Theta(\mathbf{x},\hat{\mathbf{n}},\eta)\, Y^*_{\ell m}(\hat{\mathbf{n}})\, d\Omega = \int e^{i\mathbf{k}\cdot\mathbf{x}}\, \frac{d^3k}{(2\pi)^3} \int \Theta(\mathbf{k},\hat{\mathbf{n}},\eta)\, Y^*_{\ell m}(\hat{\mathbf{n}})\, d\Omega \tag{1.30}$$

and the angular power spectrum C_ℓ is given by

$$\langle a^*_{\ell m}\, a_{\ell' m'}\rangle = C_\ell\, \delta_{\ell\ell'}\, \delta_{mm'}. \tag{1.31}$$

The temperature fluctuations in the CMB can be divided into two broad categories: *primary anisotropies* which are due to the non-uniformity of the photon distribution at last scattering and *secondary anisotropies* which are due to the interaction of the CMB photons with matter on their journey to us. In Appendices A and B, the full calculation of the temperature anisotropies is presented following the method of Dodelson (2003). In the next two Sections, selected results are presented from these Appendices and discussed more qualitatively.

Primary anisotropies

It can be shown using the equation that describes the photon distribution (A.51) and the equations that relate the photon distribution to the angular power spectrum (1.30) and (1.31), what effect we expect the different contributions to the CMB temperature anisotropies to have in the power spectrum.

The monopole and dipole moments of the photon distribution are the only non-negligible contributions in the tight-coupling regime (see Section A.2). These are modified during free-streaming in a manner which can be calculated (see Section A.3). On large scales, only the monopole term is significant and the angular power spectrum satisfies (see Appendix B)

$$\ell(\ell+1)C_\ell^{SW} = \frac{\pi}{2}\left(\frac{\Omega_m g(\eta_*)}{a(\eta_*)}\right)^2 \delta_H^2, \tag{1.32}$$

where $g(\eta_*)$ is the growth function (see Section 1.2.3) and δ_H is defined in Section 1.2.5. This is the *Sachs-Wolfe* contribution to the CMB angular power spectrum, shown in figure 1.7 as the large scale part of the line labelled $\Theta_0 + \Psi$. The form of this effect means that conventional plots of the CMB angular power spectrum show $\ell(\ell+1)C_\ell/2\pi$ against ℓ and on large scales, one expects to see the Sachs-Wolfe plateau. In fact secondary anisotropies on such scales (see Section 1.3.3), mean that the observed CMB power spectrum is not expected to be completely flat here.

On smaller angular scales, we note from equation (A.47) that the photon distribution monopole has a cosine dependence in the tight coupling regime. This oscillatory solution is damped when we consider the full free-streaming solution to the photon distribution equation by the factor given in equation (A.52) and multiplied by $j_\ell\left[k(\eta_0 - \eta_*)\right]$, it therefore displays oscillatory behaviour. This small scale behaviour of the monopole term, $\Theta_0 + \Psi$, is also shown in figure 1.7. The dipole has a sine dependence (see equation A.48) and suppressed amplitude

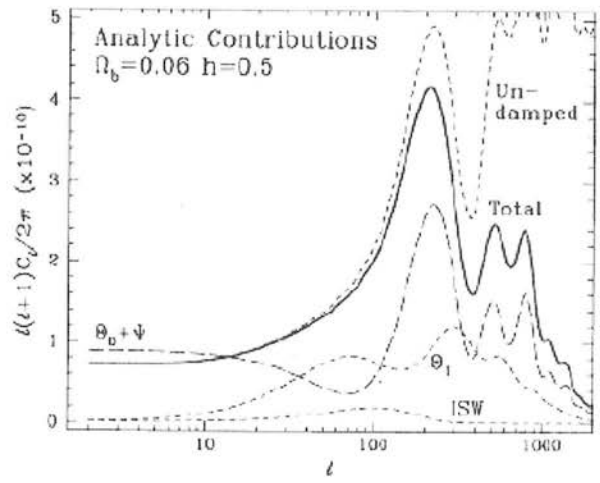

Figure 1.7: *From Hu and Sugiyama (1995)*: The CMB anisotropy power spectrum is determined by the superposition of terms in the photon distribution equation (A.51). On the largest scales ($\ell \lesssim 30$), the monopole $|\Theta_0 + \Psi|$ dominates but as we move to smaller scales the monopole and dipole terms together give rise to a series of peaks in the power spectrum. The importance of including damping due to photon diffusion can also be seen.

compared to the monopole by a factor of the sound speed c_s. The dipole is therefore also oscillatory but $\pi/2$ radians out of phase with the monopole; in figure 1.7, this is labelled Θ_1.

The total effect of all three primary anisotropies is for the angular power spectrum is to be flat on large angular scales (at low ℓ) and to have an oscillatory structure on small scales. The location of the peaks in the spectrum is determined by the monopole at last scattering and the dipole acts to fill in the troughs in the monopole distribution to some extent. The total primary anisotropy signal is also shown in figure 1.7 (with a small additional contribution from the early ISW effect, see below) and the importance of damping is evident.

Secondary anisotropies

The CMB photons will also be affected by matter that lies in their path on their journey from the surface of last scattering to us. The photon distribution (equation A.51) contains a term describing a gravitational secondary anisotropy which takes the form of an integral over potential derivatives and a spherical Bessel function. Whenever potentials are constant (as during matter domination) there is no contribution to the anisotropy power spectrum from this term; when this is not the case we obtain a contribution from this, the *Integrated Sachs-Wolfe* (ISW) effect.

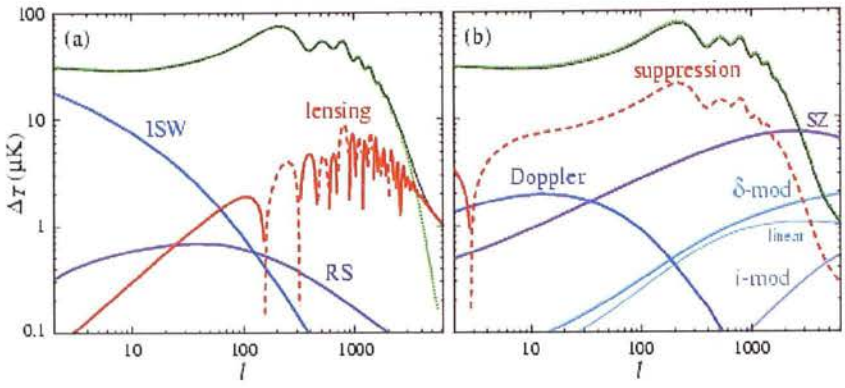

Figure 1.8: *From Hu and Dodelson (2002)*: The spectral signature of secondary anisotropies in comparison to the total angular power spectrum. (a) shows gravitational secondaries; note the linear late ISW effect (labelled ISW) and the non-linear ISW effect (labelled RS) which are significant only on the largest angular scales. (b) shows scattering secondaries including the Sunyaev-Zel'dovich effect (SZ).

In fact, there are two different ISW effects, the early ISW effect and the late ISW effect. The early ISW effect is due to time variation of potentials close to the era of last scattering when the presence of residual radiation causes potential decay. Scales most affected correspond to the horizon size at recombination, the early ISW effect therefore adds in phase with the monopole. The late ISW effect occurs recently due to the onset of Dark Energy domination and the potential decay associated with this and has a different signature in the anisotropy power spectrum (see Section 1.3.3).

The Sunyaev-Zel'dovich (SZ) effect is the most dominant of the scattering secondaries, see figure 1.8. This effect is caused by inverse Compton scattering of CMB photons by hot electrons present in dark matter halos. The SZ effect has a spectral signature that differs from other temperature fluctuations and which can be exploited to aid its detection.

The analysis above outlines what we expect the angular power spectrum of CMB anisotropies to look like with our current understanding of cosmology. The fact that observations match this prediction extremely well is strong evidence in favour of our current model of the Universe. In addition, the observations allow us to constrain free parameters in our model. For example, the position of the first peak in the observed angular power spectrum tells us that if our current cosmological model is correct then the Universe is spatially flat. The CMB power spectrum has been invaluable in putting tighter constraints on many cosmological

parameters including the baryon density, matter density and the tilt in the primordial power spectrum. The power spectra and expected forms of each of the anisotropies considered in this Section come from currently accepted theory, yet as figure 1.9 shows, theory and observation in this case are extremely consistent.

1.3.3 Integrated Sachs-Wolfe Effect

As stated above, the late ISW effect has a different signature in the CMB angular power spectrum to the early ISW effect. This is because the potentials decay over a far longer period of time than when their time variation was due to residual radiation (Hu and Dodelson, 2002). As the potential change occurs over a long timescale, the photons travel through many peaks and troughs of the perturbation and so the effect of many of the modes is cancelled out. Only modes with wavevectors perpendicular to the line of sight have an impact since then the photon does not pass through their crests and troughs; this reduces the anisotropy by a power of k for a given wavenumber k and a given line of sight. As $\ell = kD$, (where D is the distance that light can travel in the time since the imprint of the anisotropy occurred) the anisotropy is suppressed by a factor of kD in ℓ-space and hence only survives on the largest angular scales. The contribution due to the late ISW effect is shown in figure 1.8.

We can derive the form of the ISW power spectrum beginning from the temperature fluctuations induced along the line of sight (Cooray and Sheth, 2002)

$$T(\hat{\mathbf{n}}) = \frac{\Delta T^{\mathrm{ISW}}}{T_{\mathrm{CMB}}}(\hat{\mathbf{n}}) = 2\int \frac{\dot{\Phi}(\hat{\mathbf{n}}r, r)}{c^3} a(r)\, dr \tag{1.33}$$

where $\hat{\mathbf{n}}$ is a unit vector along the line of sight, r is comoving distance along that line of sight and Φ is the Newtonian gravitational potential. This is twice as large as the naive Newtonian prediction (Martinez-Gonzalez et al., 1990) due to an additional contribution from the general relativistic evolution of the spacetime curvature.

The spherical harmonic coefficients are now given by:

$$
\begin{aligned}
a_{\ell m} &= \int T(\hat{\mathbf{n}}) Y_\ell^{m*}(\hat{\mathbf{n}})\, d\hat{\mathbf{n}} \\
T^{\rm ISW}(\hat{\mathbf{n}}) &= 2 \int\int \frac{\dot{\Phi}(\mathbf{k})}{c^3} \exp(i\mathbf{k}\cdot\hat{\mathbf{n}}r)\, \frac{d^3\mathbf{k}}{(2\pi)^3}\, a(r)\, dr \\
\Rightarrow a_{\ell m}^{\rm ISW} &= \int \left(2 \int\int \frac{\dot{\Phi}(\mathbf{k})}{c^3} \exp(i\mathbf{k}\cdot\hat{\mathbf{n}}r)\, \frac{d^3\mathbf{k}}{(2\pi)^3}\, a(r)\, dr \right) Y_\ell^{m*}(\hat{\mathbf{n}})\, d\hat{\mathbf{n}} \\
a_{\ell m}^{\rm ISW} &= \int\int\int 2 \frac{\dot{\Phi}(\mathbf{k})}{c^3} \sum_{\ell' m'} 4\pi i^{\ell'} j_{\ell'}(kr) Y_{\ell'}^{m'}(\hat{\mathbf{k}}) Y_{\ell'}^{m'}(\hat{\mathbf{n}}) Y_\ell^{m*}(\hat{\mathbf{n}})\, \frac{d^3\mathbf{k}}{(2\pi)^3}\, a(r)\, dr\, d\hat{\mathbf{n}} \\
a_{\ell m}^{\rm ISW} &= \sum_{\ell' m'} i^{\ell'} \int \frac{\dot{\Phi}(\mathbf{k})}{c^3} Y_{\ell'}^{m'}(\hat{\mathbf{k}}) \int W^{\rm ISW} j_{\ell'}(kr)\, a(r)\, dr\, \frac{d^3\mathbf{k}}{2\pi^2} \int Y_{\ell'}^{m'}(\hat{\mathbf{n}}) Y_\ell^{m*}(\hat{\mathbf{n}})\, d\hat{\mathbf{n}}
\end{aligned}
$$

where $W^{\rm ISW} = 2$ and j_ℓ is a spherical Bessel function. Since

$$
\int Y_{\ell'}^{m'}(\hat{\mathbf{n}}) Y_\ell^{m*}(\hat{\mathbf{n}})\, d\hat{\mathbf{n}} = \delta_{\ell\ell'}\, \delta_{mm'},
$$

we can now express $a_{\ell m}$ in the form shown below:

$$
a_{\ell m}^{\rm ISW} = i^\ell \int \frac{\dot{\Phi}(\mathbf{k})}{c^3} Y_\ell^m(\hat{\mathbf{k}})\, I_\ell(k)\, \frac{d^3\mathbf{k}}{2\pi^2},
$$

where $I_\ell = \int W^{\rm ISW} j_\ell(kr)\, a\, dr$. The angular power spectrum is computed as follows:

$$
\begin{aligned}
C_\ell^{\rm ISW}\, \delta_{\ell\ell'}\, \delta_{mm'} &= \langle a_{\ell m}\, a_{\ell' m'}^* \rangle \\
&= \left\langle \int \frac{d^3\mathbf{k}}{2\pi^2} \frac{\dot{\Phi}(\mathbf{k})}{c^3} I_\ell(k)\, Y_\ell^m(\hat{\mathbf{k}}) \int \frac{d^3\mathbf{k}'}{2\pi^2} \frac{\dot{\Phi}^*(\mathbf{k}')}{c^2} I_{\ell'}^*(k')\, Y_{\ell'}^{m'*}(\hat{\mathbf{k}}') \right\rangle \\
&= \int\int \frac{d^3\mathbf{k}}{2\pi^2} \frac{d^3\mathbf{k}'}{2\pi^2} \left\langle \frac{\dot{\Phi}(\mathbf{k})}{c^2} \frac{\dot{\Phi}^*(\mathbf{k}')}{c^3} \right\rangle \left\langle Y_\ell^m(\hat{\mathbf{k}}) Y_{\ell'}^{m'*}(\hat{\mathbf{k}}') \right\rangle \langle I_\ell(k)\, I_{\ell'}^*(k') \rangle \\
&= \int\int \frac{d^3\mathbf{k}}{2\pi^2} \frac{d^3\mathbf{k}'}{2\pi^2} \frac{(2\pi)^3}{c^6} \delta_{\rm D}(\mathbf{k}+\mathbf{k}')\, P_{\dot{\Phi}\dot{\Phi}}(k) \left\langle Y_\ell^m(\hat{\mathbf{k}}) Y_{\ell'}^{m'*}(\hat{\mathbf{k}}') \right\rangle \langle I_\ell(k)\, I_{\ell'}^*(k') \rangle \\
&= \int \frac{d^3\mathbf{k}}{\pi} \frac{2}{c^4} P_{\dot{\Phi}\dot{\Phi}}(k) \left\langle Y_\ell^m(\hat{\mathbf{k}}) Y_{\ell'}^{m'*}(\hat{\mathbf{k}}) \right\rangle \langle I_\ell(k)\, I_{\ell'}^*(k) \rangle \\
&= \frac{2}{\pi} \delta_{\ell\ell'}\, \delta_{mm'} \int \frac{k^2}{c^6} P_{\dot{\Phi}\dot{\Phi}}(k) |I_\ell(k)|^2 dk \\
\Rightarrow C_\ell &= \frac{2}{\pi} \int \frac{k^2}{c^6} P_{\dot{\Phi}\dot{\Phi}}(k) |I_\ell(k)|^2 dk
\end{aligned}
\tag{1.34}
$$

In linear theory, $P_{\dot{\Phi}\dot{\Phi}}(k)$ can be expressed as

$$P_{\dot{\Phi}\dot{\Phi}}(k) = \frac{9}{4}\left(\frac{H_0}{k}\right)^4 \Omega_{m,0}^2 \left(\frac{d}{dt}\left[\frac{g}{a}\right]\right)^2 P_{\delta\delta}(k)$$

so we can re-express equation (1.34) as

$$C_\ell = \frac{18}{\pi}\frac{H_0^4\Omega_{m,0}^2}{c^6}\int \frac{dk}{k^2}\, P_{\delta\delta}(k) \int dr\; Hg(f-1)\, j_\ell(kr) \int dr'\; Hg(f-1)\, j_\ell(kr')$$

making use of Poisson's equation. As $\ell \to \infty$, we have

$$j_\ell(x) \to \sqrt{\frac{\pi}{2\ell+1}}\, \delta^{\mathrm{K}}(\ell + 1/2 - x)$$

and applying this above gives

$$C_\ell = \frac{9H_0^4\Omega_{m,0}^2}{(\ell+1/2)^4 c^6}\int dr\; \left[Hg(f-1)\right]^2 r^2 P\left(\frac{\ell+1/2}{r}\right).$$

which is valid for $\ell \gtrsim 10$; this is the Limber approximation (Kaiser, 1992).

As the late ISW effect is caused by the evolution of gravitational potentials at recent times, we expect – if our cosmological model is correct – a correlation between the CMB anisotropy power spectrum on large scales (where the late ISW effect is pronounced) and the matter distribution in the local Universe (Crittenden and Turok, 1996). Such a correlation has recently been detected (e.g. Scranton et al., 2003; Boughn and Crittenden, 2005) and this is evidence for the existence of Dark Energy. It is hoped that the late ISW effect may be able to put further constraints on the nature of Dark Energy, for example, whether its equation of state varies with time (Pogosian et al., 2005) and whether its sound speed may actually be less than the speed of light, implying that it has some tendency to cluster (Bean and Doré, 2004). The ability of the ISW effect to reveal the nature of Dark Energy is however strongly dependent on the form that this mysterious component takes, and the corresponding strength of the expected ISW signal.

The late ISW effect is also a key player in the quest for knowledge about the early Universe. The CMB is unique in that it is a signal from the time when the Universe became transparent to radiation; in order to learn about the Universe before this time we would need to study a component species that decoupled before the photons. The only possibilities for this, given our current understanding of the Universe, are a neutrino background or a gravitational wave background, neither of which have been detected. As such, the CMB is our only means of

probing the Universe at very high redshift. In order to use it for this purpose, we need some way to quantify the secondary anisotropies that have changed the CMB angular power spectrum since last scattering. Removal of secondary anisotropies would produce a CMB map which is a cleaner probe of the early Universe physics which gives rise to the primary anisotropies.

There are however problems with the observations of the CMB at large angular scales, due to the fact that we only have one Universe to observe. The coefficients of the spherical harmonic decomposition of the temperature anisotropies of the CMB (the $a_{\ell m}$s in the above notation) are all drawn from the same distribution for a given value of ℓ. Assuming Gaussian initial fluctuations, the mean of the distribution is zero and the variance is given by the value that we denoted C_ℓ above. As we see from equation (1.29) there are $2\ell + 1$ values of $a_{\ell m}$ for a given ℓ from which we estimate the variance C_ℓ. It is clear that the higher the value of ℓ, the more values of $a_{\ell m}$ we have and the better we can estimate the variance. Conversely, for low values of ℓ, the fact that we only have $2\ell + 1$ values of $a_{\ell m}$ from the distribution that we wish to learn about makes our determination of C_ℓ very uncertain. This uncertainty is called *cosmic variance* and is a fundamental limitation on the accuracy to which we can ever know the angular power spectrum of the temperature fluctuations on large angular scales (Dodelson, 2003):

$$\left(\frac{\Delta C_\ell}{C_\ell}\right)_{\text{cosmic variance}} = \sqrt{\frac{2}{2\ell+1}}$$

The uncertainty in the angular power spectrum of the CMB temperature fluctuations due to cosmic variance is shown in figure 1.9.

1.3.4 Sunyaev-Zel'dovich Effect

The Sunyaev-Zel'dovich (SZ) effect arises through the scattering of CMB photons from hot gas (Sunyaev and Zeldovich, 1972). There are two forms of the effect, the *thermal* SZ effect and the *kinetic* SZ effect. The thermal SZ signal is generated by inverse Compton scattering of photons from hot electrons; the kinetic SZ effect is due to temperature fluctuations introduced by the bulk flow of electrons along the line of sight.

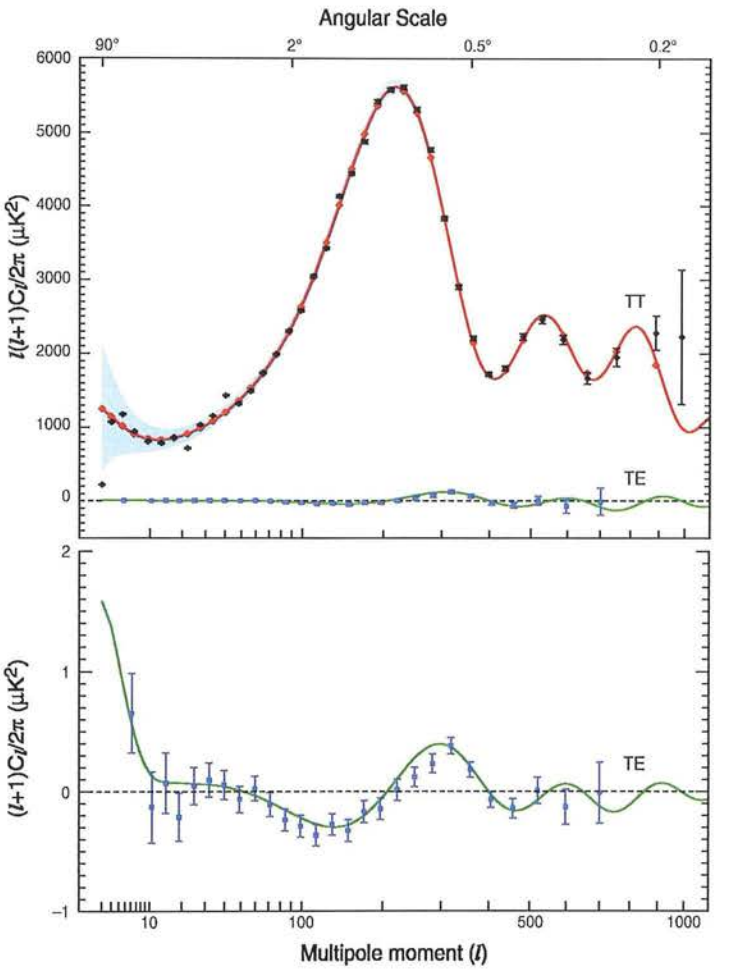

Figure 1.9: *From Hinshaw et al. (2006)*: (*Top*) A comparison of the WMAP data (black points) with the best fitting power spectrum from theory (solid line) - the agreement is striking (Hinshaw et al., 2006). Cosmic variance in the CMB angular power spectrum is shown in grey. This is a fundamental limitation on the accuracy to which we can ever measure the angular power on large scales. (*Bottom*) The WMAP polarization TE power spectrum. Accurate polarization data can pin down the epoch of reionization and could prove the existence of gravitational waves.

Thermal Sunyaev-Zel'dovich Effect

The temperature fluctuations introduced along a line of sight by the thermal SZ effect can be calculated from:

$$T(\hat{\mathbf{n}}) = \frac{\Delta T^{\rm tSZ}}{T_{\rm CMB}} = g(x) \int_r^0 a(r) \, \frac{k_{\rm B} \sigma_{\rm T}}{m_e c^2} \, n_e(r) \, T_e(r) \, dr \tag{1.35}$$

where

$$g(x) = x \coth(x/2) - 4 \qquad \text{and} \qquad x = \frac{h\nu}{k_{\rm B} T_{\rm CMB}}$$

is the spectral dependence of the effect, $k_{\rm B}$ is the Boltzmann constant, $\sigma_{\rm T}$ is the Thomson scattering cross section, m_e is the mass of an electron, c is the speed of light, n_e is the electron number density, T_e is the electron temperature, a is the scale factor and r is comoving distance. At Rayleigh-Jeans wavelengths the spectral function $g(x)$ takes the value -2. This equation follows from consideration of the manner in which an isotropic distribution of photons is scattered by a hot gas of electrons.

Following the method employed in Section 1.3.3 we can expand the thermal SZ temperature fluctuations in spherical harmonics and express the harmonic coefficients as:

$$\begin{aligned} a_{\ell m}^{\rm SZ} &= \int \frac{\Delta T^{\rm tSZ}(\hat{\mathbf{n}})}{T_{\rm CMB}} \, Y_l^{m*}(\hat{\mathbf{n}}) \, d\hat{\mathbf{n}} \\ &= i^\ell \int n_e(\mathbf{k}) \, T_e(\mathbf{k}) \, Y_\ell^m(\hat{\mathbf{k}}) \, I_\ell(k) \, \frac{d^3\mathbf{k}}{2\pi^2} \end{aligned}$$

where

$$I_\ell = \int \frac{g(x) \, \sigma_{\rm T} \, k_{\rm B} \, a(r) \, j_\ell(kr)}{m_e \, c^2} \, dr$$

Now the angular power spectrum is:

$$C_\ell^{\rm tSZ} = \frac{2}{\pi} \int k^2 \left\langle |n_e(\mathbf{k}) \, T_e(\mathbf{k})|^2 \right\rangle |I_\ell(k)|^2 \, dk \tag{1.36}$$

Kinetic Sunyaev-Zel'dovich Effect

The kinetic SZ effect has temperature fluctuations along a line of sight given by:

$$\frac{\Delta T^{\mathrm{kSZ}}}{T_{\mathrm{CMB}}} = \int_r^0 \frac{n_e \, \sigma_{\mathrm{T}}}{c} \, a(r) \, \mathbf{v}_{\mathrm{B}} \cdot \hat{\mathbf{r}} \, dr$$

with all quantities defined as above and $\mathbf{v}_{\mathrm{B}}$ the baryon velocity.

The kinetic SZ effect causes no change in the shape of the spectrum but shifts photons to a lower temperature for a baryon velocity away from the observer along the line of sight and a higher temperature for a baryon velocity towards the observer.

1.3.5 Cosmic Microwave Background Summary

To summarise, the CMB is fundamental to our understanding of cosmology. No other observable today allows us to probe the Universe back to a time when it was only around 300,000 years old. Since different cosmological models give rise to different forms of the angular power spectrum of the microwave background temperature fluctuations across the sky, and we now have accurate measurements of the observed form of the power spectrum, we have been able to rule out some cosmological models and to confirm results from other observations. Some particularly active fields of study at present are the search for non-Gaussianity in the CMB (see Section 1.2.1) and the drive to explain the low power and other anomalies in the CMB power spectrum on large angular scales. Despite the great uncertainty due to cosmic variance at very low multipoles in the WMAP CMB temperature data, there is some evidence that the quadrupole has a value that is inconsistent with the best-fitting cosmological model (e.g. Spergel et al., 2003; Hinshaw et al., 2006), that the quadrupole and octopole are aligned and that the octopole is unusually planar (de Oliveira-Costa et al., 2004). Considered individually, these anomalies have relatively low significance, however taken together this set of circumstances is fairly unlikely. There is much debate about whether these results are primordial in origin or the result of foreground signals in the data. It has been noted that the anomalies could result from artefacts arising in the region of the galactic plane, or could be related to the scan pattern (Huterer, 2006). Others have investigated whether secondary anisotropies could give rise to these signals, and if this were the case, the types of structures we should observe in the Universe (Inoue and Silk, 2006; Rakic et al., 2006).

1.4 Thesis Outline

The structure for the remainder of this thesis is as follows: Chapter 2 addresses the data and method that are used to reconstruct the local galaxy density field. Chapter 3 details the calculation of the local ISW effect using this reconstruction and discusses the implications for ISW detection and for CMB anomalies. In Chapter 4, the local thermal SZ effect is predicted, again using the reconstruction of the local Universe computed in Chapter 2 and in Chapter 5, an attempt is made to detect the ISW effect using photometric redshift data from 2MASS. Finally, in Chapter 6, prospects for future ISW and large scale SZ detection experiments are discussed and conclusions are drawn. Unless otherwise stated, a flat cosmological model with $\Omega_m = 0.25$, $\Omega_v = 0.75$, $\Omega_b = 0.045$, $\sigma_8 = 0.9$ and $h = 0.73$ is assumed.

CHAPTER 2

The Local Galaxy Density Field

One of the main aims of this PhD project is to reconstruct the local galaxy density field using a photometric redshift catalogue, i.e. to deduce the most likely form for the density field given such observations. Aside from satisfying the innate human desire to map the Universe around us, this density field has many important astrophysical applications. In this thesis, the use of the density field to predict local large-scale secondary anisotropy contributions to the CMB is explored.

This Chapter first describes in Sections 2.1 and 2.2 the data that are used to make this reconstruction and the issues that need to be addressed in moving from discrete galaxy positions to a continuous density field. The algorithm used to reconstruct the photometric redshift space density field is then detailed in Section 2.3 and the recovered density field for redshifts $z < 0.3$ is shown in Section 2.4. In Section 2.5, a correction is applied to fix a bias in the photo-zs and the results are compared to both the galaxy distribution in regions of high spectroscopic redshift completeness and previous attempts at reconstruction using other datasets. Finally, in Section 2.6 a discussion of the limitations of this reconstruction is presented. The recovered density field is used in Chapter 3 to predict the local ISW effect and in Chapter 4 to predict the local tSZ effect.

2.1 Data

The galaxies which are used in the reconstruction are taken from the Two Micron All-Sky Survey (2MASS) Extended Source Catalogue (XSC). Since old massive galaxies are red, the K_s selected 2MASS XSC catalogue is sensitive to these early type galaxies and would therefore be expected to observe most of the stellar mass in the local Universe making it ideal for density field reconstructions. Photometric redshifts have been computed for the 2MASS galaxies, using the three infrared bands of 2MASS together with optical B and R band data from SuperCOSMOS scans of photographic sky surveys. Various spectroscopic surveys which overlap with 2MASS including the Sloan Digital Sky Survey (SDSS), 2 degree Field Galaxy Redshift Survey (2dFGRS) and 6 degree Field Galaxy Survey (6dFGS) have been used to supplement the galaxy information in certain regions of the sky. Details of the photometric and spectroscopic data are given in Sections 2.1.1 and 2.1.2 respectively and the final dataset used for the reconstruction is described in Section 2.1.3. A discussion of other methods of photometric redshift determination is also included in Section 2.1.1.

2.1.1 Photometric Data

Methods of Photometric Redshift Determination

There are two basic means of photometric redshift determination: template methods and empirical methods (Collister and Lahav, 2004). Template methods are generally more suitable when there is little available spectroscopic redshift information within the population whose photometric redshifts are to be determined. When a large amount of true redshift information exists, empirical methods often lead to better results.

Template methods make use of libraries of galaxy spectral energy distributions (SEDs) and attempt to match the observed magnitude of a galaxy in different wavebands with that expected from one of these SEDs. χ^2 minimisation is often employed to choose the best fitting SED and the redshift of this template galaxy is then adopted as the observed galaxy's redshift. The template galaxy spectra must span the types of galaxies, luminosities and redshifts present within the population in order for this method to be effective. The accuracy of these results is strongly dependent on how well the template galaxies match the population. Hyper-Z (Bolzonella et al., 2000) and BPZ (Benítez, 2000) are examples of this method of redshift determination.

Empirical methods use a 'training set' of galaxies with known redshift from amongst the population as a whole, to deduce a parametrization for their photometric redshifts in terms of known photometric parameters (e.g. magnitudes in different wavebands). Again, the subsample used to determine the parametrization should be representative of the population as a whole, in order for the method to give satisfactory results when applied to the full sample. The use of a subsample of the population to determine the parametrization means that the effects of systematics in the photometry are incorporated. Empirical methods are the best choice when there is a significant amount of true redshift information for the sample, the method used for 2MASS and described below is an example of such a method. Another possible approach, adopted in ANNz (Collister and Lahav, 2004) is to use neural networks. In this case, a neural network is 'trained' on a subset of the available training set to deduce a network that gives optimal results when tested on an independent sample of the training set (so as not to overtrain the network towards the initial subset). Different initial conditions for the network often end up converging to distinct local minima and thereby define different neural networks. Using all these networks to estimate photometric redshifts and taking an average of the outputs usually gives better results than using a single network.

Photometric Redshift Determination for this Reconstruction

2MASS observed the whole sky in the near-infrared J, H and K_s bands from Mount Hopkins in Arizona and Cerro Tololo/CTIO in Chile and finished in 2001. The final 2MASS XSC dataset contains 1.6 million objects, over 98% of which are galaxies (Jarrett, 2004). To assign photometric redshifts to these galaxies, these data are supplemented with optical magnitudes for the galaxies in the B and R bands. The optical data come from SuperCOSMOS scans of photographic plates from the UKST survey in the south and POSS2 in the north. Details of the SuperCOSMOS optical catalogue construction can be found in Hambly et al. (2001). The data in these catalogues were photometrically calibrated using SDSS photometry, plate overlaps and by requiring uniformity in average colour between the B and R bands and 2MASS J, see Peacock et al., (in prep.) for further details. There is a large amount of spectroscopic overlap for the 2MASS dataset from surveys such as SDSS, 2dFGRS and 6dFGS – around 30% of the 2MASS XSC has spectroscopy. Using this as calibration, John Peacock deduced photo-zs as described below. These results are the basis of the work described here.

To compute photometric redshifts using the 5-band $BRJHK$ photometry, magnitude space was divided into cells of size 0.1 mag. (except where the number of spectroscopic objects in a cell fell below 10, when this size was increased) and in each cell, photometric redshifts equal to the average of the known spectroscopic redshifts were assigned to all objects. This makes the assumption that galaxies lying in the same region of magnitude space have the same spectral properties, but any method of photometric redshift estimation involves some assumption about the spectrum of the galaxy whose redshift is being calculated. In this case, the magnitude cells are small enough that the assumption is fair. In addition, prior information is incorporated into the redshift determination by allowing the magnitude of the galaxy in each of the wavebands to give an indication of its likely true redshift. This reduces the effect to which the determined redshift will be determined solely by the calibrating spectroscopy, which may be concentrated in a small region of the magnitude cell that does not correspond to the magnitude data for the galaxy of unknown redshift. The final photometric redshift is therefore influenced both by the naive prejudice which we have for the galaxy to be at a certain redshift based on its brightness alone and by the spectroscopic redshifts of galaxies with similar magnitudes in each of the 5 bands. In a small number of cases, magnitudes will not be available in each of the 5 bands, in this case a redshift is determined from the magnitudes available, with upper limits on the values in the unknown bands where possible.

The optical filter properties of UKST and POSS2 are slightly different, so the photometric redshift calculation was performed separately in the two hemispheres. However, due to deeper spectroscopy existing in the northern hemisphere, there may be bias in the recovered redshifts. To overcome this, a small rescaling was made to all the photo-zs to force the shape of the redshift distributions for the final galaxy sample to be the same in each hemisphere. Caution is required here, as it is easy to see how an approach dealing separately with the two hemispheres could give rise to a spurious dipole signal and possibly have effects on other low multipoles. Since the low multipole ISW signal inferred from the density field is of great interest with regard to anomalies in the large angle CMB signal (see Chapter 3), it is important to be aware of any possible influences on the low multipoles. To check the robustness of the photometric redshift determination across the whole sky, the spectroscopic catalogue in the Northern hemisphere could be restricted to match the redshift coverage available in the South and photometric redshifts computed using this restricted calibrating spectroscopy. This would mean ignoring

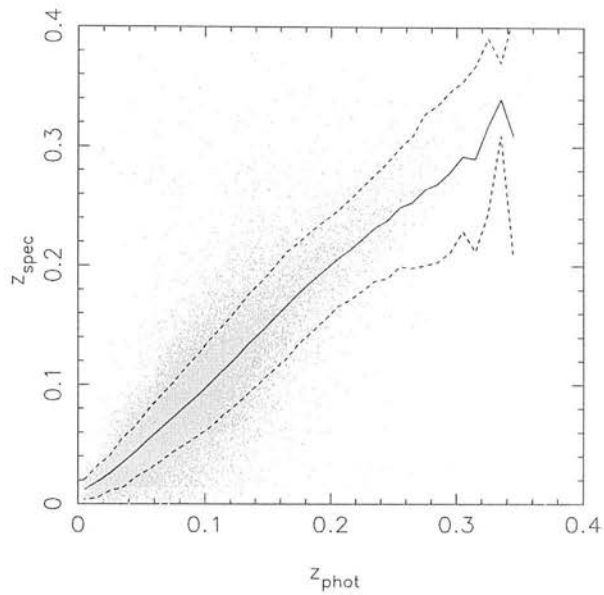

Figure 2.1: A comparison of spectroscopic and photometric redshifts for 2MASS galaxies where photometric redshifts are calculated as described in Section 2.1.1 (grey points). The solid black line shows the mean redshift in a photometric redshift bin of width 0.01 and the dashed lines show the 1σ error bars. The rms in $z_{\rm phot} - z$ is 0.033.

some useful information in determining the photometric redshifts, and would be expected to increase the uncertainty in the results, but with the gain of making the determination more uniform across the sky. Alternatively, simulations could be used to investigate the effect of different distributions of calibrating spectroscopy in the Northern and Southern hemispheres on the prediction of large angle CMB secondary anisotropies. Before drawing strong conclusions about the low multipole density field or its implications for the CMB secondary anisotropies, these effects should be investigated.

Figure 2.1 shows a comparison of spectroscopic and photometric redshifts for the 2MASS galaxies. The overall rms in $z_{\rm phot} - z$ is 0.033. This is as good or better as can be achieved by alternative means such as neural nets (M. Davidson, priv. comm.)

2.1.2 Spectroscopic Data

The photometric redshifts for the 2MASS XSC catalogue are calibrated using spectroscopy from the Sloan Digital Sky Survey (SDSS DR5, Adelman-McCarthy et al. 2007), the 2 degree Field Galaxy Redshift Survey (2dFGRS, Colless et al. 2003) and the 6 degree Field Galaxy Sur-

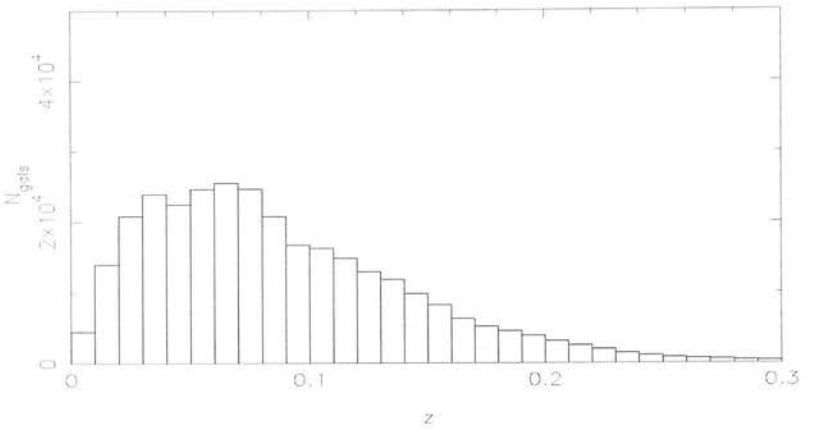

Figure 2.2: The redshift distribution of all galaxies with spectroscopic redshifts in the full 2MASS XSC catalogue.

vey (6dFGS DR1, Jones et al. 2005). Figure 2.2 shows the redshift distribution of the galaxies with spectroscopic redshifts from the whole catalogue and figure 2.3 shows their sky coverage. We note in particular the SDSS DR5 regions in the northern hemisphere and the 3 southern hemisphere stripes. 2dFGRS provides coverage mainly around the Southern Galactic Pole, with a smaller complementary region around the Northern Galactic Pole. Once completed, 6dFGS will observe the entire Southern sky (in equatorial coordinates), the data release used here (DR1) therefore contributes mainly to the spectroscopic coverage in the southern galactic hemisphere.

61% of the spectroscopic redshifts are in the northern galactic hemisphere, this sample is also slightly deeper than that available south of the galactic plane. As mentioned above (see Section 2.1.1), the discrepancy between these samples introduces a slight bias into the recovered photometric redshifts which is empirically corrected.

Using the spectroscopic subsample, we can investigate the photometric redshift errors within our final dataset. Figure 2.1 shows a comparison of the spectroscopically and photometrically determined redshifts together with the 1σ error for the photo-zs as a function of redshift. This information will be used to construct mock 2MASS datasets from simulation data for testing various procedures used throughout this thesis.

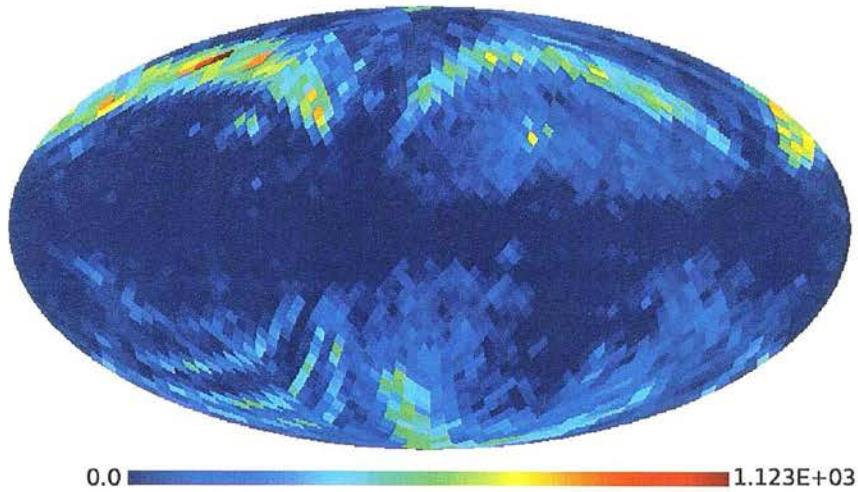

Figure 2.3: The sky coverage of the calibrating spectroscopy available for the 2MASS XSC catalogue. The colour table refers to the number of galaxies.

2.1.3 Final Dataset

The final dataset used for the density field reconstruction is a subset of the complete 2MASS dataset chosen for uniform sky coverage. In order to select this sample, a magnitude cut of $K_s < 13.8$ is imposed on the data. Figure 2.4 shows the sky coverage for the subsample with $K_s > 13.75$ after this magnitude cut has been made and for galaxies with $K_s > 14.0$ that fall outside the cut. The uniform coverage which we see away from the galactic plane (top panel) no longer holds when we consider fainter magnitudes (bottom panel). Finally, we apply a mask to the galaxy data to reduce contamination by stars near the galactic plane. The mask is constructed using the dust maps of Schlegel et al. (1998) and includes all regions with K-band reddening $A_K > 0.05$. Such regions of high extinction are expected to correlate with regions of high stellar contamination in the catalogues. This mask leaves approximately 67% of the sky uncovered. Whilst $A_K > 0.05$ is a conservative choice, Afshordi et al. (2004) note that the number density within pixels of faint galaxies with $13.5 < K_{20} < 14.0$ as a function of A_K drops off for $A_K > 0.065$. A less conservative mask, with for example $A_K > 0.1$ would still obscure a significant fraction of the sky (21%) and would introduce incompleteness issues into the analysis. Outside the mask, to a maximum redshift $z = 0.3$, the final catalogue contains 785,652 galaxies, of which 27% have spectroscopy. Figure 2.5 shows the photometric redshift distribution of this sample.

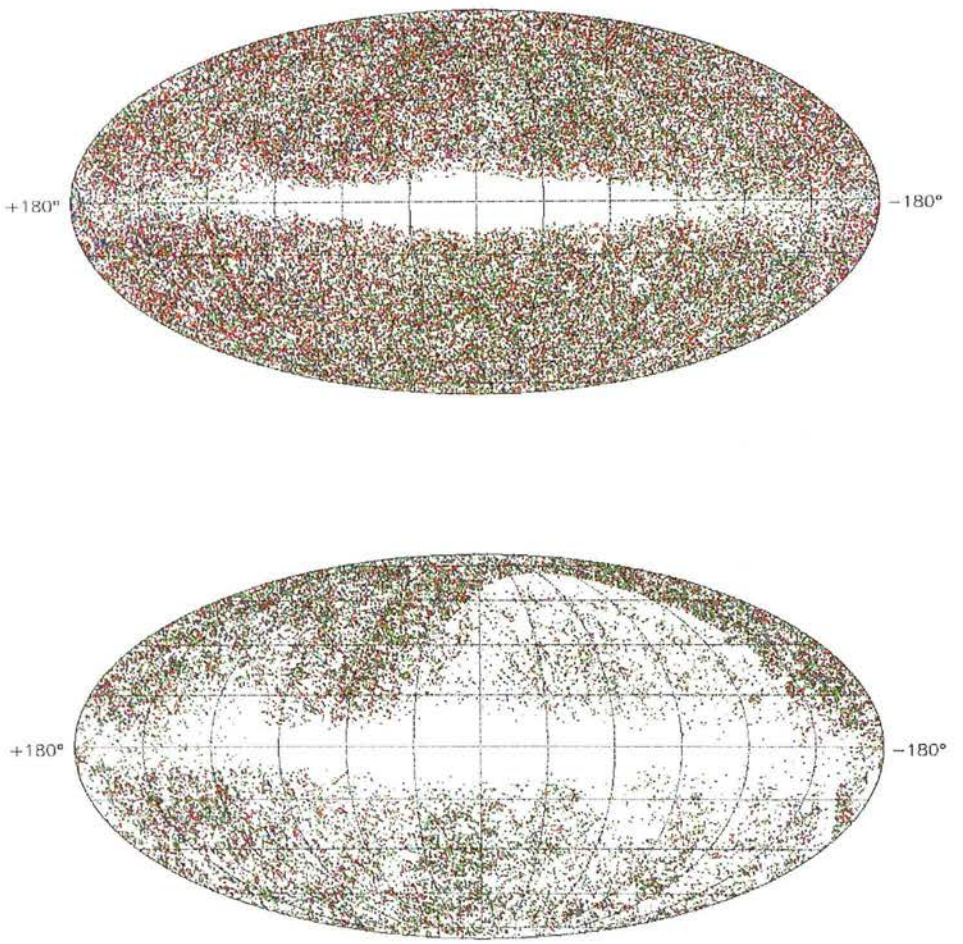

Figure 2.4: The deterioration in sky coverage as we consider fainter galaxies: (top) the positions of galaxies with $13.75 < K_s < 13.8$ and (bottom) for $K_s > 14.0$. To ensure uniform sky coverage within the final dataset, a magnitude cut of $K_s < 13.8$ is imposed.

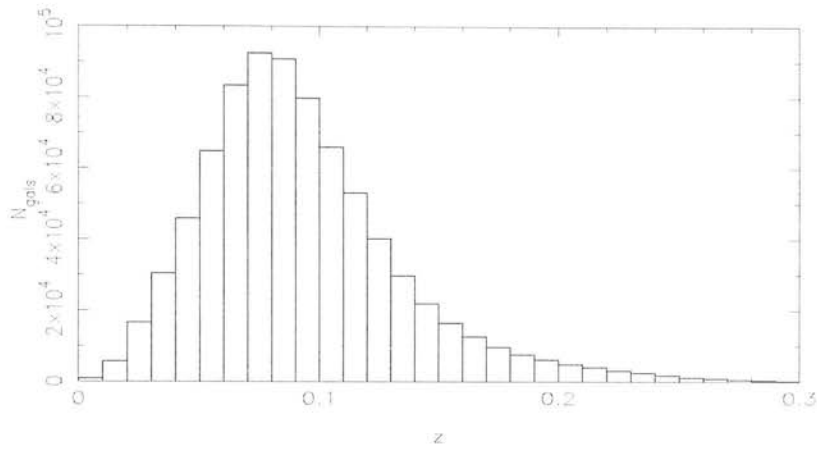

Figure 2.5: The photometric redshift distribution of the final sample used for the reconstruction.

The average number density, $\bar{n}$, of galaxies is assumed to be constant over the entire region covered by the data, with observed differences therefore due to the selection function alone. The value of $\bar{n}$ is estimated using observations at low redshift (where the selection function is assumed to be unity) and is found to be $\bar{n} = 0.011$. Figure 2.6 shows the number density of galaxies as a function of radial distance in bins of varying widths. We see that the number densities recovered using the different bins are consistent at higher redshifts whilst those at lower redshifts ($r \lesssim 150\,h^{-1}$Mpc) are noisy due to the small bin volumes here. To overcome noise when estimating $\bar{n}$ from the low redshift data, all galaxies with $r < r_{\max}$ are used to compute the number density. With $r_{\max}$ varying between $50\,h^{-1}$Mpc and $150\,h^{-1}$Mpc, $\bar{n}$ is found to be robust at $\bar{n} = 0.011$ to 2 s.f. A jackknife error analysis of the determination of $\bar{n}$ for each of these different datasets is performed. For this, the sky is split into octants and the values of $\bar{n}$ found on omitting each of the eight regions in turn are calculated. The error in $\bar{n}$ over the whole sky, $\sigma_{\bar{n}}$, is then taken as

$$\sigma_{\bar{n}} = \sqrt{\frac{7\sum(n_i - \langle\bar{n}\rangle)^2}{8}} \tag{2.1}$$

where n_i are the values of $\bar{n}$ found in the eight different subregions and $\langle\bar{n}\rangle$ is their mean. This reveals that the error in the determination of $\bar{n}$ for the final dataset is around 10% with slight variations depending on $r_{\max}$. When performing the reconstruction, a value $\bar{n} = 0.01$ is chosen for reasons discussed in Section 2.3.3, but note that this is within the 1σ error bounds found above. Several techniques for inferring $\bar{n}$ are discussed in Davis and Huchra (1982), including

the minimum variance estimator:

$$\bar{n} = \frac{\sum_i n_i w_i}{\int \phi(r) w(r)\, dV} \tag{2.2}$$

where the volume is divided into cells i, with n_i the number of galaxies in a cell, $\phi(r)$ the selection function and

$$w(r) = \frac{1}{1 + \bar{n} J_3 \phi(r)} \tag{2.3}$$

with

$$J_3 = 4\pi \int_0^\infty r^2 \xi(r)\, dr. \tag{2.4}$$

This method therefore requires an initial estimate for $\bar{n}$ and knowledge of the correlation function $\xi(r)$.

Figure 2.6 also shows the selection function, ϕ, multiplied by $\bar{n}$ to match the observed value of $n(r)$ at high redshift on this plot. At low redshift the selection function is taken to be unity and otherwise is determined empirically.

2.2 Reconstruction of Density Fields

Reconstruction of a signal entails using the available information about an imperfect observed signal, together with estimates of noise and errors, to deduce the most likely true signal. In the case of the local density field, the available information is 3D measurements of galaxy positions. The quality of the reconstruction which is possible from a given dataset depends on the quality of the data and how closely these are related to the signal which one is trying to measure. In the case of the density field, the limited accuracy to which a reconstruction is reliable is manifest as a minimum physical scale below which there is no information about the field. This results in a smoothed version of the true field being recovered using the reconstruction procedure. In the remainder of this Section, features of the galaxy data which affect the accuracy of the reconstruction are discussed. Section 2.3 then gives details of the filtering procedure which is employed to reconstruct the density field from 2MASS data.

We assume that galaxies are distributed through the Universe as a Poisson sampling of the underlying galaxy density field. There is a clear relationship between the number of galaxies

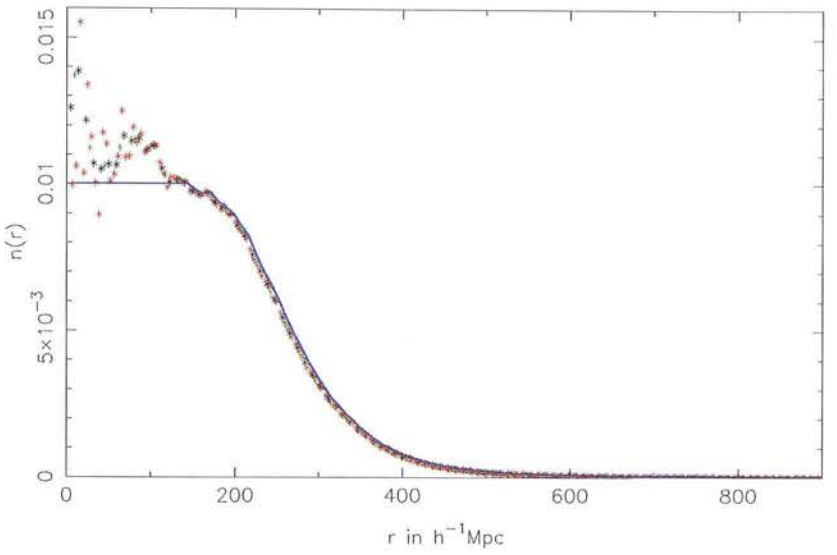

Figure 2.6: $n(r)$ for the final dataset computed using 3 different sizes of bin: $\Delta r = 9\,h^{-1}$Mpc (black), $\Delta r = 4.5\,h^{-1}$Mpc (red) and $\Delta r = 18\,h^{-1}$Mpc (green). The results agree for radii $r \gtrsim 150\,h^{-1}$Mpc but are affected by noise at lower radii. The selection function, ϕ, is taken to be the ratio of n(r) to the number density at low redshift $\bar{n} = 0.01$, the blue line shows $\bar{n}\phi$.

in a region and the density there – a higher density will tend to coincide with a higher galaxy number. A crude estimate of the galaxy overdensity in a region, δ, defined by

$$1 + \delta = \frac{\rho}{\bar{\rho}}, \tag{2.5}$$

can be made by considering the ratio of the number of galaxies observed in a region to the number expected:

$$1 + \delta = \frac{n_{\text{obs}}}{n_{\text{exp}}}. \tag{2.6}$$

This makes the assumption that all galaxies have equal mass. This estimate of the overdensity field is used as the starting point for our reconstruction. The expected number of galaxies in a region is computed with reference to the selection function at that position, see Section 2.3.

2.2.1 Redshift Errors

It is relatively easy to measure an accurate angular position for a galaxy, but to pinpoint its 3D position we also need a redshift. As described in Section 2.1, there are two main ways

in which galaxy redshifts are measured: spectroscopically and photometrically. Spectroscopic redshifts have very small errors associated with them, which are mainly introduced due to the motions of the stars in the galaxy. Photometric redshift errors are far more significant and lead to large uncertainties in the radial positions of galaxies. These errors stem from the fact that broad band observations cannot pinpoint exactly where a spectral feature is observed. This radial positional uncertainty will act to smear out the density field and blur structures along the radial axis.

2.2.2 Incompleteness in the Galactic Plane

The Milky Way contains a large amount of dust which prevents light from more distant galaxies lying in the plane of its disk being observed. This results in incompleteness in a galaxy survey since there are no observations over some fraction of the sky - the *zone of avoidance*. This needs to be rectified to produce a picture of the true matter distribution in the Universe. There are a number of ways of replacing galaxy information lost from the zone of avoidance, ranging from simply interpolating the galaxy density above and below the plane to fitting the density field away from the plane to a distribution of spherical harmonics and adopting the same harmonic coefficients to describe the whole sky (Saunders et al., 2000). Since this latter method is usually truncated at a given harmonic scale, this amounts to a smoothing of the available data across the galactic plane. Having a reliable estimate for the density field within the galactic plane is important, simply setting $\delta = 0$ here will introduce a bias into the reconstruction outside the masked region.

2.2.3 Uniformity of the Galaxy Data

It is essential to know how uniform the observations that are being used to deduce the density field are. In general, the most straightforward course of action is to impose magnitude cuts on the data in order to ensure that the sky coverage is uniform. Since the density field in a region will be estimated using the ratio of the number of observed galaxies to the expected number of galaxies, failure to account for any non-uniformity of the observations when calculating the expected number of galaxies would lead to spurious over- and underdensities in regions which were not observed to the same depth. However, as long as the angular variations in the data of this kind are well understood it is possible to use this information together with the full dataset

to recover the density field.

2.2.4 Selection Function Errors

The selection function, ϕ, describes the likelihood of a galaxy at a certain distance being observed by the survey. Figure 2.6 shows ϕ (multiplied by a constant factor of $\bar{n} = 0.01$) for the final dataset. The selection function is used to calculate the number of galaxies that we would expect to observe in a region of sky if that region were at the mean density, and hence to infer a galaxy overdensity in the region. An error in the selection function will therefore lead to incorrect determination of the galaxy overdensities. The selection function is calculated empirically from the data, assuming that at low redshift the selection function is $\phi(s) = 1$ and that the true galaxy number density is constant across the survey. Figure 2.6 shows $n(r)$ (a constant multiple of the selection function) computed for three different sizes of redshift shell. The strong agreement between these estimates for $r > 150\,h^{-1}$Mpc shows that the determination of the selection function in this manner is robust.

2.2.5 Shot Noise

The local galaxy density field is a continuous function which we aim to recover using observations of galaxies. A galaxy is a discrete object, which we assume to have been Poisson sampled from the underlying galaxy density field. The use of galaxies to reconstruct the density field will therefore inevitably introduce shot noise into the recovered field. Shot noise is greatest in sparsely sampled regions since here we are using the minimum amount of information to deduce properties of the field. Shot noise limits the scales on which the recovered field is reliable meaning that we can only accurately recover a smoothed version of the 'true' density field.

2.3 Wiener Filter Reconstruction

The upshot of the issues outlined above is that some form of filtering should be applied to the data in order to accurately recover the density field and rein in shot noise. Although there are several possible filters that could be used to this end, the Wiener filter is a natural choice and one which has been widely used by previous groups e.g. Fisher et al. (1995); Erdoğdu et al. (2006b).

2.3.1 The Wiener Filter

The Wiener filter is a weighting scheme which can be applied to the data to give the most likely field in the least squares sense. The Wiener filter acts by suppressing information in noisy regions in favour of the mean field. The construction of the Wiener filter is as follows:

- There is some signal $s(x)$ which we wish to measure. The signal is possibly convolved with a response function $r(x)$ and is subject to noise $n(x)$ so that what we actually measure is $c(x)$ where $c(x) = r * s(x) + n(x)$. We want to apply some weight to the measurements in order to recover $\tilde{s}$, the most likely signal in the least squares sense;

- If we reformulate this problem in terms of vectors, we have a measurement vector c_α where

$$c_\alpha = r_{\alpha\beta} s_\beta + n_\alpha, \tag{2.7}$$

and some weights $F_{\alpha\gamma}$ which when applied to c_α give the most likely true signal, $\tilde{s}_\alpha$, in the minimum variance sense i.e.

$$\frac{\partial}{\partial F_{\alpha\beta}} \left\langle |\tilde{s}_\alpha - s_\alpha|^2 \right\rangle = \frac{\partial}{\partial F_{\alpha\beta}} \left\langle |F_{\alpha\delta} c_\delta - s_\alpha|^2 \right\rangle = 0; \tag{2.8}$$

- Therefore,

$$\begin{aligned} 0 &= \frac{\partial}{\partial F_{\alpha\beta}} \left\langle (F_{\alpha\delta} c_\delta - s_\alpha)(F_{\alpha\gamma} c_\gamma - s_\alpha)^\dagger \right\rangle \\ &= \frac{\partial}{\partial F_{\alpha\beta}} \left\langle F_{\alpha\delta} c_\delta c_\gamma^\dagger F_{\gamma\alpha}^\dagger - s_\alpha c_\gamma^\dagger F_{\gamma\alpha}^\dagger - F_{\alpha\delta} c_\delta s_\alpha^\dagger + s_\alpha s_\alpha^\dagger \right\rangle \\ &= \left\langle c_\beta c_\gamma^\dagger \right\rangle F_{\gamma\alpha}^\dagger - \left\langle c_\beta s_\alpha^\dagger \right\rangle \\ \Rightarrow F_{\alpha\eta} &= \left\langle s_\alpha c_\beta^\dagger \right\rangle \left\langle c_\beta c_\eta^\dagger \right\rangle^{-1}; \end{aligned} \tag{2.9}$$

- Returning to the definition of c, we see that

$$\left\langle s_\alpha c_\beta^\dagger \right\rangle = \left\langle s_\alpha s_\delta^\dagger \right\rangle r_{\delta\beta}^\dagger \tag{2.10}$$

and

$$\left\langle c_\beta c_\gamma^\dagger \right\rangle = r_{\beta\mu} \left\langle s_\mu s_\eta^\dagger \right\rangle r_{\eta\gamma}^\dagger + \left\langle n_\beta n_\gamma^\dagger \right\rangle ; \tag{2.11}$$

- Therefore the Wiener filter is (Zaroubi et al., 1995)

$$F_{\alpha\gamma} = \left\langle s_\alpha s_\delta^\dagger \right\rangle r_{\delta\beta}^\dagger \left(r_{\beta\mu} \left\langle s_\mu s_\eta^\dagger \right\rangle r_{\eta\gamma}^\dagger + \left\langle n_\beta n_\gamma^\dagger \right\rangle \right)^{-1} . \tag{2.12}$$

As applied to the final dataset, for recovery of the true redshift space density field, the response function $r_{\alpha\beta}$ is the photo-z smearing and the noise n_α is shot noise. In fact, we will recover the density field in photo-z space (a smoothed version of true redshift space – although see Sections 2.3.3 and 2.5), and therefore the response function above drops out of the analysis leaving

$$F_{\alpha\gamma} = \left\langle s_\alpha s_\beta^\dagger \right\rangle \left\langle s_\beta s_\gamma^\dagger + n_\beta n_\gamma^\dagger \right\rangle^{-1} . \tag{2.13}$$

The Wiener filter therefore acts to weight data such that in regions of high signal-to-noise, the data is unaffected whereas noisy data is suppressed by a factor $\mathrm{signal}/(\mathrm{signal} + \mathrm{noise})$.

The Wiener filter can be extremely useful but certain results should be treated with caution. In the absence of data, the Wiener filter will recover the mean field – if there is no information to the contrary then the mean is the most likely value for the field to take at that point. For the galaxy density field however, an absence of data can indicate the presence of a void rather than poor sampling. In regions of high signal-to-noise where the Wiener filter leaves the measured density field largely unchanged, this characteristic does not pose a problem; in less well-sampled regions however, voids will tend rather to become underdensities of a less dramatic nature. Similarly, high density peaks are suppressed by the Wiener filter, and hence a Wiener-filtered density field has power on all scales less than or equal to that in the original field. For this reason, the Wiener filter cannot be applied iteratively, the field will merely tend to zero on all scales where the Wiener filter is less than unity i.e. where the noise is non-negligible. Other filters exist which will preserve the power in the original field, but the filtered field is then no longer defined so as to be the minimum variance solution.

In Section 2.3.2, the general process of applying the Wiener filter to reconstruct the density field is described, including:

1. expansion of the density field into the basis of choice;
2. determination of the boundary conditions;
3. calculation of the Wiener filter from the galaxy data.

In Section 2.3.3, details of the specific application of this process to the 2MASS data are described. These can be broken down into

1. approximation of the photo-z smearing and calculation of the Wiener filter signal;
2. choice of resolution;

Finally, the method developed for filling in the missing information from the galactic plane is described in Section 2.3.4.

2.3.2 Application to Data

We broadly follow the method of Fisher et al. (1995, hereafter F95) in applying the Wiener filter to the 2MASS data. This involves expanding the density field that we wish to recover in a basis composed of spherical harmonics to describe angular variations and spherical Bessel functions for radial information. A basis of this form is a sensible choice because the photometric redshift errors within the field are entirely radial and therefore in such a scheme affect only one of the basis directions. The particular choice of spherical Bessel functions as the radial function in F95 was made to simplify the computation of velocity and potential fields from the density field. The simplification arises due to the fact that spherical Bessel functions and spherical harmonics are eigenfunctions of the Laplacian. These simple relationships will be exploited in Chapter 3. Before giving details in Section 2.3.3 of the precise method used to reconstruct the density field from the 2MASS data, the reconstruction algorithm developed by F95[1] is first described below.

[1]The reconstruction algorithm contained in F95 is actually for the recovery of a real-space density field from spectroscopic data. The version presented here ignores the details of the transformation from redshift space to real space and considers only the recovery of a redshift space density field. We ignore redshift-space distortions, but note that these can still be important in photometric redshift catalogues (Padmanabhan et al., 2007; Blake et al., 2007)

From raw galaxy data (angular positions and photometric redshifts), the reconstruction algorithm proceeds by expanding the observed density field in Fourier-Bessel functions – spherical harmonics for the angular information and spherical Bessel functions for the radial information. We assume for the present that we have all-sky data; there is no loss of coverage due for example to the galactic plane. The density field at this stage will be noisy, with Fourier-Bessel coefficients for the field given by (F95)

$$\rho_{\ell mn} = \int d^3s \; \rho(\mathbf{s}) \, Y^*_{\ell m}(\hat{\mathbf{s}}) \, j_\ell(k_n s) \tag{2.14}$$

and inverse

$$\rho(\mathbf{s}) = \sum_{\ell mn} C_{\ell n} \, \rho_{\ell mn} \, j_\ell(k_n s) \, Y_{\ell m}(\hat{\mathbf{s}}) \tag{2.15}$$

where $C_{\ell n}$ is a normalization constant determined by the choice of boundary conditions. Here s refers to the comoving distance associated with a particular redshift as defined in equation (1.9).

There is an infinite set of boundary conditions which will ensure that the selected basis is composed of orthogonal functions and several possible choices of physically motivated boundary conditions from within this set (see Fisher et al., 1995, Appendix A). Here the 'potential boundary conditions' are adopted: $\delta(s)$ is assumed to vanish for $s > S_{\max}$, reflecting the fact that we have no information about the density field beyond the maximum redshift of the galaxy sample, and the logarithmic derivative of the potential field at the boundary is taken to be continuous. For this choice of boundary conditions, $C_{\ell n}$ is given by (Fisher et al., 1995, Appendix A)

$$C_{\ell n} = \frac{2}{S^3 [j_\ell(k_n S)]^2}. \tag{2.16}$$

Our best estimate for $\rho(\mathbf{s})$ is

$$\rho(\mathbf{s}) = \sum_{i=1}^{N_{\rm gals}} \frac{\delta^{\rm D}(\mathbf{s} - \mathbf{s_i})}{\phi(s_i)} \tag{2.17}$$

where $\mathbf{s_i}$ is the position of a galaxy in photometric redshift space, $\phi(s_i)$ is the observed selection function and δ^D is the Dirac delta function. This is more accurately an estimate of the *number density field* n and is equivalent to describing each galaxy by a delta function and assigning

it a weight inversely proportional to the selection function at this point. We work in terms of the number density field in what follows, this is proportional to the density field due to our assumption that all galaxies have equal mass (see Section 2.2). Combining equations (2.14) and (2.17), the coefficients describing the density field are given by

$$\rho_{\ell mn} = \sum_{i=1}^{N_{\rm gals}} \frac{1}{\phi(s_i)}\, j_\ell(k_n s_i)\, Y^*_{\ell m}(\hat{\mathbf{s}}_i). \tag{2.18}$$

We are actually more interested in the overdensity field $\delta(\mathbf{s})$ than the raw density field $\rho(\mathbf{s})$; the two are related by:

$$\delta(\mathbf{s}) = \frac{\rho(\mathbf{s}) - \bar{\rho}}{\bar{\rho}} \tag{2.19}$$

and hence using (2.14)

$$\begin{aligned}
\delta_{\ell mn} &= \frac{\rho_{\ell mn}}{\bar{\rho}} - \int_{V_S} d^3\mathbf{s}\; Y^*_{\ell m}(\hat{\mathbf{s}})\, j_\ell(k_{\rm n} s) \\
&= \frac{\rho_{\ell mn}}{\bar{\rho}} - \sqrt{4\pi} \int_0^R ds\; s^2 j_0(k_n s)\, \delta^{\rm K}_{\ell 0}\, \delta^{\rm K}_{m0} \\
&= \frac{\rho_{\ell mn}}{\bar{\rho}} - \frac{\sqrt{4\pi}}{k_n} \delta^{\rm K}_{\ell 0}\, \delta^{\rm K}_{m0} \left\{ \int_0^S \frac{\cos(k_n s)}{k_n}\, ds - \frac{S\cos(k_n S)}{k_n} \right\} \\
&= \frac{\rho_{\ell mn}}{\bar{\rho}} - \sqrt{4\pi}\, S^3\, \frac{j_1(k_n S)}{k_n S}\, \delta^{\rm K}_{\ell 0}\, \delta^{\rm K}_{m0}
\end{aligned} \tag{2.20}$$

To control the noise in the reconstructed field, we apply the Wiener filter which suppresses noisy small scale density fluctuations resulting in a smoothed version of the field. Figure 2.7 shows slices through a density field before and after the application of the Wiener filter to simulation data: the smoothing effect is apparent. With simulation data, it is possible to test that the Wiener filter is recovering the true field. Figure 2.8 compares the true density values at a series of points and the Wiener filtered values at the same points recovered from noisy versions of the true field. As one would expect, the Wiener filtered densities are biased towards lower values due to the loss of small scale information. Applying the same filter to the 'true' density field as to the noisy field reveals good correspondence and therefore indicates that the Wiener filter is operating successfully in removing the effects of noise.

Some slight modifications are made here to the method for computing the Wiener filter described by F95 to account for the fact that the data which we are using occupy photometric

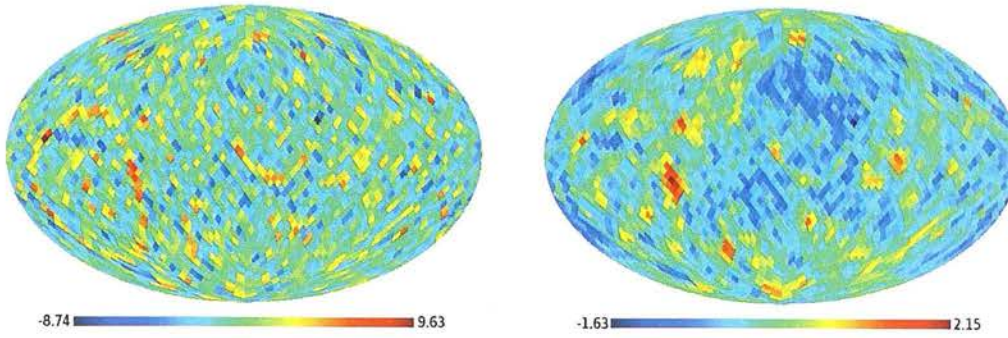

Figure 2.7: A noisy density field before (*Left*) and after (*Right*) application of the Wiener filter. The smoothing effect of the filter can clearly be seen.

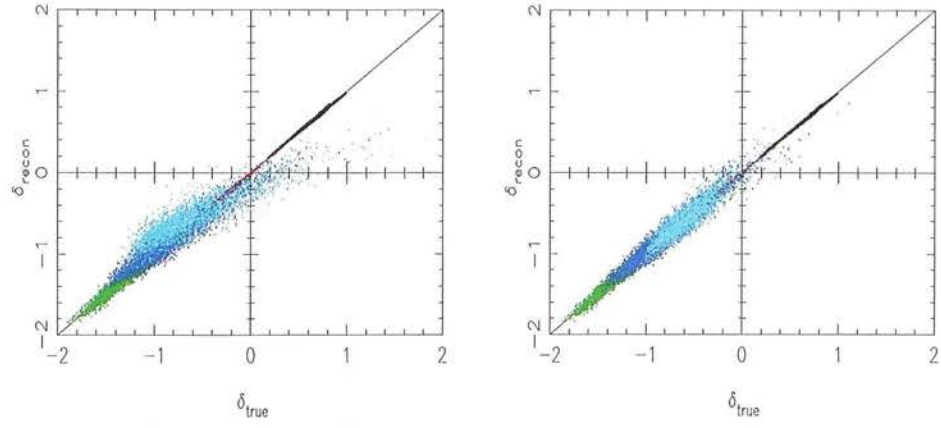

Figure 2.8: (*Left*) Density values on a series of shells of increasing radius within an N-body simulation and the recovered points from a noisy version of the simulation after application of the Wiener filter ($r = 20\,h^{-1}$Mpc (black), $r = 40\,h^{-1}$Mpc (red), $r = 60\,h^{-1}$Mpc (green), $r = 80\,h^{-1}$Mpc (blue), $r = 100\,h^{-1}$Mpc (cyan)). A selection function has been applied to create the noisy data so noise increases with radius. We see a bias in the recovered density values which tend to be smaller due to the loss of small scale information. (*Right*) The same two fields but now the Wiener filter is applied to both the noisy and true data thereby ensuring that the smoothing in each case is the same. The good agreement between the values demonstrates that the Wiener filter is successfully suppressing information on scales which are badly contaminated by noise.

redshift space rather than 'true' redshift space. Below, the basic steps of the Wiener filter calculation are outlined, as in F95, leaving the precise calculation of the Wiener filter for the 2MASS data until Section 2.3.3.

If we consider

$$\langle \delta_{\ell mn} \delta^*_{\ell' m' n'} \rangle \,, \tag{2.21}$$

then this expression will contain two terms, one for the expected signal and other for the expected noise. The cross terms vanish – by definition 'noise' and 'signal' are uncorrelated. Expressing $\delta_{\ell mn}$ in terms of the density field $\delta(\mathrm{s})$ gives

$$\delta_{\ell mn} = \int_{V_S} d^3\mathrm{s}\; \phi(s)\, w(s)\, \delta(\mathrm{s})\, j_\ell(k_n s)\, Y^*_{\ell m}(\hat{\mathrm{s}}) \tag{2.22}$$

where $\phi(s)$ is the selection function and $w(s)$ is some weight function which we apply to galaxies at a certain redshift. This weight is chosen in our analysis to be the inverse of the selection function so that at each galaxy position, we are in effect accepting that there are in fact N galaxies there, where N is the inverse of the probability that a galaxy at that redshift is observed. In addition to being a natural weighting scheme for the data, this has the advantage of simplifying the equations somewhat as $\phi(s)w(s) = 1$.

For a point distribution, the expectation of the density field is given by (F95)

$$\langle \delta(\mathrm{s}_1)\delta(\mathrm{s}_2) \rangle = \xi(|\mathrm{s}_1 - \mathrm{s}_2|) + \frac{1}{\bar{\rho}\phi(s)} \delta^{\mathrm{D}}(\mathrm{s}_1 - \mathrm{s}_2) \tag{2.23}$$

and using this together with (2.22) and the weighting scheme discussed above, $w(s)\phi(s) = 1$, gives

$$\begin{aligned}
\langle \delta_{\ell mn} \delta^*_{\ell' m' n'} \rangle &= \left\langle \int_{V_S} d^3\mathrm{s}\; \delta^S(\mathrm{s})\, j_\ell(k_n s)\, Y^*_{\ell m}(\hat{\mathrm{s}}) \int_{V_S} d^3\mathrm{s}'\; \delta^S(\mathrm{s}')\, j_{\ell'}(k_{n'} s')\, Y_{\ell' m'}(\hat{\mathrm{s}}') \right\rangle \\
&= \int ds\; s^2\, j_\ell(k_n s) \int ds'\; s'^2\, j_\ell(k_{n'} s') \\
&\quad \times \int d\Omega \int d\Omega'\; Y^*_{\ell m}(\hat{\mathrm{s}})\, Y_{\ell' m'}(\hat{\mathrm{s}}')\; \langle \delta^S(\mathrm{s}) \delta^S(\mathrm{s}') \rangle \\
&= \int ds\; s^2\, j_\ell(k_n s) \int ds'\; s'^2\, j_\ell(k_{n'} s') \frac{2}{\pi} \int_0^\infty dk\; k^2\, P^S(k)\, j_\ell(ks)\, j_\ell(ks') \\
&\quad + \frac{1}{\bar{\rho}} \int_{V_S} ds\; s^2\, \phi(s)\, j_\ell(k_n s)\, j_\ell(k_{n'} s),
\end{aligned} \tag{2.24}$$

using

$$\begin{aligned}\xi(|\mathrm{s}-\mathrm{s}'|) &= \frac{1}{(2\pi)^3}\int d^3\mathbf{k}\, P(k)\exp -i\mathbf{k}.(\mathrm{s}-\mathrm{s}') \\ &= \frac{2}{\pi}\sum_{\ell m} Y_{\ell m}(\hat{\mathrm{s}})\, Y_{\ell m}(\hat{\mathrm{s}}')^* \int_0^\infty dk\; k^2\, P(k)\, j_\ell(ks)\, j_\ell(ks'). \qquad (2.25)\end{aligned}$$

Here, isotropy in the power spectrum, $P(k)$, is assumed (see Section 2.3.3 for further discussion). Extending the limit of the integral over s' to ∞, we have

$$\begin{aligned}\langle \delta_{\ell mn}\delta^*_{\ell' m' n'}\rangle &= \frac{2}{\pi}\int_0^\infty dk\; k^2\, P^S(k)\int ds\; s^2\, j_\ell(k_n s)\, j_\ell(ks)\,\frac{\pi}{2k^2}\delta^{(1)}(k-k_{n'}) \\ &\quad +\frac{1}{\bar{\rho}}\int_{V_S} ds\; s^2\,\phi(s)\, j_\ell(k_n s)\, j_\ell(k_{n'} s) \\ &= P^S(k_{n'})\int ds\; s^2\, j_\ell(k_n s)\, j_\ell(k_{n'} s) \\ &\quad +\frac{1}{\bar{\rho}}\int_{V_S} ds\; s^2\,\phi(s)\, j_\ell(k_n s)\, j_\ell(k_{n'} s) \\ &= P^S(k_{n'})\frac{S^3[j_1(k_n)]^2}{2}\delta^{\mathrm{K}}_{nn'} + \frac{1}{\bar{\rho}}\int ds\; s^2\,\phi(s)\, j_\ell(k_n s)\, j_\ell(k_{n'} s). \qquad (2.26)\end{aligned}$$

The first term here is the expected variance in the signal and the second term is the expected variance in the noise. These can therefore be combined to form the Wiener filter which is needed

$$\Phi_\ell^{\mathrm{WF}} = S_\ell[S_\ell + N_\ell]^{-1}. \qquad (2.27)$$

In summary, given galaxy data, one can compute the Fourier-Bessel coefficients describing the density field ρ using equation (2.18) and hence the coefficients of the overdensity field, $\delta_{\ell mn}$ using equation (2.20). The necessary matrices comprising the Wiener filter can again be calculated from the data using equation (2.26) and finally all these elements can be combined such that the reconstructed density field is given by

$$\delta^{\mathrm{recon.}}_{\ell mn} = (\Phi_\ell^{\mathrm{WF}})_{nn'}\delta_{\ell mn'}. \qquad (2.28)$$

2.3.3 Photometric Redshift Space Reconstruction from 2MASS

The basic method described in Section 2.3.2 is for all-sky data and therefore cannot be applied as it stands to 2MASS, which is incomplete across the plane of the galaxy. As mentioned

in Section 2.2, this is a problem common to all reconstructions of the local density field and there are many ways in which it can be tackled, the particular method used here to obtain all-sky 'data' is described in Section 2.3.4. In this Section, the method used to deduce the local photometric redshift space density field across the whole sky is described, together with other details of the reconstruction process as applied to the final dataset. The results are shown in Section 2.4 and in Section 2.5 a correction which needs to be applied to this field to recover a smoothed version of the density field in true redshift space is discussed.

Consider first the construction of the Wiener filter for the 2MASS dataset; equation (2.26) tells us the basic form that this will take. The 'signal' part of the filter is a diagonal matrix involving the power spectrum. In this case, we are seeking the power spectrum for the convolved field. Rather than acting to smooth the density field in the same manner at all points, photometric redshift errors give rise to a convolution function which varies with redshift, as can be seen from figure 2.1. For a given photometric redshift, $z_{\rm phot}$, there is greater uncertainty about the 'true' corresponding redshift the larger the value of $z_{\rm phot}$. Note however that the use of priors in determining the photo-zs makes σ_z more nearly constant at low redshift than if the redshifts were derived from colours where instead $\sigma(z)/1+z \sim const.$ This radial variation means that the power spectrum of the convolved field is not simply related to its true redshift space counterpart and that the relationship between the power spectra of the two fields is non-trivial. To simplify the calculations involved here, we assume that the convolution function which is applied to the field at an intermediate redshift of $z \simeq 0.1$ in fact applies to the entire field. This overestimates the degree of smoothing at low redshifts and underestimates the smoothing at high redshifts.

We also choose to make a simplifying assumption about the isotropy of the convolution. In truth, the 'signal' part of the Wiener filter which we are seeking is given by a smoothing of the true redshift space power spectrum in the radial direction

$$P^{\rm S}(\mathbf{k}) = P(k)D(k_{\rm z}) \tag{2.29}$$

where k is the magnitude of $\mathbf{k}$ and $k_{\rm z}$ its radial component. The form of $\xi(\mathbf{r}_1 - \mathbf{r}_2)$ given in equation 2.25 is therefore modified to

$$\begin{aligned}
\xi(\mathbf{r}_1-\mathbf{r}_2) &= \frac{1}{(2\pi)^3}\int d^3\mathbf{k}\; P(k)\, D(k\cos\theta)\, \exp\{-i\mathbf{k}.(\mathbf{r}_1-\mathbf{r}_2)\} \\
&= \frac{1}{(2\pi)^3}\int dk\; k^2\, P(k) \int d\Omega\; D(k\cos\theta)\, \exp\{-i\mathbf{k}.(\mathbf{r}_1-\mathbf{r}_2)\} \\
&= \frac{2}{\pi}\sum_{\ell m} i^\ell \sum_{\ell' m'} (-i)^{\ell'} \int dk\; k^2\, P(k)\, j_\ell(kr_1)\, j_{\ell'}(kr_2) \\
&\quad \times \int d\Omega\; D(k\cos\theta)\, Y_{\ell m}(\hat{\mathbf{k}})\, Y^*_{\ell m}(\hat{\mathbf{r}}_1)\, Y^*_{\ell' m'}(\hat{\mathbf{k}})\, Y_{\ell' m'}(\hat{\mathbf{r}}_2) \\
&= \frac{2}{\pi}\sum_{\ell m}\sum_{\ell' m'} i^\ell (-i)^{\ell'} \int dk\; k^2\, P(k)\, j_\ell(kr_1)\, j_{\ell'}(kr_2)\, Y^*_{\ell m}(\hat{\mathbf{r}}_1)\, Y_{\ell' m'}(\hat{\mathbf{r}}_2) \\
&\quad \times \int d\Omega\; D(k\cos\theta)\, Y_{\ell m}(\hat{\mathbf{k}})\, Y^*_{\ell' m'}(\hat{\mathbf{k}}). \qquad (2.30)
\end{aligned}$$

This full calculation is complex (Heavens and Taylor, 1995), depending as it does on $\mathbf{k}$ rather than being isotropic. Although it would be possible to compute this full expression, given that the reconstruction is already inexact – redshift smearing is assumed to be constant and the galaxy data is incomplete within the zone of avoidance – the effort expended in performing the full calculation which will only slightly alter the smoothing effect of the Wiener filter in regions where neither signal nor noise strongly dominate, is not worth the gain.

Equation (2.30) is simplified by making the assumption that the smoothing of the power spectrum is isotropic and using the spherical average of $D(k\cos\theta)$ in the above expression. If $D(k\cos\theta) = \exp -(k^2\sigma^2\cos^2\theta)/2$ this spherical average is

$$\begin{aligned}
\frac{1}{4\pi}\int \exp\left\{-(k^2\sigma^2\cos^2\theta)/2\right\}\sin\theta\, d\theta\, d\phi &= -\frac{1}{2}\int_1^{-1} \exp\left\{-(k^2\sigma^2\cos^2\theta)/2\right\} d(\cos\theta) \\
&= -\frac{1}{2}\int_{k\sigma/\sqrt{2}}^{-k\sigma/\sqrt{2}} \exp\{-u^2\}\frac{\sqrt{2}\,du}{k\sigma} \\
&= \frac{(2\pi)^{3/2}}{4\pi k\sigma}\,\mathrm{erf}\left(\frac{k\sigma}{\sqrt{2}}\right) \qquad (2.31)
\end{aligned}$$

and the $D(k\cos\theta)$ term in equation 2.30 passes out of the angular integral. This simplifies the computation to

$$\xi(\mathbf{r}_1-\mathbf{r}_2) = \frac{\sqrt{2\pi}}{\pi\sigma}\sum_{\ell m}\int dk\; k^2\, P(k)\, j_\ell(kr_1)\, j_\ell(kr_2)\, \frac{\mathrm{erf}\left(k\sigma/\sqrt{2}\right)}{k}\, Y^*_{\ell m}(\hat{\mathbf{r}}_1)\, Y_{\ell m}(\hat{\mathbf{r}}_2)$$

Now the computation of the signal proceeds as in equation 2.26

$$
\begin{aligned}
(S_\ell)_{nn'} &= \frac{\sqrt{2\pi}}{\pi\sigma} \int dk\, k^2\, P(k)\, \frac{\mathrm{erf}(k\sigma/\sqrt{2})}{k} \int_0^S ds\, s^2\, j_\ell(k_n s)\, j_\ell(ks) \\
&\quad \times \int_0^S ds'\, (s')^2\, j_\ell(k_{n'} s')\, j_\ell(ks') \\
&= \frac{\sqrt{2\pi}}{\pi\sigma} \int dk\, k^2\, P(k)\, \frac{\mathrm{erf}(k\sigma/\sqrt{2})}{k} \int_0^S ds\, s^2\, j_\ell(k_n s)\, j_\ell(ks) \frac{\pi}{2k^2} \delta(k - k_{n'}) \\
&= \frac{(2\pi)^{3/2}}{4\pi\sigma}\, P(k_{n'})\, \frac{\mathrm{erf}(k_{n'}\sigma/\sqrt{2})}{k_{n'}}\, C^{-1}_{\ell n}\, \delta^{\mathrm{K}}_{nn'} \qquad (2.32)
\end{aligned}
$$

where $C_{\ell n}$ is defined in equation (2.16).

In adopting a form for the power spectrum $P(k)$ in equation (2.32) it is assumed that the galaxy density field is related to the matter density field by a linear bias factor $\delta_g = b\delta_m$. Taking the theoretical model for the linear dark matter power spectrum described in Eisenstein and Hu (1999), a linearly biased version of this is employed as the galaxy power spectrum. The bias value appropriate for $z \leq 0.1$ is used, $b = 1.0$, see Section 2.4.1.

The noise matrix N_ℓ can be computed exactly as it is given in equation (2.26). Having found both N_ℓ and S_ℓ, we are now in a position to construct the Wiener filter. This construction involves taking the inverse of the matrix $S_\ell + N_\ell$, which is achieved using an SVD algorithm (Press et al., 1992). Having determined the Wiener filter, we now look to compute the density field Fourier-Bessel coefficients before finally applying the filter to recover the local density field.

The Fourier-Bessel basis described in Section 2.3.2 can be used to express any three dimensional scalar field to arbitrary accuracy, as long as enough basis functions are used. This is due to the basis functions forming a complete set spanning 3D space. Obviously it is impossible for us to use an infinite number of basis functions to describe our field. Before any other considerations are taken into account, we only have a finite amount of information – the positions of our galaxies – and this imposes an upper limit on the number of Fourier-Bessel coefficients that we can usefully determine. In practice, for the 2MASS dataset, this number is still far too large to be computationally viable, or indeed sensible. The reconstruction approach used here is *linear* so we cannot learn anything about the density field on non-linear scales. This provides a lower limit to the scales which we would like to resolve and an upper limit on the number of Fourier-Bessel coefficients we need to use.

The angular resolution of the reconstruction is determined by the value of ℓ_{max} describing

the number of spherical harmonics used. The $Y_{\ell m}$ have an effective resolution of $\Delta\theta \sim \pi/\ell$ (Peebles, 1980, p176) and a sensible choice for the radial resolution is therefore to match this at some suitable radius. For $x \gg 1$ the zeroes of the Bessel function $j_\ell(x)$ are $x_{\ell n} \sim \pi(n + \ell/2)$, hence the resolution of a radial mode is roughly $\Delta r \sim \pi/k_{n_{\max}}$. By the boundary conditions described in Section 2.3.2, this value of k is given by

$$k_{n_{\max}} = \frac{\pi(n_{\max} + \ell_{\max}/2)}{S_{\max}} \tag{2.33}$$

and therefore $\Delta r \sim S_{\max}/(n_{\max} + \ell_{\max}/2)$.

Now one needs to choose a suitable radius at which to match the radial and angular resolutions. Since $z = 0.1$ corresponds approximately to the peak of the redshift distribution and has been used to define the smearing scale that will be assumed for the entire dataset, this seems a natural choice here also. If the radius at which the angular and radial resolutions are matched is D, then $D \sim 300\,h^{-1}$Mpc and $k_n S_{\max} \leq \ell_{\max} S_{\max}/D$. The reconstruction is performed out to a maximum redshift of $z = 0.3$. This limit was selected as shot noise here is at an acceptable level and the photometric redshift errors are still reasonable. Taking $\ell_{\max} = 30$, a choice motivated by the range of ℓ over which the ISW effect is significant, means that we use radial modes $k_n S_{\max} \leq 85$ in the reconstruction.

In computing the coefficients $\delta_{\ell mn}$ it is necessary to adopt a value of $\bar{\rho}$, the mean density or more accurately $\bar{n}$ since we work entirely in terms of number density. In Section 2.1.3, we computed $\bar{n} = 0.011$ with an error of around 10%, for the reconstruction we adopt $\bar{n} = 0.01$ since this is within the error bars and is a better fit to the value which we compute from the data using the Fourier-Bessel coefficients $\rho_{\ell mn}$

$$\bar{\rho}(\mathrm{s}) = \sum_n C_{0n}\, \rho_{00n}\, Y_{00}(\hat{\mathrm{s}})\, j_\ell(k_0 s) \tag{2.34}$$

These Fourier-Bessel coefficients are calculated by weighting the galaxies by the inverse of the selection function, so in effect the radial selection is divided out here. This value of $\bar{\rho}(\mathrm{s})$ should be constant for all s, giving $\bar{\rho}$. In fact, due to the finite nature of the expansion, a slightly oscillatory solution is found: see figure 2.9. For the 2MASS data, the centre value of this oscillation is $\bar{\rho} = 0.01$ and hence it is this value which is adopted for the reconstruction.

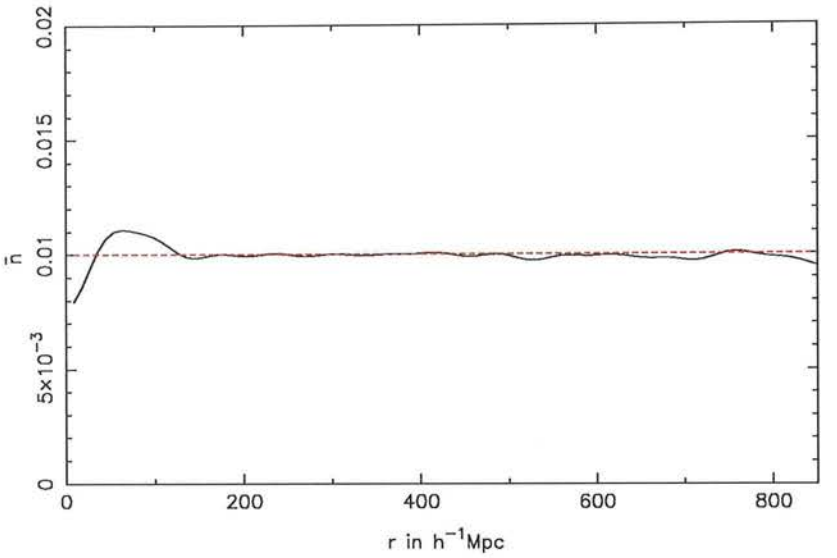

Figure 2.9: The mean number density computed from the Fourier-Bessel expansion of the density field using equation 2.34 (black line) and $\bar{n} = 0.01$ (red dashed line). These Fourier-Bessel coefficients are computed by weighting galaxies by the inverse of the selection function, so in effect the radial selection is divided out. We adopt $\bar{n} = 0.01$ for the reconstruction and note that this is within the 1σ error bars of the previous determination of $\bar{n}$ described in Section 2.1.3.

2.3.4 Filling in the Galactic Plane

Having computed the Wiener filter and chosen the resolution to which the reconstruction is performed, it remains only to deal with the incompleteness in the galactic plane. Obviously, we wish to recover the density field within the plane as accurately as possible, for more than just aesthetic purposes. If the reconstruction were to be used for any kinematic work (e.g. estimation of the local group dipole) then it would be important to attempt to replace the structures missed by the survey behind the galactic plane with a likely set of 'fake' structures. Leaving the plane unfilled is not an option; in this case it would act as a large void – a spurious 'non-structure' in the data. Similarly, filling the plane with non-existent structures will also adversely affect the kinematics. For estimation of all-sky contributions to the CMB temperature fluctuations from local structures it is also advantageous to have as accurate a full-sky reconstruction as possible.

Various methods have been employed by other groups to fill in the missing data, ranging from interpolating the galaxy distribution across the plane (Yahil et al., 1991; Erdoğdu et al.,

2006b) to fitting spherical harmonics to the data outside the cut and allowing these to determine the field inside the plane as well (Saunders et al., 2000). Another alternative is to use a Wiener approach and to invert the mask (Lahav et al., 1994). In this case, the observed Fourier-Bessel coefficients (with the masked region uniformly filled) can be related to the 'true' Fourier-Bessel coefficients in the form

$$\rho^{\rm obs}_{\ell mn} = \sum_{\ell' m'} W^{mm'}_{\ell\ell'} \rho^{\rm true}_{\ell' m' n} \tag{2.35}$$

where

$$W^{mm'}_{\ell\ell'} = \sum_{i=1}^{N_{\rm gal}} Y^*_{\ell m}(\hat{\mathbf{r}}_i) Y^*_{\ell' m'}(\hat{\mathbf{r}}_i) \tag{2.36}$$

and the mask can be inverted at the same time that the Wiener filter is applied to recover the most likely true density field in the minimum variance sense.

Here an iterative method of replacing lost structure is investigated. Beginning with a dataset that is composed of the 2MASS galaxies outside the plane and a Poisson sampling of the mean galaxy density field subject only to the selection function within the plane, we treat this as all-sky data. The Wiener filter is then applied which will tend to extend into the plane over- and underdensities which lie on the edge of it. The next iteration uses this Wiener filtered density field within the plane to compute a new sample of 'fake' galaxies here and the process continues.

Tests using simulation data revealed this process to be unstable. Over- and under-densities created in the plane by the algorithm, whilst occurring at the positions of genuine structures, tended to grow without limit over the course of 10 iterations. The algorithm proved to be extremely reliable at identifying the regions of over- and under-density that were missing from the data, but did not reliably recover the relative amplitudes of these fluctuations, see figures 2.10, 2.11 and 2.12. This instability can be curbed by limiting the number of galaxies which are sampled within the plane at each iteration to the number we would expect given the selection function. We can understand the unrestrained growth of over- and underdensities within the plane without this restriction as follows. Galaxies outside the plane give rise to some Fourier-Bessel coefficients which describe a full-sky density field giving some prediction for the density field within the plane. Each sampling of galaxies within the plane results in some extra Fourier-Bessel coefficients which describe mainly the density field within the plane for

these galaxies but also predicts small changes in the density field outside the plane. Whilst the first set of coefficients is fixed for each iteration, the second set change with each new sample of galaxies within the plane. At iteration 0, where the plane is randomly filled, the coefficients from galaxies outside the plane indicate where under- and overdensities ought to lie within the plane, exactly as they should. The galaxies are then resampled according to this resultant field. Now, the galaxies are distributed such that their contribution to the Fourier-Bessel coefficients reinforces the over- and underdense regions suggested by the distribution outside the mask. This is again what we would hope for. However, there is no limit to this process, the predicted over- and underdense regions keep growing.

In light of this, the results of 'iteration 1' are chosen as the version of the all-sky density field which is accepted. This version is created by first placing galaxies at random positions within the plane according to the selection function, using the Wiener filter on this dataset to predict a full sky density field then sampling this density field to create a final all-sky galaxy catalogue for use in the reconstruction. This is a similar approach to interpolating the galaxy distribution across the plane before performing a reconstruction. In both cases, prior information about where to place the 'fake' galaxies within the plane is used, in the method described here, this information comes from a filtering of the density field outside the plane. The advantage of this over a direct interpolation is that there is no bias towards structures which are aligned perpendicularly to the galactic equator.

Figures 2.10, 2.11 and 2.12 show the results of applying this method to simulation data within sphere of radius $850\,h^{-1}$Mpc $\simeq r(z = 0.3)$. The simulation particles are subjected to photometric redshift smearing as expected for the 2MASS dataset and a selection function is applied to produce a set of 'galaxies' from the simulation with number density as expected from the data. The mask is created using the dust maps of Schlegel et al. and includes all regions where the K-band extinction exceeds 0.05. The top 2 panels show the density field over the whole sky and the same field with the galactic plane mask applied. The lower panels show the results at various stages of the iteration process, revealing the success of the algorithm after 'iteration 1' and the instability at higher iterations.

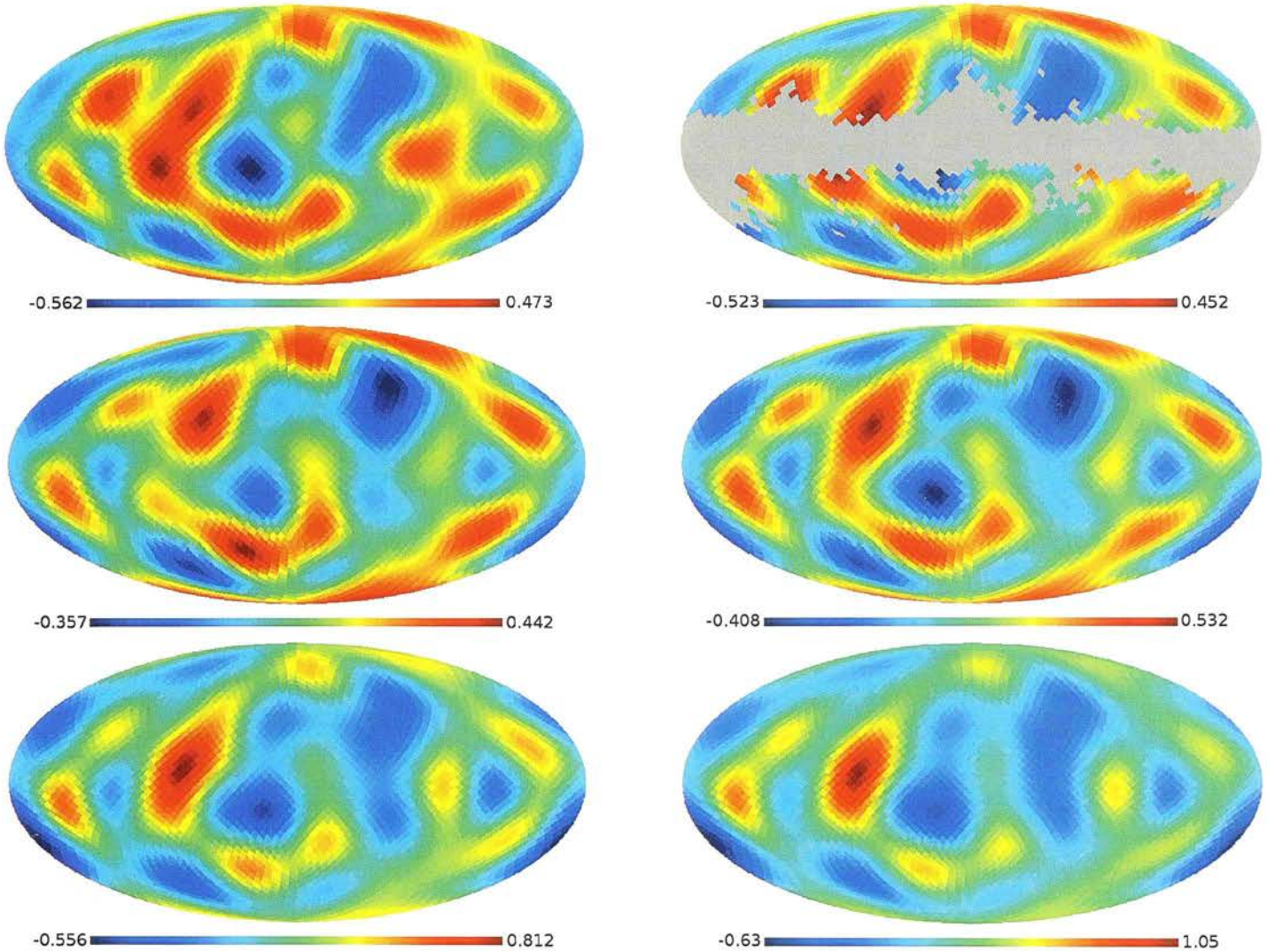

Figure 2.10: (*Top*) The true density field (*left*) with mask (*right*) at $r = 100\,h^{-1}$Mpc and the results of applying the galactic plane fill in algorithm to this density field. (*Centre left*) after placing galaxies at random in the plane, (*Centre right*) after one iteration, (*Bottom left*) after 5 iterations, (*Bottom right*) after 10 iterations . Note the instability at higher iterations but the good correspondence between the truth and the iteration 1 results.

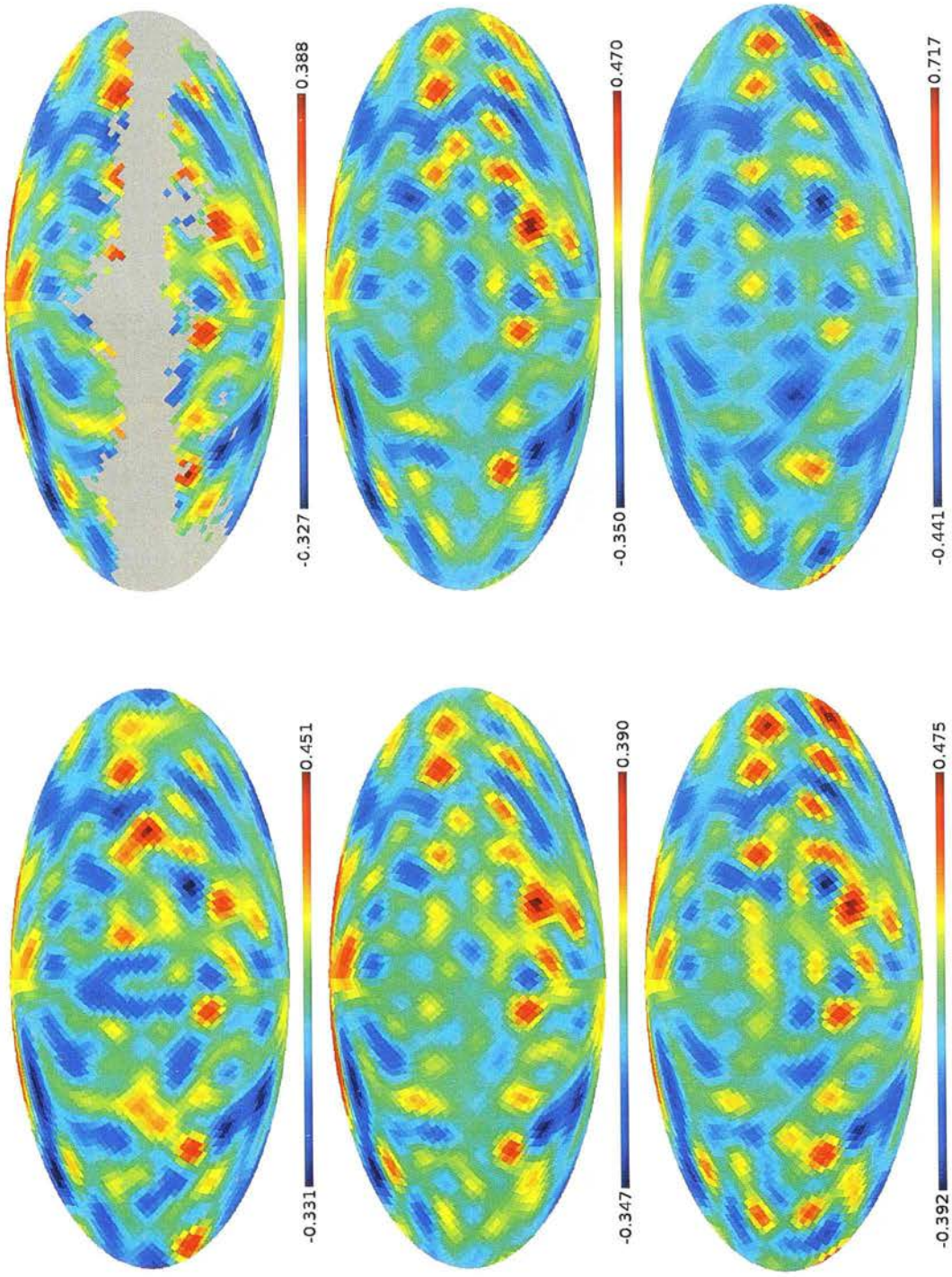

Figure 2.11: As for figure 2.10 at $r = 300\,h^{-1}$Mpc.

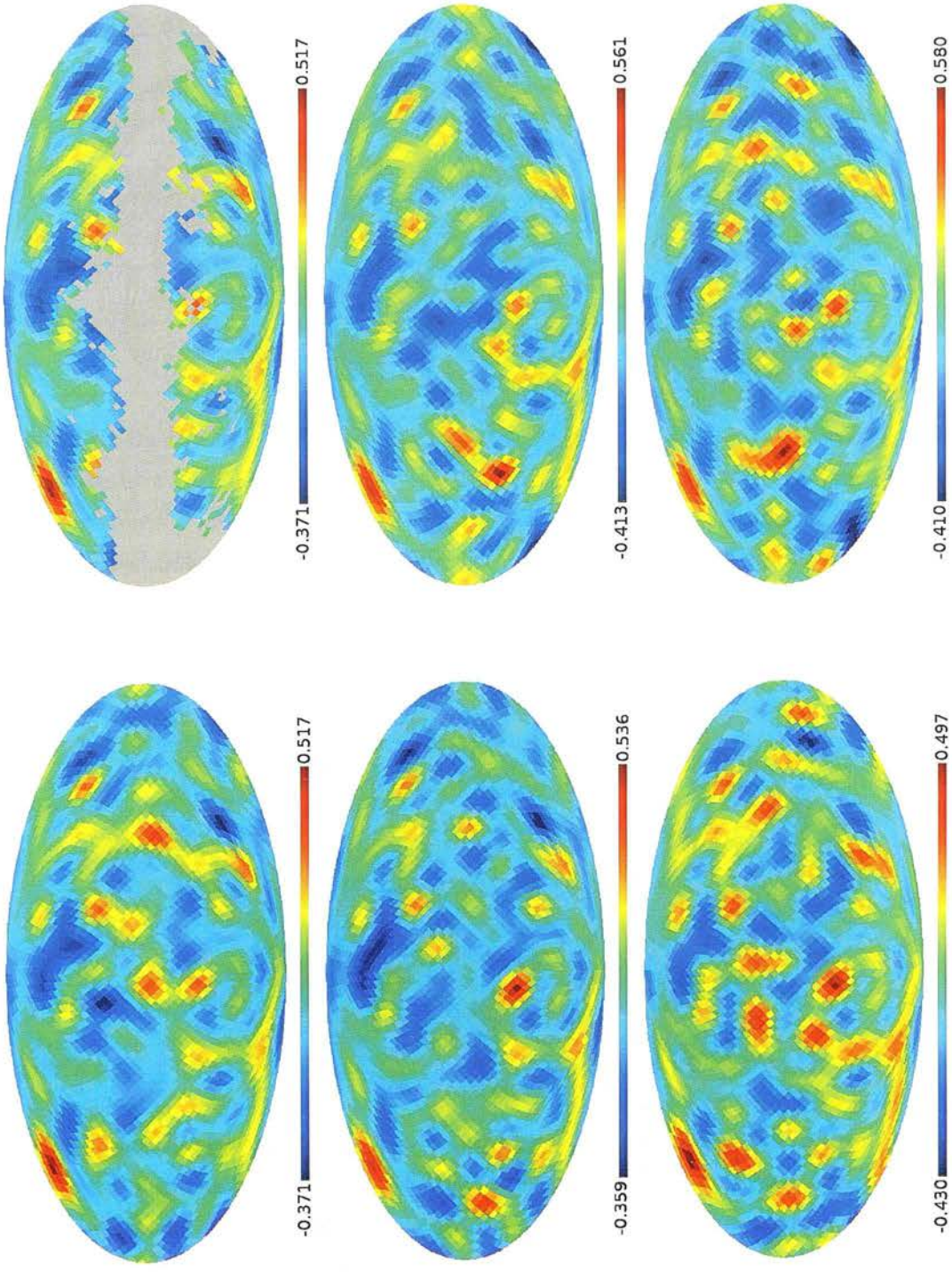

Figure 2.12: As for figure 2.10 at $r = 600\,h^{-1}$Mpc.

2.4 Results for the Real Universe

Having settled on a method of filling in the galactic plane, the reconstruction algorithm described above is applied to the final dataset. The photometric redshift space local density field recovered from 2MASS is shown in various redshift slices in figures 2.13, 2.14, 2.15 and 2.16.

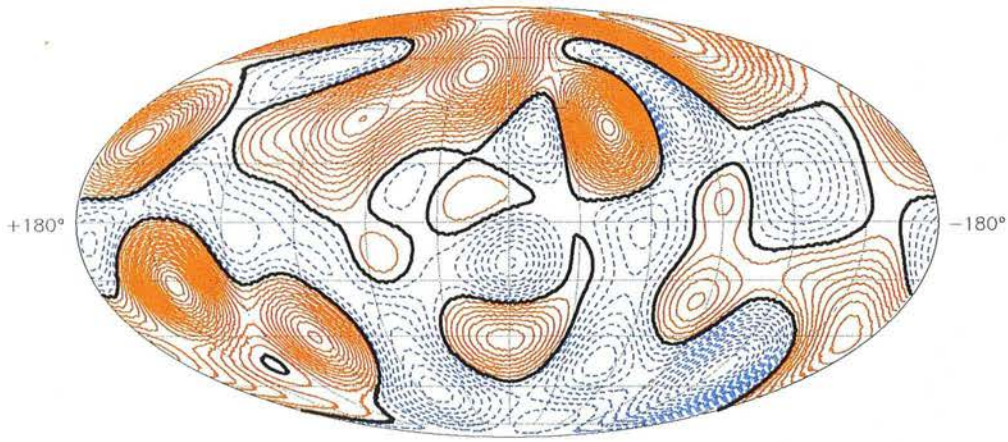

Figure 2.13: The density field at $r = 100\,h^{-1}$Mpc, $\Delta\delta = 0.05$. Solid lines show $\delta > 0$, thick solid black lines show $\delta = 0$ and dashed lines show $\delta < 0$. Main contributions are Shapley ($l \simeq 315°, b \simeq 35°$), Hercules ($l \simeq 60°, b \simeq 40°$), Perseus-Pisces ($l \simeq 140°, b \simeq -20°$), Pegasus ($l \simeq 90°, b \simeq -40°$), Abell 576 ($l \simeq 160°, b \simeq 30°$) and Leo ($l \simeq 210°, b \simeq 75°$).

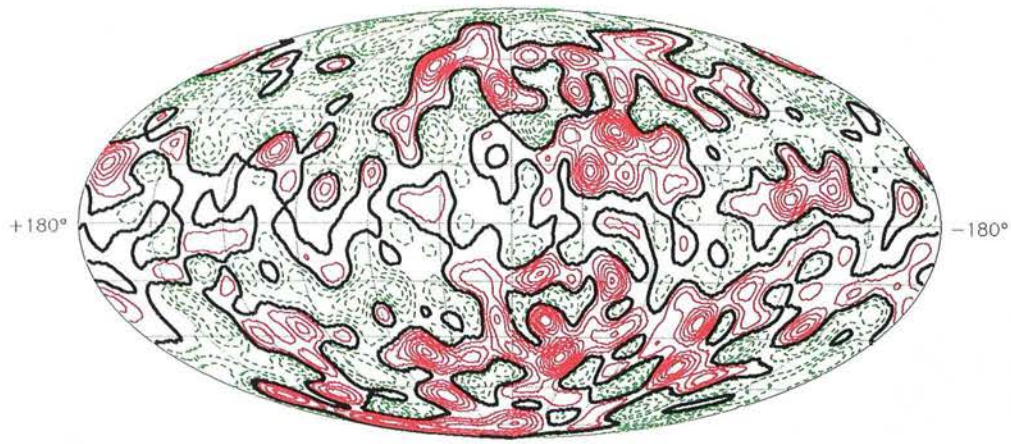

Figure 2.14: The density field at $r = 300\,h^{-1}$Mpc, $\Delta\delta = 0.1$. At higher redshifts, the typical angular size of structures is smaller than that at $r = 100\,h^{-1}$Mpc. Interconnecting structures and voids extend over vast areas of sky. Interestingly, at this distance, structure appears to be concentrated in the hemisphere with $l > 180°$, such asymmetry is not visible in the other shells.

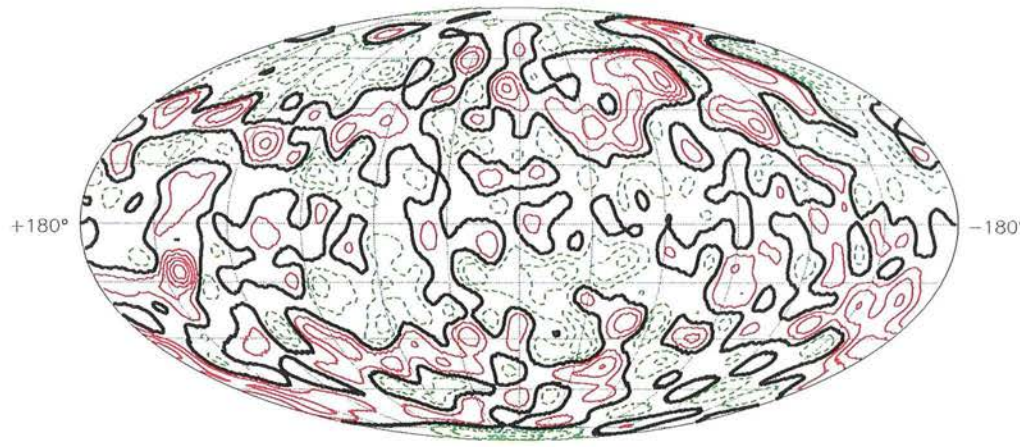

Figure 2.15: On moving to $r = 500\,h^{-1}$Mpc, retaining $\Delta\delta = 0.1$, we note that structures of the same angular size have lower densities than at $r = 300\,h^{-1}$Mpc. This is because such structures will have much larger physical sizes, so the density field is being evaluated at a coarser resolution and we therefore expect its amplitude to decrease.

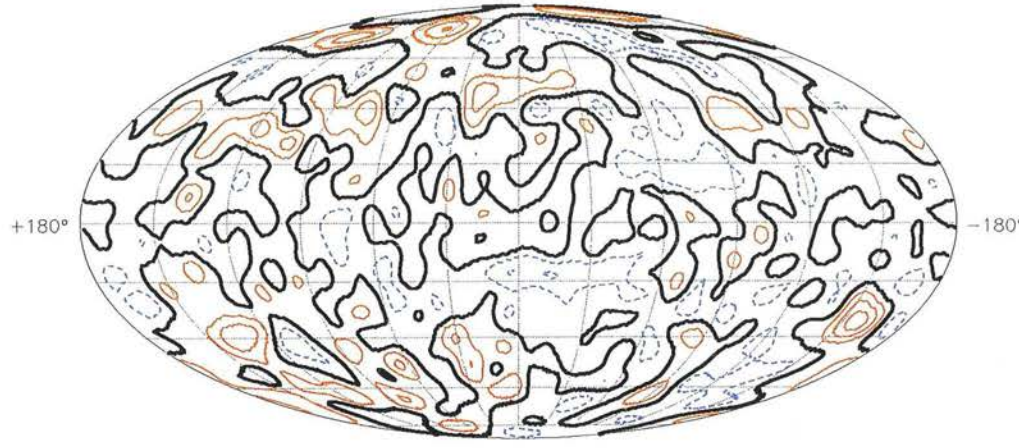

Figure 2.16: The density field at $r = 700\,h^{-1}$Mpc, $\Delta\delta = 0.05$. Density values on the same angular scales as above are smaller again since the physical scales involved are larger. Eventually, the physical smoothing scale defined by the Wiener filter will become large enough that only the mean field is recovered.

2.4.1 Galaxy Bias in the Recovered Density Field

We would like to be able to relate the recovered photometric space galaxy density field to the matter density field. Since we are concerned with the large scale density field, it is a good approximation to use a linear bias relation $\delta_g = b\delta_m$. This has already been assumed in the construction of the 'signal' matrix used for the Wiener filter (see Section 2.3.3) where $P(k) = b^2 P_{\rm CDM}(k)$ and $P_{\rm CDM}(k)$ is computed using a fitting formula (Eisenstein and Hu, 1999). The value of the bias used in this case was computed from the galaxy angular power spectrum in three photometric slices. Full details of this computation are given in Section 5.1.3, where it is used as part of a process to measure the ISW signal with 2MASS; here, the procedure is briefly outlined.

The projected density field of 2MASS galaxies in three redshift slices with $\Delta z = 0.1$ is evaluated outside the galactic plane mask and from this, the angular power spectrum in each slice is computed. This power spectrum will be suppressed due to the lack of full sky coverage, so an attempt is made to correct for the effect of the mask by accounting for lost modes

$$C_{\rm gg}^{\rm corrected}(\ell) = \frac{C_{\rm gg}^{\rm measured}(\ell)}{f_{\rm sky}} \tag{2.37}$$

where $f_{\rm sky}$ is the fraction of the sky left uncovered by the mask. This angular power spectrum will be the sum of the true angular power with a shot noise contribution which is given by

$$C_{\rm gg}^{\rm shot\ noise}(\ell) = \frac{4\pi f_{\rm sky}}{N_{\rm gals}}. \tag{2.38}$$

The true angular power spectrum can therefore be inferred from the observed spectrum and the known shot noise spectrum.

The true redshift distribution of galaxies within each photometric redshift slice can be calculated using data from the spectroscopic subsample of the 2MASS XSC. Knowing this and the true 3D matter power spectrum, and assuming a form for the bias $b(z)$, the galaxy angular power spectrum for a given cosmological model can be predicted. Here the bias is assumed to be independent of z in each slice. The bias is also assumed to be independent of scale, a simplifying assumption that observations show is reasonable on large scales (see e.g. Conway et al. 2005). The predicted angular power spectrum is then given by

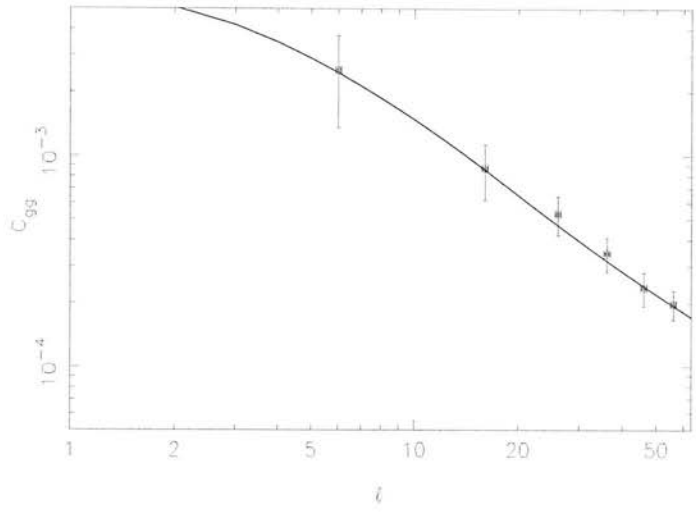

Figure 2.17: The angular power spectrum of 2MASS galaxies with $z < 0.1$ together with the predicted power for a concordance cosmological model with constant bias $b = 1.0$.

$$C_{gg}(\ell) = \frac{2b^2}{\pi} \int dk\ k^2 P_{\delta\delta}(k) \left| \int dr\ g\Theta(r) j_\ell(kr) \right|^2 \tag{2.39}$$

where b is the linear bias value, g is the growth function and Θ is given by:

$$\delta_{\text{projected}} = \int \frac{\bar{n}(r) r^2}{\int \bar{n}(r') r'^2\ dr'} \delta(r)\ dr \equiv \int \Theta(r)\delta(r)\ dr. \tag{2.40}$$

A derivation of this relationship is included in Section 5.1.2. Binning the measured power spectrum values into 6 bins for $\ell \leq 60$ and performing a maximum likelihood fit of the predicted power spectrum to this data gives $b = 0.85, b = 1.2$ and $b = 2.0$ in the three slices, see figure 2.17.

Much of the variation in bias measured in the three slices is likely to be due to the sparse sampling at higher redshifts where only the brightest, most massive galaxies are observed, which are known to be more strongly clustered (Park et al., 1994). Magliocchetti et al. (2000) find that over the redshifts of interest there is no significant evolution in bias and it therefore seems reasonable to assume that bias in the reconstructed field will be constant. The reconstruction algorithm accounts for the sparse sampling at high redshift by heavily weighting the galaxies that are observed there. Whilst this fixes the missing numbers problem, this weighted galaxy density field will still be more strongly clustered at higher redshifts due to the posi-

tions of the known galaxies, the bias of the reconstruction will therefore be affected by this to some extent. The bias in the reconstruction is therefore taken to be a galaxy number weighted average of the three bias values found in the photometric redshift slices of width $\Delta z = 0.1$, resulting in $b = 1.0$ with the cosmological model assumed here. Note that the model used in Chapter 5 is different to this, resulting in different bias values. This rather crude approximation can be tested at some level by examining the power spectrum of the reconstructed density field.

Using equation (2.26), we note that evaluating

$$\langle \delta_{\ell mn} \delta^*_{\ell' m' n'} \rangle \tag{2.41}$$

for the Wiener filtered density field should allow determination of the photometric redshift space power spectrum. This measurement will contain additional smoothing from the Wiener filter, but this is known and can be accounted for. On comparing the measured power spectrum with the predicted form of this from equation (2.32) and assuming constant bias, $b = 1.0$ does indeed provide a good fit.

2.5 Relationship to the True Redshift Space Density Field

We might hope that photometric redshifts are related to true (spectroscopic) redshifts such that the photometric redshift of a galaxy is drawn from a symmetric probability distribution centred on its true redshift. If this were true, then a photometric redshift reconstruction of the density field would merely be a simple convolution of the true redshift space density field i.e. the true density field with some additional smoothing due to the uncertainty in photo-zs. For the reconstruction described above however, there exists a bias in the photometric redshift distribution. This is most easily seen by returning to our plot of photometric redshift versus spectroscopic redshift (cf. figure 2.1). Figure 2.18 shows the same points as figure 2.1, but this time the mean and 1σ errors are plotted for photometric redshifts in spectroscopic bins of width $\Delta z = 0.01$ (as opposed to spectroscopic redshifts in photometric redshift bins of width $\Delta z = 0.01$). We note that, rather surprisingly, the mean photometric redshift is no longer in such good agreement with the corresponding spectroscopic redshift, especially at low redshift, where relative errors are significant. In other words, regressing $z_{\rm spec}$ vs. $z_{\rm phot}$ and $z_{\rm phot}$ vs. $z_{\rm spec}$ give different answers. The agreement between the mean and a line $z_{\rm spec} = z_{\rm phot}$ seen in figure 2.1 was a result of the calibration used – galaxies with photometric redshifts in some

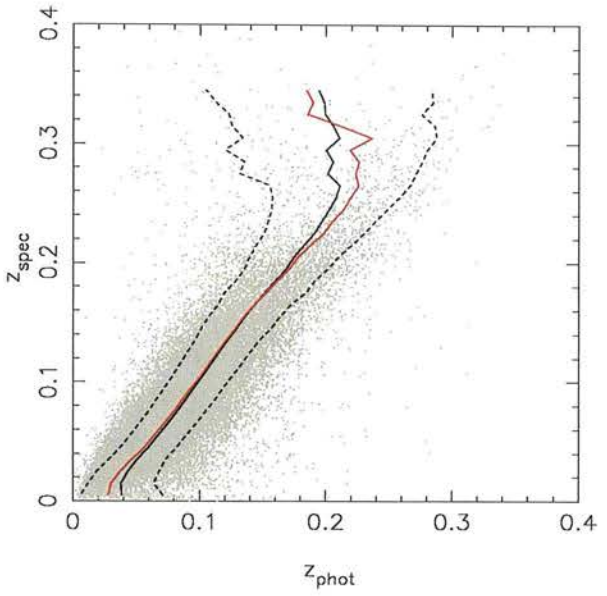

Figure 2.18: Spectroscopic and photometric redshifts for the spectroscopic subsample of the 2MASS XSC, together with the mean (solid black line) and median (red line) photometric redshift within spectroscopic redshift bins of width $\Delta z = 0.01$. The dashed black lines show the 1σ error bars. Note the bias in the mean redshift when evaluated in this way, which gives rise to a particularly large relative error at low z.

small range should be expected to have spectroscopic redshifts in this same range i.e. the mean of the associated spectroscopic redshifts should correspond to the photo-z in question. The relationship which we see in figure 2.18 reflects the fact that this does not quite work in reverse. This is due to the number of objects at low redshift with $z_{\rm phot} > z_{\rm spec}$ and those at high redshift with $z_{\rm phot} < z_{\rm spec}$ being significant with respect to the total number of galaxies in that $z_{\rm spec}$ bin. A bias of this kind will be a feature of most methods of calculating photo-zs and has implications for the reconstruction.

In order to achieve a reconstruction which is simply a smoothed version of the true redshift space density field, this bias needs to be corrected. We need to transform to a situation where galaxies at a given true redshift have photometric redshifts distributed symmetrically about this point or equivalently, where density peaks in both the photometric and spectroscopic density fields coincide rather than displaying a shift as we note at present (see figure 2.19). A coordinate transformation and the associated Jacobian matrix are used to this end.

Figure 2.20 shows the relationship between the 'true' radial distance and the mean of the distances computed using the spectroscopic redshifts of galaxies whose photometric redshifts

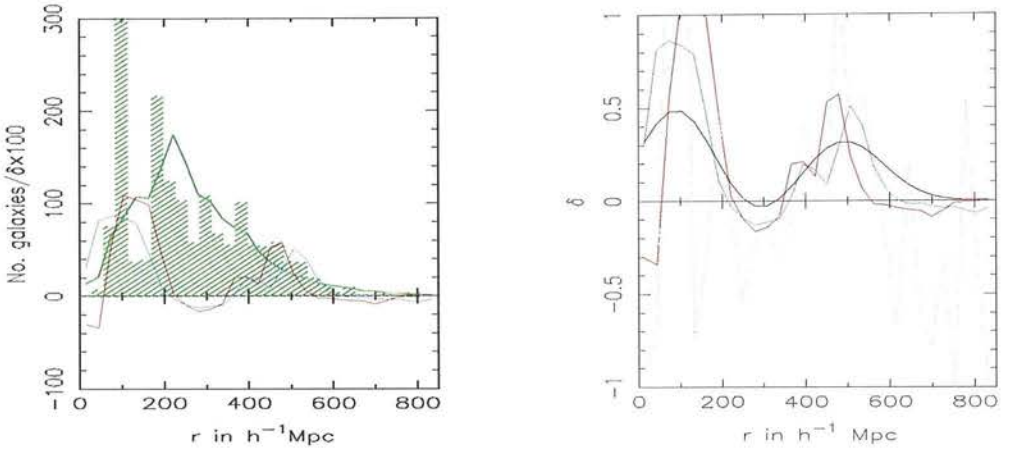

Figure 2.19: An illustration of the bias present in the photometric redshift reconstruction. (*Left*) Histogram of true galaxy positions and expected number of galaxies in each redshift bin (green line) together with the (scaled) overdensity predicted from the reconstruction (red line). Note the shift in the low redshift density peak to higher redshift. (*Right*) The reconstruction overdensity (red line), together with an estimate of the true density field (grey dashed line) computed from raw galaxy numbers (and therefore very noisy) together with a smoothed version of this (see Section 2.5 for details). The shift of the density peak is again visible. In both plots the blue lines show the density field corrected for this bias. See figure 2.21 for further examples.

indicate them to lie within a narrow distance bin centred on this true value. We can make a fit to the mean distance computed from photometric redshifts as a function of distance computed from spectroscopic redshift

$$\bar{r}_{\rm phot} = f(r_{\rm spec}). \tag{2.42}$$

Then, defining $r_{\rm new} = f(r_{\rm spec})$ and $r_{\rm old} = r_{\rm spec}$ we have

$$\int_V \rho(r_{\rm new})\ d^3 r_{\rm new} = \int_V \rho(r_{\rm old})\ d^3 r_{\rm old} \tag{2.43}$$

Defining the Jacobian matrix $J_{ij} = \partial r_{{\rm old},i}/\partial r_{{\rm new},j}$, we then see:

$$\int_V \rho(r_{\rm new})\ d^3 r_{\rm new} = \int_V \rho(r_{\rm old})|J|\ d^3 r_{\rm new}. \tag{2.44}$$

Considering figure 2.20, we want to achieve a situation where the mean within each bin and the 'true' value are the same, at present this is not the case. By fitting a line to the data shown

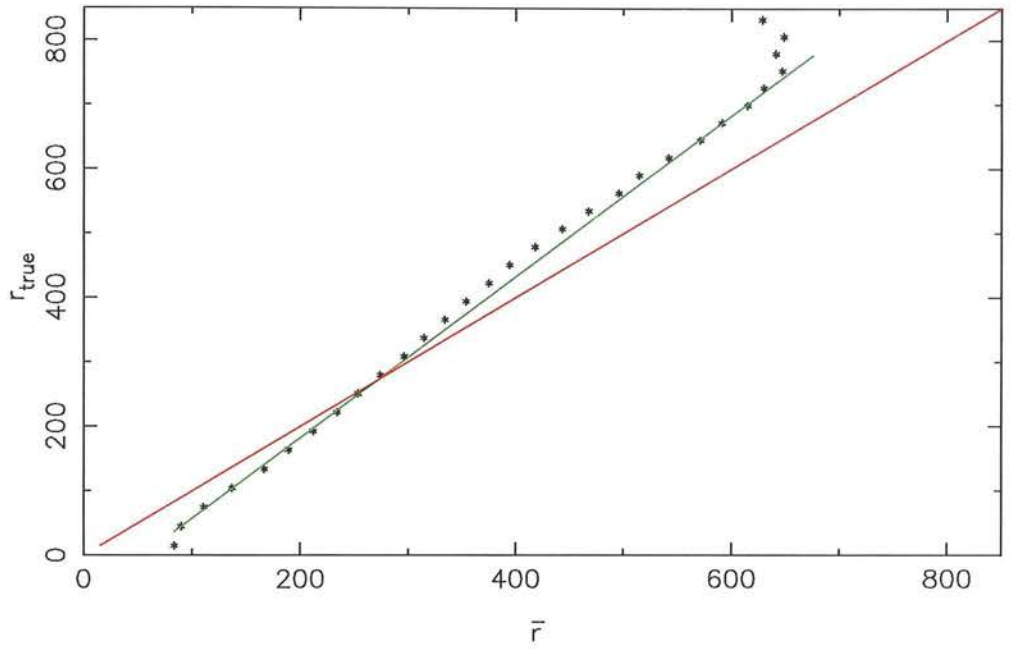

Figure 2.20: The mean galaxy distance computed from photometric redshifts with corresponding spectroscopic redshifts in a bin of width $\Delta z = 0.01$ (black points), together with a fit to these (green line) and the line $r_{\rm spec} = \bar{r}$ (red line).

in this figure, a transformation $r_{\rm old} \rightarrow r_{\rm new}$ can be deduced such that the required relationship is attained. This transformation is found to be

$$r_{\rm new} = 1.25 r_{\rm old} - 68 \tag{2.45}$$

Using spherical polar coordinates (r,θ,ϕ) we find that the Jacobian of this transformation is simply $|J| = 1/1.25$ and hence the new density field is easily computed. Figure 2.21 shows the old and new overdensity fields within a few pixels in the SDSS region together with the overdensity that one would compute using the spectroscopic positions of galaxies in these pixels – a noisy version of the true density field. We are looking for the corrected density field to be a smoothed version of this noisy 'true' field with over- and underdensities centred on their 'true' counterparts. We note that the new density field does indeed achieve this to a greater extent than the old, biased density field as hoped.

To attempt a more quantitative assessment of the quality of the unbiased reconstruction, I

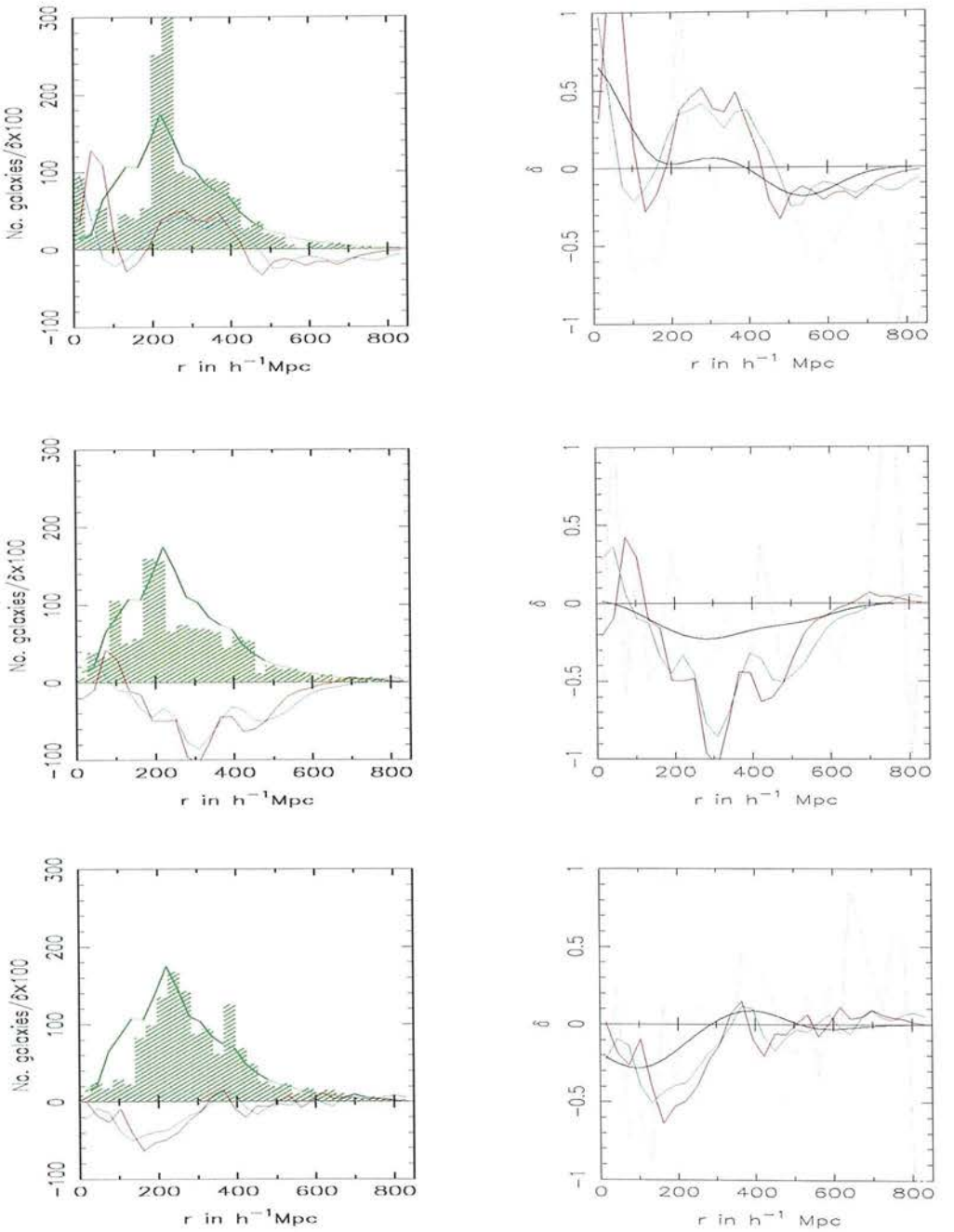

Figure 2.21: (*Left*) A histogram of the galaxy positions within a pixel together with the average number of galaxies in each redshift bin in the SDSS region (green line). When the histogram falls below the green line one would expect negative overdensities and when the histogram is above the green line, positive overdensities. Also plotted are the scaled reconstruction overdensities $\delta \times 100$ in the biased (red line) and corrected (blue line) case. (*Right*) The 'true' overdensity (grey line) computed using true galaxy positions; a smoothed (see text for details) version of this (black line); together with the biased (red) and corrected (blue) reconstruction δ values.

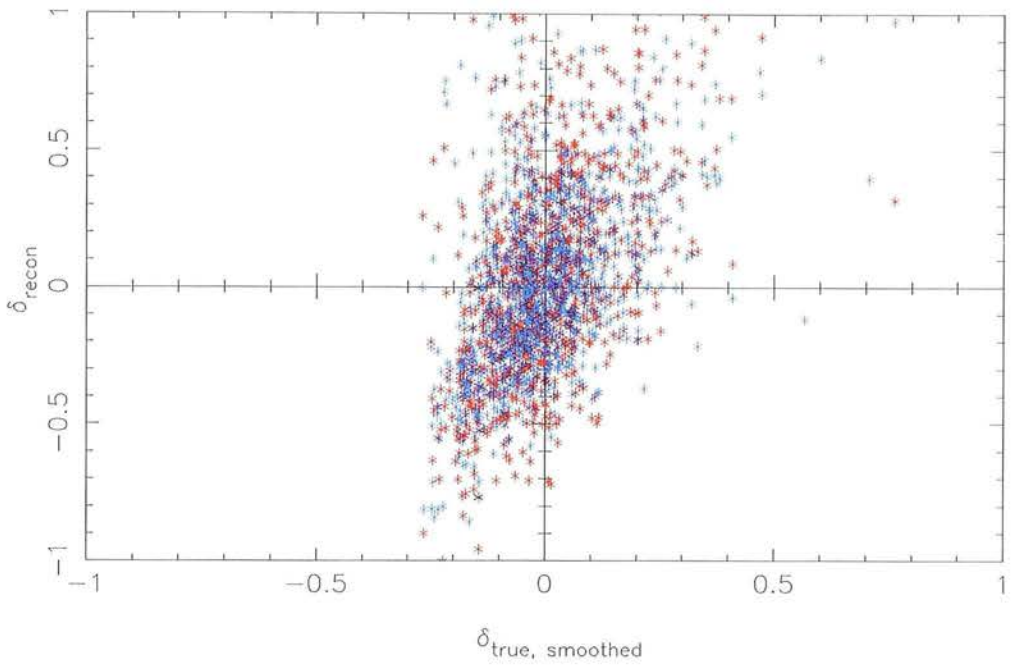

Figure 2.22: Comparison of smoothed true δ values with the reconstructed δ values in regions of high spectroscopic completeness before (red) and after (blue) correction for the bias in the photo-zs. The rms in $\delta_{\rm true} - \delta_{\rm recon}$ decreases from 0.35 to 0.28 after the correction is applied.

have compared values of the smoothed true density field with the reconstructed values in bins $\Delta z = 0.01$. An example of the smoothed field used is shown in figure 2.21 and is computed by smoothing the raw true δ values with a Gaussian whose width is given by the photometric redshift error. The smoothing is carried out only for true density values with $r < 600\,h^{-1}$Mpc ($z \sim 0.2$) as noise dominates the field beyond this point. Figure 2.22 shows a comparison of these smoothed true density values together with the biased and corrected reconstruction values with $r < 600\,h^{-1}$Mpc. We note a pleasing agreement between the smoothed 'true' density field and the reconstruction and the fact that the corrected, unbiased field has a smaller scatter than the biased reconstruction, with rms in $\delta_{\rm true} - \delta_{\rm recon}$ of 0.28 as opposed to 0.35.

The corrected density field i.e. a smoothed version of the true redshift space density field is shown in various radial shells in figures 2.23, 2.24, 2.25, 2.26, 2.27, 2.28, 2.29 and 2.30.

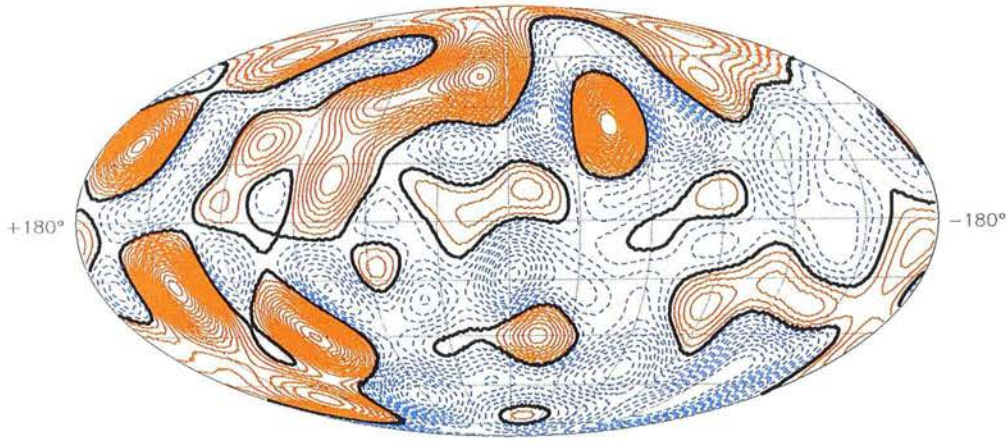

Figure 2.23: The density field at $r = 100\,h^{-1}$Mpc, with $\Delta\delta = 0.05$ shown in Galactic Mollweide projection. The Shapley concentration is again prominent ($l \simeq 310°, b \simeq 30°$), together with Hercules ($l \simeq 60°, b \simeq 40°$) and Pisces-Perseus ($l \simeq 140°, b \simeq -20°$).

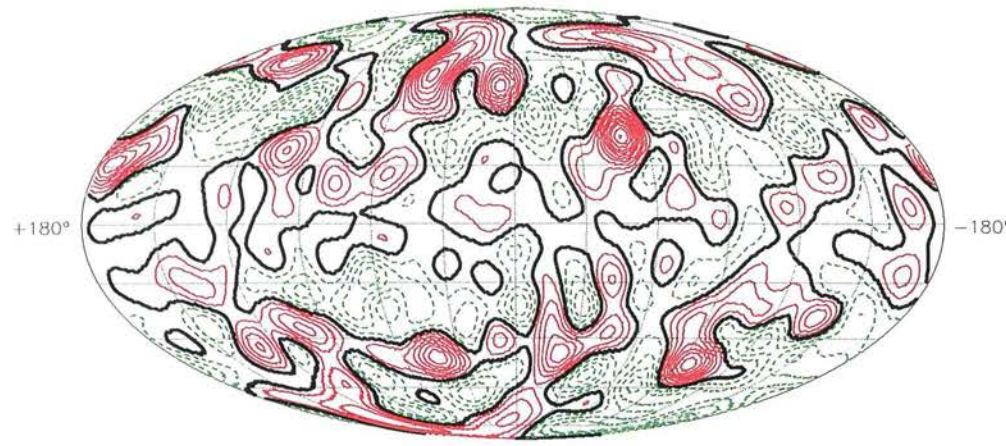

Figure 2.24: The density field at $r = 200\,h^{-1}$Mpc, with $\Delta\delta = 0.1$. The Shapley concentration is still prominent, and we see a general trend of decreased angular size for structures reflecting the fact that this shell is at a larger radius and a given physical scale will therefore subtend a smaller angle.

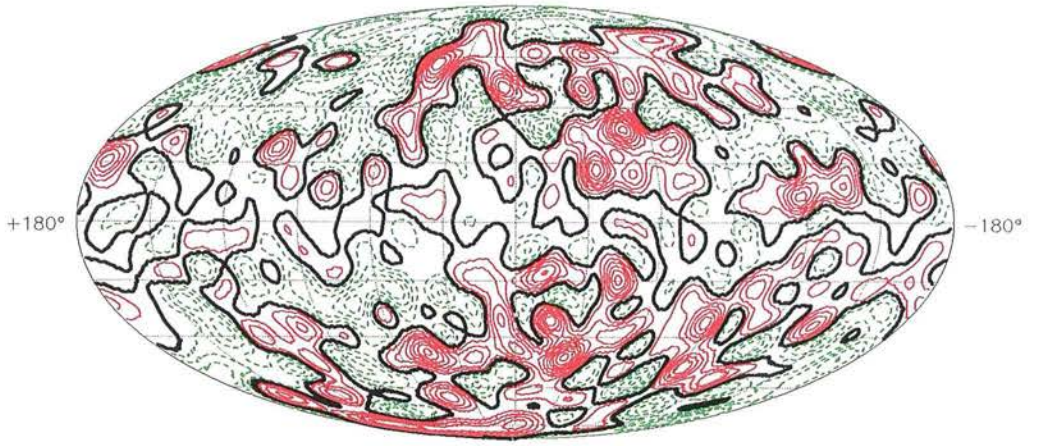

Figure 2.25: $r = 300\,h^{-1}$Mpc, $\Delta\delta = 0.1$. The upper left quadrant of the map is noticeably underdense.

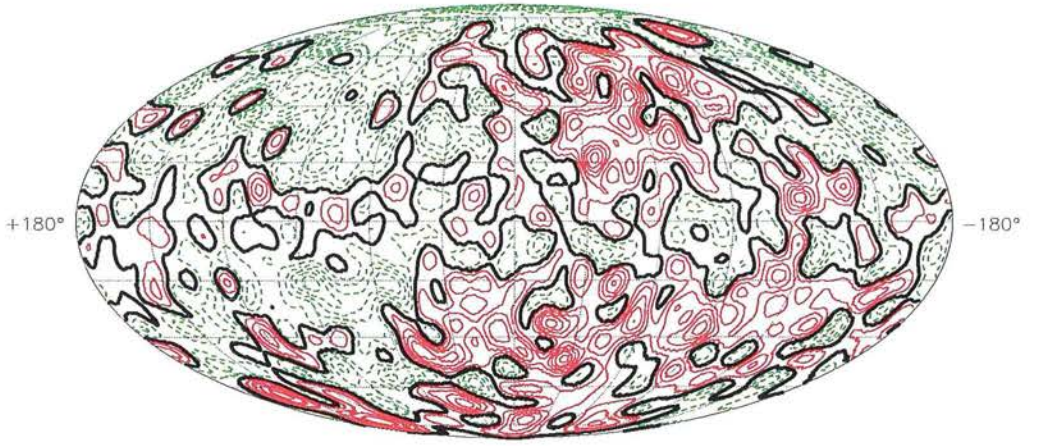

Figure 2.26: $r = 400\,h^{-1}$Mpc, $\Delta\delta = 0.1$. Underdensity in the northern equatorial hemisphere is noticeable, but this does not continue in higher redshift slices.

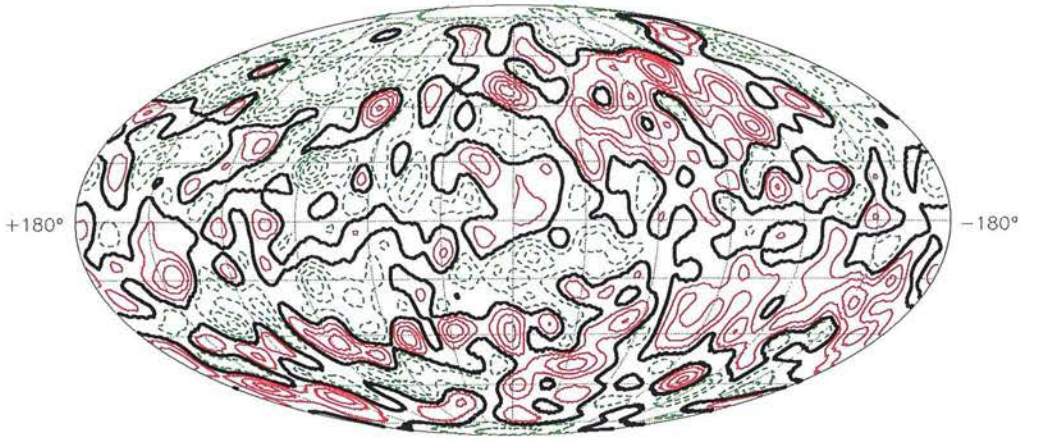

Figure 2.27: $r = 500\,h^{-1}$Mpc, $\Delta\delta = 0.1$.

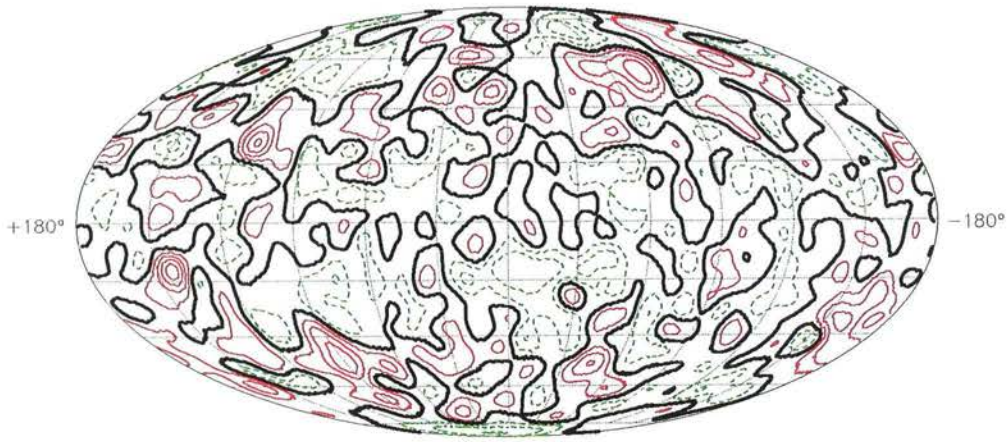

Figure 2.28: $r = 600\,h^{-1}$Mpc, $\Delta\delta = 0.1$.

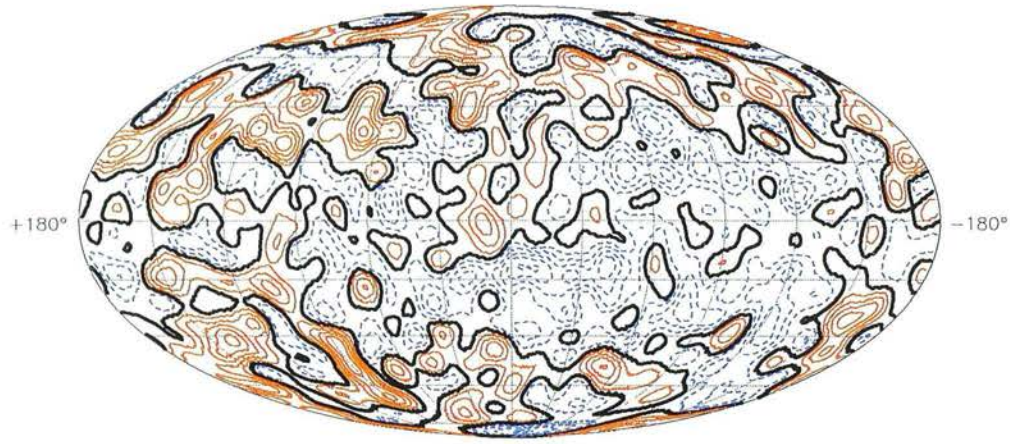

Figure 2.29: $r = 700\,h^{-1}$Mpc, $\Delta\delta = 0.05$. At such redshifts, the data is noisy and the Wiener filter causes the recovered density field to be a good approximation to the mean field.

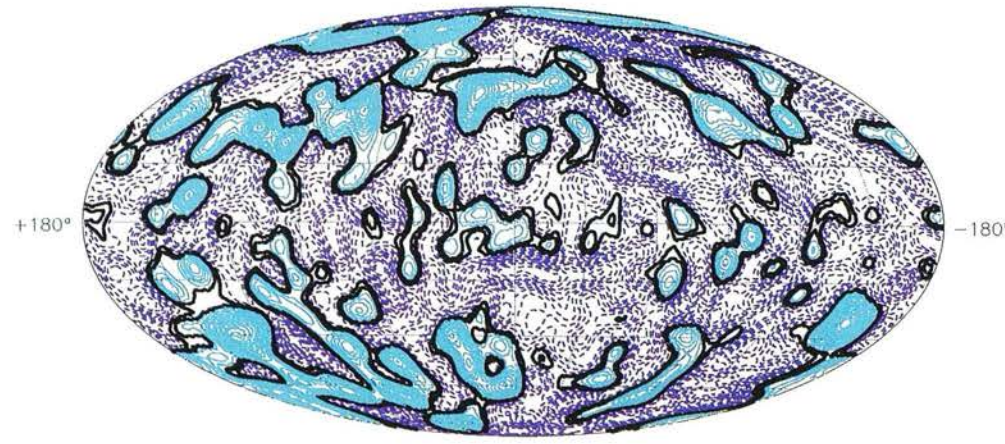

Figure 2.30: $r = 800\,h^{-1}$Mpc, $\Delta\delta = 0.01$.

2.6 Properties of the Reconstruction - A Summary

In this Chapter, the photometric redshift dataset from 2MASS which is used throughout this thesis is presented. The general principles behind reconstruction of a density field are outlined and specifics of the Wiener filter technique are discussed. An existing reconstruction algorithm is modified to apply to the final dataset described in Section 2.1.3 and a novel method of replacing lost information from the Galactic Plane is developed. The reconstruction performed in this Chapter recovers the local density field out to a maximum redshift of $z = 0.3$. The correction of bias in the photometric redshifts used to compute the final density field means that the recovered overdensity field can be viewed as a smoothed version of the density field in true redshift space. In this Section the advantages and disadvantages of this type of reconstruction are considered and the results are compared with those of other groups who have recovered the density field using spectroscopic datasets.

2.6.1 Limitations of this Reconstruction

The resolution of the reconstruction presented here is quite low, due both to the use of photometric redshifts which affect the radial resolution and the large volume over which the reconstruction is computed. The latter is an issue because setting the angular resolution small will mean that at low redshifts we are dealing with non-linear scales when the analysis is constructed around the assumption of linear theory. Placing an upper limit on the values of k used in the reconstruction could ensure that only linear scales are considered. Leaving the resolution coarse enough that no significant low redshift volume is affected by this means that the physical scales which are resolved angularly with $\ell_{\rm max} = 30$ at high redshift are large. Whether the low resolution is an issue depends of course on the science which one wants to do with the reconstruction. For the estimation of large scale CMB secondary anisotropies considered here, this reconstruction is sufficient; the ISW effect is only a significant proportion of the total CMB power for multipoles $\ell \lesssim 30$ and the fact that these anisotropies are computed as integrals over the line of sight means that the radial resolution can be accounted for. For smaller scale work such as the detailed constrained simulations of the local volume which have been performed using other reconstructions (Mathis et al., 2002), such resolution would not be acceptable. The information which is available about the density field at very low redshifts is also limited, for such applications, a reconstruction using a spectroscopic redshift survey would give much

better results.

2.6.2 Previous Reconstructions of the Local Density Field

A number of groups have reconstructed the local density field using different datasets, details of some of these reconstructions and their applications are outlined below. Comparison between the results in this Chapter and those of other groups is not straightforward since previous reconstructions have only been carried out using spectroscopic redshift data (thereby giving reconstructions with finer radial resolution than can be achieved here) and the volumes covered are as a result far smaller than that of this reconstruction. A qualitative consideration of the different methods can however be made and the merits of working with photometric and spectroscopic redshifts analysed.

Fisher et al., 1995

The reconstruction method which underlies the work in this Chapter was developed in F95 and applied to the *IRAS* 1.2Jy survey. This survey found redshifts for 5313 galaxies over 87.6% of the sky, the galactic plane was filled in by smoothly interpolating the redshift distribution over the missing regions. The reconstruction was performed in a sphere of radius $r = 200\,h^{-1}$Mpc with $\Delta r \sim 6\,h^{-1}$Mpc and $\ell_{\max} = 15$. A transformation of the redshift space density field coefficients to real space is made with the aid of assumptions which are valid under linear theory. The Great Attractor and Perseus-Pisces superclusters dominate both the density and potential fields in the supergalactic plane. Figure 2.31 shows their reconstructed density field in the supergalactic plane together with a slice through the same plane from the reconstruction developed here and from that of Erdoğdu et al. (2006b) (see below). The broad agreement between over- and underdense regions is good and the difference in radial resolution is immediately apparent. Also clear is the radial smearing in the reconstruction of the density field computed in this Chapter caused by the use of photometric redshifts.

Erdoğdu et al., 2006

Using 23,200 galaxies from the Two Mass Redshift Survey (2MRS) for which spectroscopic redshifts are available, Erdoğdu et al. (2006b) reconstructed the local density field and predicted local velocity fields. Their method is also based on that of F95, employing a Fourier-Bessel

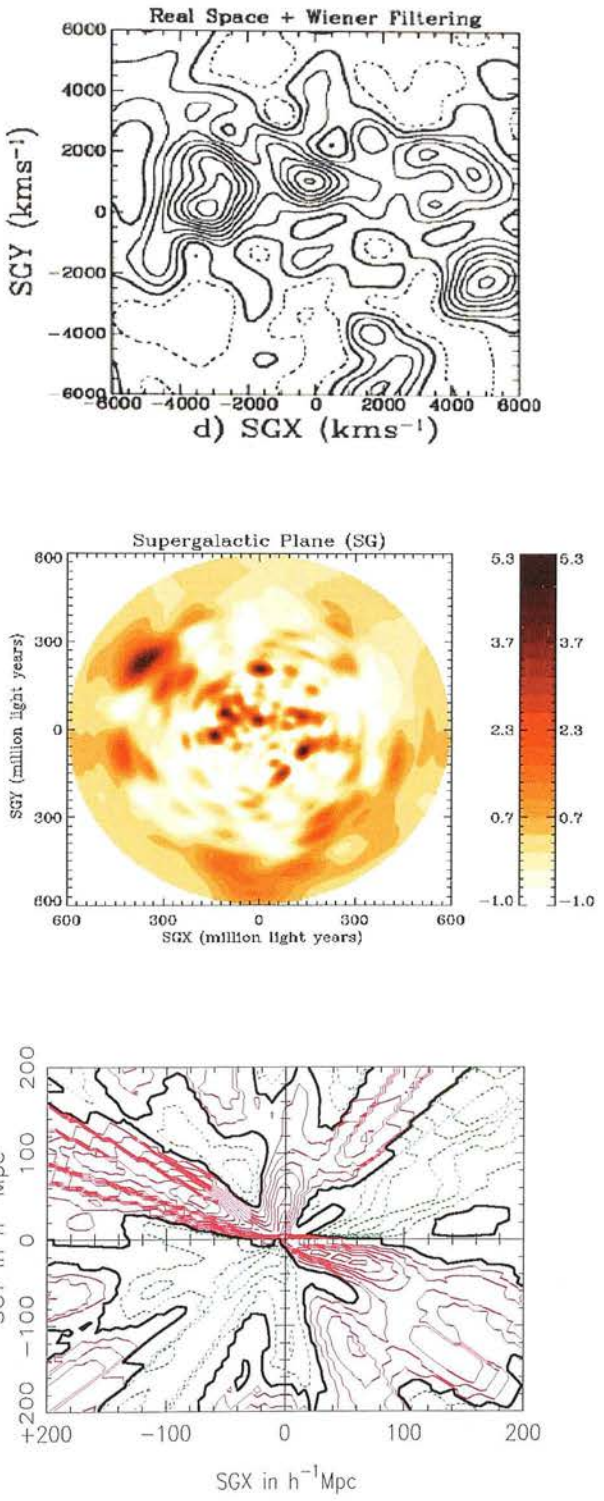

Figure 2.31: (*Top*) The density field in the supergalactic plane as computed by F95; (*Centre*) as computed by Erdoğdu et al. (2006b) and (*Bottom*) for this work where pink contours are positive densities and green contours negative densities with $\Delta\delta = 0.1$.

basis and Wiener filtering technique. The transformation from redshift space to real space was achieved by inverting a matrix which describes the effect of redshift space distortions and linear bias was assumed to relate the galaxy density field to the underlying matter density field. The galactic plane was filled by dividing it into longitude and distance bins and sampling galaxies from the corresponding bins above and below the plane. The number of galaxies sampled was chosen as a random Poisson deviate whose mean is equal to the mean number of galaxies in these adjacent bins. The maximum redshift for this reconstruction was $z \sim 0.05$ and a resolution of $\Delta r \sim 6\,h^{-1}$Mpc was achieved. Example slices through the density field at $r = 80\,h^{-1}$Mpc, $r = 100\,h^{-1}$Mpc and $r = 120\,h^{-1}$Mpc are shown in figure 2.32, together with the reconstruction from this thesis at $r = 100\,h^{-1}$Mpc.

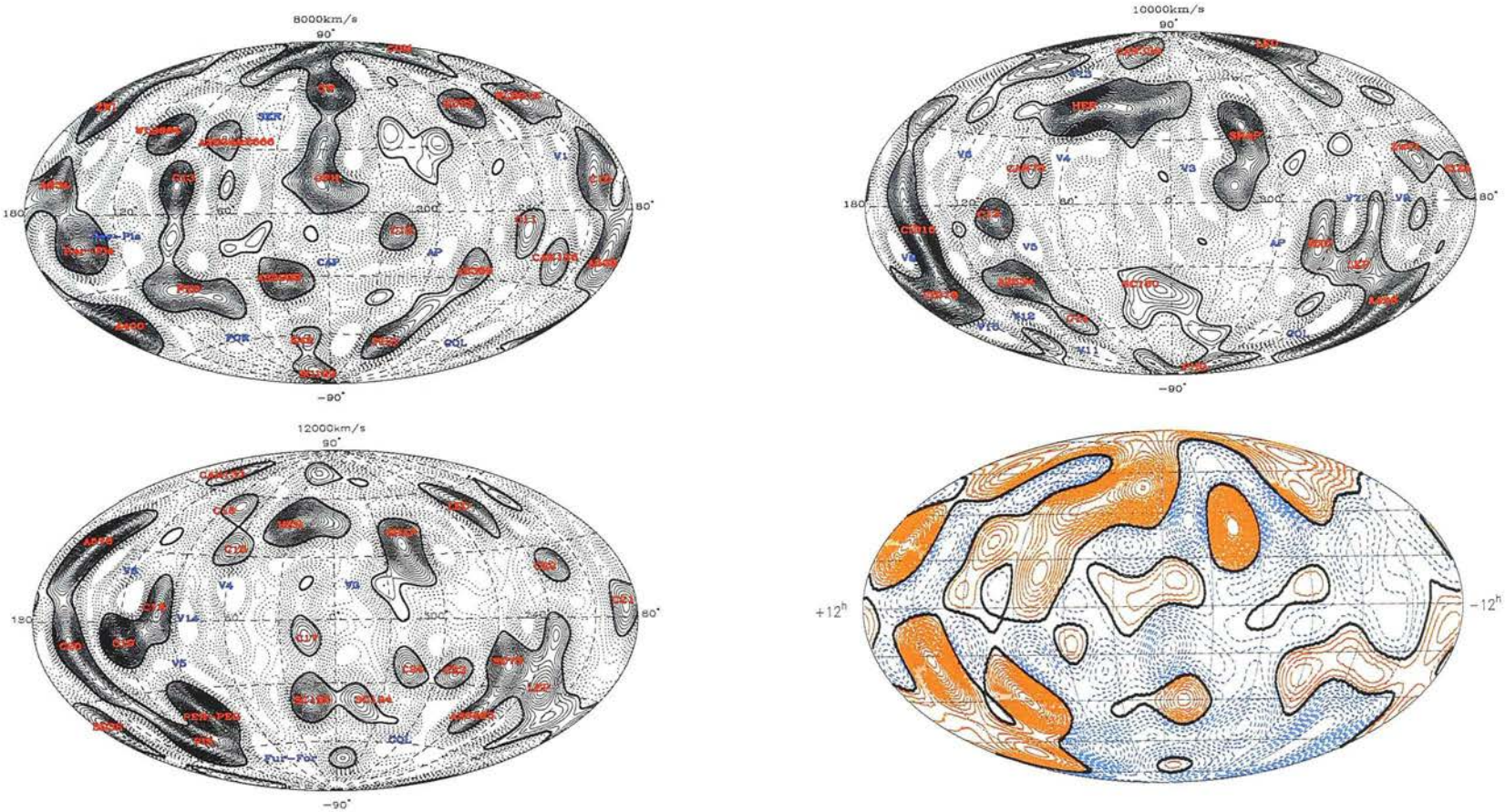

Figure 2.32: The density field as recovered by Erdoğdu et al. (2006b) at (*Top left*) $r = 80\,h^{-1}$Mpc, (*Top right*) $100\,h^{-1}$Mpc and (*Bottom left*) $120\,h^{-1}$Mpc and (*Bottom right*) from the reconstruction determined in this thesis at $r = 100\,h^{-1}$Mpc. We can see some of the effects of using photometric redshifts – structures such as Perseus-Pegasus are not visible in their reconstruction at $r = 100\,h^{-1}$Mpc but appear at $r = 120\,h^{-1}$Mpc; the radial smoothing due to the photo-zs means that this structure is however present in the $r = 100\,h^{-1}$Mpc map from this reconstruction.

Comparing these images with slices through my reconstructed density field at similar radii, one immediately notes the differing resolutions of the reconstructions. In contrast to the $\Delta r \sim 6\,h^{-1}$Mpc resolution used by Erdoğdu et al. (2006b), a resolution of $\Delta r \sim 30\,h^{-1}$Mpc has been used in this thesis, chosen to match the angular resolution at the characteristic redshift of the survey in each case. Whilst this reconstruction recovers the major regions of over- and underdensity found by Erdoğdu et al. (2006b) at each radius shown here, the use of photometric redshifts causes structures to be smeared along the line of sight and to contribute to the density field over a broad range of radii. Thus some of the overdensities seen in radial slices for this reconstruction will in reality be from a structure at a different radial position. For example, at $r = 100\,h^{-1}$Mpc, we note lingering overdensities around ($l = 120°, b = -30°$) from Perseus-Pisces, Perseus-Pegasus and Pegasus which are absent from the corresponding Erdoğdu map, but present at $r = 80\,h^{-1}$Mpc or $r = 120\,h^{-1}$Mpc.

CHAPTER 3

The Local ISW Effect

Having recovered the local density field in photometric redshift space in Chapter 2, some applications of this are now considered. In this Chapter a prediction of the local ISW effect is made and in Chapter 4 the large scale SZ effect is predicted. These two effects are the only significant large-scale CMB secondary anisotropies. In Sections 3.1 and 3.2, the method used to predict the ISW signal from a photometric redshift reconstruction of the density field is described. In Section 3.3 the cross-correlation between this predicted ISW map and the observed CMB temperature fluctuations is calculated and compared to the expected signal. A prediction of the local ISW signal is also made from a 2D reconstruction of the density field in redshift slices for comparison with the full 3D result; Section 3.4 describes this process. Finally in Section 3.5 the issue of whether the late ISW effect could give rise to any of the anomalies which have been noted in the CMB data is addressed.

3.1 Predicting the Local ISW Effect

The choice of spherical harmonics and spherical Bessel functions as the basis for the reconstruction in Section 2.3.3 is particularly useful for recovery of the potential field because the product of these functions is an eigenfunction of the Laplacian.

To see this, begin with the definition of $Y_{\ell m}$

$$Y_{\ell m} = \begin{cases} A P_{\ell m}(x)\, e^{im\phi} & m \geq 0 \\ A P_{\ell |m|}(x)\, e^{im\phi} & m < 0 \\ 0 & |m| > \ell \end{cases}$$

where $x = \cos\theta$ and

$$A = \sqrt{\frac{2\ell+1}{4\pi}\frac{(\ell-m)!}{(\ell+m)!}}$$

We then have the derivatives

$$\begin{aligned} \frac{\partial}{\partial\theta}\left(\sin\theta\frac{\partial}{\partial\theta}Y_{\ell m}(\theta,\phi)\right) &= A\,\sin\theta\, e^{im\phi}\left(-2x\frac{\partial}{\partial x}P_{\ell m}(x) + \sin^2\theta\frac{\partial^2}{\partial x^2}P_{\ell m}(x)\right) \\ &= A\sin\theta\, e^{im\phi}\left(-\ell(\ell+1) + \frac{m^2}{\sin^2\theta}\right)P_{\ell m}(x) \qquad (3.1) \\ \frac{\partial^2}{\partial\phi^2}Y_{\ell m}(\theta,\phi) &= -A\, m^2\, e^{im\phi}\, P_{\ell m}(\cos\theta), \qquad (3.2) \end{aligned}$$

using the fact that $P_{\ell m}$ solves

$$\frac{d}{dx}\left[(1-x^2)\frac{dy}{dx}\right] + \left[\ell(\ell+1) - \frac{m^2}{1-x^2}\right]y = 0. \qquad (3.3)$$

Now, by the definition of $j_\ell(kr)$ (Jackson, 1998, page 427)

$$\frac{1}{r}\frac{d^2}{dr^2}\left(r j_\ell(kr)\right) = \frac{1}{r^2}\frac{\partial}{\partial r}\left(r^2\frac{\partial}{\partial r}j_\ell(kr)\right) = \left[\frac{\ell(\ell+1)}{r^2} - k^2\right]j_\ell(kr). \qquad (3.4)$$

Hence, from (3.1), (3.2) and (3.4)

$$\begin{aligned} \nabla^2 &= \left\{\frac{1}{r^2}\frac{\partial}{\partial r}\left(r^2\frac{\partial}{\partial r}\right) + \frac{1}{r^2\sin^2\theta}\frac{\partial^2}{\partial\phi^2} + \frac{1}{r^2\sin\theta}\frac{\partial}{\partial\theta}\left(\sin\theta\frac{\partial}{\partial\theta}\right)\right\} \\ \Rightarrow \nabla^2\left[j_\ell(k_n r)Y_{\ell m}(\hat{\mathbf{r}})\right] &= \left(\frac{-\ell(\ell+1)}{r^2} + \frac{\ell(\ell+1)}{r^2} - k_n^2\right)Y_{\ell m}(\hat{\mathbf{r}})\, j_\ell(k_n r) \\ &= -k_n^2\left[j_\ell(k_n r)\, Y_{\ell m}(\hat{\mathbf{r}})\right]. \end{aligned}$$

Since the potential and density fields are related via Poisson's equation

$$\nabla^2\Phi(\mathbf{r}) = 4\pi G\rho_m\delta(\mathbf{r}), \qquad (3.5)$$

expressing the potential field in terms of the same Fourier-Bessel basis used for the reconstruction leads to

$$\begin{aligned}
\Phi(\mathbf{r}) &= \sum_{\ell mn} C_{\ell n}\, \Phi_{\ell mn}\, j_\ell(k_n r)\, Y_{\ell m}(\hat{\mathbf{r}}) \\
\Rightarrow \nabla^2\Phi &= \sum_{\ell mn} C_{\ell n}\, \Phi_{\ell mn}\, (-k_n^2)\, j_\ell(k_n r)\, Y_{\ell m}(\hat{\mathbf{r}}) = 4\pi G\rho_m \sum_{\ell mn} C_{\ell n}\, \delta_{\ell mn}\, j_\ell(k_n r)\, Y_{\ell m}(\hat{\mathbf{r}}) \\
\Rightarrow \Phi_{\ell mn} &= -\frac{3}{2}\frac{H_0^2\,\Omega_{m,0}}{k_n^2}\,\delta_{\ell mn}. \qquad (3.6)
\end{aligned}$$

Now, the ISW temperature fluctuations along a line of sight $\hat{\mathbf{n}}$ are described by equation (1.33) i.e. by an integral over the time derivative of the potential field. In linear theory, we can simply express this derivative in terms of the growth function defined in equation (1.24). Again from Poisson's equation,

$$\Phi_k = -\frac{3}{2}\frac{H_0^2\,\Omega_{m,0}}{k^2}\,\frac{g}{a}\,\delta_k(a=1) \qquad (3.7)$$

where all the time dependence of the density field is expressed in the factor g. This means that the time dependence of the potential field is given by g/a. The ISW temperature fluctuation along a line of sight is therefore

$$\frac{\Delta T^{\mathrm{ISW}}(\hat{\mathbf{r}})}{T_{\mathrm{CMB}}} = \frac{2}{c^2}\int \frac{d}{dt}\left[\frac{g}{a}\right]\Phi(\mathbf{r}, a=1)dt \qquad (3.8)$$

in the limit of linear perturbations.

The method described throughout this Section could be applied exactly as described to predict the local ISW effect if the reconstruction described in Chapter 2 produced a Fourier-Bessel expansion of the real space density field. Instead, we have the Fourier-Bessel coefficients of the photometric redshift derived density field, which is biased in the manner described in Section 2.5. This differs from the desired real space field in four key ways: it is biased; photometric redshift errors have caused radial smoothing; it is in redshift rather than real space and it is Wiener filtered. Tools are available to immediately solve two of these issues: we saw in Section 2.5 how to remove the photo-z bias from the density field, and it is possible to transform a redshift space reconstruction to real space by treating redshift space as a perturbation to real space and deducing a transformation matrix to move between the two. In fact, it will become clear that these measures are not justified, because the smoothing of the reconstructed density

field cannot easily be overcome; a different approach is therefore adopted to resolving these issues.

The ISW signal is computed by integrating the time derivative of the potential field along the line of sight. All the above differences between the real space density field and the reconstructed field recovered in Chapter 2 are independent of direction i.e. vary only in the radial coordinate. One would therefore expect the ISW signal calculated using the photometric redshift reconstruction to resemble the true ISW signal, but with an amplitude which may be affected by these differences. This is an important point, which will turn out to be true (see Section 3.2), and means that the photometric redshift reconstruction described in Chapter 2 can be used directly to draw useful conclusions about the local ISW effect.

3.2 Simulating the ISW Effect

Simulated density fields are used to demonstrate that the discrepancy between the true ISW signal and that calculated using a photometric redshift reconstruction is almost entirely in amplitude alone. Each simulation output can be used to construct a mock 2MASS catalogue of galaxies based on the simulated density field and the characteristics of the 2MASS survey e.g. its selection function and photometric error distribution. This mock catalogue is then treated in exactly the same way as the 2MASS data to create a reconstruction of the simulated density field and to compute the ISW signal from this. One can also go a step further and investigate the effect of the mask by creating all-sky galaxy catalogues for which no galactic plane mask is applied.

A set of five N-body simulations are used to investigate the ISW effect from a photometric redshift reconstruction. These simulations were performed in a box of side $1700\,h^{-1}$Mpc, large enough to contain the region which was reconstructed in Chapter 2 with $z_{\rm max} = 0.3$. These PM N-body simulations used over 17 million particles and a Fourier mesh of 256^3 cells, affording relatively low resolution. This is sufficient for our purposes as the radial resolution of the reconstruction is $\sim 30\,h^{-1}$Mpc, (around 5 times coarser than the cell size here) and the ISW effect is a large-scale phenomenon. The simulation data is then used in two ways: the ISW effect which would be observed at the centre of each simulation is computed and a mock 2MASS dataset corresponding to the simulation's final density field is constructed. This dataset is then passed through the reconstruction procedure described in Chapter 2 and the recovered

density field used to predict the ISW effect as described in Section 3.1. The measurement of the 'true' ISW signal for each simulation and the construction of the mock 2MASS dataset are described in more detail below.

3.2.1 True ISW Signal

The true ISW signal in each simulation box, as observed from the centre, is easily computed using Fourier methods. A fast Fourier transform algorithm (Press et al., 1992) was used to compute the potential field from the $z = 0.0$ simulation output and then linear theory was used in conjunction with this to evaluate the time derivative of the potential field and hence the ISW effect. From equation 1.33,

$$T(\hat{\mathbf{n}}) = \frac{\Delta T^{\mathrm{ISW}}}{T_{\mathrm{CMB}}}(\hat{\mathbf{n}}) = 2 \int \frac{\dot{\Phi}(\hat{\mathbf{n}}r, r)}{c^3}\, a(r)\, dr \tag{3.9}$$

Using a ray tracing technique similar to that described for the SZ effect in Section 4.1.1, the ISW signal is calculated by approximating the ISW integral as a sum of the form:

$$\frac{\Delta T^{\mathrm{ISW}}}{T_{\mathrm{CMB}}}(\hat{\mathbf{n}}) = 2 \int \frac{\dot{\Phi}(\hat{\mathbf{n}}r, r)}{c^3}\, a(r)\, dr \simeq 2 \sum_{i=1}^{N} \frac{\dot{\Phi}(\hat{\mathbf{n}}r(i\Delta z), r(i\Delta z))\, \Delta z}{c^2 H(i\Delta z)\ (1 + i\Delta z)} \tag{3.10}$$

where $N = z_{max}/\Delta z$.

Within linear theory, the growth function describes the evolution of the density field, see Section 1.2.3. As the density field is related to the potential field via the Poisson equation, it is also possible to describe the evolution of the potential field in terms of the growth function and in turn to express the time derivative of the potential field in these terms:

$$\begin{aligned} \Phi(r, z) &= \left[\frac{g(a)}{a}\right] \Phi(r, z = 0) \\ \Rightarrow \dot{\Phi}(r, z) &= \frac{d}{dt}\left[\frac{g(a)}{a}\right] \Phi(r, z = 0) \end{aligned} \tag{3.11}$$

using this method, the time derivative of the potential field at any redshift can be calculated from the potential field at redshift $z = 0.0$.

In a manner exactly analogous to the procedure applied to calculate the SZ effect and described in more detail in Section 4.1.1, HEALPix[1] (Górski et al., 2005) routines are used to

[1] http://healpix.jpl.nasa.gov

pixelise the sky and calculate the temperature fluctuations due to the ISW effect introduced in each pixel. The angular power spectrum of the ISW effect is also calculated using HEALPix software.

3.2.2 Construction of Mock 2MASS Data

To produce a mock sample of galaxies from each simulation density field with the same properties as 2MASS, it is necessary to reproduce the photometric redshift errors and selection function of this survey. The survey selection function arises because only the brightest galaxies at high redshift will have an apparent magnitude small enough to be observed by the 2MASS instruments. The survey selection function can be thought of as the spectroscopic selection function of 2MASS. This differs from the photometric selection function because although the same galaxies are used to deduce the two functions, photometric redshifts will introduce errors into the galaxy positions and hence alter the form of the selection function. To accurately reproduce the properties of 2MASS, a galaxy sample should be inferred from the simulation density field by Poisson sampling, and then the spectroscopic selection function applied, before finally the galaxy positions are altered for the effects of photometric redshifts.

The spectroscopic selection function for 2MASS can be estimated from the luminosity function of 6dFGS (Jones et al., 2005) since 6dFGS is a spectroscopic survey whose targets are selected from the 2MASS XSC. Given this luminosity function, the spectroscopic selection function is (Strauss and Willick, 1995)

$$\phi_{\rm spec}(r) = \frac{\int_{4\pi r^2 f_{\rm min}}^{\infty} \Phi(L)\, dL}{\int_{L_{\rm s}}^{\infty} \Phi(L)\, dL}$$

where $\Phi(L)$ is the number density of galaxies of luminosity L per unit luminosity, $f_{\rm min}$ is the minimum flux observed and $L_{\rm s} = 4\pi r_{\rm s}^2 f_{\rm min}$ for some small $r_{\rm s}$. In practice, the 6dFGS luminosity function (Jones et al., 2006) is given as a function of absolute magnitude rather than luminosity and therefore appropriate absolute magnitude limits need to be selected. K- and evolutionary corrections for the K-band luminosity function are taken from Poggianti (1997) and the absolute magnitude limits used to compute the spectroscopic selection function take these into account. In reality, precise knowledge of the spectroscopic selection function is unnecessary. We merely seek a sensible method of reducing the artificially large number of high redshift galaxies which could end up in the sample after being moved to lower redshifts

during photometric redshift smearing. After photometric redshift errors have been introduced for the remaining galaxies, the photometric redshift selection function is used to ensure that the galaxy distribution in the final sample closely mimics that of 2MASS.

3.2.3 Results from Simulated Density Fields

Having constructed these mock galaxy catalogues, the reconstruction algorithm of Chapter 2 is applied to each one, both with and without the mask described in Section 2.1.3, and the method outlined in Section 3.1 is used to compute the ISW effects. A comparison of the power spectra of the different simulated ISW signals is presented in figure 3.4. We can see that the true simulation power spectra agree very well with a ΛCDM prediction. The power spectra of the masked and unmasked reconstruction maps are fairly similar, but the masked reconstruction gives slightly less power on small angular scales. This is due to the algorithm used for filling in the density field within the galactic plane mask being less successful at recovering smaller scale features than large scale trends.

The ISW signals from the various simulated density fields are shown in figures 3.1, 3.2 and 3.3. We note that in general large scale hot and cold regions are faithfully recovered by both reconstructions except when such extrema lie completely within the mask as for example with the third simulation, see top panel of figure 3.2. However, even in this extreme case, the recovered ISW signal still bears a fair resemblance to the truth. The amplitudes of the ISW signals differ on small scales, but this is something that can be corrected easily given that the temperature extrema are well-reproduced by the reconstruction. We therefore expect the local ISW signal calculated from the reconstruction to be a reasonable estimation of the true signal.

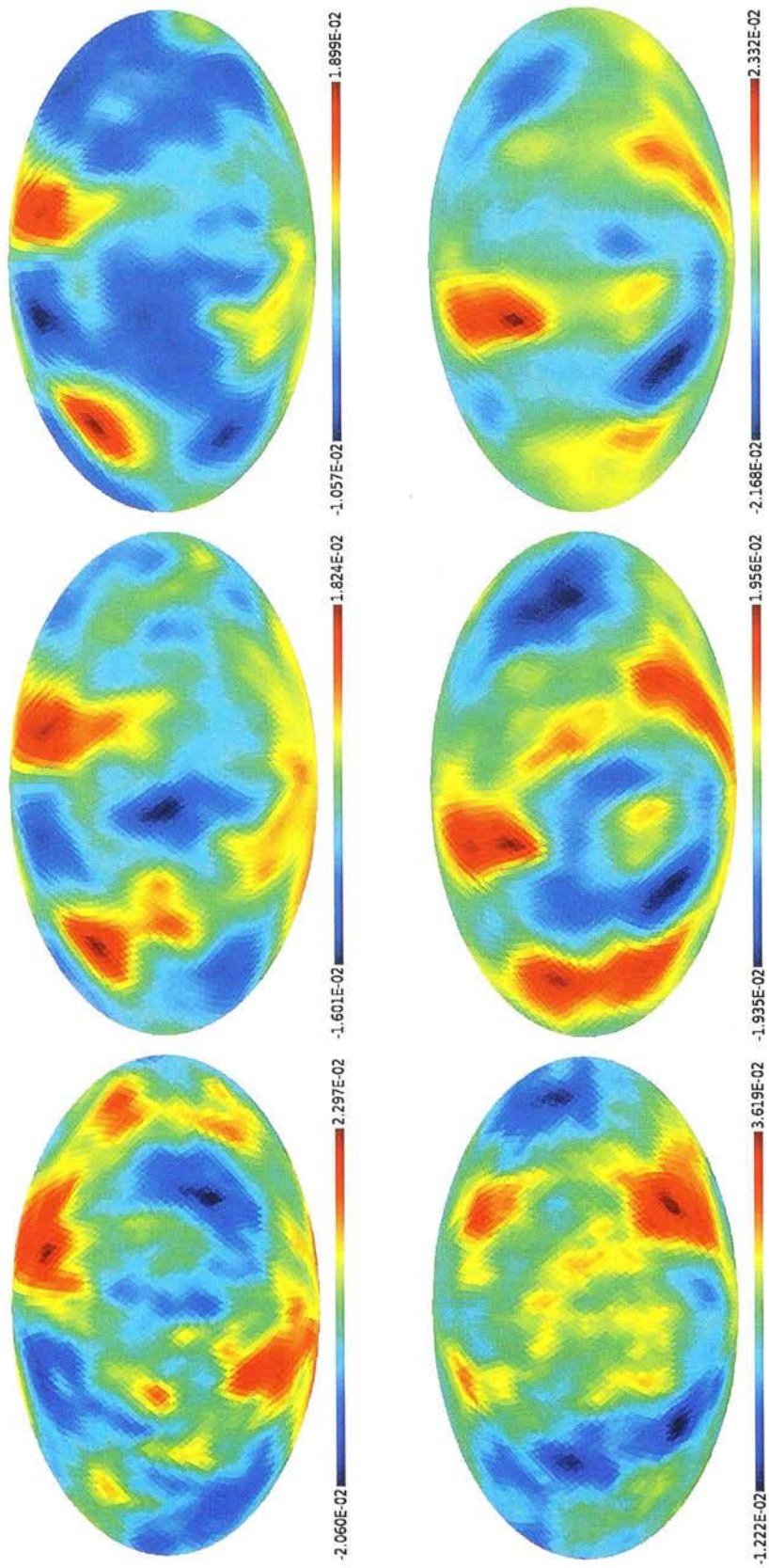

Figure 3.1: From *left* to *right*, the 'true' ISW effect, that computed from an unmasked reconstruction and that computed from a masked reconstruction for two distinct density fields (top and bottom). All in mK.

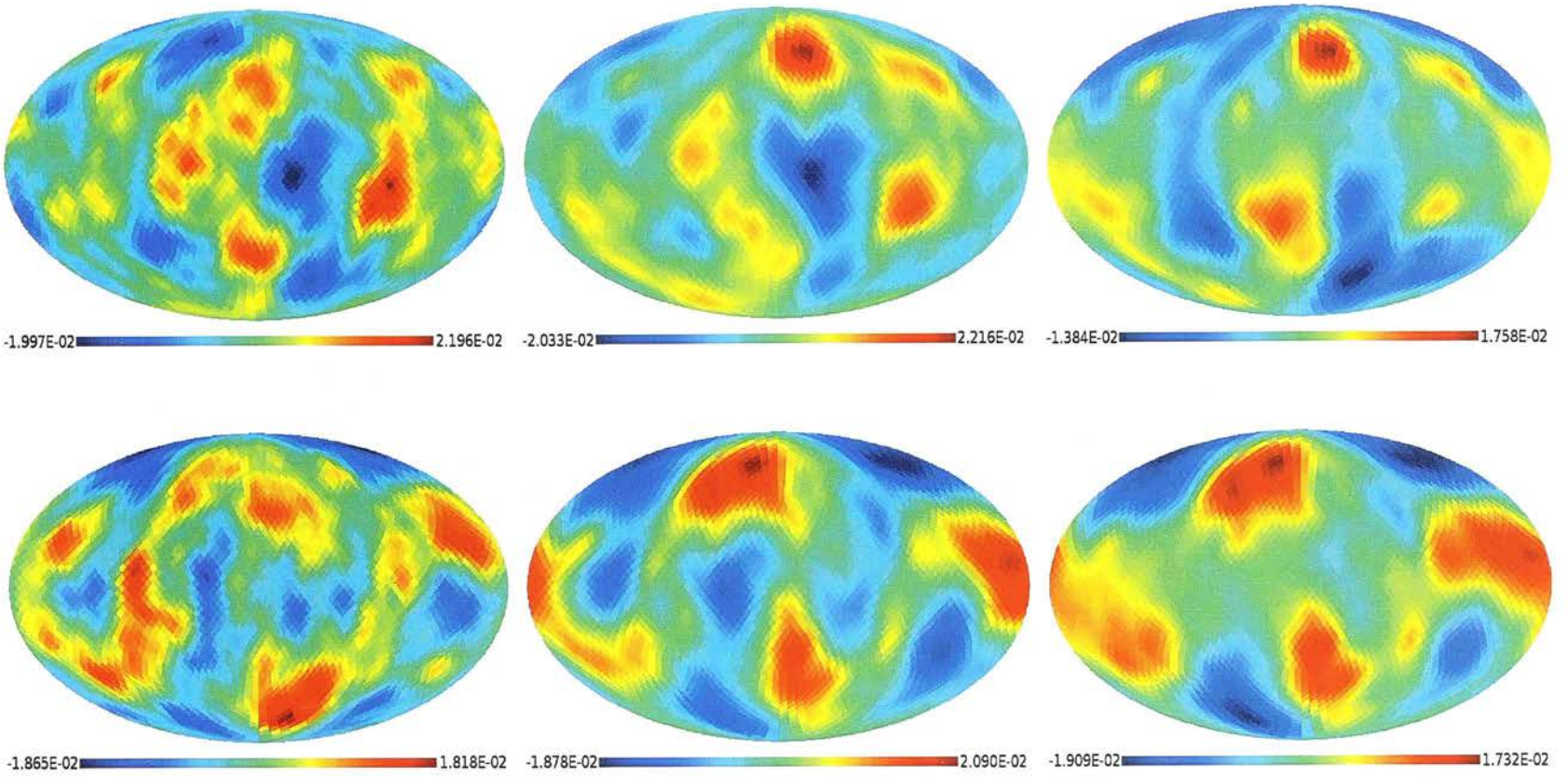

Figure 3.2: From *left* to *right*, the 'true' ISW effect, that computed from an unmasked reconstruction and that computed from a masked reconstruction for two distinct density fields (top and bottom). All in mK.

Figure 3.3: From *left* to *right*, the 'true' ISW effect, that computed from an unmasked reconstruction and that computed from a masked reconstruction. All in mK.

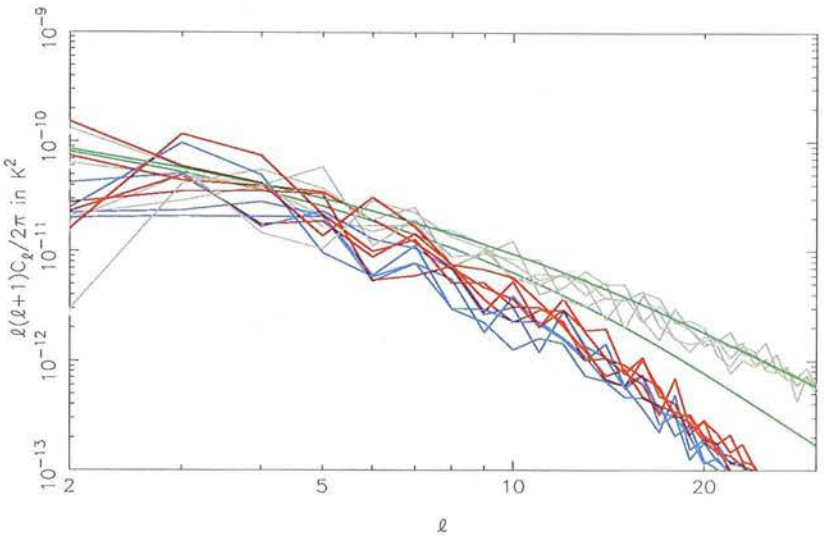

Figure 3.4: The 'true' ISW power spectra from 5 N-Body simulations (grey lines) and the signal computed from their unmasked (red) and masked (blue) reconstructions. The upper green line shows the true predicted ISW power and the lower green line the predicted ISW power spectrum using a photometric redshift density field with no additional smoothing. The discrepancy between the lower green line and the reconstruction ISW power spectra is therefore due to the Wiener filter and effects of the photo-z bias.

3.3 ISW Effect in the Local Universe

Figure 3.5 shows the ISW signal in the local Universe computed from the biased reconstruction for $z < 0.3$. We note that the most significant hotspot, above and to the right of centre corresponds to the location of the Shapley concentration and in general to a region which tends to be overdense for $z \leq 0.3$; the cold spot above and to the left of centre is in a region which tends to be underdense at these redshifts. There are two significant cold regions in the southern hemisphere, which lie close to the edge of the masked region (see also Section 3.4.2). These are investigated in detail in Section 6.3 and found to be robust. A discussion of these features is deferred until Chapter 6 and the predicted ISW map computed here is used throughout the remainder of this Chapter.

The power spectrum of this map is shown in figure 3.6 together with the predicted spectrum in a ΛCDM universe. We note the good agreement at low ℓ and an underestimation of power compared to the expected signal on smaller angular scales as expected given the simulation

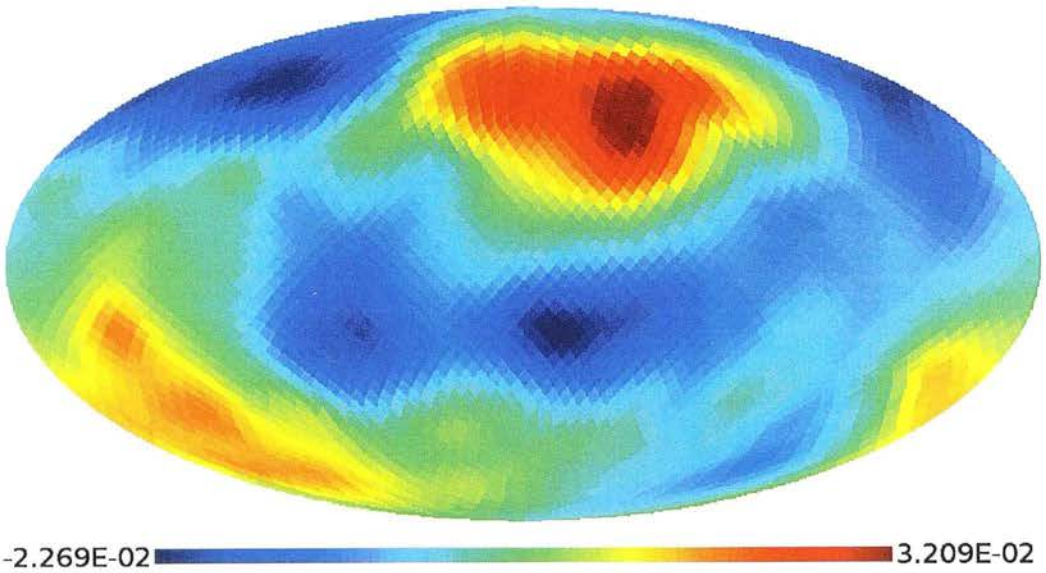

Figure 3.5: The $z \leq 0.3$ ISW signal in mK as computed from the 2MASS photo-z reconstruction of the density field. A hotspot in the vicinity of the Shapley concentration at ($l \simeq 300°, b \simeq 30°$) can be seen.

results. This underestimation arises from the use of photometric redshifts, the smoothing of the Wiener filter and any effects due to the bias in the photo-zs.

3.3.1 Cross-Correlation with the CMB

The cross-correlation between the CMB and the predicted ISW signal is interesting in the context of ISW detection. The late-time ISW signal is superimposed on the intrinsic CMB temperature fluctuations from the surface of last scattering and these signals are expected to be completely independent. When the predicted ISW signal is cross-correlated with the CMB, one would therefore expect to recover the power spectrum of the ISW effect. However, this is not the whole story, as the signal which is actually measured is

$$\left\langle a_{\ell m}^{\mathrm{ISW}} (a_{\ell' m'}^{*\mathrm{CMB}} + a_{\ell' m'}^{*\mathrm{ISW}}) \right\rangle = \left\langle a_{\ell m}^{\mathrm{ISW}} a_{\ell' m'}^{*\mathrm{CMB}} \right\rangle + \left\langle a_{\ell m}^{\mathrm{ISW}} a_{\ell' m'}^{*\mathrm{ISW}} \right\rangle . \tag{3.12}$$

where $a_{\ell m}^{\mathrm{CMB}}$ contains all contributions to the temperature fluctuations except the late ISW signal and noise on these scales is negligible.

However, although the expected value of the intrinsic CMB-ISW cross-correlation is zero, it will not vanish in every one of an ensemble of universes. We only have one universe to

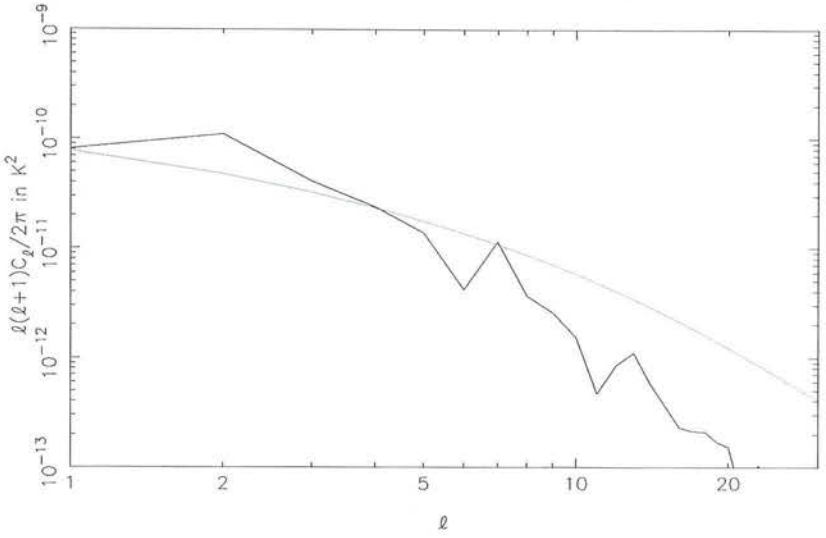

Figure 3.6: The power spectrum of the local ISW signal computed from the photometric redshift reconstruction (black line). The discrepancy from the predicted signal (blue line) is due to the effects of photo-z errors and bias and the Wiener filter smoothing.

observe, in which we do not know the value of this cross-correlation; the form of this term will have an impact on our ability to detect the ISW effect. As an extreme example, if the intrinsic CMB signal happened to be a perfect negative version of the ISW signal, the total CMB-ISW cross-correlation would vanish even though the ISW signal exists. Figure 3.7 shows the predicted local ISW signal and the year-3 WMAP ILC map with this signal removed, for $\ell \leq 30$. Ideally, the cross-correlation of these maps would give the intrinsic CMB-ISW cross-correlation that we are interested in; unfortunately, this is not the case. The predicted local ISW signal calculated from a photometric redshift reconstruction and the true local ISW signal differ slightly, as we have seen in Section 3.2, and therefore neither of these maps is precisely the one we would like.

Consider instead a full-sky CMB map and the predicted local ISW signal. The CMB map will contain the true local ISW signal which we expect to be correlated with the predicted ISW signal and an intrinsic CMB signal which we do not. Other contributions to the CMB on large scales such as noise and the thermal SZ effect are negligible. The first step in determining whether the intrinsic CMB and local ISW signal in the Universe have any interesting correlations is therefore to establish what this ISW-ISW cross-correlation should be.

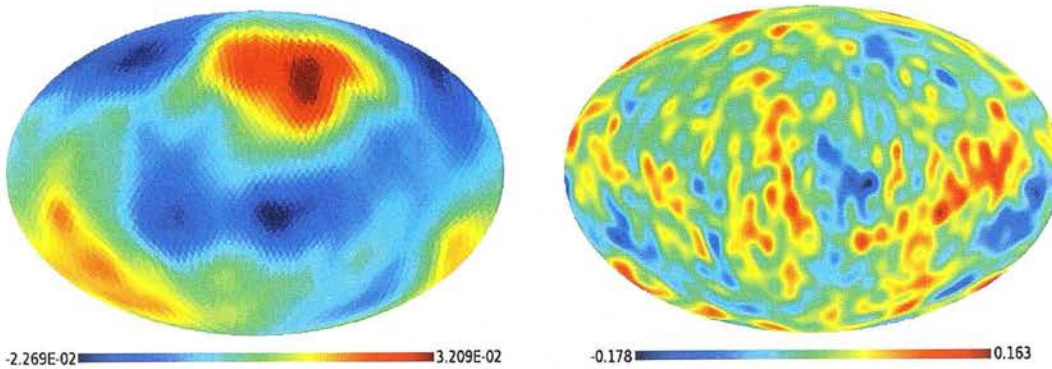

Figure 3.7: (*Left*) The predicted local ISW signal and (*right*) a full sky map of the CMB for multipoles $\ell \leq 30$ after removal of this effect, both in mK.

Figure 3.8 shows the mean, together with error bars, of the cross-correlation between the true ISW signal and the predicted ISW signal from a reconstruction, calculated for the simulations described in Section 3.2. Of course, 5 simulations is nowhere near enough to obtain meaningful statistics, so the error bars are intended as a rough guide only. However, we note that the ISW-ISW signal is reasonably well-determined and we therefore adopt this as the expected CMB-ISW cross-correlation. The measured CMB-ISW cross-correlation is also shown in this figure. In a ΛCDM universe, we expect this signal to be centred on the ISW-ISW cross-correlation and to show variations around this due to the intrinsic CMB-ISW cross-correlation term.

The spread in this cross-correlation is large and it is therefore difficult to comment with certainty on whether the intrinsic CMB has a form that helps, hinders or has no effect on ISW detection. Assuming a ΛCDM universe, we can attempt to answer the question of whether the measured cross-correlation prefers being centred on the expected ISW-ISW cross-correlation signal and therefore the intrinsic CMB is uncorrelated with the local ISW signal, or whether it is centred around zero, which in a ΛCDM universe would suggest that the intrinsic CMB is anti-correlated with the ISW signal. This latter case would also occur if there were no ISW effect present in the CMB. Using error bars computed from the binned cross-correlation of the predicted ISW signal with 10000 Gaussian CMB maps generated using the best-fitting WMAP power spectrum, a χ^2 analysis prefers the former situation where the intrinsic CMB and the ISW signal are uncorrelated and the ISW signal exists. The evidence is not particularly strong, with a likelihood ratio of $\sim 2:1$, nonetheless there is no evidence that the particular form of the intrinsic CMB will hinder ISW detection or that there is no ISW effect of the form

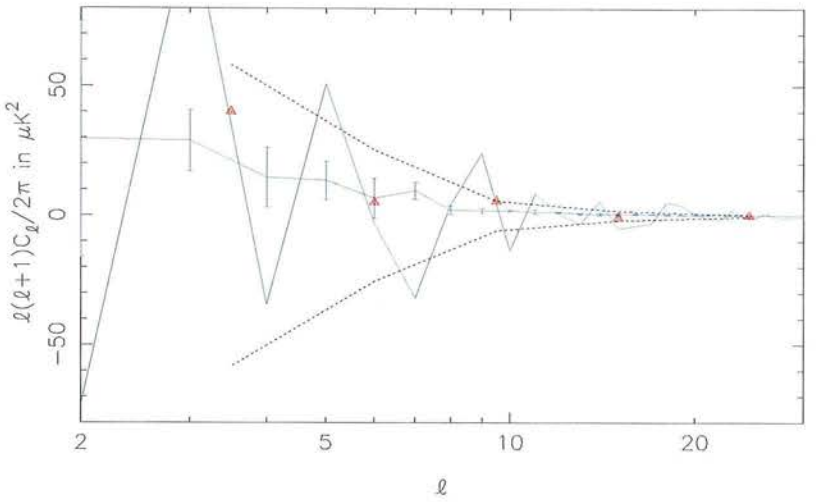

Figure 3.8: The mean cross-correlation between the true ISW signal and that predicted from a 3D reconstruction of the density field as calculated from 5 simulations (blue line) together with error bars for each multipole. The green line shows the measured cross-correlation between the predicted local ISW signal and the CMB. The red triangles show the ISW-CMB cross-correlation binned logarithmically by multipole and the black dashed lines show the standard deviation in these bins of the cross-correlation of 10000 Gaussian CMB skies with the predicted local ISW signal.

expected in a ΛCDM universe.

Before considering the influence of the predicted local ISW signal on the CMB anomalies, the local ISW effect is estimated using an independent technique based on reconstructing the 2D density field in redshift slices. Having two estimates of the local ISW signal improves the robustness of any results when considering its influence on CMB anomalies. A good correspondence between the signals calculated using different methods will increase the confidence which one can have in the determination of the local ISW signal, although since the same data are used in each case, this is only a test of the methods used. Section 3.4 describes the new prediction of the ISW effect and finally in Section 3.5 the influence of the ISW effect on the CMB anomalies is investigated.

3.4 The Local ISW Signal from a 2D Reconstruction

In Chapter 5 the final 2MASS dataset is used to attempt to detect the local ISW signal using an analysis in thick redshift slices ($\Delta z = 0.1$). Here, we borrow some of the results from that Chapter to perform a 2D Wiener reconstruction of the density field in redshift slices and to predict the local ISW effect from the results. The method used to estimate the local ISW signal from this 2D analysis is very different to the 3D approach employed above and can therefore serve as a somewhat independent test of the results bearing in mind that the same galaxy data is used in each case. A slightly different cosmological model is used in Chapter 5 ($\Omega_m = 0.3, \Omega_v = 0.7, \Omega_b = 0.05, h = 0.7, \sigma_8 = 0.75$) and some of the results from that Chapter are used here for the 2D reconstruction, hence the same cosmological model is used to estimate the ISW signal in this case. This should be borne in mind when comparing the results.

In Section 3.4.1 the 2D reconstruction method is described and applied to the 2MASS galaxy data. In Section 3.4.2, Poisson's equation is used to deduce the local ISW signal from the 2D reconstruction and a comparison of the results with respect to those of the full 3D ISW prediction is made.

3.4.1 2D Density Field Reconstruction

The projected galaxy density field is known outside the masked region in each of the three redshift slices we are interested in: $0.0 < z < 0.1$, $0.1 < z < 0.2$ and $0.2 < z < 0.3$. A Wiener filter can be applied to these datasets to determine the optimal galaxy density field in the least squares sense and to recover lost information from the masked region using the technique developed in Section 2.3.4. A discussion of the use of the Wiener filter with 2D density fields is given in Zaroubi et al. (1995).

The masked region in each of the density slices is initially filled with a random Poisson sampling of galaxies according to the number density observed outside the plane. The Wiener filter appropriate for each slice is

$$\Phi_{\rm WF}(\ell) = \frac{C_{\rm gg}(\ell)}{C_{\rm gg}(\ell) + C_{\rm noise}(\ell)} \tag{3.13}$$

where $C_{\rm gg}$ is the galaxy angular power spectrum which is calculated as described in Section 5.1.2 and $C_{\rm noise}(\ell)$ is the shot noise power spectrum given by

$$C_{\rm noise}(\ell) = \frac{4\pi}{N_{\rm gals}} \tag{3.14}$$

where $N_{\rm gals}$ is the number of galaxies in the entire slice.

Using a process analogous to that described in Section 2.3.4, initially the Wiener filter is applied to the spherical harmonic coefficients describing the density field in each slice with the plane randomly filled with galaxies. The resultant density field is then re-sampled for galaxies within the plane and a new set of spherical harmonic coefficients calculated for the density field resulting from this new sampling and the original 2MASS galaxies outside the plane. The Wiener filter is then applied to this field to give the reconstructed density field in each of the three redshift slices, see figure 3.9.

3.4.2 2D ISW Estimation

Given a projected galaxy density field in a thick redshift slice, the ISW temperature fluctuations which would be observed due to this density field can be calculated via Poisson's equation

$$\begin{aligned}
\frac{\Delta T_{\ell m}}{T} &= 2\int \frac{d}{dt}\left[\frac{g(a)}{a}\right]\frac{a^2\Phi_{\ell m}(a)}{g(a)}\,\frac{dr}{c^3} \\
&\simeq \frac{2}{c^3}H(\bar{a})\left(\frac{dg}{da}(\bar{a}) - \frac{g(\bar{a})}{\bar{a}}\right)\frac{\bar{a}^2}{g(\bar{a})}\int \Phi_{\ell m}\,dr \\
&\simeq \frac{3H_0^2\Omega_m}{\ell(\ell+1)c^3}\left(1 - \bar{a}\frac{g'(\bar{a})}{g(\bar{a})}\right) r^2(\bar{a})\,H(\bar{a})\,\Delta r\,\frac{\delta_{\ell m}}{b},
\end{aligned} \tag{3.15}$$

where δ is the projected galaxy density field in the redshift slice under consideration and $\bar{a} = (1+\bar{z})^{-1}$ and $\bar{z}$ is the redshift at the midpoint of the slice. Figure 3.9 shows the ISW signal in each of the redshift slices considered here and figure 3.10 shows the total predicted ISW effect for $z < 0.3$ from this technique. Comparison with the ISW signal estimated from the full 3D reconstruction (see figure 3.5) reveals a very similar temperature distribution although the amplitude of the ISW signal estimated from the 2D reconstruction is slightly larger. Looking at the highest redshift slice $0.2 < z < 0.3$, we note again an underdense/cold feature near the centre of the maps at $l \simeq 330°$ close to the lower edge of the region which is masked during the reconstruction, another such feature is seen at $l \simeq 60°$ in the $0.0 < z < 0.1$ ISW map, although this is not so clear in the density field (see also Section 3.3). The fact that these features occur near to the edge of the mask and are a significant contribution to the total ISW signal means

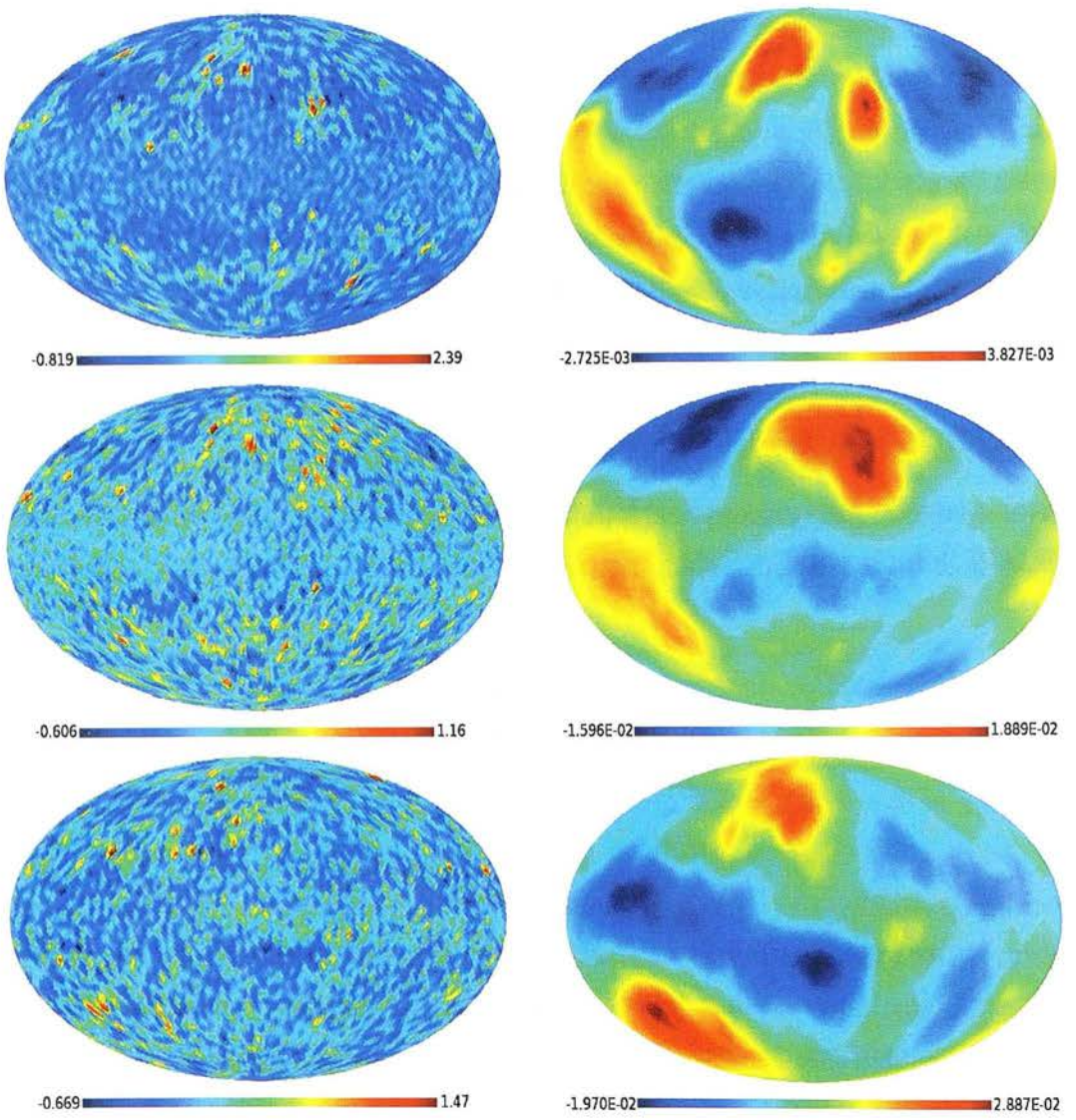

Figure 3.9: (*Left*) The 2D reconstruction of the local density field described in Section 3.4.1 in three photometric redshift slices: $0.0 < z < 0.1$ (*Top*), $0.1 < z < 0.2$ (*Centre*) and $0.2 < z < 0.3$ (*Bottom*). (*Right*) The corresponding ISW signal in mK computed from the reconstructed density field using equation (3.15).

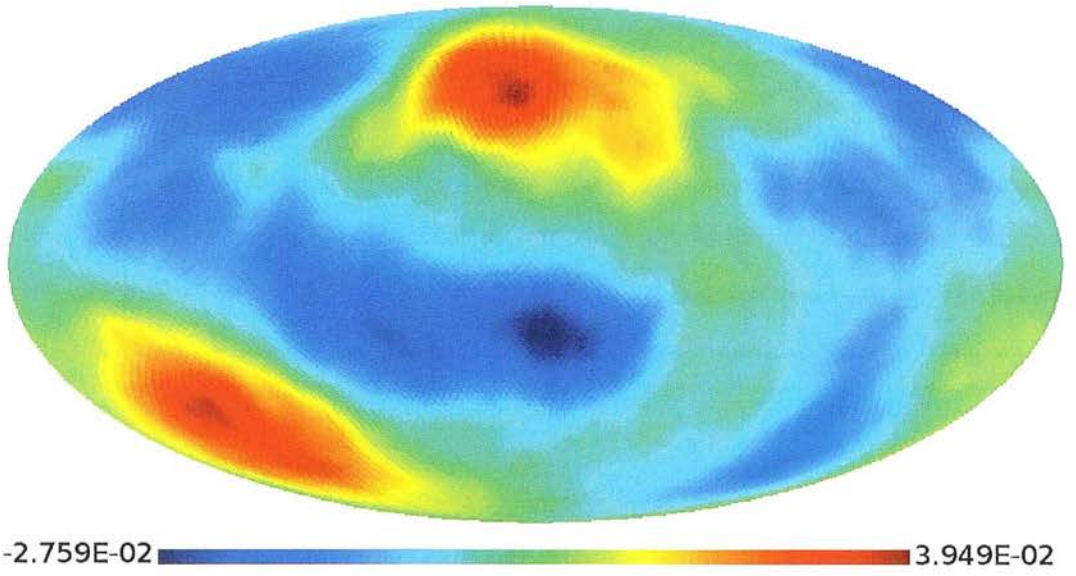

Figure 3.10: The total local Universe ISW signal in mK for $z < 0.3$ predicted from a 2D reconstruction of the density field. Comparison with figure 3.5 reveals a very similar large scale temperature distribution although the amplitude for the ISW signal predicted from the 2D reconstruction is larger by a factor $\lesssim 1.5$. Some of this discrepancy will be due to the different cosmological models used to predict the ISW signal.

that they merit further investigation to ensure that they are not merely artefacts of the data. We note however that the 3D reconstruction maps (see Section 2.5) show no particularly unusual underdensities corresponding to this location, yet the cold region is also present in the predicted ISW signal from the 3D reconstruction. Throughout the rest of this Chapter, we use the 2D and 3D predicted ISW maps complete with these features. A detailed analysis of the robustness of this cold region is then presented in Section 6.3.

Figure 3.11 shows the angular power spectrum of the ISW signal in each of the redshift slices and for the total ISW signal at $z < 0.3$. We note that the total ISW signal has greater power than would be expected for multipoles $\ell \lesssim 5$, which comes from the two highest redshift slices. This excess of power at low multipoles is not easily explained, although it is interesting that both this prediction of the ISW effect and the full 3D reconstruction ISW prediction show an excess of power on these scales (see figure 3.6). Here, a bias $b = 1.2$ is used due to the lower value of σ_8 employed in this 2D analysis. This ensures that the value of $b\sigma_8$, and therefore the normalisation of the power spectrum, is the same for both the 3D and the 2D analysis.

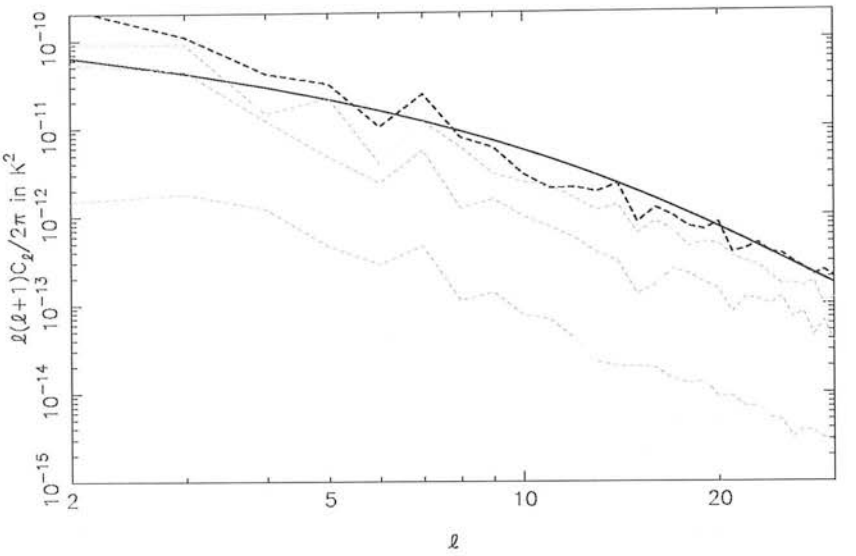

Figure 3.11: The power spectrum of the ISW signal calculated in each of the three redshift slices (grey dashed lines): $0.0 < z < 0.1$ (bottom), $0.1 < z < 0.2$ (middle) and $0.2 < z < 0.3$ (top). The black solid line shows the predicted signal for the total ISW signal out to $z = 0.3$ calculated using the photometric redshift space power spectrum with bias $b = 1.2$. The black dashed line shows the power spectrum measured for the $z < 0.3$ ISW signal.

3.5 Implications for the CMB Anomalies

As mentioned briefly in Section 1.3, there are various large-scale features in the CMB which can be considered to be anomalous. Taken individually, these features are not unexpected given our preferred cosmological model. However, the presence of multiple features of this type purely by chance is claimed by some to be extremely unlikely e.g. Huterer (2006), at the level of a 1-in-1000 probability (de Oliveira-Costa and Tegmark, 2006) and therefore indicative of incompleteness within our cosmological model. Others note that many of these anomalous features are seriously affected by uncertainties in galactic foreground removal (Spergel et al., 2006). We should also allow for the fact that we are 'looking for trouble' with regard to the CMB anomalies. There are many other features which could have been investigated for anomalous behaviour, and therefore whilst the *a priori* probability of the anomalies which have been found all occurring is extremely low, the *a posteriori* probability is higher (de Oliveira-Costa et al., 2004).

Secondary anisotropies such as the ISW and thermal SZ effects contribute to the CMB

temperature distribution on large angular scales and thereby provide another possible source for these large scale anomalies; the ISW effect is the larger of these two signals. It is therefore interesting to investigate the effect on the anomalies of removing this signal from the CMB. In Section 3.5.1, the all-sky CMB maps used here are described and in Section 3.5.2 the estimation of the kinetic Doppler Quadrupole contribution is addressed. In Section 3.5.3 a review of some of the anomalous features is presented before the effect of ISW removal is assessed in Section 3.5.4.

3.5.1 All-sky CMB Maps

WMAP ILC Maps

The Internal Linear Combination (ILC) map constructed by the WMAP team is a full sky map composed as a weighted sum of observed CMB maps at different frequencies (Bennett et al., 2003a). The weights are chosen to minimise the variance of the ILC map assuming that the CMB signal and residuals (noise and foregrounds) are uncorrelated. Minimising the variance of the linear combination map is therefore equivalent to minimising the variance of the residuals. There are ILC maps available for both the year-1 and year-3 WMAP data releases (hereafter ILC1, ILC3 respectively).

TOH Maps

The year-1 and year-3 CMB maps of Tegmark et al. (2003, hereafter TOH1) and de Oliveira-Costa and Tegmark (2006, hereafter TOH3) are constructed using a slightly different technique to the ILC approach. For these maps, no assumptions are made about the CMB power spectrum, foregrounds, detector noise or external templates; it is only assumed that the CMB has a black-body spectrum. The weights which are used here to minimise the foreground contribution are a function of ℓ and the minimization is carried out in harmonic space rather than real space as for the ILC map.

Despite the different methods used to construct these maps, there is very little difference between the final results. The anomalies which have been noticed in the CMB data are present in all the maps, although the significance varies.

3.5.2 Kinetic Doppler Quadrupole

Finally, before the CMB maps can be studied for anomalies the contribution of the kinetic Doppler Quadrupole (DQ) should be removed. This quadrupolar signal arises due to the motion of the Sun with respect to the CMB frame (Kamionkowski and Knox, 2003). The Doppler Quadrupole is a small contribution to the cosmological quadrupole, with a quadrupole power of $\sim 4\mu\mathrm{K}^2$ (Tegmark et al., 2003). The Doppler Quadrupole is actually frequency dependent and therefore its contribution to the all-sky CMB maps described above is approximated by

$$\left(\frac{v}{c}\right)^2 \bar{T}\left(\cos^2\theta - 1/3\right) \tag{3.16}$$

where v is the velocity of the solar system with respect to the CMB ($\sim 370\mathrm{kms}^{-1}$) and θ is the angle between the direction of this motion ($l = 264°, b = 48°$) and the direction in which the Doppler Quadrupole is required. Whilst this is a very small adjustment to the power at low multipoles, it can be significant when alignments are investigated and should be accounted for in such analyses.

3.5.3 Introduction to CMB Anomalies

Low Quadrupole Power / Lack of Power on Large Scales

WMAP has a measurement error of the order of $7\mu\mathrm{K}^2$ on large scales and a measured quadrupole power $C_2 = 236\mu\mathrm{K}^2$, therefore the quadrupole is certainly non-zero; however its power is low within the concordance cosmology. First noted in the COBE data (Gould, 1993; Hinshaw et al., 1996), the low quadrupole power was confirmed by WMAP in both the first and third year data (Spergel et al., 2003; Hinshaw et al., 2006). This anomaly can be thought of as being 'statistically isotropic', it is not a directional anomaly such as the alignments or particular features discussed below. Figure 3.12 shows the CMB quadrupole and figure 3.13 shows the CMB two point angular correlation function together with the best-fitting cosmological model prediction and 1σ error bars. The removal of the Doppler Quadrupole has a negligible effect on these functions. The low value of the quadrupole power is symptomatic of a lack of power on all scales larger than $\theta \sim 60°$. Whilst the quadrupole is only moderately low, moving to real space and considering the angular correlation function reveals a surprising lack of power on *all* large scales (Spergel et al., 2003).

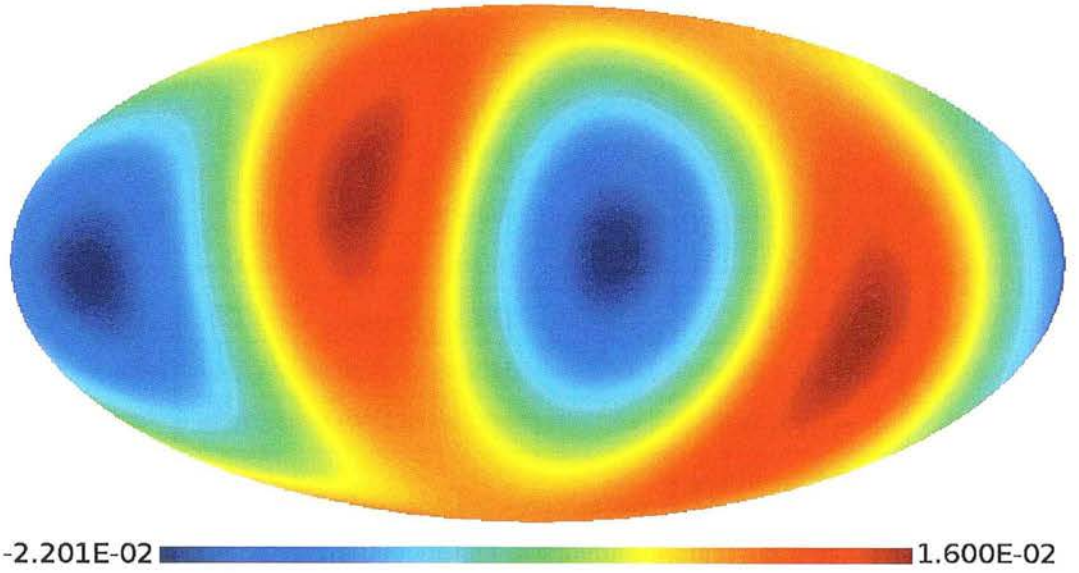

Figure 3.12: The CMB quadrupole from the year-3 WMAP ILC map in mK. The power is lower than expected in a ΛCDM universe for this multipole.

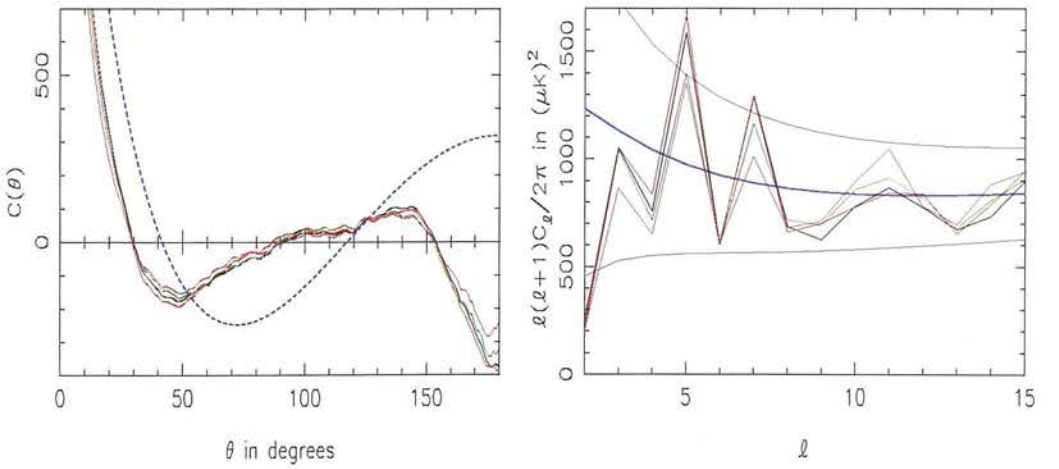

Figure 3.13: (*Left*) The CMB angular correlation function $C(\theta) = (4\pi)^{-1} \sum_\ell (2\ell + 1)\, P_\ell(\cos\theta)\, C_\ell$ for the WMAP1 ILC map (red) the WMAP3 ILC map (black), the TOH1 map (purple) and the TOH3 map (green) together with the predicted signal (blue) for the best-fitting cosmological model. (*Right*) the angular power spectrum for the same maps, together with the best fitting prediction and the 1σ error bars (blue). Note the underestimation of the signal on large angular scales.

Map	Quadrupole Power, C_2 in μK^2	p-value
ILC1	204.4	2.2%
TOH1	211.1	2.4%
ILC1 - DQ	195.9	2.0%
TOH1 - DQ	203.3	2.2%
ILC3	260.3	3.8%
TOH3	219.5	2.7%
ILC3 - DQ	250.6	3.5%
TOH3 - DQ	214.3	2.4%
Model prediction	1291.4	

Table 3.1: The quadrupole power and its significance for various CMB maps. Note that the Doppler Quadrupole has very little effect on the power and that the year-3 data give rise to a slightly larger quadrupole.

Table 3.1 shows the values of the quadrupole measured from the all-sky CMB maps before and after correction for the Doppler Quadrupole together with the significance of these results. The quadrupole power has a chi-square distribution with 5 degrees of freedom and hence the probability of a given power is

$$P(C_2^{\rm model} \leq C_2^{\rm obs}) = \frac{\gamma(5/2\,,\, 5/2\, C_2^{\rm obs}/C_2^{\rm model})}{\Gamma(5/2)}, \tag{3.17}$$

where γ and Γ are the incomplete and complete Gamma functions respectively. We note that the quadrupole power is still low in the year-3 data but slightly larger than the year-1 estimate.

The low quadrupole power has been the focus of much recent speculation and has encouraged a series of new cosmological models which can explain this low value e.g. Luminet et al. (2003); Sawicki and Carroll (2005). However, it has been found that the ILC map has a tendancy to give rise to a low quadrupole value by virtue of the method used to remove foregrounds (Chiang et al., 2007), and Magueijo and Sorkin (2007) find that this anomaly is insignificant when Occam's razor techniques are applied to the CMB data.

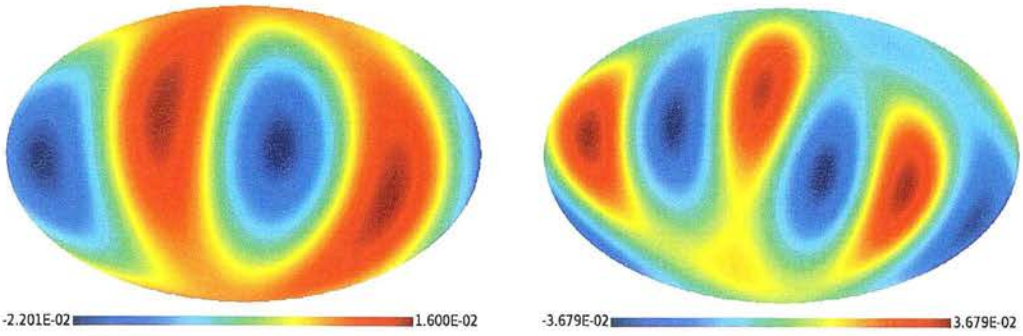

Figure 3.14: (*Left*) The CMB quadrupole and (*right*) octopole in mK from the WMAP3 ILC map. The alignment of the temperature extrema for these multipoles has lead to the definition of an 'Axis of Evil' whose existence is unlikely according to our current cosmological model.

Planarity of the Octopole and Alignment with the Quadrupole

Figure 3.14 shows the ILC quadrupole and octopole. It is immediately obvious that the temperature extrema for the octopole are aligned in a plane and that the quadrupole shares this alignment (Tegmark et al., 2003). The probability of this occurring by chance lies at the 1 in 60 level (de Oliveira-Costa et al., 2004). This alignment and its extension to higher multipoles defines a preferred axis termed the 'Axis of Evil' (Land and Magueijo, 2005) which points in the approximate direction ($l = 250°, b = 60°$) towards Virgo. Given that this plane appears to approximately coincide with the galactic plane where contamination from foregrounds is most severe, it was thought that this feature was likely to disappear from the third year WMAP data where foreground contamination is reduced. In fact, the feature persists (Land and Magueijo, 2007). This anomaly is found to remain significant after Occam's razor techniques are applied to the CMB data (Magueijo and Sorkin, 2007).

To be more quantitative about the alignment between the octopole and quadrupole and the planarity of the octopole, it is necessary to find a statistic which describes the degree of alignment. Preferred axes for the quadrupole and octopole need to be identified in an unambiguous manner and the degree of planarity of the octopole must be assessed. We choose to define preferred axes by maximising the angular momentum dispersion as suggested by de Oliveira-Costa et al. (2004). In this formalism, the temperature fluctuation map is regarded as a wave function, ψ, and the axis $\hat{\mathbf{n}}$ about which the angular momentum dispersion,

$$\langle \psi \,|\, (\hat{\mathbf{n}} \cdot \mathbf{L})^2 \,|\, \psi \rangle = \sum_m m^2 |\, a_{\ell m}(\hat{\mathbf{n}}) \,|^2, \tag{3.18}$$

Map	$\hat{\mathbf{n}}_2 \cdot \hat{\mathbf{n}}_3$	Separation angle	Probability
ILC1	0.9567	16.9°	4.3%
TOH1	0.9832	10.5°	1.7%
ILC1 - DQ	0.9669	14.8°	3.3%
TOH1 - DQ	0.9843	10.2°	1.6%
ILC3	0.9944	6.0°	0.56%
TOH3	0.9711	13.8°	2.3%
ILC3 - DQ	0.9991	2.4°	0.09%
TOH3 - DQ	0.9881	8.9°	1.2%

Table 3.2: The separation angles between the preferred axes of the quadrupole and octopole for various CMB maps and the probability of such an alignment occurring by chance. The Doppler Quadrupole is seen to have some influence on these results, making the alignments closer.

is maximised is adopted as the 'preferred axis' for that multipole. Table 3.2 shows the value of $\hat{\mathbf{n}}_2 \cdot \hat{\mathbf{n}}_3$ for various all-sky CMB maps where $\hat{\mathbf{n}}_2$, $\hat{\mathbf{n}}_3$ are the preferred axes for the quadrupole and octopole respectively. The probability of such an alignment occurring by chance is also given, where this is defined as the probability that a random axis falls within a circle whose radius is determined by the separation between the preferred quadrupole and octopole axes.

The octopole planarity is quantified using the 't' statistic of de Oliveira-Costa et al. (2004). This defines the maximum percentage of octopole power that can be attributed to $|m| = 3$

$$t = \max_{\hat{\mathbf{n}}} \frac{|\, a_{3\,-3}(\hat{\mathbf{n}})\,|^2 + |\, a_{3\,3}(\hat{\mathbf{n}})\,|^2}{\sum_m |\, a_{3m}(\hat{\mathbf{n}})\,|^2}. \tag{3.19}$$

The significance of the 't' values which are found can be assessed by considering a large number of Gaussian random realisations of the $a_{\ell m}$ and computing the probability of obtaining a value of t at least as large as that found from the data. Table 3.3 shows the values of the 't' statistic for the various maps and gives an indication of the significance of each value computed from 10000 Monte-Carlo simulations of a_{3m}s. Relatively large 't' values are not unexpected for the quadrupole and octopole because a random, statistically isotropic multipole will always have a frame in which most of the power is concentrated in a single m multipole (Magueijo and Sorkin, 2007). For small ℓ, it is not unlikely that $|m| = \ell$.

Map	t value	Probability
ILC1	0.9345	$\sim 13\%$
TOH1	0.9457	$\sim 10\%$
ILC3	0.9213	$\sim 17\%$
TOH3	0.9269	$\sim 15\%$

Table 3.3: The value of the 't' statistic for various CMB maps and the probability of this degree of planarity in the octopole occurring by chance. The significance of this anomaly is slightly reduced in the year-3 data.

North-South Power asymmetry

Looking at the sum of the CMB quadrupole and octopole reveals a divide between the largest temperature extrema and the smallest (see figure 3.15), or equivalently a mis-match in power between the hemispheres on either side of the ecliptic plane (Eriksen et al., 2004; Wandelt et al., 2004). This divide is coincident with the ecliptic plane across approximately a third of the sky (Copi et al., 2006) which is unusual at the 95% confidence level (Schwarz et al., 2004). There has been no plausible explanation as to why the ecliptic plane – usually associated with the solar system – should have an effect on the CMB. Investigation of possible foreground contamination or details of the scanning strategy which could give rise to such an association have failed to provide an explanation. Galactic foregrounds are seen to cause galactic alignments (Huterer, 2006) and therefore using full sky CMB maps to determine preferred axes (necessary for robust results) which may contain some residual galactic foreground signal, would not be expected to cause alignment with the ecliptic.

The Cold Spot

The 'cold spot' is an individual feature in the CMB which has a temperature significantly lower than expected (Vielva et al., 2004). Many inflationary models predict a Gaussian intrinsic CMB, where spherical harmonic coefficients describing the field for a given multipole are drawn from a Gaussian distribution with zero mean and variance equal to the power spectrum for that multipole. The cold spot is a non-Gaussian feature with scale $1^\circ - 10^\circ$, located at $(l = 207.8, b = -56.3)$. NVSS observations have revealed that the density of radio sources as projected on the sky is also anomalously low in this direction (Rudnick et al., 2007). The

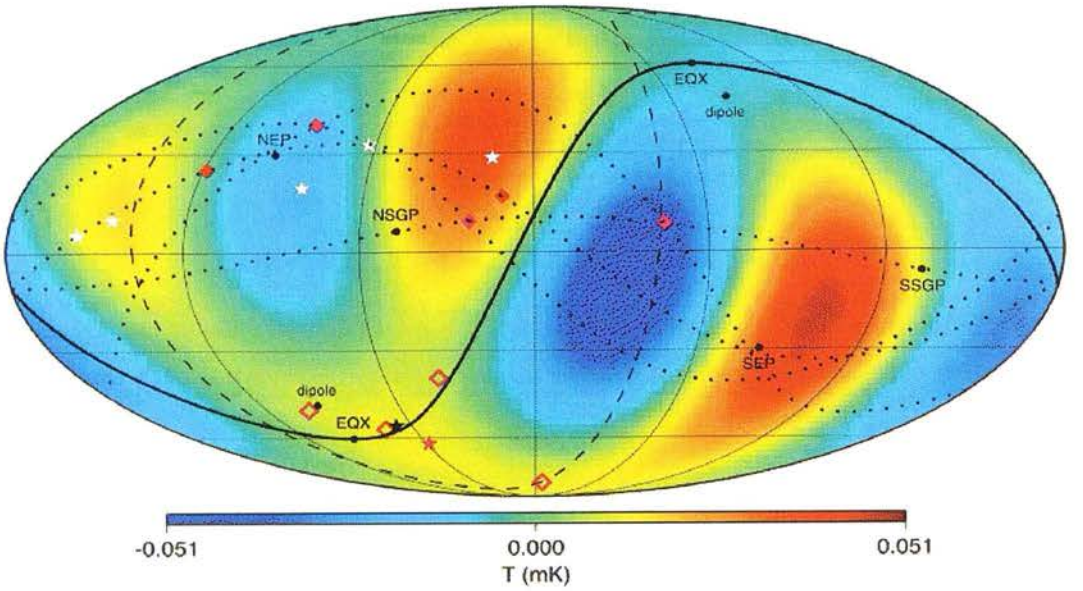

Figure 3.15: *From Copi et al. (2006)*: The sum of the CMB quadrupole and octopole as measured by WMAP together with the ecliptic plane. Note the North-South asymmetry in the temperature extrema on either side of the ecliptic and the coincidental position of a large segment of the ecliptic plane with a null portion of the temperature map between one of the largest and one of the smallest temperature extrema.

interpretation is therefore that there is a large void along this line of sight which gives rise to the cold spot via the ISW or Rees-Sciama effects. To give rise to this temperature fluctuation a completely empty void of radius ~ 140Mpc and redshift $z \lesssim 1.0$ is needed. This is an unlikely large scale structure and hence the anomaly is not completely removed by this interpretation; the unusual behaviour is merely shifted to another aspect of cosmology.

3.5.4 Effect of the Local ISW Signal on CMB Anomalies

Having made predictions of the ISW signal from the local density field in Sections 3.3 and 3.4, these can be subtracted from the observed CMB to recover a signal which is closer to the primary anisotropy signal on large scales. It is then possible to see what effect the removal of some part of the secondary anisotropy signal has on the CMB anomalies described above.

From the point of view of investigating the low ℓ CMB anomalies, it is perhaps slightly disturbing that the power of the predicted local ISW signals on such scales is slightly stronger than we would expect, see figures 3.6 and 3.11. Although some fluctuation about the ΛCDM

values is expected, the quadrupole power which is recovered for the local ISW signal is outside the 1σ cosmic variance errors for both maps. To ensure that the conclusions which are drawn about CMB anomalies are not reliant on this excessive power, which we could certainly imagine having an influential effect on the low value of the quadrupole, a 'rescaled' version of the predicted ISW signal is also considered for each map. The rescaled signals have the same ISW temperature pattern as the local Universe predictions, but the amplitudes of the spherical harmonic coefficients are adjusted so that the power spectrum of the map is equal to the expected power. The re-scaling therefore proceeds via

$$a_{\ell m} \rightarrow \sqrt{\frac{C_\ell^{\Lambda\mathrm{CDM}}}{C_\ell^{\mathrm{obs}}}}\, a_{\ell m} \tag{3.20}$$

where C_ℓ^{obs} is the ISW power spectrum for the local Universe prediction and $C_\ell^{\Lambda\mathrm{CDM}}$ is the expected ΛCDM power. This rescaling is applied for $\ell \leq 30$ and therefore also has the effect of raising the power on small scales for the 3D prediction. We have seen in Section 3.3 that a suppression in power is expected on such scales due to the smoothing used in the reconstruction, the rescaling here therefore raises the power to the level which we would expect on such scales and gives a good representation of the true local ISW signal assuming that the effect of using a photometric redshift reconstruction is almost entirely in the amplitude rather than the phases of the ISW signal. Figures 3.1, 3.2 and 3.3 show this to be the case. In practice, for CMB anomalies, this small scale renormalization will only affect the investigation of the cold spot.

Having computed the rescaled ISW maps, which are shown in figure 3.16, we now consider subtracting these and the raw local Universe ISW predictions from the Doppler Quadrupole corrected CMB maps.

Low Power on Large Scales

The quadrupole of the ILC3 map before and after the subtraction of the predicted local ISW signal from the 3D reconstruction is shown in figure 3.17. The positions of the temperature extrema are shifted slightly and in the new map these extrema have larger values indicating that the quadrupole power may be increased somewhat. Studying the angular power spectra and correlation functions in figure 3.18 reveals this to be the case and shows that the subtraction of the local ISW signal alleviates the anomalously low power on large scales. Even if the

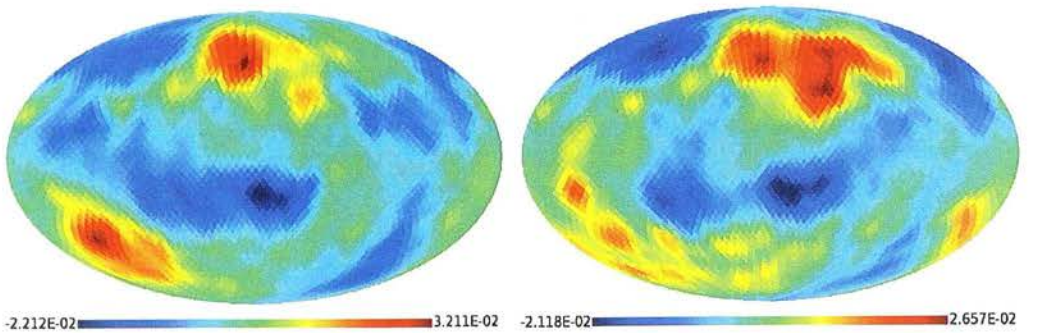

Figure 3.16: (*Left*) The predicted local ISW signal in mK from the 2D reconstruction and (*Right*) the 3D reconstruction after rescaling of the amplitudes as described in equation (3.20).

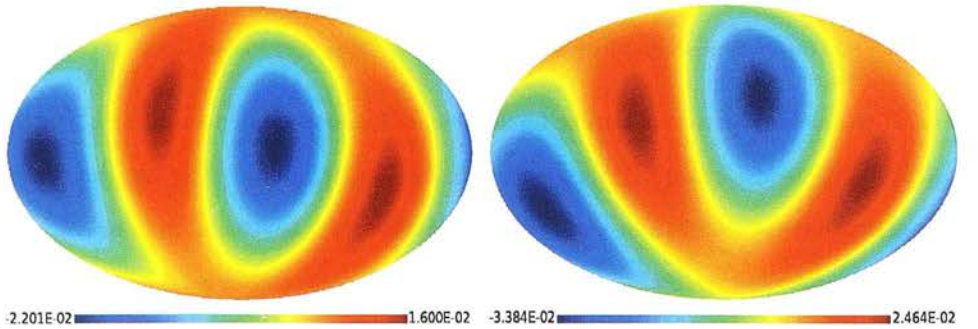

Figure 3.17: (*Left*) The ILC quadrupole in mK before and (*right*) after subtraction of the predicted local ISW signal from the 3D reconstruction. Note that the locations of the temperature extrema – particularly the minima – alter to define a plane with a different orientation.

rescaled ISW signal is subtracted, the quadrupole power is still increased. Table 3.4 shows the significance of the new quadrupole values for all the maps considered and reveals that in all cases the quadrupole power is no longer unusual at even the 1-in-20 level. For most of the ISW subtracted maps, the power is no longer outside the 1σ cosmic variance error bars about the best-fitting cosmological model. The quadrupole which results from removal of the full 2D ISW signal is similar in amplitude to the corresponding 3D ISW subtracted values. This is unsurprising as the ISW quadrupoles from the two different methods are very similar, see figure 3.19.

Quadrupole/Octopole alignment

In figure 3.20 the ILC3 quadrupole and octopole are shown before and after ISW subtraction. The shift in the positions of the quadrupolar temperature extrema define a new preferred axis for this multipole whilst the octopole remains largely unchanged. It appears therefore that

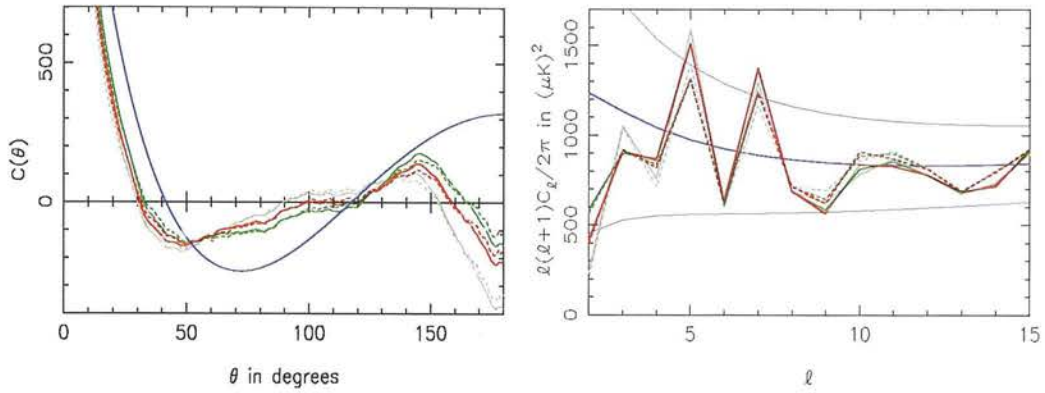

Figure 3.18: (*Left*) The Angular correlation function of the CMB before subtraction of any ISW signal (grey), after subtraction of the predicted local ISW signal from the 3D reconstruction (green) and after subtraction of the rescaled ISW signal (red). The dashed lines are for the TOH3 map and the solid lines for the ILC3 map. The blue line shows the expected signal in a ΛCDM universe. Note that the ISW subtracted signal is stronger on the largest scales than the ILC signal. (*Right*) The angular power spectrum at low ℓ, together with the expected signal (blue) and 1σ error bars.

Map	Quadrupole Power, C_2	p-value
ILC3 - DQ	250.6	3.5%
TOH3 - DQ	214.3	2.4%
ILC3 - DQ - 3D ISW	615.6	20.6%
TOH3 - DQ - 3D ISW	593.2	19.3%
ILC3 - DQ - 3D ISW (rescaled)	436.8	11.0%
TOH3 - DQ - 3D ISW (rescaled)	418.7	10.1%
ILC3 - DQ - 2D ISW	600.7	19.8%
TOH3 - DQ - 2D ISW	608.2	20.1%
ILC3 - DQ - 2D ISW (rescaled)	372.7	8.0%
TOH3 - DQ - 2D ISW (rescaled)	359.3	7.5%
Model prediction	1291.4	

Table 3.4: The quadrupole power and its significance for various CMB maps before and after ISW subtraction. Note that the subtraction of the rescaled ISW effect does not raise the quadrupole power as much as the full ISW removal, but that the resultant power is still not unusual.

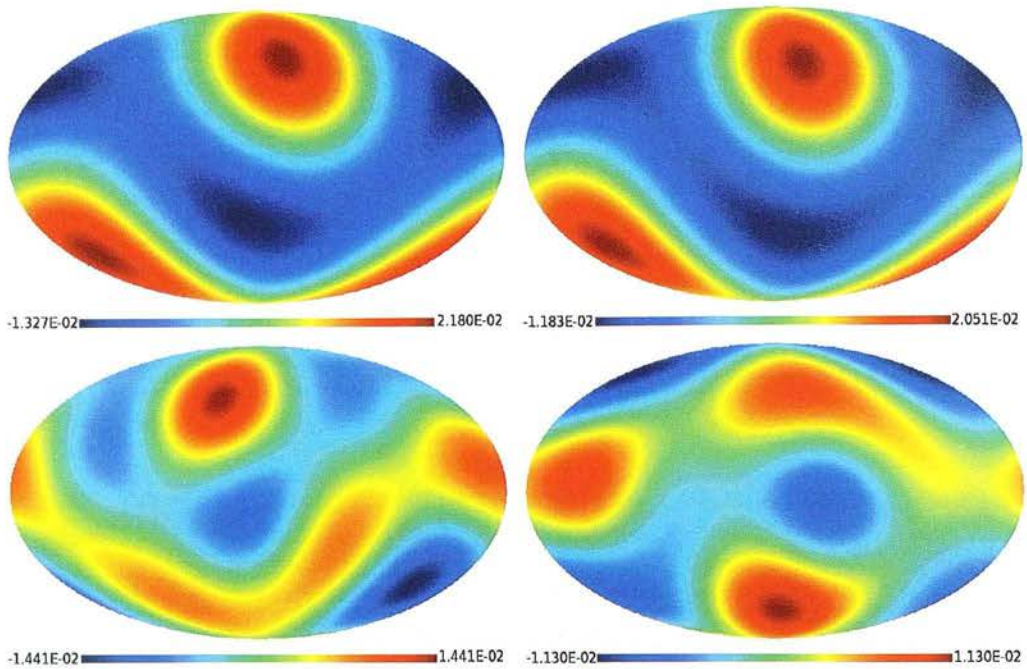

Figure 3.19: (*Top left*) The ISW quadrupole calculated from the 2D density reconstruction and (*Top right*) for the 3D density reconstruction and (*bottom*) the octopoles for the same ISW signals, all in mK. There is very little difference between the quadrupoles although the octopoles show some variation.

the alignment between the preferred axis of these multipoles may be broken. Table 3.5 gives the new separation angle between the preferred axes for each of the maps considered and the probability of this occurring by chance. Figure 3.19 shows the ISW quadrupoles and octopoles as calculated using both 2D and 3D reconstructions of the density field. The octopoles differ slightly between ISW calculations and we may therefore expect differences in the planarity of the CMB octopole and the quadrupole/octopole alignment from the two ISW predictions. In all cases, we find that subtraction of the ISW signal from the CMB map reduces the alignment, which is no longer unusual at the 1-in-20 level.

Octopole Planarity

Figure 3.20 shows that the alignment of the octopole is not significantly changed by the removal of the predicted ISW signal. It is therefore little surprise to learn that the octopole remains planar; table 3.6 shows the new values of the 't' statistic. We note that in fact the octopole becomes slightly more planar after subtraction of the ISW signal, with the probability of such planarity occurring by chance varying between $\sim 1.6\%$ and $\sim 12\%$ for the various

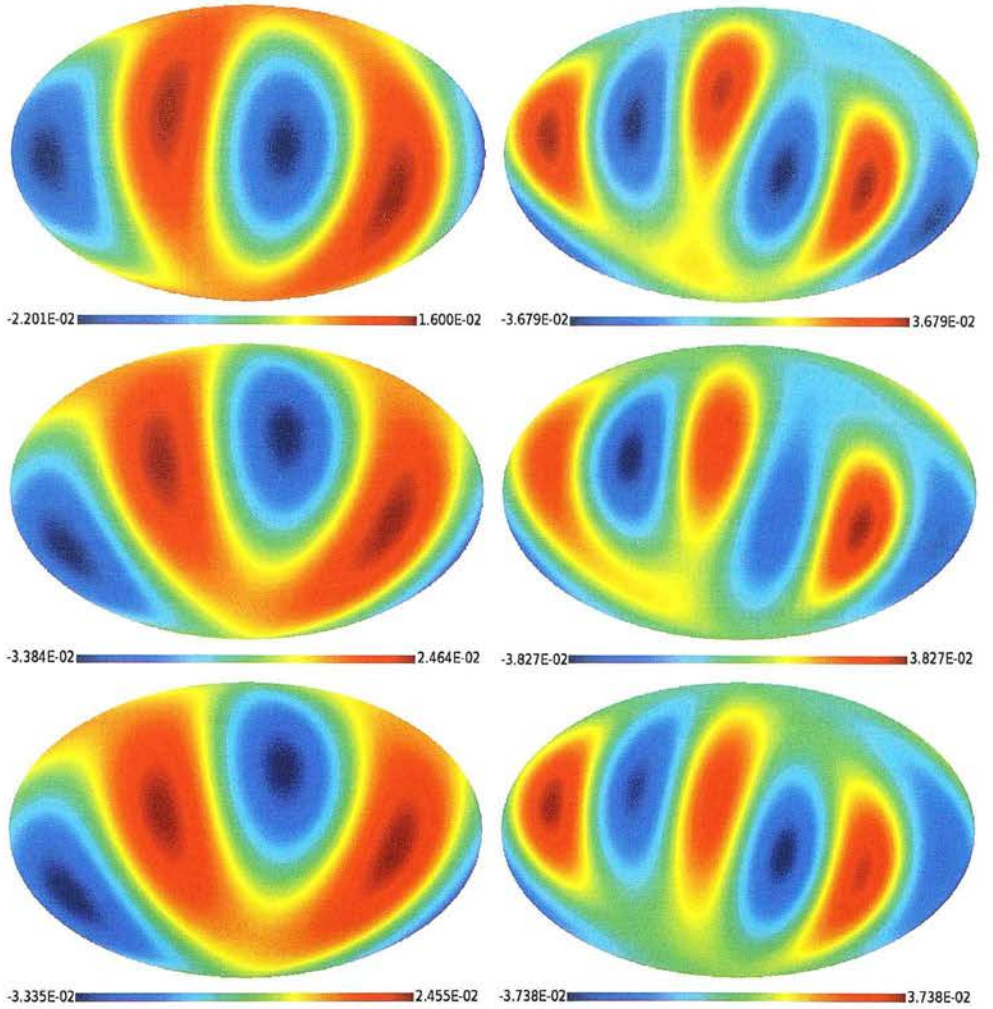

Figure 3.20: (*Top left*) The ILC3 quadrupole and (*Top right*) octopole; (*Centre left*) the ILC3 quadrupole and (*Centre right*) octopole after subtraction of the local ISW signal as predicted from the 3D reconstruction; (*Bottom left*) the ILC3 quadrupole and (*Bottom right*) octopole after subtraction of the local ISW signal as predicted from the 2D reconstruction, all in mK. We note that whilst the quadrupole alignment is changed by the subtraction, the octopole is not and therefore the alignment between these multipoles is broken. The octopole retains its planar structure.

Map	$\hat{\hat{\mathbf{n}}}_2 \cdot \hat{\hat{\mathbf{n}}}_3$	Separation angle	Probability
ILC3 - DQ	0.9991	2.4°	0.09%
TOH3 - DQ	0.9881	8.9°	1.2%
ILC3 - DQ - 3D ISW	0.9116	24.3°	8.8%
TOH3 - DQ - 3D ISW	0.8886	27.3°	11%
ILC3 - DQ - 3D ISW (rescaled)	0.9467	18.8°	5.3%
TOH3 - DQ - 3D ISW (rescaled)	0.9268	22.1°	7.3%
ILC3 - DQ - 2D ISW	0.7548	41.0°	24.5%
TOH3 - DQ - 2D ISW	0.6712	47.8°	32.9%
ILC3 - DQ - 2D ISW (rescaled)	0.8873	27.5°	11.3%
TOH3 - DQ - 2D ISW (rescaled)	0.8158	35.3°	19.4%

Table 3.5: The separation angles between the preferred axes of the quadrupole and octopole for various CMB maps before and after ISW subtraction and the probability of such an alignment occurring by chance. We note that even with the subtraction of the rescaled ISW effects, the alignment between the axes is no longer particularly unusual, at worst occurring at the 1-in-20 level.

ISW subtracted maps. The ILC3 map has a more planar octopole than the TOH3 map after ISW subtraction.

North-South Asymmetry

Figure 3.21 shows the sum of the quadrupole and octopole after subtraction of the predicted ISW signals together with the ecliptic plane. The ecliptic no longer lies along a null portion of the map after the ISW signal has been removed although the largest temperature extrema are still located in the southern hemisphere. This is true for all the ISW maps considered here. Before ISW subtraction, Schwarz et al. (2004) found the power asymmetry together with the coincidence of the ecliptic with a node line of the temperature distribution across 1/3 of the sky to be unusual at the 95% level. We therefore expect that the breaking of the coincidence of the ecliptic and a temperature node, which occurs after ISW removal, would reduce the significance of this anomaly further. Given that there are only six temperature extrema to consider in the $\ell = 2+3$ map, it is not particularly surprising that the three largest should be grouped together.

Map	t value	Probability
ILC3	0.9213	$\sim 17\%$
TOH3	0.9269	$\sim 15\%$
ILC3 - 3D ISW	0.9783	$\sim 2.4\%$
TOH3 - 3D ISW	0.9389	$\sim 12\%$
ILC3 - 3D ISW (rescaled)	0.9820	$\sim 1.9\%$
TOH3 - 3D ISW (rescaled)	0.9510	$\sim 9.0\%$
ILC3 - 2D ISW	0.9841	$\sim 1.6\%$
TOH3 - 2D ISW	0.9653	$\sim 5.0\%$
ILC3 - 2D ISW (rescaled)	0.9675	$\sim 4.9\%$
TOH3 - 2D ISW (rescaled)	0.9530	$\sim 8.0\%$

Table 3.6: The value of the 't' statistic for various CMB maps before and after ISW subtraction, and the probability of this degree of planarity in the octopole occurring by chance. The significance of this anomaly is slightly increased after subtraction of the ISW signal and the planarity is more unusual for the ILC3 map.

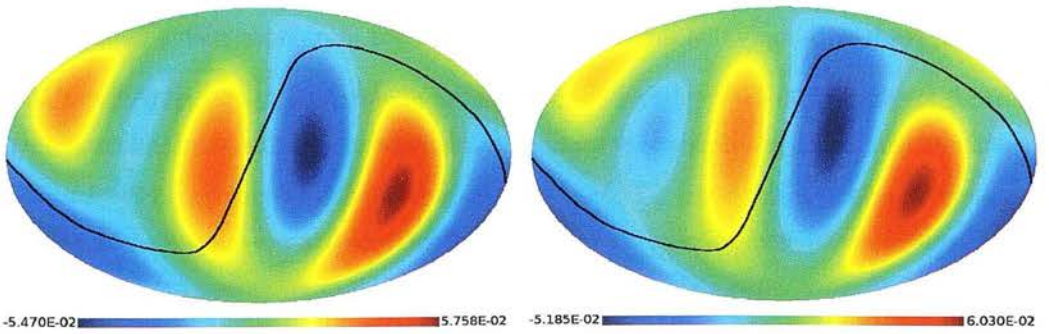

Figure 3.21: (*Left*) The sum of the ILC3 quadrupole and octopole after subtraction of the local ISW signal computed from the 2D reconstruction and (*right*) the 3D reconstruction, both in mK. The ecliptic plane no longer lies along a null portion of the temperature distribution after the subtraction although the power asymmetry remains.

The Cold Spot

Figure 3.22 shows the change in pixel temperature around the cold spot after ISW subtraction. The removal of either of the predicted ISW signals suggests that this region becomes warmer. The amplitude of the temperature increase is larger for the ISW map computed from the 2D reconstruction by a factor ~ 2. The difference between the temperature shift due to subtraction of the full ISW prediction and the rescaled version of this map is less pronounced in this case because the 2D ISW signal does not show a suppression of small scale ISW power in the same way as the 3D ISW signal. For the 3D ISW signal, the temperature in the vicinity of the cold spot is raised by $\sim 3\mu$K whereas for the 2D ISW signal it is raised by $\sim 7\mu$K. Some of this discrepancy can be attributed to the use of different cosmological models in predicting the ISW signals. The results of Cruz et al. (2005) show that the cold spot has a temperature of -73μK when smoothed on a 4° scale. The Spherical Mexican Hat Wavelet (SMHW) analysis which they perform on the data to quantify the significance of the cold spot is applied for both the year-1 (Cruz et al., 2005) and year-3 WMAP data (Cruz et al., 2007). They find varying significances, which depend on the precise statistics used to quantify the spot, but determine that their most robust figure is a p-value of 1.85% from the year-3 data. Without repeating in detail their analysis, it is difficult to quantify the effect on this significance of removing the local ISW signal from the CMB map, but a temperature increase of any form will certainly increase the p-value and therefore reduce the significance of this feature.

The elevation in the temperature in this region is certainly insufficient to completely explain the cold spot, but it will imply that the size of the void needed to produce such a temperature decrement is reduced to $\sim 95\%$ of the current estimate, $r \simeq 140$Mpc, (Rudnick et al., 2007). This smaller void is slightly more likely to occur, but it should be noted that such a void remains an extremely unusual feature.

3.6 Discussion

Having predicted the local ISW signal for $z < 0.3$ using both a 2D and 3D reconstruction of the local density field, we have seen good agreement between the results. Both ISW predictions predict hot and cold spots in the same regions and both suggest a larger power than would be expected in the ISW signal on the very largest scales. Considering the influence on the CMB anomalies of the removal of these predicted ISW signals, we find in general consistent results

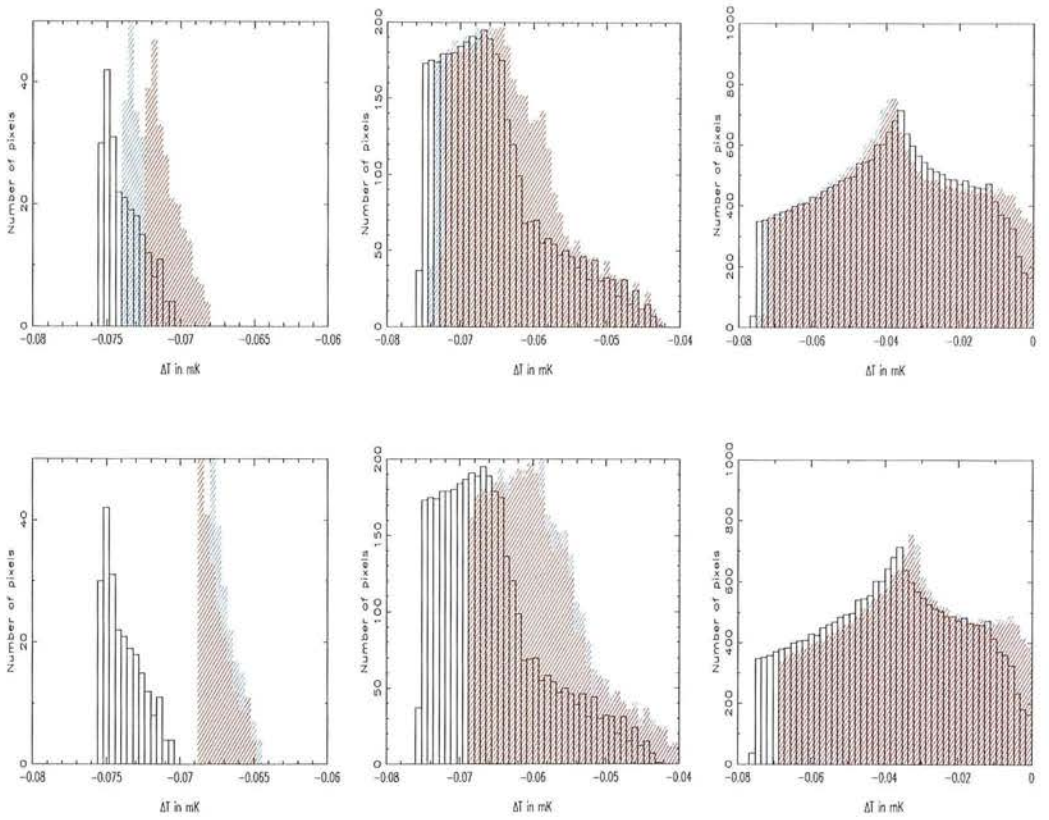

Figure 3.22: (*Left*) The temperature in pixels within 1°, (*centre*) 4° and (*right*) 10° of the centre of the cold spot before ISW removal (black outline histogram), after removal of the predicted ISW signal (blue hatched histogram) and after removal of the rescaled ISW signal (red histogram) after smoothing on a 10° scale. The top row of plots is for the ISW signal computed from the 3D reconstruction and the bottom row that computed from the 2D reconstruction. Subtraction of the corrected local ISW signal raises the temperature of the whole region by $3 - 7\mu$K.

for both maps and rescaled versions of these which are chosen to have the expected ΛCDM ISW power spectrum. In all cases, the removal of the ISW signal suggests that the quadrupole power is no longer unusually low, the quadrupole and octopole preferred axes are no longer aligned and the ecliptic plane no longer lies along a node line of the temperature distribution. The planarity of the octopole persists and in fact becomes a little more planar after subtraction of the ISW effect; depending on the ISW map used, the probability of such planarity occurring by chance is between 1.6% and 12%. The temperature of pixels surrounding the cold spot is increased by the removal of the local ISW signal implying that a slightly smaller high redshift void than previously believed could give rise to this feature via the ISW or Rees-Sciama effects.

The results in this Chapter demonstrate that the local ISW signal can be used to mitigate 'anomalous' signals in the CMB effectively. It should be borne in mind that only the ISW signal from $z < 0.3$ has been considered here and therefore there is further scope for influence on the observed CMB from the ISW effect at $0.3 < z \lesssim 1$. In combination with better estimation of foreground contamination in the CMB maps, it is clearly necessary to attempt to estimate the contribution of secondary anisotropies to the temperature fluctuations before concluding that the large scale intrinsic CMB is anomalous or otherwise. However, since the ISW signal should itself be close to Gaussian, the existence of significant anomalies in the CMB which were removed after subtraction of the local ISW signal would in turn raise questions about the anomalous nature of the ISW effect. It is therefore reassuring that none of the original CMB anomalies are individually particularly significant and that the ISW removal, whilst alleviating many of them, does not do so in a manner which inspires us to seriously question the nature of the ISW signal.

Whilst these results are promising, it must be acknowledged that a thorough investigation of the effects of differing amounts of calibrating spectroscopy across the sky should be undertaken before the local ISW effect is claimed as the cause of CMB anomalies. Such non-uniformities in the data could give rise to spurious signals in the low multipoles of the density field and hence to a misleading ISW signal. As mentioned in Chapter 2, these effects could be investigated using simulations or by excluding a portion of the calibrating data to force uniformity.

CHAPTER 4

Sunyaev Zel'dovich Effect in the Local Universe

The Sunyaev-Zel'dovich (SZ) effect has two forms: the thermal SZ effect and the kinetic SZ effect. Both describe temperature fluctuations which are introduced into the CMB by the interaction of CMB photons with hot gas. The SZ effect is usually studied on small scales where it is due to the gas in individual clusters; its contribution to the CMB angular power spectrum is largest at such multipoles. Whilst the signal is much weaker, the large-scale SZ effect is interesting in terms of diffuse gas in the local Universe. Although the bulk of the thermal SZ (tSZ) signal is generated in collapsed structures, $\sim 15\%$ of the total large-scale signal comes from the Warm-Hot Intergalactic Medium (WHIM) in filaments and superclusters (Hernández-Monteagudo et al., 2006), making the tSZ signal an important probe of the poorly understood baryon distribution in the local Universe. It is also important to consider all large-scale foregrounds when analysing the reported anomalies in the CMB data. We have seen in Chapter 3 that the local ISW signal can have a significant effect on the CMB on such scales and that its removal can alleviate many of the reported anomalies in the observed CMB. Since the SZ effect is the only other secondary anisotropy which is non-negligible on such scales, we would like to investigate its influence as well. It has also been suggested that the SZ signal could contaminate estimates of cosmological parameters from the CMB data (Myers et al., 2004).

This Chapter addresses the calculation of the large scale SZ effect in the local Universe. Section 4.1 describes the development of a method to compute the large-scale thermal and kinetic SZ effects given only a matter density field and Section 4.2 describes the application of this method to compute the thermal SZ effect in the local Universe. Using this estimate, in Section 4.3 a comparison is made between these results and those of other groups and in Section 4.4 the impact of the local tSZ effect on WMAP CMB data is addressed.

4.1 Scaling Relations for the Large Scale SZ Effects

As CMB photons travel through the Universe towards us from the surface of last scattering, they interact with the matter distribution. This interaction can be purely gravitational, as in the case of the ISW effect (see Chapters 3 and 5), or the photons can interact with the hot baryonic gas that is present. The Sunyaev-Zel'dovich effect, as outlined in Section 1.3.4, is the result of an interaction between the CMB photons and hot gas.

The aim of this Chapter is to estimate the local large scale SZ effect. The reconstruction described in Chapter 2 can be used to deduce the dark matter density field in the local Universe. The temperature fluctuations due to the local SZ effect cannot be calculated directly from this alone since information about the state of the baryons is needed. Therefore, to estimate the thermal SZ signal, it is necessary to deduce values for gas properties relevant to this effect, such as the electron number density and gas temperature, from the underlying dark matter density field. If one wishes to estimate the kinetic SZ effect then the baryon velocity also needs to be related to the dark matter velocity field.

Here, two high resolution hydrodynamic simulations are used to develop a method for assigning gas properties to a general dark matter distribution. In Section 4.1.1, the construction of SZ temperature maps from such a simulation is described and the form in which the dark matter distribution will be used is discussed. In Section 4.1.2, the process of using outputs of these hydrodynamic simulations to construct a robust method of deducing the gas properties which would be expected to correspond to a given dark matter density and velocity is presented in detail. Finally, in Section 4.1.3 an analysis of the method is performed and its accuracy is tested.

4.1.1 Method: Ray Tracing

To make a map of the SZ temperature fluctuations across the sky and to calculate the angular power spectra of the effects, HEALPix[1] (Górski et al., 2005) software is used. The sky is pixelised and the SZ temperature fluctuation induced in each pixel is calculated. Once the temperature fluctuations for each pixel are known, HEALPix routines can be used to calculate angular power spectra for the thermal and kinetic SZ effects.

Each pixel corresponds to a radial path which a photon travels along towards an observer, we wish to evaluate the temperature fluctuation induced on many such photons due to the SZ effect. To this end, each photon is moved along its particular radial path in a series of timesteps, or more accurately, redshift steps. The SZ calculation to be performed at each step is given by changing variable in the SZ integral given in equation (1.35) to redshift and by approximating the integral itself as a sum:

$$\begin{aligned}
\frac{\Delta T^{\mathrm{tSZ}}}{T_{\mathrm{CMB}}} &= g(x)\int_r^0 a(r)\,\frac{k_{\mathrm{B}}\sigma_{\mathrm{T}}}{m_e c^2}\,n_e(r)\,T_e(r)\,dr \\
&= g(x)\int_r^0 \frac{k_{\mathrm{B}}\sigma_{\mathrm{T}}}{m_e c^2}\,n_e(r)\,T_e(r)\,\frac{dl}{dz}\,dz \\
&= g(x)\int_r^0 \frac{k_{\mathrm{B}}\sigma_{\mathrm{T}}}{m_e c^2}\,n_e(r)\,T_e(r)\,\frac{cdt}{da}\,\frac{da}{dz}\,dz \\
&= -g(x)\int_r^0 \frac{k_{\mathrm{B}}\sigma_{\mathrm{T}}}{m_e c^2}\,n_e(r)T_e(r)\,\frac{c}{H\,(1+z)}\,dz \\
&\simeq g(x)\frac{k_{\mathrm{B}}\sigma_{\mathrm{T}}}{m_e c}\sum_{i=1}^{N}\frac{n_e(r(i\Delta z),i\Delta z)\,T_e(r(i\Delta z),i\Delta z)}{H(i\Delta z)\,(1+i\Delta z)}\,\Delta z
\end{aligned} \tag{4.1}$$

where $N = z_{max}/\Delta z$. An exactly analogous procedure is applied to express the kinetic SZ integral as a sum.

The method developed to assign gas properties to a dark matter density field uses the co-moving density field evaluated on a $10\,h^{-1}$Mpc grid. This grid size is selected since it is small enough to allow the angular scales of interest here ($\ell \leq 30$) to be adequately modelled whilst large enough that advection of gas between cells can be ignored. Given such a dark matter grid value, a gas temperature and electron number density can be assigned to this particular grid cell. A photon path will intersect a large number of these cells, see figure 4.1, and points along the path at which the SZ integral is evaluated will fall in particular cells at a particular redshift.

[1] http://healpix.jpl.nasa.gov

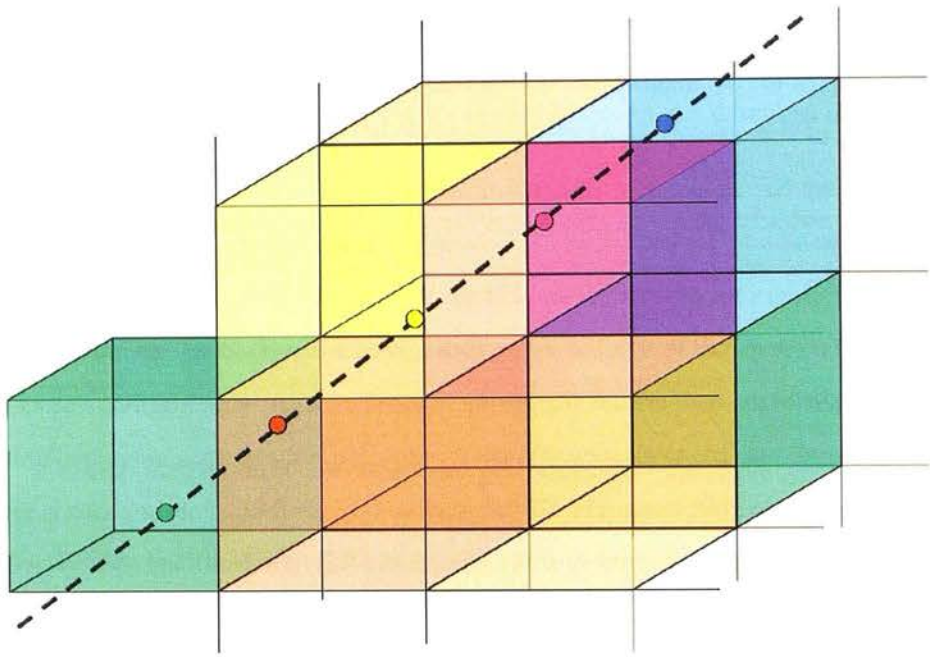

Figure 4.1: Illustration of the path that a photon make take through simulation cells. Circles denote positions where the SZ sum may be evaluated, the colour of the circle corresponds to the simulation cell whose gas property values would be used for that step of the calculation.

The value of the gas temperature and electron density assigned will depend on the redshift at which they are required. When using hydrodynamic simulations during the development of this method, the dark matter density field is inferred from particle positions. In each cell of a given redshift output, the dark matter density is evaluated using the comoving number density of dark matter particles together with their mass.

When applying this method to the local Universe reconstruction where the overdensity field δ is known, it is necessary to first evaluate δ on a $10\,h^{-1}$Mpc grid and then to convert this to a comoving dark matter density as follows:

$$\begin{aligned} \rho_{dm}^{com} &= \bar{\rho}_{dm}^{com}\,(1+\delta) \\ &= \Omega_{dm}\,\rho_{crit}^{com}\,(1+\delta) \\ &= \Omega_{dm}\,\rho_{crit,0}^{com}\,(1+\delta) \end{aligned} \tag{4.2}$$

4.1.2 Method: Relating Gas Properties to the Dark Matter Distribution

In hydrodynamic simulations, the properties of both dark matter and gas particles starting from the same initial conditions are followed simultaneously. In the case of the dark matter particles, the relevant information is just their positions and velocities; for the gas, additional properties such as their temperature and density may also be stored. Hydrodynamic data from the Millennium simulation gas project (Pearce et al., 2007) is used here to deduce the gas-dark matter relationships required for computing the SZ effect. The Millennium simulation gas project follows the evolution of 5×10^8 particles of both gas and dark matter in a simulation box with comoving side length $500\,h^{-1}$Mpc. The dark matter simulation particles have a mass of $1.422h^{-1}10^{10}\mathrm{M}_{\odot}$ and that of the gas particles is $0.312h^{-1}10^{10}\mathrm{M}_{\odot}$. The two simulations use different models of gas physics; one is a purely adiabatic model and the other a 'pre-heating + cooling' model. The adiabatic model represents the simplest, consistent gas physics which can be implemented. 'Adiabatic' refers to the fact that the simulation is an isolated system in which entropy is constant. Non-adiabatic processes can occur within the simulation e.g. two clumps of gas can collide and be shock-heated, but the system as a whole is adiabatic. Such simulations are known not to reproduce the Universe which we observe; there is no radiative cooling included in such simulations, so the gas will not collapse to form stars. However, simply implementing radiative cooling does not improve the simulation results, in such cases the gas tends to overcool forming too many stars. The solution to this is to include pre-heating in the simulations in addition to cooling. 'Pre-heating' refers to an injection of entropy into the system at reasonably high redshift before structure formation has begun in earnest. The amount of entropy introduced and the redshift at which this takes place are chosen so that the simulation at $z = 0.0$ matches observations today. This pre-heating causes gas to escape from shallow potential wells and heats the gas found in larger potential wells. The result is a reduction in the number of visible small satellite galaxies (alleviating the substructure problem) and prevention of over-cooling. This simulation is expected to be a better match to the true Universe and therefore, unless otherwise stated, all the results illustrated here use this model of gas physics.

In order to incorporate evolution into the derived gas-dark matter relationships, three distinct redshift outputs from the Millennium simulation at $z = 0.5$, $z = 0.2$ and $z = 0.0$ are used.

The stages involved in deducing the correspondence between dark matter and gas properties are:

- Evaluating the dark matter and gas properties of each output on a $10\,h^{-1}$Mpc grid to infer 'cell properties'. For the thermal SZ effect, gas temperature, electron density and dark matter density within each cell need to be computed.
- Binning the cell data according to dark matter density/velocity and determining a distribution for each gas property within every dark matter bin.
- Using the different redshift outputs from the Millennium simulation at $z = 0.0$, $z = 0.2$ and $z = 0.5$ to derive redshift scaling relationships which account for evolution of gas properties.

Once all these steps are complete, calculating the thermal and kinetic SZ temperature fluctuations present in the CMB is straightforward given a dark matter density field.

Dark Matter and Gas Properties in Cells

Particle data from each redshift output of the Millennium simulation is first binned into cells of side $10\,h^{-1}$Mpc. For each cell, the following data are available: dark matter density, gas density, gas temperature, dark matter velocity and gas velocity. Dark matter density is evaluated using the comoving number density of dark matter particles in a cell and gas and dark matter velocities are taken to assume the mean values from these particles.

The temperatures of gas particles in the Millennium simulation are adapted slightly before cell gas temperatures are calculated. As the hydrodynamic code used to generate the simulation has no mechanism to describe photoionization, gas particles exist with temperatures lower than the ionisation temperature of hydrogen (10^4 K). These particles are unphysical since in reality such gas would be photoionized. This is dealt with by artificially boosting the temperature of any particle with $T < 10^4$ K to $T = 10^4$ K creating a 'temperature floor' in the data, see figure 4.3. After this correction has been applied, gas temperature for a cell is taken as the mean temperature of the particles within it.

Each gas particle within the Millennium simulation has an SPH density assigned to it: this is a measure of the gas density in the area surrounding the particle computed by looking at the size of the region containing its N nearest neighbours where N is some threshold. Whilst

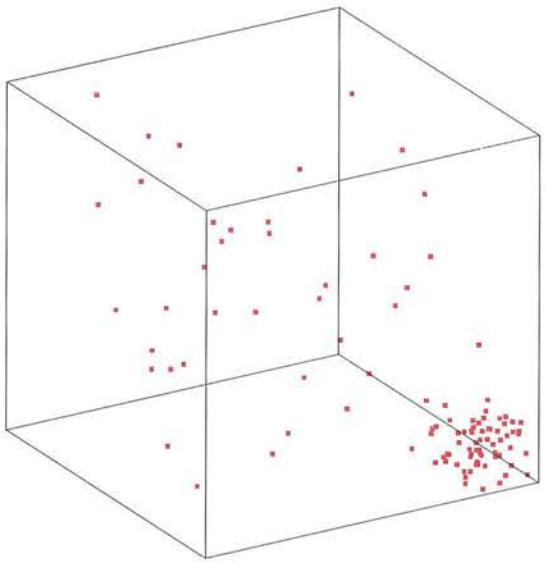

Figure 4.2: An illustration of a situation which would give rise to an erroneously high value for the gas density over the cell if SPH densities were used as an estimator rather than the number density.

this can be a useful quantity, these values are not used here to infer the cell gas density. When computing the large scale SZ signal, information on scales smaller than the size of the cell is ignored. It is therefore irrelevant where precisely within the cell each gas particle resides; using a number density approach to calculate the cell gas density respects this. However, if SPH gas densities are used, we can imagine many situations where the gas particles within the cell are clustered in a small region, leading to an artificially high value for the cell gas density (see figure 4.2).

Once the cell gas density has been calculated, an electron number density for the cell, n_e, can be found by assuming that the gas is a fully ionised gas of hydrogen and helium with a hydrogen mass fraction $X = 0.76$:

$$n_e = \rho_{\rm gas}^{\rm cell} \left(\frac{0.76}{m_{\rm H}} + \frac{2.0 \times 0.24}{m_{\rm He}} \right) \tag{4.3}$$

Having evaluated the gas and dark matter properties on a grid we now search for a relationship between the dark matter properties and those of the gas which can be exploited to infer gas properties from the dark matter field alone. Figure 4.3 shows the values of cell dark matter densities and cell gas temperatures. We see that there is a relationship here in that hotter gas

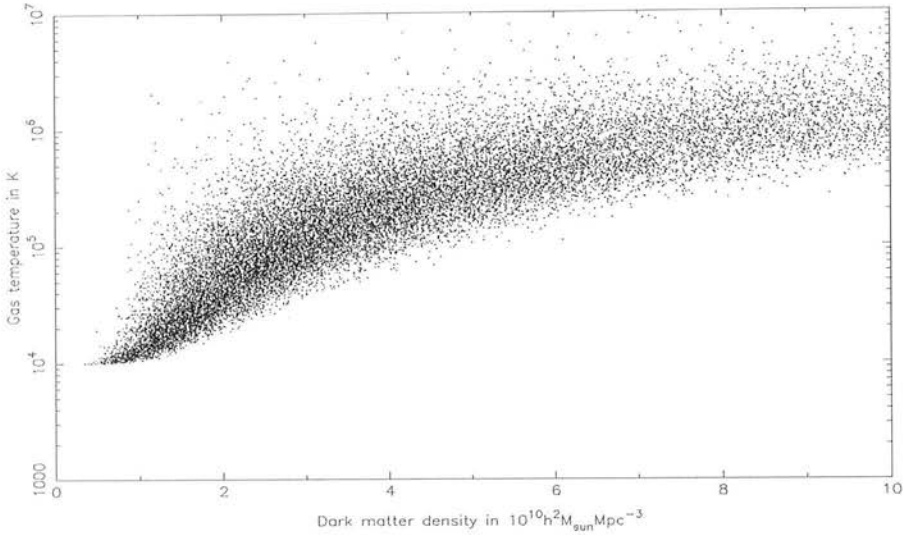

Figure 4.3: Dark matter density in a cell compared to cell gas temperature calculated as outlined in the text, the 'temperature floor' visible in the data is introduced artificially to mimic photoionization. The data here is from redshift $z = 0.2$.

is found in regions where the dark matter density is higher, but that for a given range of dark matter densities there is a distribution of gas temperatures that could correspond to it. Relationships such as this between dark matter and gas properties are what allow the calculation of the SZ effect from only a dark matter field to succeed.

Distributions of Gas Properties

Consider one redshift output from the Millennium simulation. Within a particular range of cell dark matter densities/velocities there will be a distribution of cell gas properties associated with these densities/velocities. Knowing for example the parameters of the n_eT distribution within each dark matter density bin, one can deduce an appropriate value for this quantity given a random dark matter density; this is the approach used here.

Equation (1.35) describing the temperature fluctuations introduced by the thermal SZ effect, is an integral over the density-weighted temperature. Evaluation of this integral along a line of sight using the method developed here will require the dark matter density at a particular step in the photon's progress being used to infer an appropriate value of n_eT which will be used in the calculation. In order to compute the tSZ effect from a dark matter field, it is therefore only strictly necessary to relate values of n_eT to ρ_{dm}. However, since it is important to check that

the gas temperature and electron density distributions demonstrate sensible behaviour, these have been considered separately as well as modelling the distribution of $n_e T$. Results show that it actually makes little difference whether separate values of n_e and T or values of $n_e T$ are used in the tSZ calculation, implying that these distributions are fairly independent.

Figure 4.4 shows the gas properties within cells whose dark matter density $\rho_{dm}^{\rm cell}$ has $9.0 \times 10^{10} h^2 M_\odot {\rm Mpc}^{-3} < \rho_{dm}^{\rm cell} < 9.1 \times 10^{10} h^2 M_\odot {\rm Mpc}^{-3}$ or whose dark matter velocity components, v, lie in the range $-100 {\rm kms}^{-1} < v < -90 {\rm kms}^{-1}$. The electron number densities and gas temperatures are modelled as lognormal distributions within each dark matter density bin and the velocities are modelled as Gaussian distributions within each dark matter velocity bin. This allows a mean and variance for the distribution in each bin to be found. To ensure that there is sufficient data in each dark matter density bin to deduce a reliable mean and variance estimate for the gas distribution, the bin sizes increase with dark matter density. Given a dark matter density and velocity for a simulation cell, it is now possible to derive values for gas temperature, electron number density or their product $n_e T$, as well as gas velocity, for this cell.

Non-Evolutionary Testing

So far, this method for assigning gas properties has been developed using only one output from the Millennium simulation i.e. using gas properties at one redshift. Since photons passing through a density field will undergo interactions at redshifts between $z = 0$ near the centre of the field and $z = 0.3$ near the limits it is necessary to incorporate evolution into the determination of gas property distributions, (see below). However, in the interests of testing this SZ calculation technique, it is instructive first to consider gas properties and a dark matter distribution from a single redshift output and put aside for the moment this issue of evolution.

The advantage of considering non-evolving gas and dark matter distributions is that the SZ computation is testable using the Millennium simulation. For a given redshift output, we know the relevant gas properties in each cell, yet we can also use the distributions which have just been computed to infer such quantities from the dark matter density alone. If the technique of drawing values for gas properties from a distribution determined solely by the dark matter density is successful, the SZ temperature fluctuations calculated via the different methods should only differ slightly. Any problems with the technique that is employed to estimate non-evolving

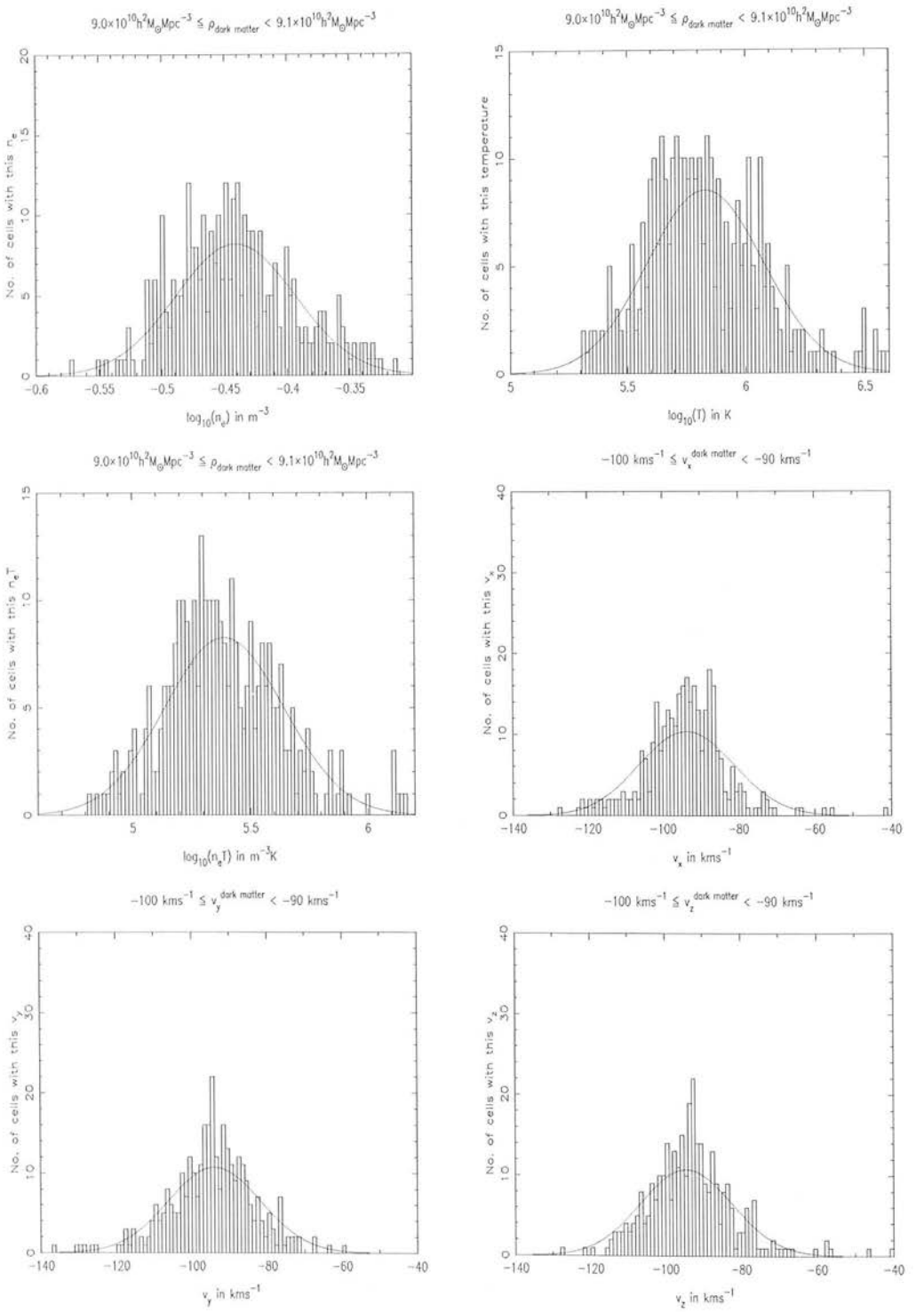

Figure 4.4: Plot showing the number of cells in this dark matter density/velocity bin with particular values for each gas property. The red line shows the distribution which values of the gas property in question are drawn from for simulation dark matter densities in this bin. These plots are for the preheating model of gas physics and the redshift $z = 0.0$ output.

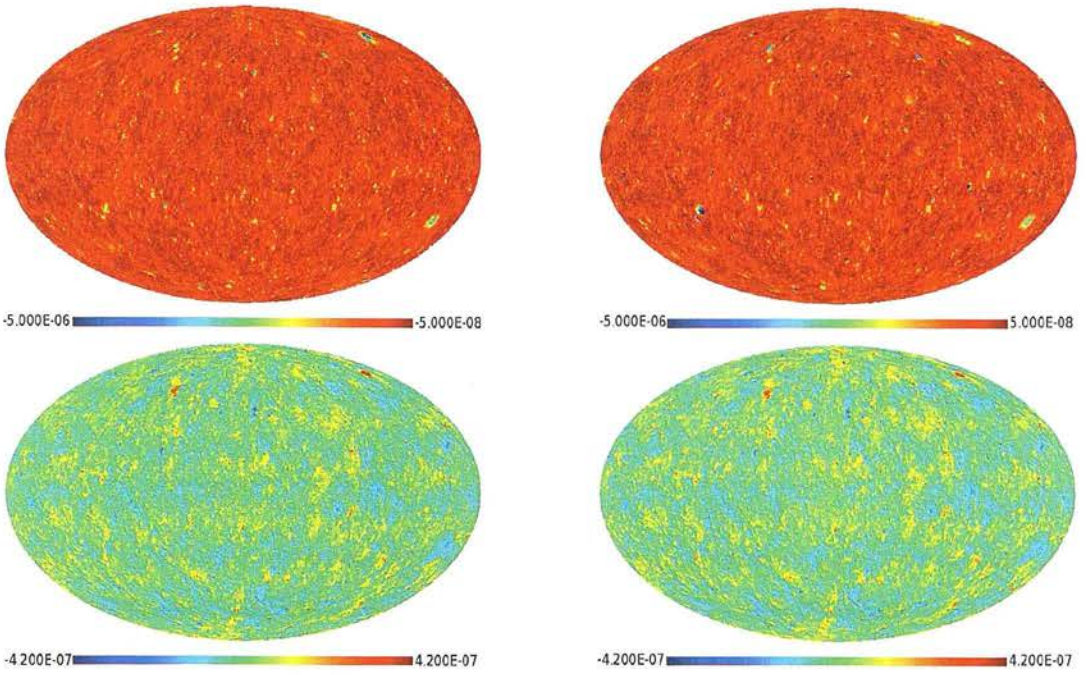

Figure 4.5: (*Top left*) The thermal SZ temperature fluctuations $\Delta T^{\mathrm{tSZ}}/T_{\mathrm{CMB}}$ across the simulated sky calculated using the distribution method and (*top right*) true gas properties. (*Bottom left*) The kinetic SZ temperature fluctuations $\Delta T^{\mathrm{kSZ}}/T_{\mathrm{CMB}}$ across the simulated sky calculated using the distribution method and (*bottom right*) true gas properties.

gas properties should be revealed in this analysis.

Figure 4.5 shows the temperature fluctuations obtained using the two methods. We see strong agreement between the temperature fluctuations for both the thermal and kinetic SZ effects. In particular, features in the temperature distributions are observed in the same positions. The magnitudes of the temperature fluctuations show some slight differences. A clearer means of comparison for the different methods comes from consideration of their angular power spectra, see figure 4.6. Again we see here a close match between the 'true' SZ angular power and that calculated using gas property distribution relations with the dark matter simulation. This indicates that at least for non-evolving gas properties and an SZ signal calculated on simulation cells of the size employed here, the method of deducing gas temperature, density and velocity values from the dark matter distribution is valid.

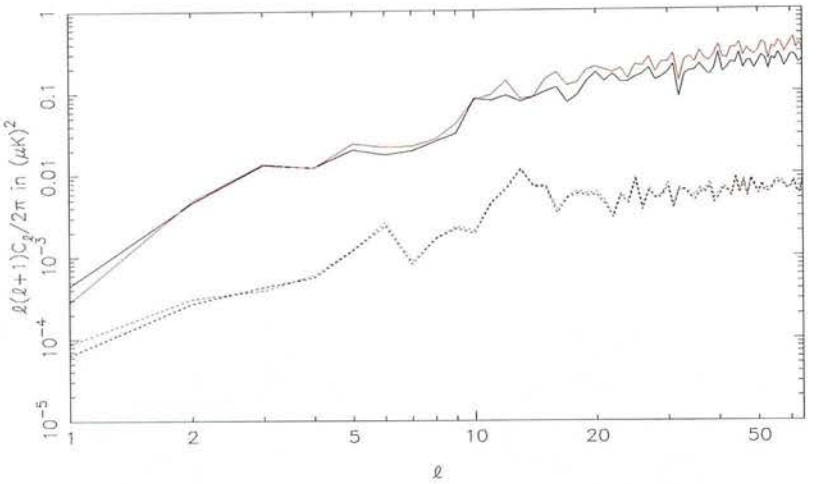

Figure 4.6: Angular power spectra of the thermal (solid lines) and kinetic (dashed lines) SZ effects, calculated using the distribution method to derive gas properties (black) and using the gas properties taken directly from the Millennium simulation (red).

Evolving Gas Properties

Now it is necessary to consider evolving gas properties instead of allowing one redshift output from the hydrodynamic simulation to completely determine the gas distribution at all times. To tackle this issue, outputs from the Millennium gas simulation at redshifts $z = 0.0$, $z = 0.2$ and $z = 0.5$ are analysed in exactly the manner described above. The comoving dark matter density and velocity bins used in each case are the same, and within each bin values for the mean and standard deviation of the relevant distributions are found. The evolution of the temperature distribution parameters is shown in figure 4.7. Comoving dark matter densities and velocities are used so that the results from different redshift outputs are directly comparable.

We see a slight evolution in the temperature distribution parameters with redshift, particularly in lower density cells. The evolution of the standard deviation is less pronounced than that of the mean and shows only a weak dependence on dark matter density. Modelling the evolution of all the distribution parameters will allow extrapolation of the gas property distributions to intermediate redshifts.

To incorporate evolution, we seek to describe a distribution mean and standard deviation as a simple function of redshift and dark matter density. To do this, the relationship between the mean of a gas property and the dark matter density for the redshift $z = 0.0$ output is taken

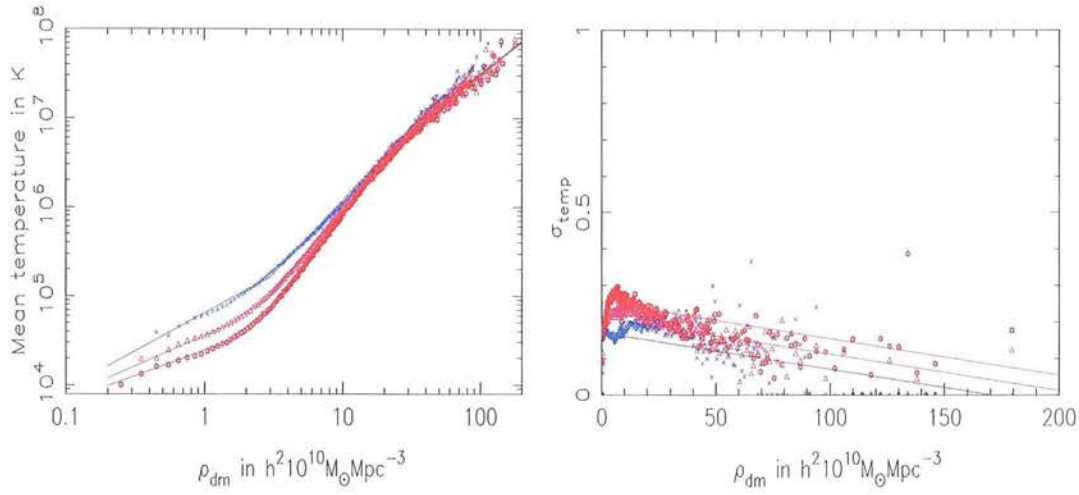

Figure 4.7: (*Left*) Mean of the gas temperature distribution in each comoving dark matter density bin and (*right*) standard deviation of the gas temperature distribution in each dark matter density bin for $z = 0.0$ (pink), $z = 0.2$ (purple) and $z = 0.5$ (blue) and the preheating model of gas physics. The lines show fits to the data incorporating a redshift scaling relation.

and a series of power laws in log space are fitted to this data as shown for the gas temperature in figure 4.7. The aim is now to find some simple redshift scaling which will transform this fit to coincide with the data at the other redshift outputs: $z = 0.2$ and $z = 0.5$. Once this has been found, it seems a reasonable assumption that the scaling relation will hold at intermediate redshifts also. The fits to the redshift $z = 0.2$ and $z = 0.5$ data shown in figure 4.7 are actually redshift scaled versions of the $z = 0.0$ fit. The redshift scaling relation for the mean temperature was found to be:

$$\log_{10}\left(\bar{T}\right) = \begin{cases} 0.57(1+z)\log_{10}(\rho_{dm}) + 4.39 + \frac{z}{1.2} & \text{if} \quad \rho_{dm} < 1.5 \\ \frac{1.98\log_{10}(\rho_{dm})}{(1+z/2.5)} + 3.92 + z & \text{if} \quad 3.0 \leq \quad \rho_{dm} < 29.0 \\ \frac{1.29\log_{10}(\rho_{dm})}{1+z/5} + 4.9 + z/2 & \text{if} \quad 31.0 \leq \quad \rho_{dm} \end{cases} \tag{4.4}$$

for the ranges of dark matter density shown and an interpolation between these for points outwith the ranges covered i.e. for $1.5 \leq \rho_{dm} < 3.0$ and $29.0 \leq \rho_{dm} < 31.0$.

This process is repeated to find fits to the $z = 0$ relationships between dark matter density and the means and standard deviations of the other relevant gas properties. Scaling laws to

evolve these with redshift and recover the $z = 0.2$ and $z = 0.5$ behaviour are then found. A similar process is applied to deduce gas velocity parameters at a given redshift.

Some of the fits to gas parameters used to deduce scaling relations, particularly for standard deviations, are fairly crude. This is because examination of results shows the difference between the SZ effect calculated from distributions using a crude fit and that calculated using a value of σ computed by interpolation of the σ values from two adjacent redshift outputs is negligible. Both the angular power spectra and temperature maps for the two methods are indistinguishable.

The outcome of the work described so far is a method to allocate appropriate gas properties to a dark matter field which can then be used to compute the SZ effect for this field. The accuracy of this method is considered in Section 4.1.3 and some of the tests which were performed on the method are described.

4.1.3 Analysis and Testing the Method

As mentioned above, one of the simplest means to check whether details of the gas property distributions are functioning correctly is to consider a non-evolving scenario and one output from the Millennium simulation. In addition to the basic check of the process of assigning gas properties to dark matter densities described in Section 4.1.2, a number of other aspects of the algorithm are also tested.

In general, the SZ power spectra expected within a given cosmological model cannot be predicted analytically without assumptions being made about the relationship between the gas distribution and the dark matter distribution e.g. via their power spectra. However, in certain special cases such a prediction is possible e.g. for a constant temperature distribution of gas, $T = T_0$. In this case:

$$\begin{aligned} \frac{\Delta T^{\mathrm{tSZ}}}{T_{\mathrm{CMB}}} &= g(x) \int dr\, a(r)\, \frac{k_{\mathrm{B}}\sigma_{\mathrm{T}}}{m_e c^2}\, n_e(r)\, T(r) \\ &= g(x)\, \frac{k_{\mathrm{B}}\sigma_{\mathrm{T}}}{m_e c^2}\, T_0 \int dr\, a(r)\, n_e(r) \\ &= g(x)\, T_0\, \bar{n}_e\, \frac{k_{\mathrm{B}}\sigma_{\mathrm{T}}}{m_e c^2} \int dr\, a(r)\, \frac{n_e(r)}{\bar{n}_e} \end{aligned} \tag{4.5}$$

Let $\delta_e = n_e/\bar{n}_e$, then by analogy with equations (1.35) and (1.36) we see that

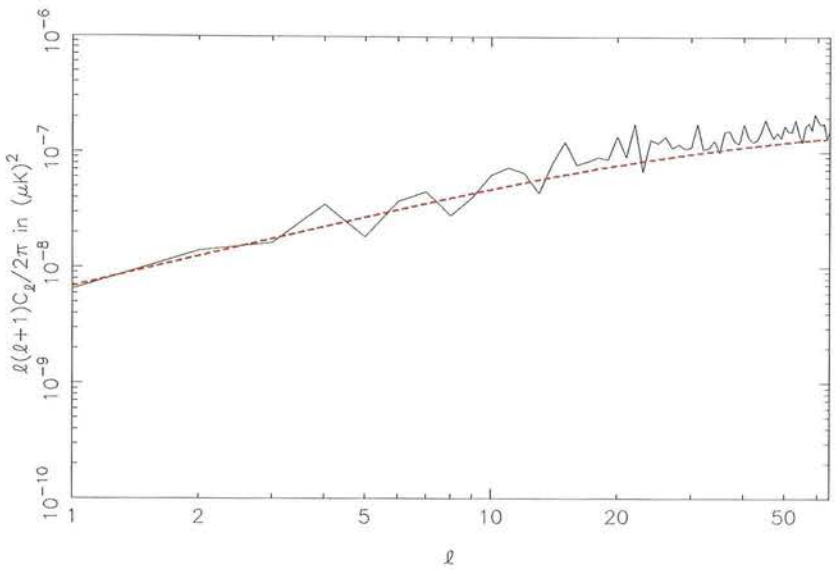

Figure 4.8: The measured power spectrum for a simulation with constant gas temperature, $T_0 = 10^4$K (black solid line). The red dashed line shows an analytic prediction of this power spectrum accounting for bias between matter and electron number densities.

$$C_\ell^{\rm tSZ} = \frac{2}{\pi} \int k^2 \left\langle |\delta_e(k)|^2 \right\rangle |I_\ell(k)|^2 \, dk \tag{4.6}$$

where

$$I_\ell(k) = g(x)\, T_0\, \bar{n}_e\, \frac{k_{\rm B}\sigma_{\rm T}}{m_e c^2} \int a(r)\, j_\ell(kr)\, dr \tag{4.7}$$

Replacing the true temperature values in the simulation with $T = T_0$ for some T_0, allows a comparison of the predicted and computed power spectra in this special case. Figure 4.8 shows the result for $T_0 = 10^4$K. Here the dark matter power spectrum is calculated using the fitting formulae of Eisenstein and Hu (1999) and the bias between δ_e and δ_m has been accounted for.

A slightly more complex procedure can be used to obtain a 'semi-analytic' prediction of the tSZ angular power spectrum for a non-constant temperature distribution. From the Millennium simulation gas and dark matter particle data, $P_{n_eTn_eT}(k)$ and $P_{\delta\delta}(k)$ can be measured directly. Comparison of these two power spectra allows the bias between them to be estimated on different scales. This information can then be used to predict the tSZ power spectrum for the Millennium simulation given a theoretical dark matter power spectrum

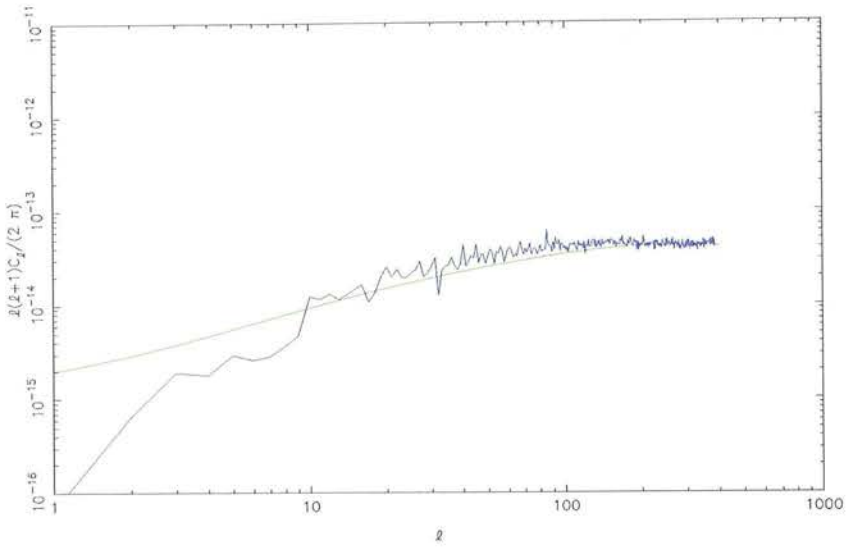

Figure 4.9: The measured thermal SZ power spectrum from a simulation (blue line) together with a semi-analytic prediction of the power spectrum using a fit to the bias between the CDM power spectrum $P(k)$ and the electron pressure power spectrum $P_{n_eTn_eT}(k)$.

$$C_\ell^{\mathrm{tSZ}} = \frac{2}{\pi} \int k^2 \left\langle |n_e T(k)|^2 \right\rangle |I_\ell(k)|^2 \, dk, \tag{4.8}$$

where

$$I_\ell(k) = g(x) \frac{k_\mathrm{B} \sigma_\mathrm{T}}{m_e c^2} \int a(r) \, j_\ell(kr) \, dr. \tag{4.9}$$

The predicted tSZ power spectrum from this method and that measured from the simulation is shown in figure 4.9.

To obtain an estimate of possible systematic errors inherent in my SZ estimation, the two different models for the gas physics used in the simulation are considered, as mentioned in Section 4.1.2. Figure 4.10 shows the SZ signals calculated using both methods. We see that there is a factor of approximately 2 difference between the power spectra of the signals computed from the different models, with the adiabatic model of gas physics giving the larger signal. This is consistent with other groups who have performed a similar analysis (White et al., 2002; Dolag et al., 2005). The 'preheating+cooling' simulation is expected to better describe the real Universe with the larger power noted in the adiabatic simulations due to the lack of radiative cooling here.

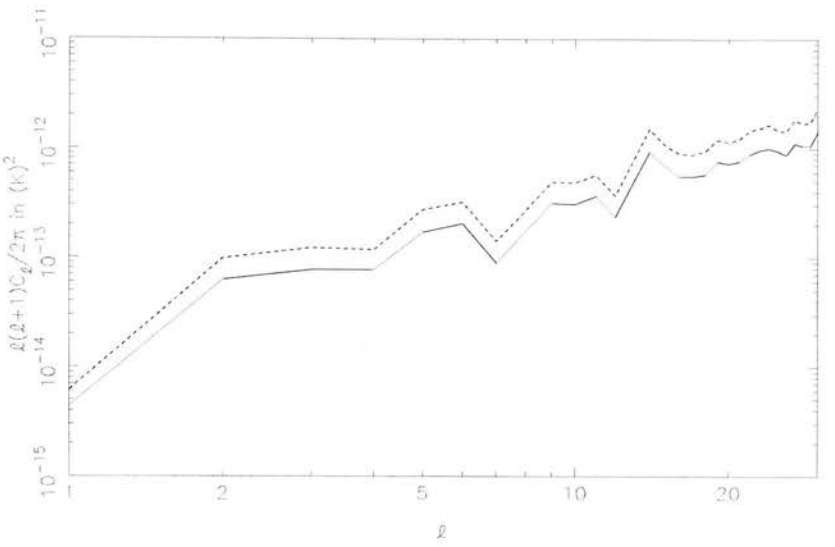

Figure 4.10: The thermal SZ signal computed using the preheating+cooling models of gas physics (solid line) and the adiabatic model of gas physics (dashed line) for the same density field to a maximum redshift $z = 0.44$. Note that there is a factor of ~ 2 difference in the amplitude of the spectra with the adiabatic model giving the larger signal.

The above analysis gives a fair representation of the error in any SZ signals calculated in this manner, *assuming that the SZ signal computed using the true cell gas values is correct.* Due to the cell size used for the calculation, we would expect a small discrepancy between the actual SZ signal and that calculated from the 'true' cell gas values on small angular scales where there is a loss of SZ signal at very low redshifts. We can attempt to quantify this discrepancy by looking at smaller and smaller cell sizes in the simulation and find that for $\ell \lesssim 15$ there is no effect. On smaller scales, the effect can be as large as a factor of ~ 2 underestimation for the largest multipole considered ($\ell = 30$). This is of the same order as the discrepancy between the power spectra from different physical models.

4.2 Application to Local Universe

Despite having developed a method for computing both the thermal and kinetic SZ effects from dark matter properties, only the thermal SZ effect is predicted in the local Universe for two main reasons. Firstly, the kinetic SZ effect is expected to be much smaller than the tSZ effect on the scales of interest (e.g. Cooray and Sheth 2002) and secondly, kinetic SZ prediction

requires knowledge of the velocity field. Whilst the velocity field can be estimated from the density field under linear theory, its determination is far less robust, we therefore neglect the kinetic SZ effect from now on.

It is of interest to try to compute the large scale thermal SZ effect in the local Universe for many reasons. This is an effect which has yet to be detected, and whilst current CMB data do not have the frequency range to allow this (Hernández-Monteagudo et al., 2004; Hansen et al., 2005), future CMB missions such as *Planck* should find it within their realm (Dolag et al., 2005). The detection prospects of *Planck* are investigated in more detail in Section 6.2. Also, as seen in Chapter 3, removal of the predicted local ISW signal from the observed CMB temperature distribution can offer interesting insights into CMB anomalies. We should therefore consider whether the local SZ effect can also have an impact.

In Section 4.2.1 the particular method used to apply the technique described in Section 4.1 to 2MASS data is discussed and the results for the local Universe are presented in Section 4.2.2.

4.2.1 Application to 2MASS Data

In Section 4.1 the development of a method of computing the large-scale SZ effect given a dark matter density field evaluated on a 3D grid with cell size $10\,h^{-1}$Mpc is described. To compute the local tSZ effect, there are two possible ways in which to proceed: firstly, the photometric density field reconstruction could be corrected for redshift errors and then this field could be used to compute the SZ effect or secondly, the photometric reconstruction could be used to estimate the SZ effect and this estimate could be corrected to account for photo-z errors. The latter approach is adopted here since this method is more direct: errors are corrected at the point of interest, in this case the SZ signal. By choosing to correct the final output of the calculation – the SZ signal itself – all sources of error introduced by using the photo-z reconstruction can be accounted for, including the bias in the photo-zs.

In more detail, the following algorithm is used to recover the thermal SZ signal in the local Universe:

- The SZ signal from the reconstructed photo-z density field is computed using the algorithm outlined in Section 4.1.

- N-body simulations and mock 2MASS data are used to compute the required 'smearing correction' to be applied to this SZ signal.

- The smearing correction is applied to the 2MASS SZ signal computed from the photo-z reconstruction.

- The simulations are further used to quantify the error expected in the estimated local SZ signal.

The 'smearing correction' involves a simple rescaling of the spherical harmonic coefficients describing the tSZ signal. The phases of the signal are left unaltered, only the amplitudes are rescaled by the ratio of the true SZ power computed from simulation to the photo-z SZ power:

$$a_{\ell m}^{\text{corrected}} = \sqrt{\frac{C_\ell^{\text{true}}}{C_\ell^{\text{photo-}z}}}\, a_{\ell m}^{\text{photo-}z} \tag{4.10}$$

This technique is expected to work since the difference between the 'true' and 'photo-z' SZ signals should almost entirely appear in the amplitude of the signal alone (as proved to be the case for the ISW signal), this is confirmed by simulations. This is because photo-z errors introduce an uncertainty into the radial positions of galaxies but leave their angular positions unchanged. An overdensity along the line of sight will therefore remain overdense once photometric redshift errors are applied, but the magnitude of the overdensity will be reduced and it will span a larger radial extent. The SZ signal one would compute for such an overdensity will be reduced since the SZ signal is strongly dependent on the very largest densities; a greater extent of less dense matter will not compensate entirely for the missing signal. However, there will still be a significant temperature decrement in the SZ signal computed from photo-zs wherever a sizeable overdensity exists. Since the difference between 'true' and 'photo-z' maps is expected not to affect the phases of the signal, the power spectra of the simulated true and photo-z maps can be used to quantify the amount by which the photo-z signal should be boosted to recover the truth as far as possible.

In the remainder of this Section, the first two steps of the SZ estimation process are described in more detail. The results and a discussion of the expected accuracy is deferred until Section 4.2.2.

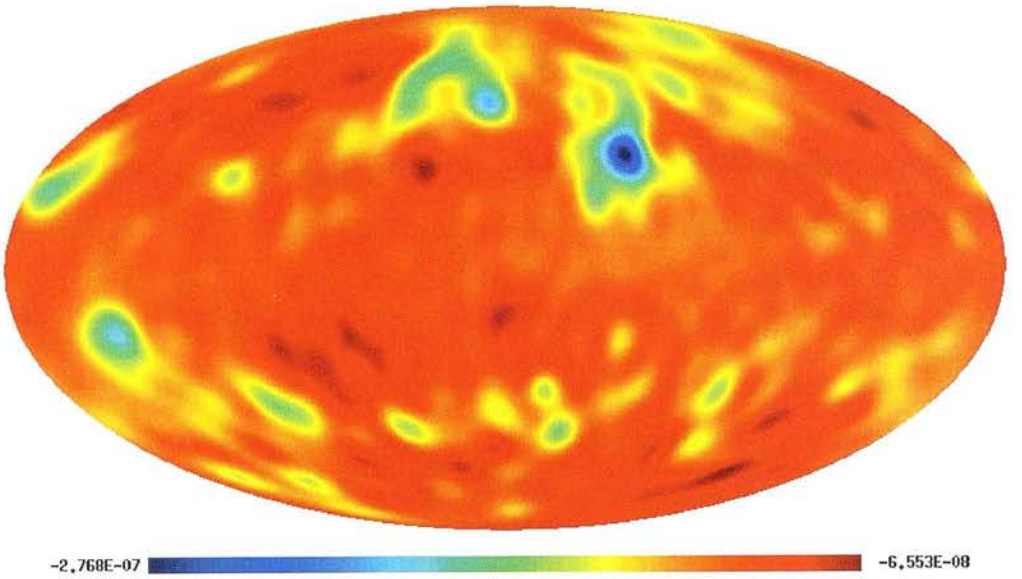

Figure 4.11: The thermal SZ signal as computed using the photometric redshift reconstruction of the local density field. The scale here shows $\Delta T/T$ and is for Rayleigh-Jeans wavelengths. A significant contribution to the large scale SZ effect is observed from the Shapley concentration (slightly above and to the right of centre) and for the Perseus-Pisces supercluster (far left, just below centre).

SZ Signal from Photo-z Reconstruction

The reconstruction is used to evaluate the local photo-z density field on a grid of side $10\,h^{-1}$Mpc. The resolution of the reconstruction is larger than the grid size at all redshifts meaning that density values can be assigned to grid cells unambiguously – there is no need for additional smoothing over that already imposed. The radial resolution of the reconstruction is smaller than the photo-z error so we obtain a faithful representation of the photo-z density field on the grid. A constant bias $b = 1.0$ is assumed, for the same reasons outlined in Section 2.4.1. The SZ signal arising from this density field is shown in figure 4.11. The amplitude is lower than we would expect for the large scale SZ effect, but this is natural given the smearing properties of photo-z errors. Ignoring the amplitude for the present, we see a large temperature decrement in the vicinity of the Shapley concentration, and another in the direction of Perseus-Pisces.

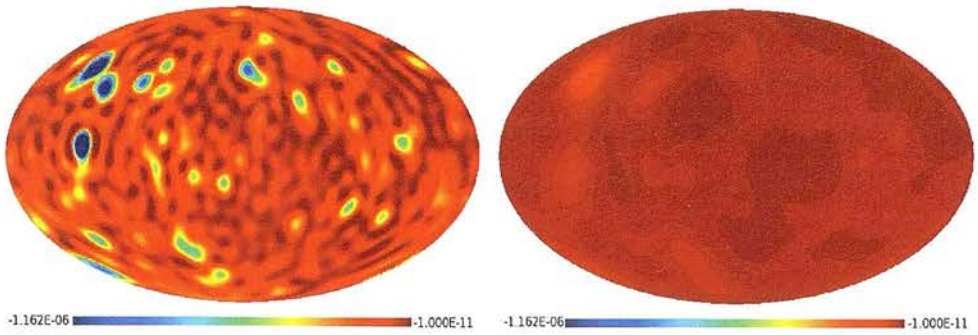

Figure 4.12: The 'true' (left) and uncorrected (right) tSZ signal from a simulation for $0.0 < z < 0.05$. We note that the amplitude of the signal from the photometric reconstruction of the density field is much lower than the true signal, the correction calculated from the simulation data will rectify this.

Computation of the smearing correction

The 5 low resolution particle mesh N-body simulations described in Section 3.2 are used together with the SZ algorithm to find 5 simulated 'true' SZ signals. The masked and unmasked reconstructions of these simulations are also used together with the SZ algorithm to produce mock 2MASS SZ signals. Figure 4.12 shows the 'true' SZ signal and that which would be computed from a reconstruction using photo-z data (no mask). We note that the amplitude of the 'true' signal is greater but that the phases of the signal seem largely unaffected – hot and cold spots seem to align. The use of both masked and unmasked data allows the effect of filling in the galactic plane as described in Section 2.3.3 to be assessed.

The comparison of the true SZ and the mock 2MASS SZ power spectra for each simulation are used to calculate a correction for the effects of photo-z smearing. The correction will vary depending on the redshift range for which the signal is calculated. The signal is considered both over the entire reconstruction region ($0.0 < z < 0.3$) and in 6 smaller redshift slices ($\Delta z = 0.05$). The angular power spectra of the simulated 'true' and corresponding 'photo-z' SZ maps in each of these redshift ranges are computed and the corrections for each set of simulations as defined in equation (4.10) are found. Figure 4.13 shows the correction for each of the 5 simulations in each redshift range, together with a least squares fit of a smooth function to their mean. In most cases, this is a simple quadratic in ℓ, but in some cases an exponential cutoff was also necessary ($0.0 < z < 0.05$) or a slightly different power law ($0.05 < z < 0.1$). This smooth fit will be used to correct the 2MASS SZ maps in each of the redshift ranges considered. As we see in figures 4.13 and 4.14, it makes little difference

whether the correction is calculated from masked or unmasked simulation data, the masked data leads to a slightly greater correction in some cases, as expected since the reconstruction of the missing plane information will tend to underestimate density fluctuations there leading to a smaller SZ signal, but in general the difference is small.

Figure 4.15 shows the results of applying the correction to the simulated 'photo-z' map in figure 4.12. We immediately see that the amplitude discrepancy is drastically reduced and that the agreement between the maps is good. Figure 4.16 shows the same corrected SZ signal as in figure 4.15 but this time the photo-z data were masked and reconstructed exactly as for 2MASS. Away from the plane, the SZ signal is relatively unaffected by the mask. Within the plane, large scale trends within the signal are picked up but smaller scale features tend to be absent or underestimated. We can however imagine situations where the density field contains large overdensities within the masked region which would not be so well recovered. A more quantitative examination of the effect of the mask is included in the next Section.

The simulations described above will again prove useful when the error in the local Universe SZ signal is considered in Section 4.2.2. Since we expect the bulk of the large scale SZ signal to come from low redshift (where structures of a given physical size subtend a larger angle) these simulations will prove useful in estimating another useful quantity: the maximum redshift to which there is a significant contribution to the large scale SZ effect.

4.2.2 Results

Figure 4.17 shows the SZ signal in the local Universe, as calculated from a photo-z reconstruction and corrected for the underestimation due to redshift errors. We see significant contributions at low redshift from the Shapley concentration and Hercules and Perseus-Pisces superclusters. The amplitude of the signal is small, around 10% that of the ISW effect. As we move to higher redshift, the amplitude of the large scale SZ signal falls, as we would expect, since the structures giving rise to the largest SZ decrements now subtend smaller angles on the sky. Also, matter is less strongly clustered in the past, so we expect smaller SZ power here. The lowest redshift slice is very noisy on small scales ($\ell \gtrsim 20$) when corrected in this fashion because there is very little signal here. Correcting the entire $z < 0.3$ SZ signal at once is far less subject to noise as the total signal to be boosted by the correction is greater than the signal in smaller redshift slices. The total $z < 0.3$ tSZ signal is therefore the source of most of the

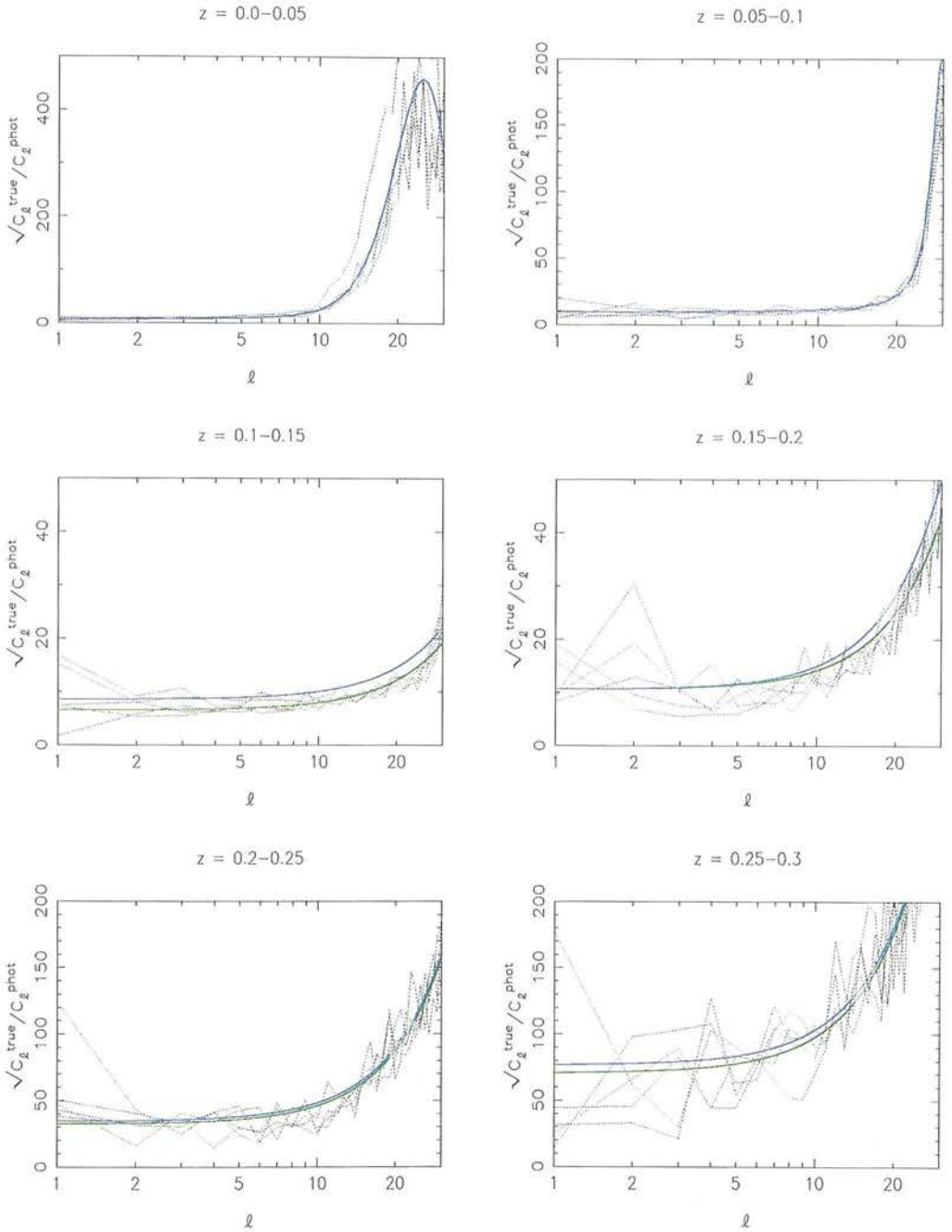

Figure 4.13: The correction factors calculated from each of the 5 simulated unmasked datasets (grey dashed lines), a fit to the mean of these (green solid line) and the fit to the corresponding masked dataset correction factors (blue solid line). We see that there is little difference between the correction factors computed using masked and unmasked data but that the masked data sometimes leads to a greater underestimation (and therefore larger correction) on large scales. This is expected since the recovery of the density field within the galactic plane will tend to underestimate density fluctuations here and lead to further underestimation of the true SZ signal.

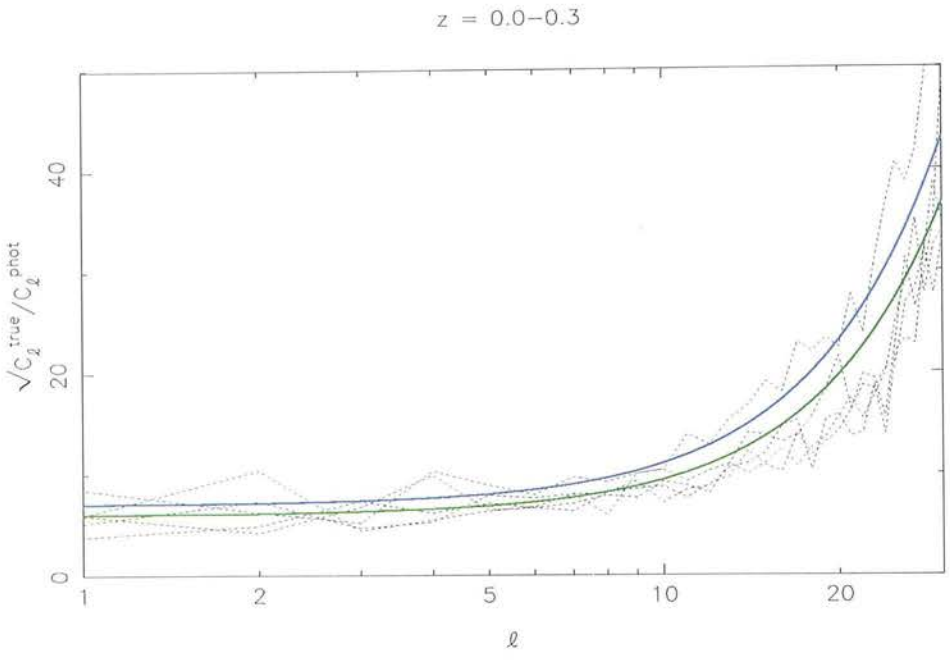

Figure 4.14: As for figure 4.13 but for the entire dataset $0.0 < z < 0.3$.

results presented here.

The total large scale SZ effect to $z_{\max} = 0.3$ is shown in figure 4.18. As expected from the maps of the signal within redshift slices, the total signal is dominated by the contribution from low redshift. We again note the strong contribution from the Shapley concentration (above and slightly right of centre) coming from low redshift ($z < 0.1$) and in the direction of Perseus-Pisces (far left, slightly below centre), although this appears to be a superposition of signal from very low redshift (the Perseus-Pisces supercluster) and from intermediate redshift ($0.15 < z < 0.2$). The redshifts of structures contributing to the largest tSZ decrements are included in this figure.

Using the adiabatic model of gas physics as opposed to the preheating model gives a slightly larger SZ signal by a factor of around 1.5, see figure 4.19, whose phases are nonetheless identical. We can interpret this result as putting some constraint on the uncertainty of the computed SZ effect due to our lack of precise understanding of the physical processes which take place within the gas distribution.

Having examined the effect of the uncertainty in gas physics, we move to consider the errors introduced due to the use of the photometric reconstruction to deduce the SZ signal. To do this, simulation data is used once again. Here, both the true signal and the signal calculated from a

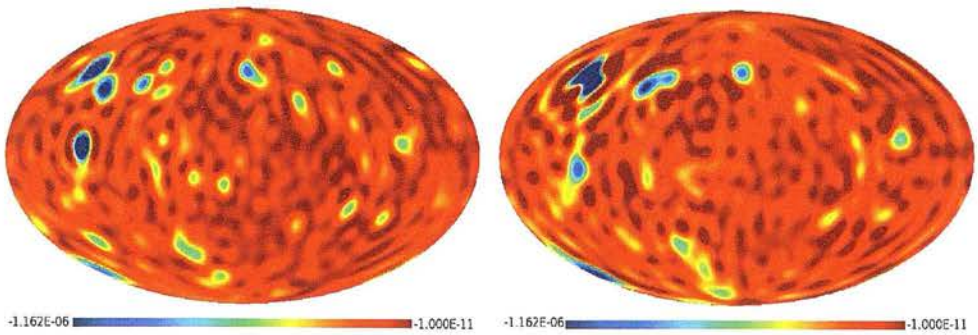

Figure 4.15: The 'true' (left) and corrected (right) tSZ signals from a simulation for $0.0 < z < 0.05$. The correction is derived from and applied to unmasked data.

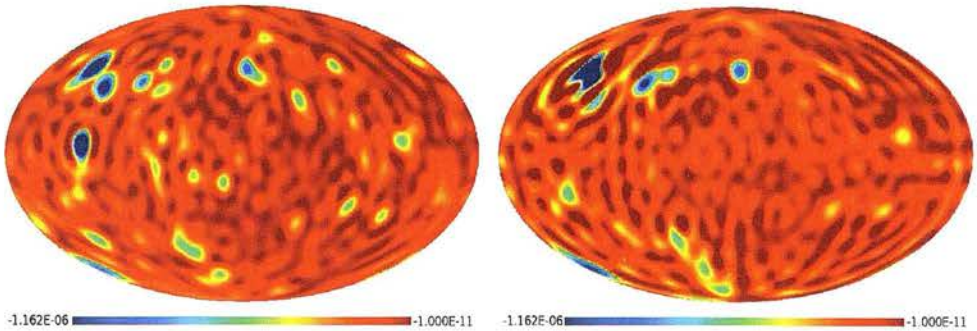

Figure 4.16: The 'true' (left) and corrected (right) tSZ signals from a simulation for $0.0 < z < 0.05$. In this case the correction is applied to and derived from masked data. We note that in this case that effect of the mask is small. A more substantial deviation between the corrected SZ signal here and in Fig. 4.15 would be expected within the masked region if there were a significant overdensity here.

photo-z reconstruction of the simulated density field which has exactly the same properties as the local Universe reconstruction[2] are known. One can ask whether the photo-z reconstruction reproduces the main features of the true SZ signal and quantify the degree of correspondence using the correlation coefficient:

$$r(\ell) = \frac{\left\langle a_{\ell m}^{\rm true}\, a_{\ell m}^{*\rm phot} \right\rangle}{\left\langle a_{\ell m}^{\rm true}\, a_{\ell m}^{*\rm true} \right\rangle}. \tag{4.11}$$

Figures 4.20 and 4.21 show the average correlation coefficient for both masked and unmasked

[2]The 'true' signal here is that calculated using the scaling relations applied to a $10\,h^{-1}$Mpc grid. From the analysis in Section 4.1.3 we know that the scaling relation gives a very good match to the true SZ signal calculated from gas properties *evaluated on the same grid.* Therefore, not included here is the error introduced by using this grid. As discussed in Section 4.1.3, this will only be important at the smallest angular scales, perhaps leading to an underestimation in the largest multipoles $\ell \simeq 30$ by a factor of around 2.

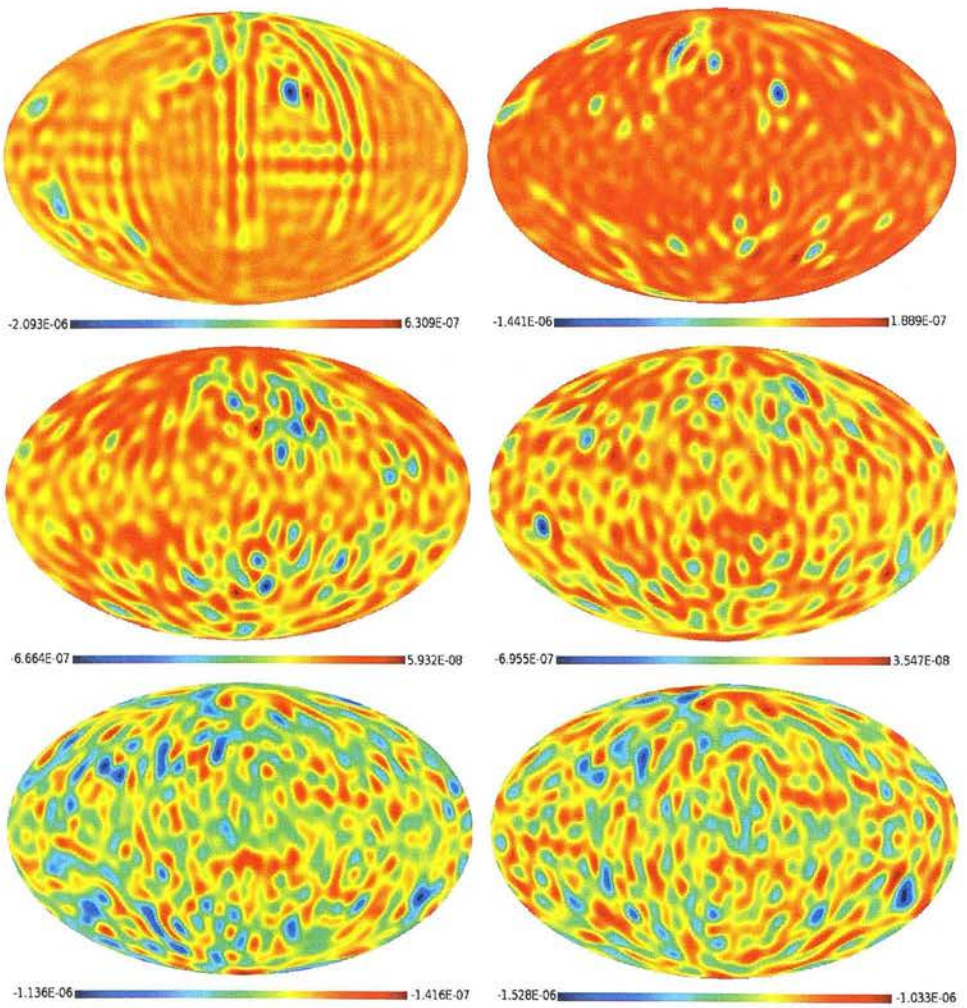

Figure 4.17: The corrected local SZ signal in redshift slices of width $\Delta z = 0.05$. Note the contribution at low redshift from the Shapley concentration and the noise on small angular scales for $0.0 < z < 0.05$ where there is little signal.

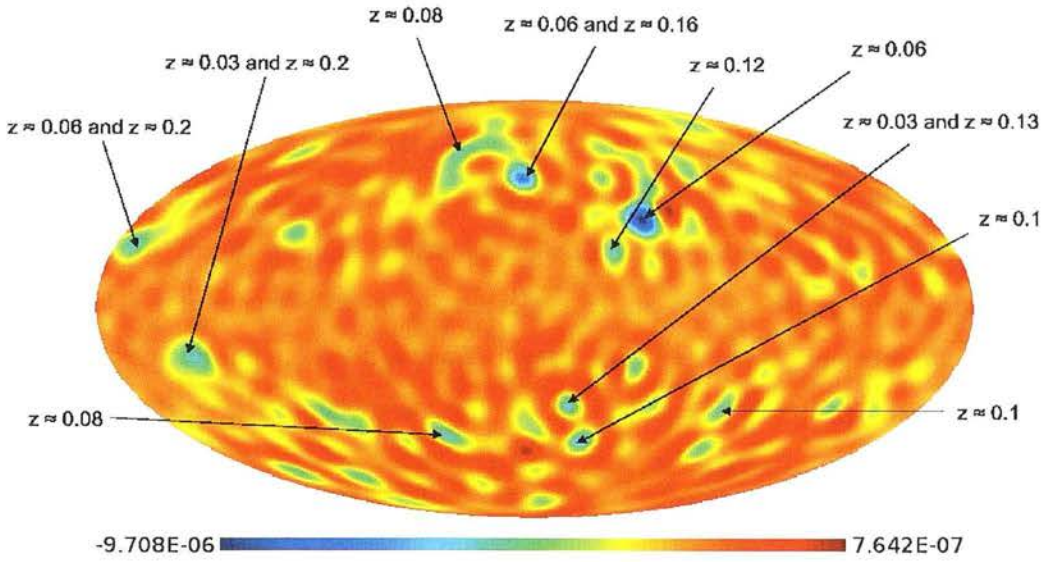

Figure 4.18: The large-scale thermal SZ signal in K for redshifts $z < 0.3$. We note several significant temperature decrements which can be identified with various structures whose redshifts are given. These include the largest contribution which is due to the Shapley concentration (slightly above and to the right of centre).

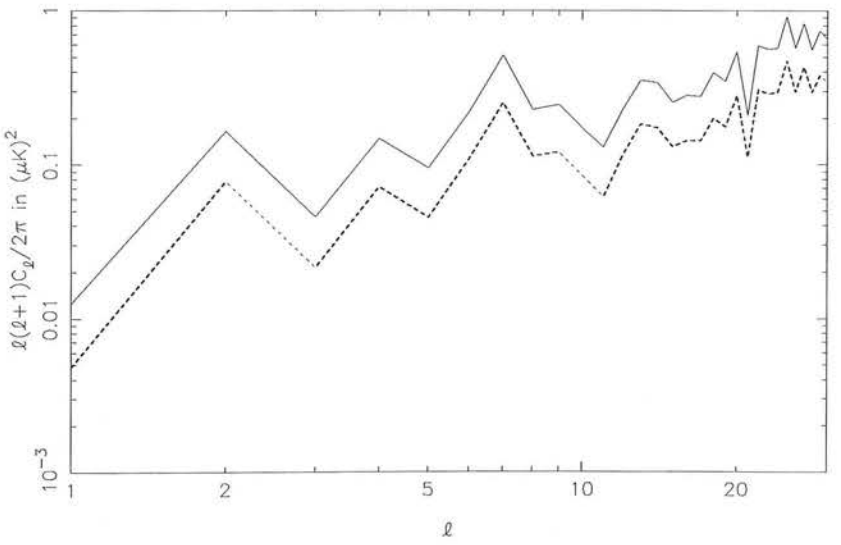

Figure 4.19: The angular power spectrum of the local large scale tSZ effect to a maximum redshift of $z = 0.3$. The solid line shows the results using the adiabatic gas model and the dashed line those of the preheating model.

reconstructions in individual redshift slices together with the correlation coefficient for the cumulative SZ signal for the masked maps. As expected, the unmasked reconstruction fares better, but the correlation for the masked data is not much smaller in each case. As we move to higher redshift, the correlation worsens, this is also visible in the accompanying 'true' and corrected SZ maps for each slice. Above $z = 0.2$, the signal is lost completely and only noise is recovered. This is because the large scale SZ signal is smaller at higher redshift (SZ producing structures at these redshifts subtend smaller angles causing the SZ signal to peak at higher ℓ), and shot noise is comparable to the signal strength. We note the poor correlation between the true and recovered SZ signals on *small* angular scales at low redshift where the SZ signal from the reconstruction is dominated by noise.

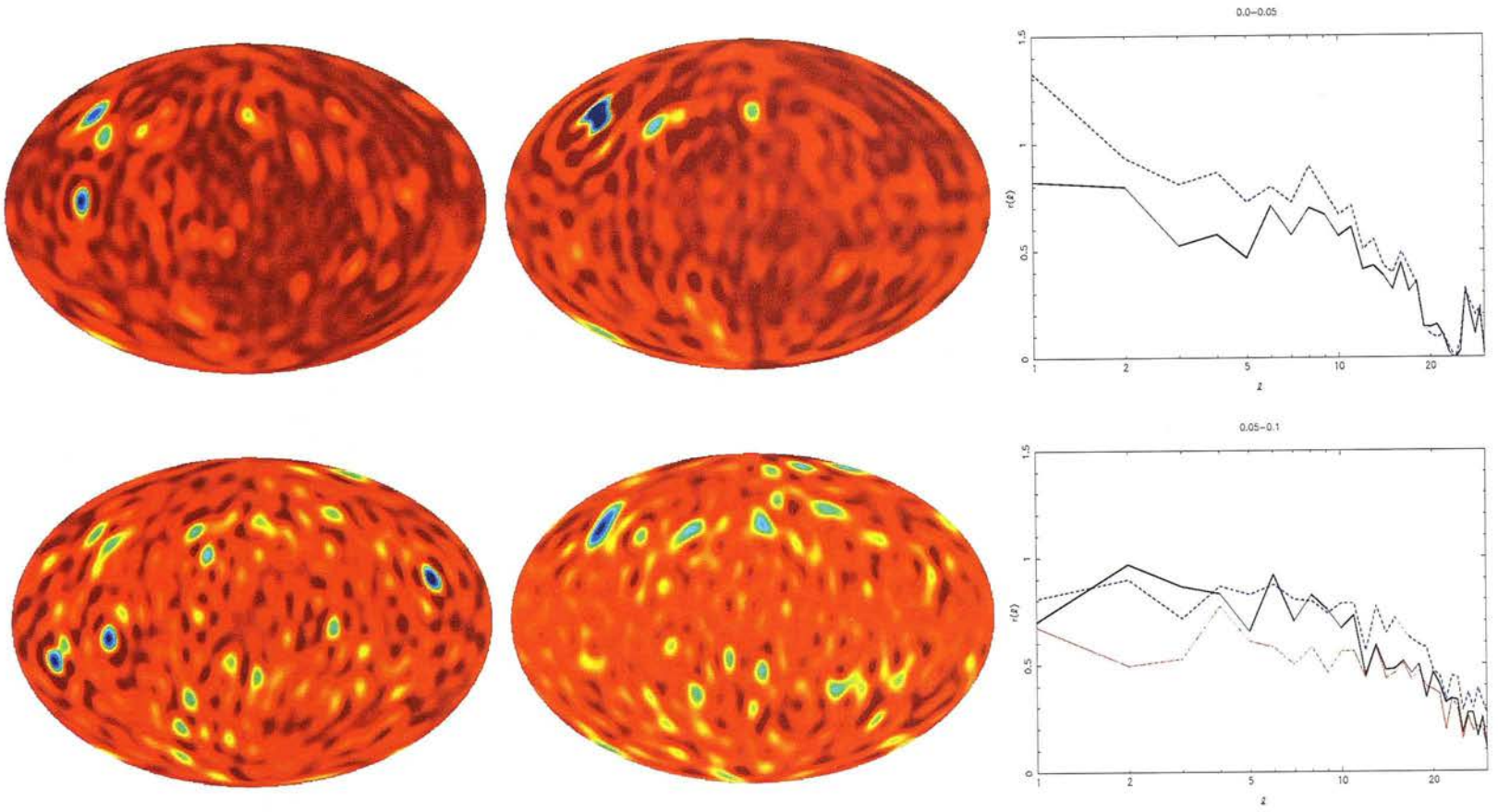

Figure 4.20: (Left) The true thermal SZ signal for a simulated density field, (centre) the SZ signal computed from a reconstruction of this density field and (right) the correlation coefficient of the unmasked reconstruction SZ signal with the truth (blue), that of the masked reconstruction with the truth (red) and the correlation coefficient for the cumulative SZ signal out to that redshift for the masked reconstruction (black). The redshift slices are: (*top*) $0.0 < z < 0.05$ and (*bottom*) $0.05 < z < 0.1$.

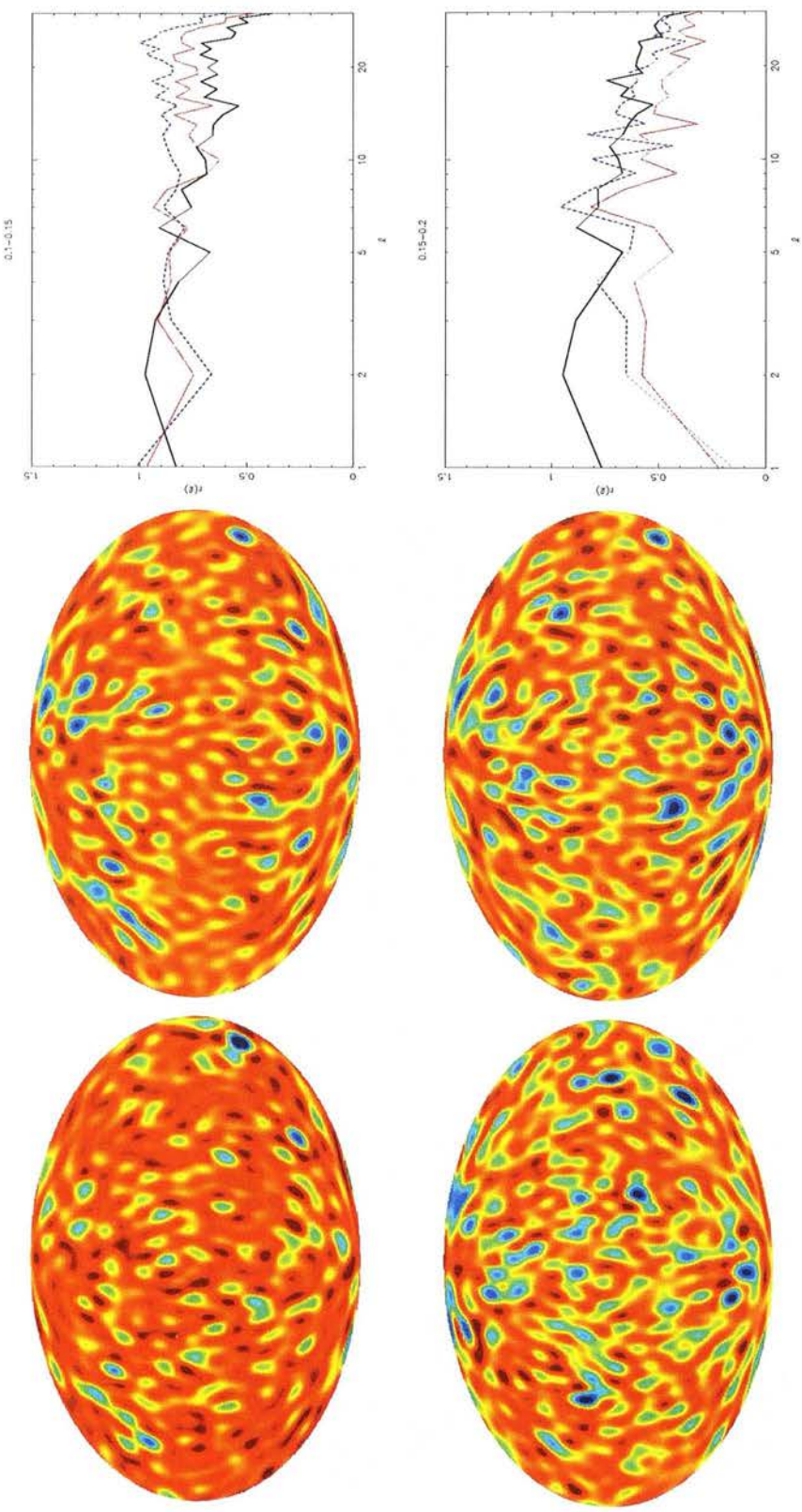

Figure 4.21: As above but for (*top*) $0.1 < z < 0.15$ and (*bottom*) $0.15 < z < 0.2$. We note that the cumulative signal has a correlation coefficient above ~ 0.5 out to $z = 0.2$. Above this redshift, the cross-correlation between the reconstructed SZ signal and the true SZ signal vanishes as it becomes dominated by shot noise.

The error we can expect in the determination of the local SZ effect is therefore described by the following:

- On large angular scales ($\ell \lesssim 10$), the correlation coefficient of the inferred tSZ effect compared with the truth is around 0.8, this falls to ~ 0.45 as we move to smaller angular scales. This tells us that the ratio of the cross-correlation of the recovered and true signals to the true auto-correlation is always $\gtrsim 0.5$. Assuming a perfect phase match between the recovered signal and the truth, this would mean that the recovered signal is at most a factor 0.5 smaller than the true signal. Of course, this perfect phase match assumption is an ideal case, and will not apply perfectly here.

- The 'true' SZ signal above is itself imperfect in that it can differ by a factor $\lesssim 2$ due to different assumptions about gas physics in the simulations used to develop the scaling relations. Also, on scales $\ell \gtrsim 15$ the signal may be underestimated by a factor up to ~ 2 due to the size of the grid used to perform the calculation.

In total, accounting for errors in the tSZ calculation method and due to the use of a photo-z reconstruction, we expect that the predicted local SZ signal outside the masked region is reliable to within a factor < 10.

Figure 4.22 displays the build up of the true SZ signal with increasing depth, we see that most of the large scale ($\ell \leq 30$) signal is generated for $z < 0.15$. 2MASS is therefore able to give a good measurement of the SZ signal on these scales.

4.3 Comparison with Other Groups

Several groups have used a variety of methods to estimate the diffuse SZ signal in the local Universe, most notably Hansen et al. (2005) and Dolag et al. (2005). It is useful to summarise briefly their methods and results to facilitate comparison with my findings.

Hansen et al. (2005) compute the large scale thermal SZ signal within a radius of $80\,h^{-1}$Mpc. They perform cross-correlations of this estimate together with WMAP observations of the CMB to investigate whether the SZ effect from diffuse gas in the local Universe can be detected in the current CMB data and whether it could therefore be a contaminating factor on large scales; they conclude that detection is not possible with current observations. The authors use a constrained hydrodynamic simulation of the local Universe in a box of side

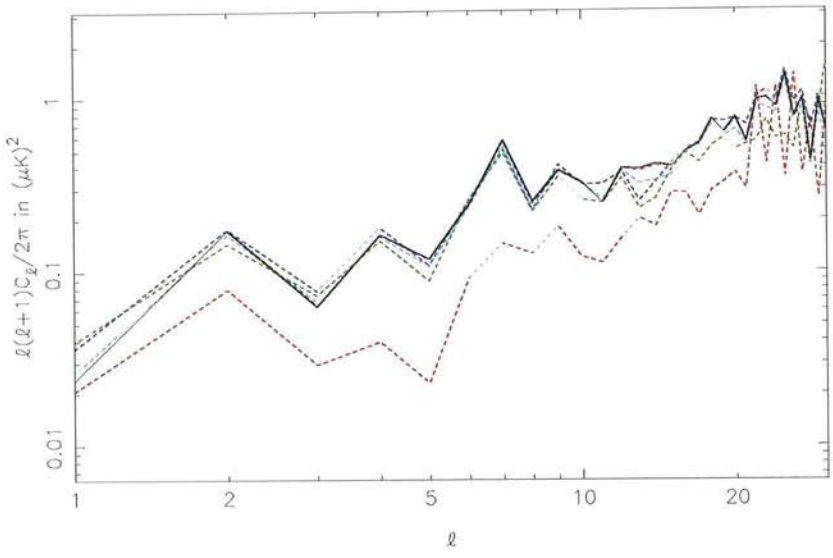

Figure 4.22: The build up of tSZ power over successive redshift slices in the local Universe. With dashed lines: $z < 0.05$ (red), $z < 0.1$ (green), $z < 0.15$ (blue), $z < 0.2$ (cyan), $z < 0.25$ (purple). The solid black line shows the total tSZ signal for $z < 0.3$.

$240\,h^{-1}$Mpc with only the high density region within $80\,h^{-1}$Mpc containing gas physics. Their SZ map of the local Universe shows significant contribution from the Virgo cluster and from Perseus-Pisces.

Dolag et al. (2005) take a similar approach to Hansen et al. (2005) and indeed, use the same simulation as part of their work. In this case, the constrained simulation is also used with a model of gas physics which includes radiative cooling, star formation and supernova feedback in addition to the adiabatic model described above.

Since the SZ maps produced by each group have $r_{\rm max} = 80\,h^{-1}$Mpc, meaningful comparison with my results is not really possible. At such low redshifts, the effect of bias in my photo-zs is important and the resolution of my reconstruction is far too coarse to give an accurate impression of the SZ signal over such a small volume. This is not such a concern for the corrected map produced out to $z = 0.3$, and we have seen from the analysis using simulations that the correspondence between the true signal and that estimated to this maximum redshift is good.

Dolag et al. (2005) find that the central Compton y-parameter for the thermal SZ effect is larger by a factor of up to 2 in the adiabatic model. The results of this Chapter also show

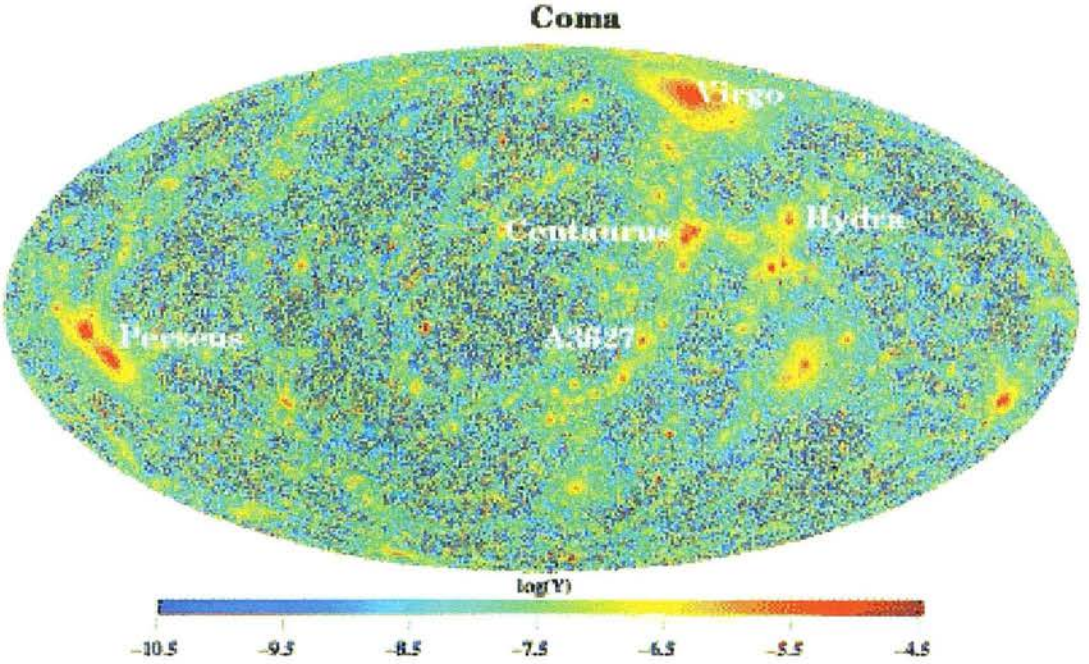

Figure 4.23: *From Dolag et al. (2005)*: The thermal SZ signal in the local Universe as computed by Dolag et al. (2005) from a constrained hydrodynamic simulation, supplemented with resimulations of clusters at higher redshift by Schäfer et al. (2006).

that the thermal SZ signal is boosted when an adiabatic model of gas physics is used, with approximately the same increase in signal observed. Interestingly, White et al. (2002) notice the same effect in simulations of the SZ effect on a much smaller scale.

Dolag et al. (2005) supplement their SZ maps from the local Universe simulation with the results of Schäfer et al. (2006), who use hydrodynamic re-simulations of single clusters to build SZ maps from the *Hubble volume simulation*. This allows a deeper SZ map to be constructed and reduces the loss of small scale information caused by limiting the depth of the analysis (see figure 4.23). The addition of this information raises the mean Compton y-parameter by a factor of around 10 over that of the local Universe SZ maps alone, and boosts the angular power spectrum at larger multipoles. They find a mean value of $y = 3.3 \times 10^{-7}$ from the supplemented map.

Comparing the tSZ angular power spectrum computed here with their results reveals good agreement for $\ell \lesssim 25$ and a slight underestimation at higher multipoles. Some of this discrepancy will be due to the fact that for $\ell \gtrsim 15$, the grid method which is used to estimate the SZ signal underestimates the true signal by up to a factor $\lesssim 2$. Figure 4.24 shows a histogram of

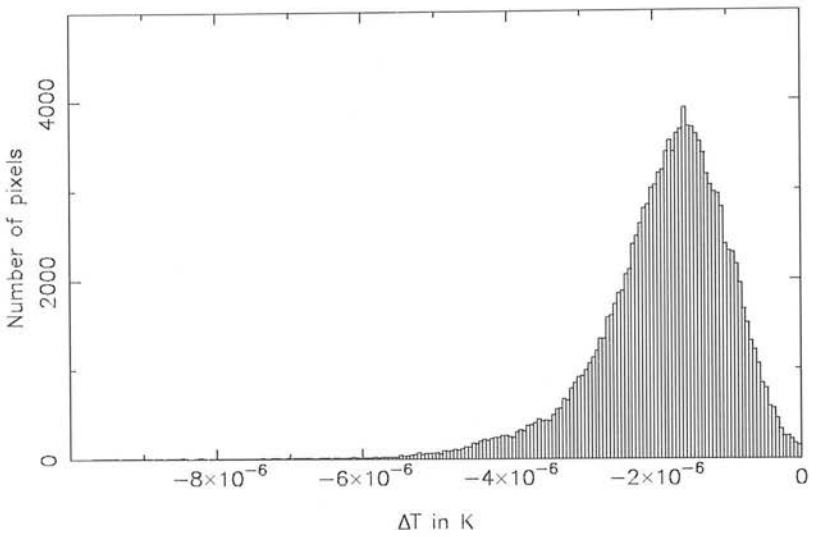

Figure 4.24: A histogram of local Universe tSZ temperature decrements outside the mask.

SZ temperature decrements in pixels outside the mask. We note a lognormal distribution of values, which is also noted by Roncarelli et al. (2007) and find a mean temperature decrement of $\Delta T^{\mathrm{tSZ}} \sim -2 \times 10^{-6}$K. This is comparable with the value found for the mean Compton y-parameter by Dolag et al. (2005) and smaller than the value $\Delta T \simeq -6.5 \times 10^{-6}$K found by Roncarelli et al. (2007), as expected since they use a maximum redshift $z = 6$.

In conclusion, the statistical agreement between the prediction of the local tSZ signal presented here and that of other groups is good; both the power spectrum and mean Compton y-parameter agree well with published results. A meaningful comparison of temperature decrement maps is not possible, since the maps which exist in the literature cover only a small volume which is not well resolved in the prediction described here.

4.4 Impact on WMAP Data

There have been suggestions that the SZ effect could be a serious contaminant in the CMB, influencing the positions of the acoustic peaks and affecting the determination of cosmological parameters (Myers et al., 2004), although this is refuted by Huffenberger et al. (2004) who find no contamination in cosmological parameter estimation from an SZ signal. Others have suggested that a tSZ foreground signal from the local supercluster could provide an explanation for large-scale CMB anomalies (Abramo et al., 2006), although again doubt is cast on this

suggestion by the results of Hansen et al. (2005) and Dolag et al. (2005).

4.4.1 CMB Anomalies

In Chapter 3, we saw that the predicted local ISW signal can significantly affect the CMB at low multipoles and that its removal can reduce the significance of reported anomalies in the CMB data. The tSZ effect has a much smaller amplitude than the ISW effect, especially on the very large angular scales where most of the anomalies have been found, it is therefore unsurprising that the removal of the tSZ signal from the observed CMB data has a negligible effect on the large-scale anomalies (Dolag et al., 2005).

The only significant small scale anomaly considered is the cold spot, an anomalous feature at $l = 207.8°, b = -56.3°$. In Chapter 3, we found that removal of the predicted local ISW signal from the CMB can raise the temperature in this region by approximately 7μK. The removal of the tSZ signal in the same region also raises the temperature slightly, but the difference is at the sub-μK level and therefore insignificant in comparison.

4.4.2 Cosmological Parameter Estimation

The tSZ angular power spectrum on scales $\ell \leq 30$ is between 3 and 4 orders of magnitude smaller than the CMB angular power spectrum. This is far too small to significantly affect cosmological parameter estimation. A crude estimate of the χ^2 fit of the WMAP best-fitting cosmological model to the CMB data before and after tSZ removal shows a difference $\Delta\chi^2 = 0.2\%$. The estimate is crude because only the diagonal elements of the Fisher matrix describing the errors on the measurements are used rather than the full matrix which would account for correlations between multipoles. However, the effect of removing the SZ contribution is so small that using a full analysis will not affect the conclusion – that the large-scale tSZ effect has no significant effect on cosmological parameter estimation.

4.5 Discussion

A novel method of predicting the large-scale thermal and kinetic SZ signals from dark matter density and velocity fields alone is presented. Hydrodynamic simulations are used to develop scaling relations which allow gas properties to be assigned to a dark matter distribution whose

density and velocity fields are known on a coarse grid. Evolution of the gas properties is incorporated into the algorithm which is tested on simulation data. It is found to accurately reproduce the thermal and kinetic SZ signals computed from hydrodynamic data and to agree well with analytic predictions of simple physical models. This method is applied to the reconstruction of the local Universe computed in Chapter 2 and used to predict the large-scale tSZ signal. A correction is made to the tSZ prediction to account for the photometric redshift smearing present in the reconstructed density field; this is derived from simulated density fields and mock 2MASS reconstructions. The prediction of the large-scale tSZ effect agrees well statistically with previous estimates; both the power spectrum and mean Compton y-parameter are consistent with results in the literature. The large-scale tSZ effect is found to have a negligible effect on the CMB anomalies and to have no impact on cosmological parameter estimation from the CMB data on these scales.

CHAPTER 5

ISW Detection with 2MASS

As mentioned in Section 1.3.2, the Integrated Sachs-Wolfe (ISW) effect arises due to a net change in the energy of CMB photons as they pass through evolving matter potential wells. There are two forms of the ISW effect – the early ISW effect and the late ISW effect; here we are concerned only with the late ISW effect. A late ISW signal is produced if matter potential wells are currently evolving on large scales, this is not the case in a flat matter dominated universe; however, in a Dark Energy dominated universe (or a closed or open universe), matter potential wells will evolve on the relevant scales and we expect an ISW signal. Since evidence from the CMB points to a flat Universe (Spergel et al., 2006) to within a few percent, detection of the ISW effect provides evidence for Dark Energy.

In this Chapter, we investigate whether the addition of photometric redshifts to the 2MASS data can improve previous inconclusive detections of the ISW effect with this dataset. In Section 5.1, the detection method and the data used are described. In Section 5.2 details of the data analysis are given and finally in Section 5.3 we consider how good an ISW detection experiment we expect this to be.

5.1 Method for Detection

The ISW signal is small and therefore hard to separate from the primary anisotropy signal using CMB temperature maps alone. For this reason, detections of the ISW effect are attempted by

cross-correlating CMB temperature maps with tracers of large scale structure (Crittenden and Turok, 1996). In a ΛCDM Universe, the expected cross-correlation is achromatic and positive at large angular scales i.e. overdensities in the matter distribution should correspond to hotspots in the CMB. Detections of the ISW effect have been reported by many groups using different observations as tracers of the matter distribution e.g. radio sources (Nolta et al., 2004), infra-red (Afshordi et al., 2004), SDSS (Scranton et al., 2003; Fosalba et al., 2003) and X-ray (Boughn and Crittenden, 2005). The significance of the detections ranges from 2σ to 4σ. The WMAP3 CMB data are signal dominated on large scales where the ISW effect is significant (Spergel et al., 2006), meaning that improvement in ISW detection will mainly come from 'better' large scale structure surveys. In Chapter 6, we consider whether 'better' should be deeper or just fainter with a similar $z_{\rm max}$ to current surveys. However, as the ISW effect is a large scale phenomenon, detection significance is fundamentally limited by cosmic variance.

Afshordi et al. (2004) cross-correlated 2MASS with WMAP1 data (Bennett et al., 2003b) claiming an ISW detection at 2.5σ. Recently, updating this work, Rassat et al. (2006, hereafter R06) used the 2MASS XSC catalogue, together with WMAP3 data (Hinshaw et al., 2006) to look for an ISW signal. Dividing their galaxy sample into 4 apparent K-band magnitude ranges, they adopted fits for the redshift distribution of galaxies in each range using the 2MASS K_{20} luminosity function. It has been suggested that an ISW analysis using a galaxy survey such as LSST covering redshifts $0 < z < 3$ divided into photometric redshift bins could place important constraints on the nature of Dark Energy via detection of the ISW effect (Pogosian, 2006). Here we investigate whether adding photometric redshift information to 2MASS and dividing the galaxy sample by these redshifts into three slices of thickness $\Delta z = 0.1$ can boost the significance of any detection. For consistency with R06 and ease of comparison with their results, a cosmological model with $\Omega_m = 0.3$, $h = 0.7$, $\Omega_b = 0.05$, spectral index $n = 1$ and $\sigma_8 = 0.75$ is used in this Chapter.

5.1.1 Data

2MASS

The 2MASS XSC galaxy catalogue is described in Section 2.1. For this analysis it is necessary to exclude regions of the sky where the 2MASS catalogue is unreliable due to galactic extinction. The mask applied to the 2MASS data is the same as that used by R06 (and that

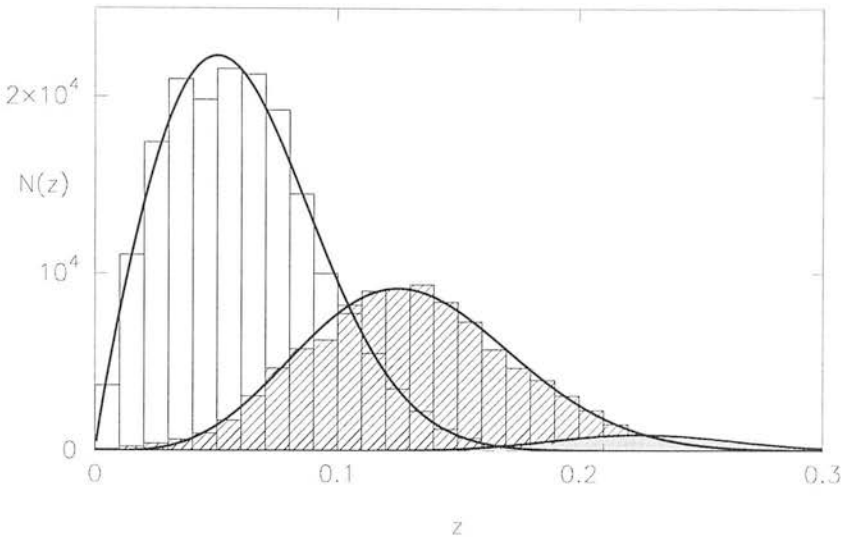

Figure 5.1: The true redshift distribution of galaxies selected by photometric redshift to lie in slices $z = 0.0 - 0.1$, $z = 0.1 - 0.2$ and $z = 0.2 - 0.3$

used for the reconstruction in Chapter 2) and defined by excluding all regions with K-band extinction $A_K > 0.05$ according to the dust maps of Schlegel et al. (1998). Around 27% of the XSC galaxies outside this mask have spectroscopic redshifts. The true redshift distribution for galaxies in each photometric redshift slice used in the analysis can therefore be computed using only galaxies for which spectroscopic information is also available. The redshift distributions are shown in figure 5.1, the fit is calculated assuming a parametrization of the form

$$\frac{dN}{dz} \propto z^{\alpha} \exp\left\{-(z/z_*)^{\beta}\right\}, \tag{5.1}$$

and performing a least squares fit to obtain the distribution parameters. These are given in table 5.1.

A magnitude cut of 12 <K< 13.8 is also applied to the extinction-corrected XSC catalogue in order to ensure that the sky coverage of the galaxies used is uniform. HEALPix[1] (Górski et al., 2005) software is used to generate maps of galaxy overdensity and to compute the spherical harmonic coefficients, $a_{\ell m}$, used in the cross-correlation analysis. Figure 5.2 shows the smoothed galaxy overdensity in the three redshift slices. We note that the artefact mentioned in Section 3.4.2 is again present at $l \simeq 330°$, $b = -15°$ in the highest redshift slice, this is

[1] http://healpix.jpl.nasa.gov

Slice	$N_{\rm gals}$	α	β	z_*
$0.0 < z < 0.1$	451329	0.88	2.24	0.076
$0.1 < z < 0.2$	258673	3.46	2.27	0.104
$0.2 < z < 0.3$	19162	17.4	2.12	0.083

Table 5.1: The redshift distribution of galaxies in each photometric redshift slice is described by equation (5.1). The table gives the number of galaxies and best-fitting values of α, β and z_* for each photometric redshift slice.

discussed further in Section 6.3.

The galaxy bias is expected to vary across the three redshift slices since the furthest redshift shell is only populated by the brightest, most massive galaxies at those redshifts which are known to be more strongly clustered and hence have an increased bias (Park et al., 1994; Loveday et al., 1995). We estimate the bias in each redshift slice using the galaxy angular power spectrum, see Section 5.1.3.

WMAP3

The CMB data used in the analysis are the *foreground reduced* sky maps in the Q, V and W bands and also the Internal Linear Combination (ILC) map. The construction of these maps is such that models for the synchrotron, free-free and dust emission have been subtracted. It is however prudent to mask the WMAP maps at low galactic latitude and the WMAP Kp2 mask is used to this end leaving 85% of the sky unmasked.

The fact that both the galaxy maps and the CMB maps are masked will mean that spherical harmonic coefficients estimated from the maps for use in the cross-correlation calculation will not be exact. The masks cause a loss of sky coverage and introduce correlations between different multipoles

$$\left\langle \delta^{\rm g}_{\rm obs} \delta^{\rm T}_{\rm obs} \right\rangle = \left\langle W^{\rm g} \delta^{\rm g}_{\rm true} W^{\rm T} \delta^{\rm T}_{\rm true} \right\rangle ,$$

where $\delta_{\rm obs}$ is the observed density or temperature field, $\delta_{\rm true}$ is the exact density or temperature field and W is the mask. A full treatment of the masking effects would examine the cross-correlation of the masks and seek to 'undo' the effects of loss of coverage and multipole mixing. This can be achieved under the assumption that the data and masks are independent (Afshordi

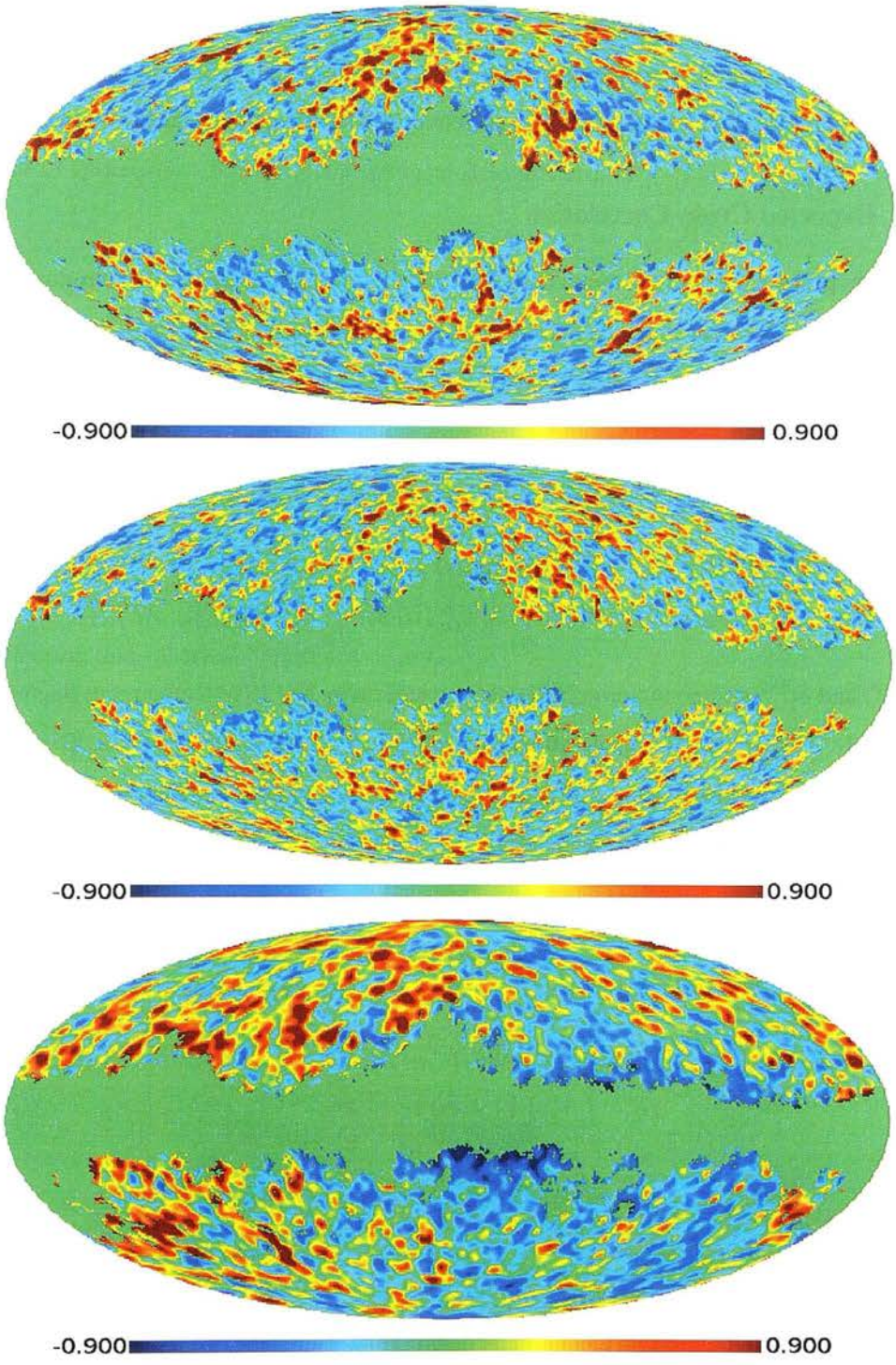

Figure 5.2: Maps of the 2MASS galaxy overdensity in each of the 3 redshift slices considered: $0.0 < z < 0.1$ (top), $0.1 < z < 0.2$ (middle) and $0.2 < z < 0.3$ (bottom). The density field is smoothed with a Gaussian of FWHM = $100'$ for the $z = 0.0 - 0.1$ and $z = 0.1 - 0.2$ slices and of FWHM = $200'$ for the $z = 0.2 - 0.3$ slice.

et al., 2004). In practice compensating for the lack of coverage alone via the factor $f_{\rm sky}$ in equation (5.14) produces very similar results (K. Land, Priv. comm.). A full covariance matrix analysis of the data takes into account any correlations between different multipole bins.

5.1.2 Expected Cross-Correlation

The two hypotheses to be tested are: a null hypothesis where the expected cross-correlation vanishes $C_{\rm gT} = 0$ and a fiducial hypothesis where $C_{\rm gT}$ is as expected in a ΛCDM Universe. Within the context of linear theory, the expected ΛCDM $C_{\rm gT}$ is found by considering the cross-correlation

$$C_{\rm gT}(\ell)\,\delta^{\rm K}_{\ell\ell'}\,\delta^{\rm K}_{mm'} = \langle a^{\rm g}_{\ell m} a^{\rm T*}_{\ell m}\rangle \tag{5.2}$$

$$= \left\langle \int_\Omega \delta_{\rm g}\, Y^*_{\ell m}(\hat{\mathbf{n}})\, d\Omega \int_\Omega \delta^{\rm ISW}_{\rm T}\, Y_{\ell m}(\hat{\mathbf{n}})\, d\Omega \right\rangle, \tag{5.3}$$

where δ_g and $\delta^{\rm ISW}_T$ denote the projected galaxy overdensity and ISW temperature fluctuations respectively, $Y_{\ell m}$ denotes the spherical harmonics and δ^K is the Kronecker delta. To calculate the form of the projected galaxy overdensity it is necessary to integrate the overdensity along the line of sight with appropriate weighting

$$\begin{aligned}
1+\delta_{\rm projected} &= \frac{\text{number of galaxies along line of sight}}{\text{expected number of galaxies along line of sight}} \\
&= \frac{\Delta\Omega \int n(r)\, r^2\, dr}{\Delta\Omega \int \bar{n}(r')\, r'^2\, dr'} \\
&= \frac{\int \bar{n}(r)\, \{1+\delta(r)\}\, r^2\, dr}{\int \bar{n}(r')\, r'^2\, dr'} \\
\Rightarrow \delta_{\rm projected} &= \int \frac{\bar{n}(r)\, r^2}{\int \bar{n}(r')\, r'^2\, dr'}\, \delta(r)\, dr \\
&\equiv \int \Theta(r)\, \delta(r)\, dr.
\end{aligned}$$

Hence,

$$\begin{aligned}
a^{\rm g}_{\ell m} &= \int_\Omega \int \delta_{\rm g}(r)\, \Theta(r)\, Y^*_{\ell m}(\hat{\mathbf{n}})\, dr\, d\Omega \\
&= \int_\Omega Y^*_{\ell m}(\hat{\mathbf{n}}) \int g(r)\, \Theta(r)\, b_g \int \frac{\delta_{\mathbf{k}}}{(2\pi)^3}\, \exp\{i\mathbf{k}\cdot\hat{\mathbf{n}}r\}\, d^3\mathbf{k}\, dr\, d\Omega,
\end{aligned} \tag{5.4}$$

where b_g is the linear bias relation between galaxies and dark matter, $\delta_{\mathbf{k}}$ are the Fourier coefficients of the dark matter density field evaluated today and $\delta_g(r)$ is the three-dimensional galaxy density field. Using Rayleigh's equation, the exponential in equation (5.4) can be re-expressed in terms of spherical harmonics and a spherical Bessel function:

$$\exp\{i\mathbf{k}\cdot\hat{\mathbf{n}}r\} = \sum_{\ell m} 4\pi i^{\ell}\, j_{\ell}(kr)\, Y^{*}_{\ell m}(\hat{\mathbf{k}})\, Y_{\ell m}(\hat{\mathbf{n}}) \tag{5.5}$$

Now, equation (5.4) becomes

$$\begin{aligned} a^{\mathrm{g}}_{\ell m} &= \frac{4\pi b_g}{(2\pi)^3}\sum_{\ell' m'} i^{\ell'}\int_{\Omega} Y^{*}_{\ell m}(\hat{\mathbf{n}})\, Y_{\ell' m'}(\hat{\mathbf{n}})\, d\Omega \int g(r)\,\Theta(r)\int \delta_{\mathbf{k}}\, j_{\ell'}(kr)\, Y^{*}_{\ell' m'}(\hat{\mathbf{k}})\, d^3\mathbf{k}\, dr \\ &= \frac{4\pi b_g i^{\ell}}{(2\pi)^3}\int g(r)\,\Theta(r)\int \delta_{\mathbf{k}}\, j_{\ell}(kr)\, Y^{*}_{\ell m}(\hat{\mathbf{k}})\, d^3\mathbf{k}\, dr \end{aligned} \tag{5.6}$$

remembering that spherical harmonics satisfy

$$\int_{\Omega} Y_{\ell m}(\hat{\mathbf{n}})\, Y^{*}_{\ell' m'}(\hat{\mathbf{n}})\, d\Omega = \delta^{\mathrm{K}}_{\ell\ell'}\,\delta^{\mathrm{K}}_{mm'}.$$

Similarly, we can consider the temperature distribution:

$$\begin{aligned} a^{\mathrm{T}}_{\ell m} &= \int_{\Omega} \Delta T^{\mathrm{ISW}} Y^{*}_{\ell m}(\hat{\mathbf{n}})\, d\Omega \\ &= \int_{\Omega} T_{\mathrm{CMB}}\left(2\int_0^{r(z_{\mathrm{LS}})}\frac{\dot{\Phi}}{c^3}\, a(r)\, dr\right) Y^{*}_{\ell m}(\hat{\mathbf{n}})\, d\Omega \\ &= \frac{2T_{\mathrm{CMB}}}{c^3}\int_{\Omega} Y^{*}_{\ell m}(\hat{\mathbf{n}})\int a(r)\int \dot{\Phi}_{\mathbf{k}}\,\exp\{i\mathbf{k}\cdot\hat{\mathbf{n}}r\}\,\frac{d^3\mathbf{k}}{(2\pi)^3}\, dr\, d\Omega \\ &= \frac{-3H_0^2\Omega_{m,0}T_{\mathrm{CMB}}}{c^3}\int_{\Omega} Y^{*}_{\ell m}(\hat{\mathbf{n}})\int a(r)\left[\frac{\dot{g}}{a}\right]\int \frac{\delta_{\mathbf{k}}}{k^2}\,\exp\{i\mathbf{k}\cdot\hat{\mathbf{n}}r\}\,\frac{d^3\mathbf{k}}{(2\pi)^3}\, dr\, d\Omega \end{aligned}$$

recalling Poisson's equation (1.15) to relate gravitational potential to density. Here $\delta_{\mathbf{k}}$ are the Fourier coefficients of the dark matter density field evaluated today. Once again Rayleigh's equation (5.5) is used to re-express the exponential

$$a^{\mathrm{T}}_{\ell m} = \frac{-12\pi i^{\ell} H_0^2\Omega_{m,0}T_{\mathrm{CMB}}}{c^3(2\pi)^3}\int a(r)\left[\frac{\dot{g}}{a}\right]\int \frac{\delta_{\mathbf{k}}}{k^2}\, j_{\ell}(kr)\, Y^{*}_{\ell m}(\hat{\mathbf{k}})\, d^3\mathbf{k}\, dr. \tag{5.7}$$

Now we use equations (5.6) and (5.7) together with (5.2) to obtain:

$$
\begin{aligned}
C_{\mathrm{gT}}(\ell) &= \frac{-48\pi^2 H_0^2 \Omega_{m,0} b_g T_{\mathrm{CMB}} i^\ell (-i)^{\ell'}}{c^3 (2\pi)^6} \left\langle \int dr\; g(r)\, \Theta(r) \int d\bar{r}\; a(\bar{r}) \left[\frac{\dot{g}}{a}\right] \right. \\
&\quad \left. \times \int\int \delta_{\mathbf{k}}\, \delta^*_{\mathbf{k}'}\, j_\ell(kr)\, j_{\ell'}(k'\bar{r})\, Y_{\ell m}(\hat{\mathbf{k}}) Y^*_{\ell' m'}(\hat{\mathbf{k}}')\, \frac{d^3\mathbf{k}'}{k'^2}\, d^3\mathbf{k} \right\rangle \\
&= \frac{-48\pi^2 H_0^2 \Omega_{m,0} b_g T_{\mathrm{CMB}} i^\ell (-i)^{\ell'}}{c^3 (2\pi)^3} \int dr\; g(r)\, \Theta(r) \int d\bar{r}\; a(\bar{r}) \left[\frac{\dot{g}}{a}\right] \\
&\quad \times \int\int P(k)\, j_\ell(kr)\, j_{\ell'}(k\bar{r})\, Y_{\ell m}(\hat{\mathbf{k}}) Y^*_{\ell' m'}(\hat{\mathbf{k}})\, \frac{d^3\mathbf{k}}{k^2} \\
&= \frac{-48\pi^2 H_0^2 \Omega_{m,0} b_g T_{\mathrm{CMB}}}{c^3 (2\pi)^3} \int g(r)\, \Theta(r) \int a(\bar{r}) \left[\frac{\dot{g}}{a}\right] \int P(k)\, j_\ell(kr)\, j_\ell(k\bar{r})\; dk\; d\bar{r}\; dr \\
&= \frac{-6 H_0^2 \Omega_{m,0} b_g T_{\mathrm{CMB}}}{\pi c^3} \int dk\; P(k) \int Hg(f-1)\, j_\ell(k\bar{r})\; d\bar{r} \int g(r)\, \Theta(r)\, j_\ell(kr)\; dr \qquad (5.8)
\end{aligned}
$$

where f is the growth function defined in equation (1.25). For small angular scales ($\ell \gtrsim 10$) the *Limber* equation can be used to re-express the spherical Bessel functions:

$$\lim_{\ell\to\infty} j_\ell(x) = \sqrt{\frac{\pi}{2\ell+1}}\, \delta^{\mathrm{K}}(\ell + 1/2 - x)$$

this gives:

$$C_{\mathrm{gT}}(\ell) = \frac{-3H_0^2 \Omega_{m,0} b_g}{(\ell+1/2)^2 c^3} \int P\left(\frac{\ell+1/2}{r}\right) \Theta(r)\, g^2(r)\, H(r)\, (f-1)\; dr \qquad (5.9)$$

Figure 5.3 shows the expected cross-correlation signal in each of the three redshift slices considered for a constant bias in each slice $b = 1.4$. The peak of the cross-correlation signal shifts to higher multipoles as the redshift increases, this is due to the peak of the matter power spectrum shifting to smaller angular scales (a given physical scale will subtend a smaller angle the further away it is).

Following an exactly analogous method, the galaxy angular power spectrum C_{gg} is

$$C_{\mathrm{gg}}(\ell) = \frac{2b^2}{\pi} \int dk\; k^2 P_{\delta\delta}(k) \left| \int dr\; g\, \Theta(r)\, j_\ell(kr) \right|^2 \qquad (5.10)$$

or on applying the Limber approximation (Kaiser, 1992),

$$C_{\mathrm{gg}}(\ell) = b^2 \int dr\; \frac{\Theta^2}{r^2} g^2 P\left(\frac{\ell+1/2}{r}\right). \qquad (5.11)$$

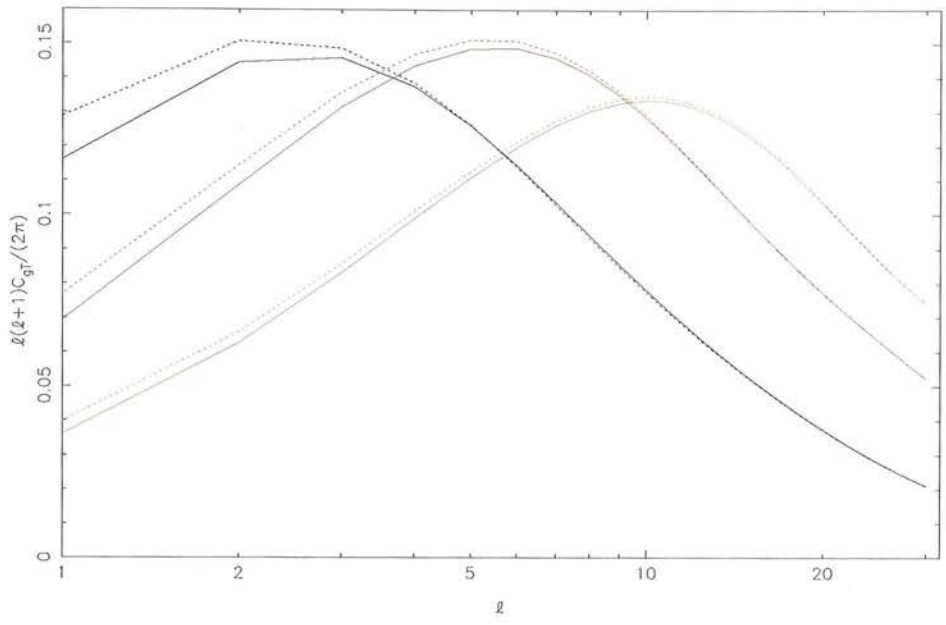

Figure 5.3: The expected cross-correlation signal in μK for each of the 3 redshift slices $0.0 < z < 0.1$ (black), $0.1 < z < 0.2$ (red) and $0.2 < z < 0.3$ (green) assuming a constant bias $b = 1.4$ in each. The Limber approximation (dashed lines) and exact (solid lines) signals are plotted. The peak of the cross-correlation shifts to higher multipoles for higher redshift slices.

5.1.3 Estimating the Bias

In order to determine the bias in each redshift slice, the galaxy angular power spectra are used. The form of the angular power spectrum in each slice can be predicted given a three-dimensional power spectrum using equations (5.10) and (5.11). The bias of the predicted spectrum can then be adjusted to match observations, assuming a constant bias within each slice. In linear theory, bias cannot be determined independently of σ_8 which also acts to renormalize the power spectrum, $C_\ell \propto (b\sigma_8)^2$. In what follows, we therefore fix the value of σ_8 at 0.75 and fit only for b.

CAMB (Lewis et al., 2000) is used to generate non-linear matter power spectra for the cosmological model used here and output the three-dimensional spectra at redshifts at the mid-point of each redshift shell in question. Although only strictly valid in linear theory, we evolve the non-linear power spectrum for each slice according to the growth function, this is thought to be a good approximation to the non-linear power spectrum on the linear and quasi-linear scales where we will fit for the bias. There are two sources of data which can be used to measure the angular power in each redshift slice: the photometric redshift data and the subset

	$0.0 < z < 0.1$	$0.1 < z < 0.2$	$0.2 < z < 0.3$
photo-z only	1.22	1.65	2.86
with SDSS	1.03	1.90	2.22

Table 5.2: Best fit values for the bias calculated using the photometric redshift data only and the photometric data replaced by SDSS data in bins where the latter is accurate.

of this in the SDSS region with spectroscopic redshifts. Since the spectroscopic data exists only in a subregion, the angular power measured using this data will not be accurate on large scales. However, we expect reasonable agreement between the photometric angular power and the spectroscopic angular power on smaller scales, up to differences due to sample variance and mask. Figure 5.4 shows the shot noise corrected photometric and spectroscopic angular power spectra binned for $\ell \leq 60$ in bins of width $\Delta\ell = 10$ and the best fit predicted spectra for each of the redshift slices.

The fit is made using a maximum likelihood approach where the error bars are due to cosmic variance alone and are calculated from the model power spectra rather than the data. The likelihood is

$$\mathcal{L} \propto |\mathrm{M}|^{-1/2} \exp\{-(\mathrm{d}^{\mathrm{T}}\mathrm{M}^{-1}\mathrm{d})/2\}, \tag{5.12}$$

assuming the covariance matrix M to be diagonal and therefore neglecting correlations between multipole bins (Blake et al., 2007). The vector d is of differences between model and data, $d_i = C_{\mathrm{gg}}^{\mathrm{model}} - C_{\mathrm{gg}}^{\mathrm{data}}$ in each bin, and the diagonal elements of M are

$$\sigma(C_{\mathrm{gg}}) = \sqrt{\frac{2}{f_{\mathrm{sky}}(2\ell+1)}}\, C_{\mathrm{gg}}. \tag{5.13}$$

The fit is performed firstly for the photometric redshift data alone and secondly for the spectroscopic data only. Both datasets show a trend of increasing bias with redshift so we can be confident that this is a real effect. The best-fitting values for the bias are given in table 5.2.

5.2 Cross-Correlation Analysis

When detecting the ISW effect we are looking to choose between two hypotheses, one with no ISW effect and one with expected ISW signal given by our chosen cosmological model.

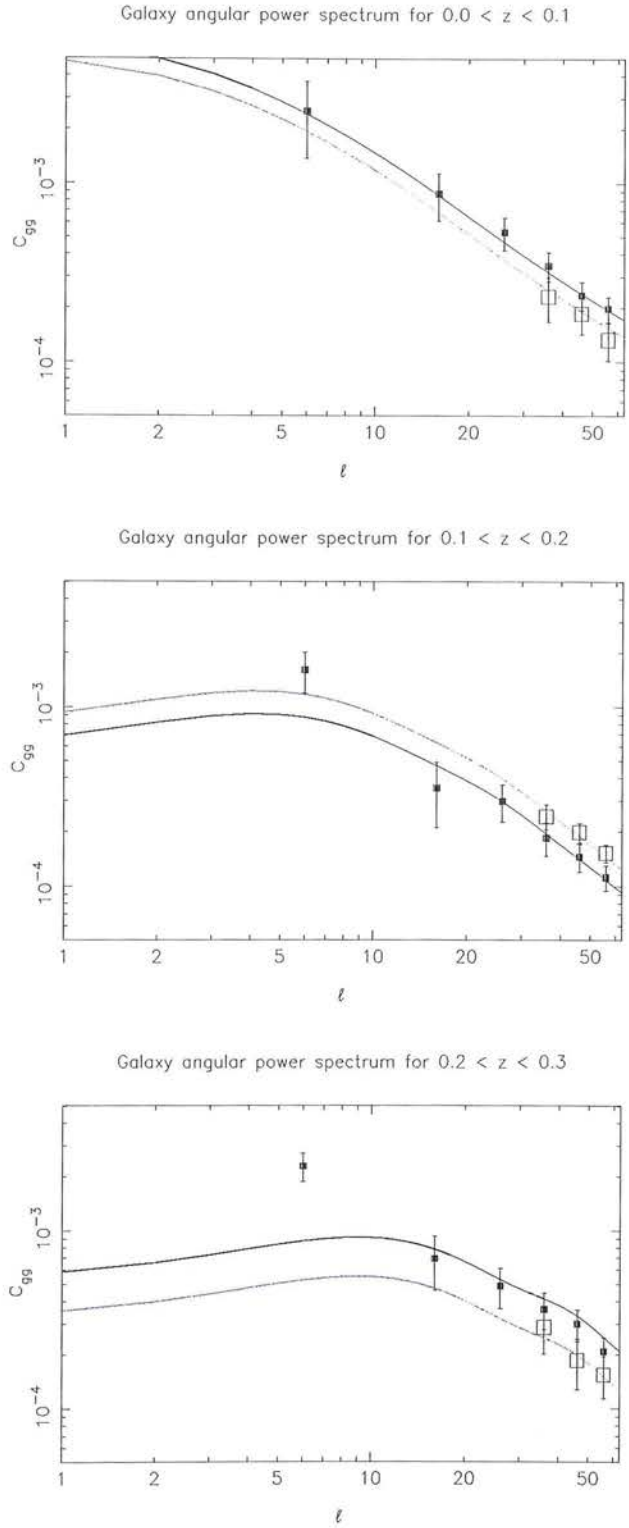

Figure 5.4: Fits to the measured galaxy angular power spectra in each redshift slice used to determine the bias. The black line and solid points are fits to the photometric data only; the blue line and open points are for the spectroscopic data only. Error bars are calculated for the model spectrum.

The null hypothesis used here will be of no ISW effect – that the cross correlation $C_{\mathrm{gT}}(\ell)$ is zero for all multipoles. The fiducial hypothesis to be tested is that of the cross-correlation that would be expected in a ΛCDM Universe which is calculated using linear theory, see Section 5.1.2. The next step is to look to see whether the cross correlations calculated from the data with appropriate error bars support the null hypothesis or lead to its rejection.

As the ISW effect is a large scale signal, multipoles $3 \leq \ell \leq 30$ are used in the analysis, consistent with R06. The cross-correlation signal from these multipoles is binned into 5 logarithmically spaced bins. The data in these bins will be correlated due to the use of masks on all the maps considered; there may also be correlations between different redshift slices due to inaccuracies in photometric redshifts causing galaxies from the same structure at the same redshift to be placed in different slices. To account for such correlations, a full covariance matrix is computed to calculate the χ^2 statistics which will be used to indicate the likelihood of each of the hypotheses. A likelihood ratio test is then used to investigate whether one hypothesis is strongly preferred over the other given current data and a cosmological model.

The cross-correlation for a pair of galaxy and temperature maps is calculated using

$$C_{\mathrm{gT}} = \frac{1}{(2\ell+1)} \sum_{m=-\ell}^{\ell} \frac{a^{\mathrm{g}}_{\ell m}}{\sqrt{f^{\mathrm{g}}_{\mathrm{sky}}}} \frac{a^{\mathrm{T}*}_{\ell m}}{\sqrt{f^{\mathrm{T}}_{\mathrm{sky}}}} \tag{5.14}$$

where the f_{sky} factors describe the fraction of the sky that is outside the mask and therefore attempt to compensate for the loss of sky coverage due to the masks. The cross-correlations measured in each redshift slice for each of the WMAP bands are shown in figure 5.5. The signal is the same for each of the CMB maps considered, i.e. it is achromatic, as expected for the ISW effect.

The χ^2 statistic for each hypothesis is calculated via

$$\chi^2 = \sum_{i,j} d_i \, (C^{-1})_{ij} \, d_j \tag{5.15}$$

where C_{ij} is the covariance matrix calculated from simulations of the data, see Section 5.2.1. The d_i are values of $(C^{\mathrm{data}}_{\mathrm{gT},i} - C^{\mathrm{hyp}}_{\mathrm{gT},i})$, where $C^{\mathrm{data}}_{\mathrm{gT},i}$ are the cross-correlation values measured from the 2MASS and WMAP data and i labels the binned measurements. For the null hypothesis, $C^{\mathrm{hyp}}_{\mathrm{gT},i} = 0$; for the fiducial hypothesis $C^{\mathrm{hyp}}_{\mathrm{gT},i}$ is given by equations (5.8) and (5.9).

The likelihood of each hypothesis is determined using

$$\mathcal{L} \propto |C|^{-1/2} \exp\left\{-(\mathbf{d}^{\mathrm{T}} C^{-1} \mathbf{d})/2\right\}, \tag{5.16}$$

with $\mathbf{d}$ the data vector whose components are defined above and C the covariance matrix. Then

$$-2 \log\left\{\frac{\mathcal{L}_1}{\mathcal{L}_2}\right\} = \Delta\chi^2, \tag{5.17}$$

where $\mathcal{L}_1$ and $\mathcal{L}_2$ are the likelihoods for the two hypotheses. The covariance matrix used in each case is calculated from simulations of the null hypothesis, since this is what we are seeking to reject.

5.2.1 Covariance Matrix Estimation

500 simulations of independent CMB and galaxy density fields are used to estimate the covariance matrix. Reducing this number to 250 does not have a significant effect on the results (χ^2 values change by < 0.1) and therefore the number of simulations is adequate for our purposes. The power spectrum used for the CMB Gaussian realizations is the best-fitting theoretical angular power spectrum found by the WMAP team (Spergel et al., 2006). The fact that the CMB simulations used to estimate the covariance matrix contain no ISW signal means that we are quantifying the degree of scatter that one would expect in the correlations if there were no ISW effect, large scatters will act to reduce the χ^2 values.

Simulations of the galaxy density fields are generated by assuming a lognormal form for the measured 2MASS density field (Coles and Jones, 1991)

$$1 + \delta_{\mathrm{LN}} = \exp(\delta_{\mathrm{G}} - \sigma^2/2), \tag{5.18}$$

where δ_G is an underlying Gaussian field with zero mean and variance σ^2. The relation

$$1 + \xi_{\mathrm{LN}} = e^{\xi_{\mathrm{G}}} \tag{5.19}$$

allows us to calculate the variance of the underlying Gaussian density field corresponding to the 2MASS data. Using equation (5.18) the Gaussian density fields corresponding to each of the observed lognormal density fields in our 3 redshift slices are calculated. The pixelisation used at this stage is coarse enough to ensure that there are no pixels with $\delta_{\mathrm{pix}} = -1$ where δ_{G} would be ill-defined. For each of these Gaussian density fields, the angular power spectrum

can be calculated and corrected for shot noise; a series of Gaussian fields with the same power spectrum can then be generated. These fields have the same pixelisation as was used to calculate the original Gaussian fields. For each simulated Gaussian density field, equation (5.18) is used to convert back to a lognormal density field. Galaxies are positioned by Poisson sampling this density field using the expected number of galaxies from the 2MASS data. We then have a set of simulated CMB and 2MASS galaxy maps with the same shot noise properties as the data. These maps can be analysed in exactly the same way as the data to compute simulated cross-correlations and allow us to estimate the error bars on the data measurements. The measured V band cross-correlation and the error bars on each data point calculated from simulation are shown in figure 5.5.

The covariance matrix is estimated from the simulated data

$$C_{ij} = \langle (d_i - \langle d_i \rangle)(d_j - \langle d_j \rangle) \rangle \,, \tag{5.20}$$

where for a particular pair of simulated maps (CMB and galaxy) $d_i = C^{\rm sim}_{{\rm gT},i} - C^{\rm hyp}_{{\rm gT},i}$. Here i refers to the bin in question, $C^{\rm sim}_{\rm gT}$ is the cross-correlation from the simulated maps and $C^{\rm hyp}_{\rm gT}$ is the cross-correlation expected for the hypothesis in question.

5.2.2 Results

Plotting the cross-correlation data in each of the redshift slices together with error bounds on the null hypothesis it is immediately obvious that the null hypothesis will not be conclusively rejected with this analysis (see figure 5.5). The error bars are large at low redshift due to cosmic variance, as we move to higher redshifts, cosmic variance decreases but shot noise increases.

χ^2 values for each hypothesis are computed using the different WMAP band temperature maps and a selection of bias values. The results are given in tables 5.3, 5.4 and 5.5 for bias values computed from photometric data only, SDSS data only and for $b = 1.4$ consistent with R06 respectively. Each table has data for each redshift slice and for an analysis of all three slices together. As can be seen from the tables, there is some dependence on the values adopted for the bias in each slice. This does not affect the covariance matrix because the data are used to compute the power spectra for generation of simulations of the galaxy data. Values for the bias only affect the final χ^2 results through an alteration of the expected $C_{\rm gT}$ signal.

We see that in general, the χ^2 results are low for the number of degrees of freedom, this is

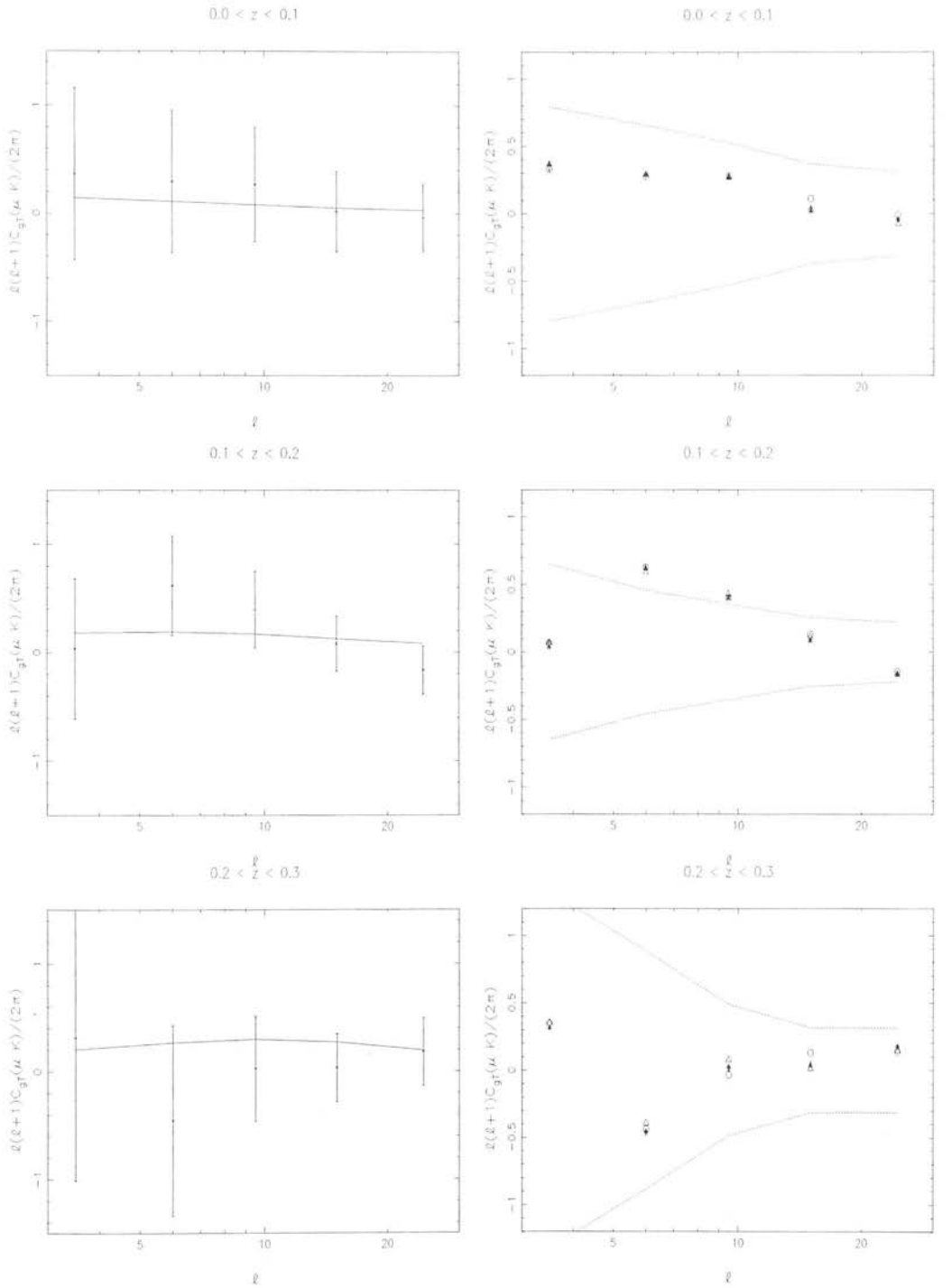

Figure 5.5: (*Left*) The cross-correlations for the V-band CMB data in the different redshift slices. Error bars are calculated from simulated CMB skies and 2MASS galaxy maps. (*Right*) The cross-correlation results using all the WMAP3 data: ILC (open triangle), Q (open circle), V (star) and W (filled triangle). The achromatic nature of the signal is expected for the ISW effect. The error bounds on the null hypothesis show that the data will not strongly reject it.

	$0.0 < z < 0.1$		$0.1 < z < 0.2$		$0.2 < z < 0.3$		$0.0 < z < 0.3$		
WMAP Band	$\chi^2_{\rm null}$	$\chi^2_{\rm fid}$	$\chi^2_{\rm null}$	$\chi^2_{\rm fid}$	$\chi^2_{\rm null}$	$\chi^2_{\rm fid}$	$\chi^2_{\rm null}$	$\chi^2_{\rm fid}$	$\Delta\chi^2$
ILC	0.70	0.41	3.8	2.6	0.52	1.3	5.0	4.3	0.7
Q	0.68	0.32	3.7	2.5	0.68	1.2	5.1	3.9	1.2
V	0.63	0.33	3.9	2.8	0.65	1.4	5.2	4.4	0.8
W	0.63	0.33	3.6	2.6	0.67	1.3	4.9	4.3	0.6

Table 5.3: χ^2 values for the two hypotheses for each WMAP band analysed. The first three sections of the table show the χ^2 values for the three redshift slices separately, the final section of the table shows χ^2 and $\Delta\chi^2$ values for the entire dataset. We see that the first two redshift slices prefer a ΛCDM ISW signal whilst the third prefers the null hypothesis. The whole dataset prefers a ΛCDM ISW signal. The significance of this result is discussed in 5.2.2.

	$0.0 < z < 0.1$		$0.1 < z < 0.2$		$0.2 < z < 0.3$		$0.0 < z < 0.3$		
WMAP Band	$\chi^2_{\rm null}$	$\chi^2_{\rm fid}$	$\chi^2_{\rm null}$	$\chi^2_{\rm fid}$	$\chi^2_{\rm null}$	$\chi^2_{\rm fid}$	$\chi^2_{\rm null}$	$\chi^2_{\rm fid}$	$\Delta\chi^2$
ILC	0.70	0.44	3.8	2.6	0.52	0.86	5.0	3.9	1.1
Q	0.68	0.36	3.7	2.4	0.68	0.82	5.1	3.5	1.6
V	0.63	0.37	3.9	2.7	0.65	0.96	5.2	4.0	1.2
W	0.63	0.37	3.6	2.6	0.67	0.96	4.9	3.9	1.0

Table 5.4: As above except that bias values in the three redshift slices are calculated using spectroscopic measurements of the angular power spectrum (see Section 5.2.2).

	$0.0 < z < 0.1$		$0.1 < z < 0.2$		$0.2 < z < 0.3$		$0.0 < z < 0.3$		
WMAP Band	$\chi^2_{\rm null}$	$\chi^2_{\rm fid}$	$\chi^2_{\rm null}$	$\chi^2_{\rm fid}$	$\chi^2_{\rm null}$	$\chi^2_{\rm fid}$	$\chi^2_{\rm null}$	$\chi^2_{\rm fid}$	$\Delta\chi^2$
ILC	0.70	0.38	3.8	2.7	0.52	0.55	5.0	3.6	1.4
Q	0.68	0.28	3.7	2.6	0.68	0.58	5.1	3.4	1.7
V	0.63	0.30	3.9	2.8	0.65	0.65	5.2	3.6	1.6
W	0.63	0.30	3.6	2.7	0.67	0.67	4.9	3.8	1.1

Table 5.5: As above but assuming a constant bias $b = 1.4$ in all three redshift slices as in R06.

also noted by R06. We would expect values around $\chi^2 \sim 5 \pm \sqrt{10}$ for the individual redshift slices and $\chi^2 \sim 15 \pm \sqrt{30}$ for the analysis of all slices together, but only the second redshift slice gives χ^2 values that fall within these expected ranges. The usual reason for 'too good' a χ^2 fit is an over-estimation of the measurement errors. However, an analytic estimation of the error bars (Afshordi et al., 2004)

$$\sigma^2(C_{\rm gT}) = \frac{1}{f_{\rm sky}(2\ell+1)}(C_{\rm gT}^2 + C_{\rm gg}C_{\rm TT}), \tag{5.21}$$

suggests errors that are even larger than those used here (except for the lowest ℓ bin in the third redshift slice), so over-estimation seems unlikely.

As mentioned above, the data are consistent with no ISW effect. However, the difference in the χ^2 values for each hypothesis gives an indication of how much one hypothesis is preferred over another. For the total analysis using the biases calculated from the photometric data alone, $\Delta\chi^2 = \chi^2_{\rm null} - \chi^2_{\rm fid} \sim 0.825$ which translates to a likelihood ratio of

$$\frac{L({\rm ISW}|{\rm data})}{L({\rm no\ ISW}|{\rm data})} \sim e^{0.41} \sim 1.5 \tag{5.22}$$

i.e. the fiducial hypothesis is preferred at a level of around $1.5 : 1$. This is a long way from decisive evidence for the ISW effect. Using the other bias values we prefer the fiducial hypothesis at levels of $1.8 : 1$ and $2.1 : 1$ for the SDSS biases and $b = 1.4$ respectively. This latter scenario ($b = 1.4$) is used by R06 and we find $\Delta\chi^2$ values very similar to their results in this case: $\Delta\chi^2 \simeq 1.5$ against their $\Delta\chi^2 \simeq 1.6$. The differences in our analyses are the use of photometric redshifts on our part to bin the data into redshift slices, a slightly different magnitude cut $12 < K < 13.8$ rather than $12 < K < 14$ and our use of simulations of the galaxy data as well as the CMB data to compute the error bars. We would expect the error bars we use in our analysis to be larger and our χ^2 values to therefore be smaller as indeed is the case. There is certainly no great improvement in the detection from the use of photometric redshifts here. In Section 5.3.1, we look to see how powerful we would *expect* this method to be in terms of discriminating between the two hypotheses.

5.3 Statistical Power of ISW Detection Surveys

On the scales of the ISW effect, the CMB data are already signal dominated (Spergel et al., 2006). To improve the significance of any ISW detection from this method we therefore need

improved large scale structure data. In Section 5.3.1 a measure of the ability of a survey to detect an ISW effect is defined and applied to the 2MASS experiment described above. Following on from this, in Chapter 6 improved large scale structure surveys and their ISW detection prospects are considered. In particular, we will investigate the effect of increasing the number of galaxies in the sample (for example, by using a fainter magnitude limit, see Section 6.1.1) and the effect of increasing the depth of the survey i.e. adding more redshift slices, see Section 6.1.2.

5.3.1 Statistical Power of 2MASS

From the simulation data which is used in the above analysis to estimate the covariance matrix we can compute another useful set of statistics. By treating the simulated results as 'data' and passing these 'data' C_{gT} values through the χ^2 calculation apparatus a distribution of $\Delta\chi^2 = \chi^2_{\mathrm{null}} - \chi^2_{\mathrm{fid}}$ values for the simulated maps is found. Since the simulated CMB skies are Gaussian and have no ISW signal, the distribution of $\Delta\chi^2$ values that we calculate will indicate the distribution of $\Delta\chi^2$ values we would expect if the null hypothesis were true i.e. the distribution

$$P(\Delta\chi^2 = x | H_0 \text{ true}). \tag{5.23}$$

Here $\Delta\chi^2$ is a statistic computed in the knowledge of both H_0 and H_1 but *under the assumption that H_0 is true*.

Now we can consider repeating this process but this time for each pair of simulated maps (galaxy density and CMB) adding the expected ISW signal calculated from the galaxy map to the CMB map. The expected ISW signal in each redshift slice can be estimated via (see Section 3.4.2)

$$\frac{\Delta T^{\mathrm{ISW}}_{\ell m}}{T_{\mathrm{CMB}}} = \frac{3H_0^2\Omega_{m,0}}{\ell(\ell+1)c^3}\left(1 + \frac{(1+\bar{z})\,g'(\bar{z})}{g(\bar{z})}\right) r^2(\bar{z})\,H(\bar{z})\,\Delta r\,\frac{\delta_{\ell m}}{b_g} \tag{5.24}$$

where $\bar{z}$ is the redshift at the midpoint of the slice, δ is the projected galaxy density field in that slice and Δr is the width of the slice. This creates a dataset where the the ISW effect that we expect is included in the CMB maps. On passing this data through the χ^2 apparatus, we obtain the distribution of $\Delta\chi^2$ values that we would expect if the alternative hypothesis of ISW effect as expected in a ΛCDM Universe is true. Since we perform hypothesis tests under the

assumption that the null hypothesis is true, the covariance matrix that is used here is the same as above i.e. calculated from the simulations of the null hypothesis. These two distributions[2] are plotted in figure 5.6 for the redshift shells individually and for the entire dataset.

To compare the detection prospects of a number of surveys, a measure of the likelihood of correct ISW detection for a survey is defined called the 'Optimal Power'. The *power* of a statistical test is the probability that the alternative hypothesis will be accepted when it is true

$$\text{power} = 1 - P(s_*), \tag{5.25}$$

where $P(s_*)$ is the probability of making a Type II error (of accepting the null hypothesis when in fact the alternative is true). The $\Delta\chi^2$ distributions can be used to compute the probabilities of making Type I and II errors as a function of threshold for rejection of the null hypothesis. The 'Optimal Power' is the statistical power of an experiment evaluated at the threshold which gives equal probabilities of making Type I and II errors.

In the context of the $\Delta\chi^2$ histograms shown in figure 5.6, a powerful statistical test would see that data clearly offset from each other with little overlap between them. This reduces the chance of making Type I and II errors since fewer measured $\Delta\chi^2$ values would be fairly likely to be found under both of the hypotheses. Unsurprisingly, given the inconclusive results calculated in Section 5.2.2, we see very little offset between the distributions for the 2MASS experiment.

Studying figure 5.6 more closely, we note that as we move to higher redshift slices, the peaks of the $\Delta\chi^2$ distributions separate slightly, although the effect is small. We also see that the histograms for the third redshift slice are broader, this is due to shot noise. The final panel – an analysis of the whole 2MASS dataset together – reveals that if the alternative hypothesis were true, only for very large $\Delta\chi^2$ values would the null hypothesis be confidently rejected. A threshold in $\Delta\chi^2$ of 15 for example would gave a 5% chance of a Type I error, which is acceptable, but would only be observed $\sim 8\%$ of the time in a ΛCDM universe. If one were to use the Jeffreys' criterion of $\Delta\chi^2 > 5$ constituting 'strong' evidence for rejection of the null hypothesis, then 23% of the time this would result in a Type I error. The Optimal Power for the 2MASS experiment using the full dataset is $\Upsilon = 0.54$.

[2]By using simulations to determine a probability distribution for $\Delta\chi^2$ under the assumption of two different hypotheses, we are taking a frequentist approach to the problem. This approach, rather than a Bayesian methodology, will be used throughout the remainder of this Chapter and in Section 6.1.

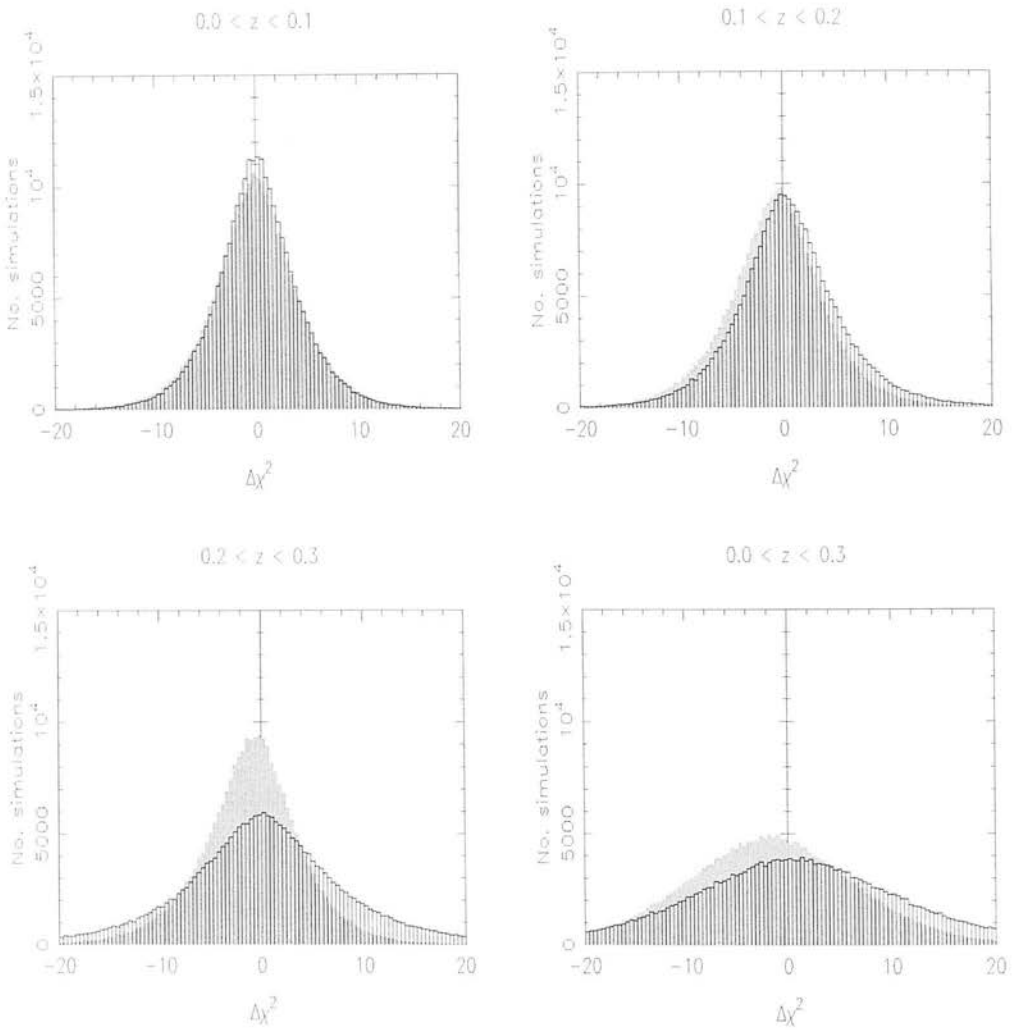

Figure 5.6: The filled histograms shows the values of $\Delta\chi^2$ calculated from simulation for the null hypothesis; the outline histograms are for the values of $\Delta\chi^2$ from the alternative hypothesis. Since $\Delta\chi^2 = \chi^2_{\rm null} - \chi^2_{\Lambda CDM}$, a survey with good ISW detection prospects would be expected to generate positive $\Delta\chi^2$ values if the ΛCDM hypothesis is correct and negative values if the null hypothesis is correct. Histograms are plotted for $0.0 < z < 0.1$ (top left), $0.1 < z < 0.2$ (top right), $0.2 < z < 0.3$ (bottom left) and the full data set $0.0 < z < 0.3$ (bottom right). We see little offset in the $\Delta\chi^2$ distributions in all cases.

5.4 Discussion

An attempt was made to detect the ISW effect by cross-correlating photometric galaxy data from 2MASS with WMAP3 CMB data; the results are inconclusive with a weak preference for a ΛCDM ISW signal over that of no signal arising from a likelihood ratio test. Having investigated the detection prospects of 2MASS, the non-detection of the ISW effect is unsurprising. An experiment such as 2MASS has little statistical power for such a detection and in fact, even if the results obtained from the cross-correlation analysis had been more conclusive, these should have been treated with caution. Investigation of the detection prospects of this experiment reveals that there is a high probability of making a Type I error with this data. If we take $\Delta\chi^2 > 5$, as indicating 'strong' evidence for the ISW effect, this data will lead one to make a Type I error 23% of the time. It is interesting to consider how 'good' a large scale structure survey of this type would need to be to decisively detect the ISW effect. In Chapter 6, three possible surveys which extend 2MASS are considered and the detection prospects of each are analysed using the methodology outlined here.

Given the results of Chapter 3, where we saw that removal of the predicted local ISW signal could have a significant effect on the significance of reported anomalies in the large scale CMB signature, it may seem strange that the ISW effect is not conclusively detected. This can be explained, at least in part, by the fact that only multipoles $\ell \geq 3$ are used in this Chapter in the ISW detection analysis whereas it is mainly the $\ell = 2$ quadrupole whose subtraction causes the the greatest change with regard to the detected significance of anomalies in Chapter 3. For this reason, it is especially important that the robustness of the low multipoles of the recovered density field is investigated for possible effects caused by differences in calibrating spectroscopy across the sky, before strong conclusions are drawn about the ability of the local ISW effect to explain the CMB anomalies.

CHAPTER 6

Future Prospects and Conclusions

A photometric redshift dataset taken from the 2MASS XSC has been used to reconstruct the local density field and to predict local large-scale secondary anisotropies in the CMB. In Chapter 5 an attempt was made to detect the ISW effect using 2MASS data with little success, it is therefore interesting to consider the prospects of future surveys both for building on the reconstruction work presented in this thesis and for detection of these CMB foregrounds. In Section 6.1, hypothetical photometric redshift surveys are considered with regard to their ISW detection prospects and evaluated in terms of the Optimal Power defined in Section 5.3.1. In Section 6.2, the large scale tSZ detection prospects of *Planck* are addressed. This signal has yet to be detected, as WMAP has only been able to place upper limits on the effect (Hansen et al., 2005). Cold regions near the mask are analysed in more detail in Section 6.3 and in Section 6.4, an evaluation of this PhD project is presented. Finally, in Section 6.5, extensions to the work presented in this thesis are discussed.

6.1 ISW Detection Prospects of Future Surveys

In Chapter 5, we saw that 2MASS is not expected to be a successful ISW experiment and in light of this, rather unsurprisingly, failed to find any substantial evidence of an ISW signal with this data. Inspired by this result, we now consider hypothetical photometric redshift surveys with fainter magnitude limits and deeper coverage than 2MASS and evaluate their ability to

detect the ISW effect. In Section 6.1.1, a survey which is otherwise identical to 2MASS but which observes more galaxies near the redshift limit $z \lesssim 0.3$ is considered before deeper surveys are investigated in Section 6.1.2. The 'best possible' ISW detection experiment that one could envisage is studied in Section 6.1.3 and finally conclusions are drawn about the suitability of such surveys for ISW detection and the implications of the results of the 'best possible' survey for claimed ISW detections.

6.1.1 2MASS with a Fainter Magnitude Limit

Consider a survey with the same parameters as 2MASS but which has a fainter magnitude limit and therefore observes more galaxies at higher redshift. To determine the numbers of galaxies observed in such a survey above $z = 0.1$, the comoving number density of galaxies observed by 2MASS for $z < 0.1$, $n_{\rm com}$, is taken as constant and indicative of the 'true' number density of galaxies at higher redshift. It is also assumed that if all these galaxies were observed, the bias in the higher redshift slices would become equal to that measured in the lowest redshift slice for 2MASS. This is consistent with the assumption that the evolution in bias measured in Section 5.1.3 is entirely due to the fact that only the brightest, most massive galaxies are observed at higher redshift. Following a similar procedure to that described in Section 5.2.1, 2MASS galaxy distributions for $0.1 < z < 0.2$ and $0.2 < z < 0.3$ are simulated with bias $b = 1.22$ and number of galaxies given by $n_{\rm com}$.

The predicted angular power spectrum deduced from equations (5.10) and (5.11) is valid for the density field as we observe it, which we assume to have lognormal form as in Section 5.2.1. To simulate new galaxy distributions for $z > 0.1$, it is therefore necessary to find the Gaussian field which underlies each of the relevant lognormal fields since it is these Gaussian fields that one can make random realizations of. To estimate this Gaussian field for $z > 0.1$, 10 realizations of the lognormal field are made, calculated using the predicted angular power spectrum with random phases assigned. This procedure is strictly only valid for a Gaussian power spectrum, but as the density field is small and therefore close to Gaussian, it should be a good approximation here as well. For each of the 10 realizations, the lognormal density values are converted to Gaussian values using equation (5.18) and the angular power spectra are calculated. The average of these is then adopted as the generating power spectrum for the simulations.

Exactly the same method as described in Section 5.2.2 is used to analyse the simulation data and evaluate the power of this survey as a means of detecting the ISW effect. Figure 6.1 shows the $\Delta\chi^2$ distributions for such a survey. On comparison with the same distributions for the 2MASS data, we note that the alternative hypothesis $\Delta\chi^2$ histogram is narrower in this case for the highest redshift slice. This is as a result of the decrease in shot noise due to observing more galaxies. Comparing the final panel of figure 6.1 with that of figure 5.6 reveals that the peak of the alternative hypothesis distribution has moved to higher $\Delta\chi^2$ values and that this distribution has become narrower. This results in an increase in the separation of the peaks of the two distributions making this a more powerful test. The Optimal Power for this survey is $\Upsilon = 0.59$, an improvement over 2MASS as one would expect from the $\Delta\chi^2$ distributions.

For this survey, using the Jeffreys' criterion of $\Delta\chi^2 > 5$ for rejection of the null hypothesis and assuming that the ΛCDM hypothesis is true, one would have an 18% chance of making a Type I error; taking a more stringent threshold of $\Delta\chi^2 > 12$ chosen to make the probability of a Type I error 5%, one would expect to reject the null hypothesis $\sim 11\%$ of the time. The improvement in ISW detection prospects via the inclusion of more galaxies is slight but clearly present. It is now interesting to consider the effect of adding more redshift slices to the analysis i.e. probing a larger volume.

6.1.2 More Redshift Slices

A survey with a fainter magnitude limit would observe more galaxies than 2MASS out to $z = 0.3$ as described in Section 6.1.1, but would also be sensitive to large numbers of galaxies at higher redshift. Such a survey could therefore be used with an analysis extending deeper than that considered above. Here two such surveys are investigated, one with a characteristic redshift of $z_{\rm m} = 0.3$ and the other with $z_{\rm m} = 0.75$. The redshift distribution for each survey is taken to be that which we would observe for the constant number density of galaxies measured by 2MASS at $z < 0.1$ together with an exponential cut-off, dependent on the characteristic redshift $z_{\rm m}$:

$$n(z) = n_{\rm com}(z) \exp\{-(z/z_{\rm m})^{1.6}\}. \tag{6.1}$$

Figure 6.2 shows the redshift distribution used for the $z_{\rm m} = 0.3$ survey.

For both surveys, redshift slices of thickness $\Delta z = 0.1$ out to $z_{\rm max} = 0.7$ are considered.

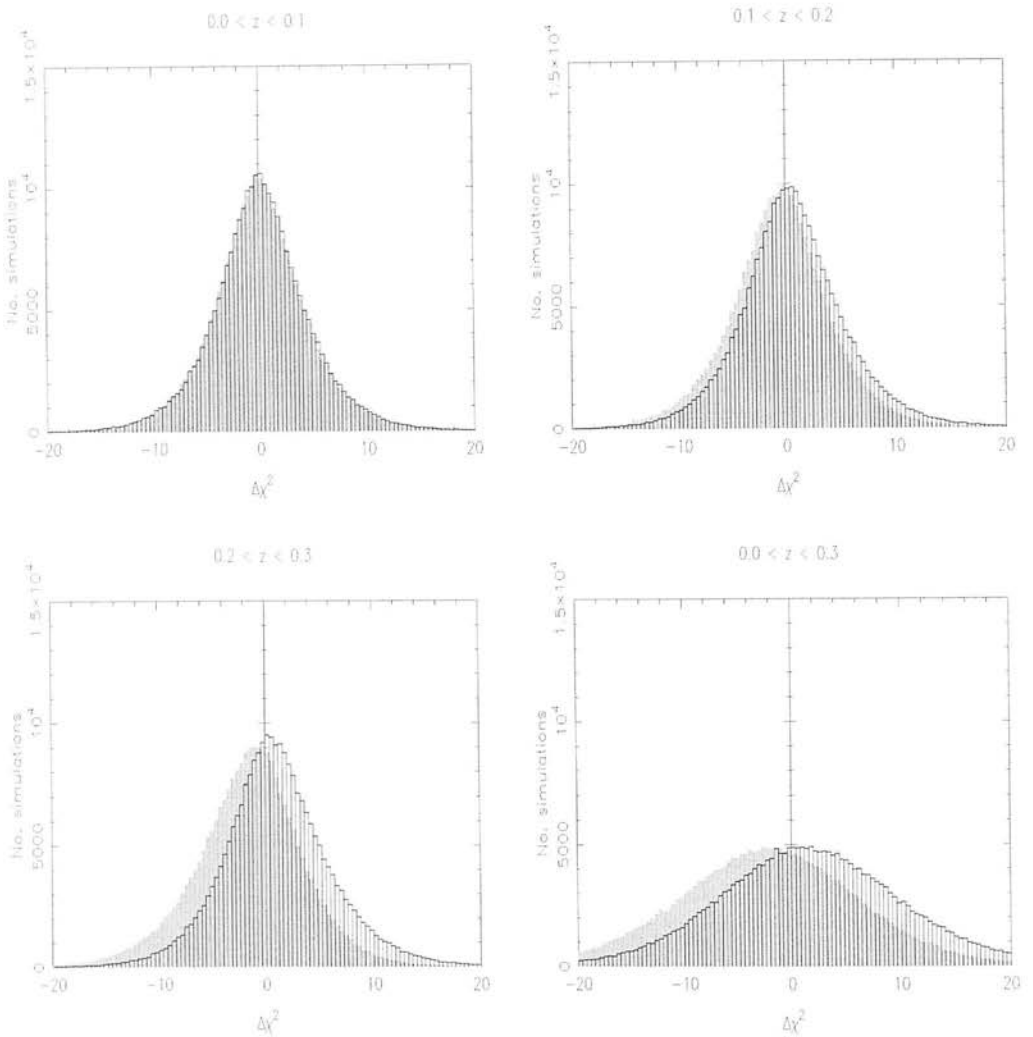

Figure 6.1: Results for a hypothetical ISW detection experiment, otherwise identical to 2MASS but observing more galaxies. The filled histograms show the values of $\Delta\chi^2$ calculated from simulation for the null hypothesis; the outline histograms are for the values of $\Delta\chi^2$ for the alternative hypothesis. Histograms are plotted for $0.0 < z < 0.1$ (top left), $0.1 < z < 0.2$ (top right), $0.2 < z < 0.3$ (bottom left) and the full data set $0.0 < z < 0.3$ (bottom right). Comparison with the data histograms (see figure 5.6) shows narrower alternative hypothesis distributions for the second and third redshift slices leading to reduced overlap and increased offset in the peaks of the distributions for the entire dataset (see Section 6.1.1).

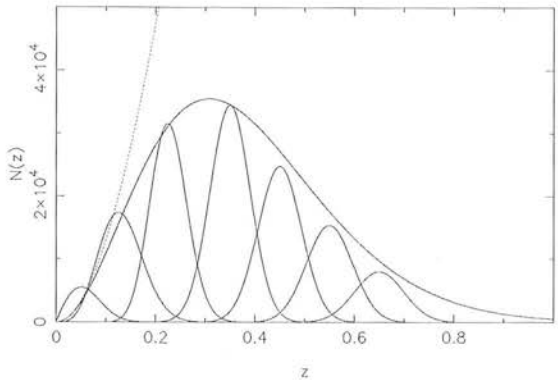

Figure 6.2: The number of galaxies we would expect to observe in redshift bins of width $\Delta z = 0.001$ for a survey with $z_{\rm m} = 0.3$ also divided into photometric redshift slices. The red dotted line shows the number of galaxies expected if the comoving number density $n_{\rm com}$ is constant; the black line is the adopted redshift distribution given by $n_{\rm com}$ and an exponential cut-off.

The true redshift distribution of galaxies selected by photometric redshift to lie in a certain slice is assumed to be that measured for the 2MASS data at low redshift ($z < 0.3$) and for higher redshifts a Gaussian centred at the midpoint of the slice with width $0.03(1 + z)$. An estimate of the galaxy bias in each slice is found by assuming that bias is determined solely by the fraction of galaxies that are observed in the slice. This means that bias is not intrinsically redshift dependent – the only reason that higher redshift slices have higher biases is because only the brightest, most massive galaxies are observed here. This seems a reasonable assumption given that Magliocchetti et al. (2000) observe little evolution in bias over such redshifts. The measured bias values in the first 3 redshift slices from the 2MASS data are used together with the fraction of galaxies observed in each slice (computed assuming a constant $n_{\rm com}$) to deduce a relationship between these quantities. Figure 6.3 shows this data and the best-fitting relationship

$$b = 1.2 f_{\rm gals}^{-0.13}, \tag{6.2}$$

where $f_{\rm gals}$ is the fraction of galaxies observed.

To check whether the assumptions made here about the true redshift distribution of galaxies in each slice seem reasonable, an unbiased prediction of the angular power spectrum in each redshift slice is compared to measurements of the angular power spectrum made using Lumi-

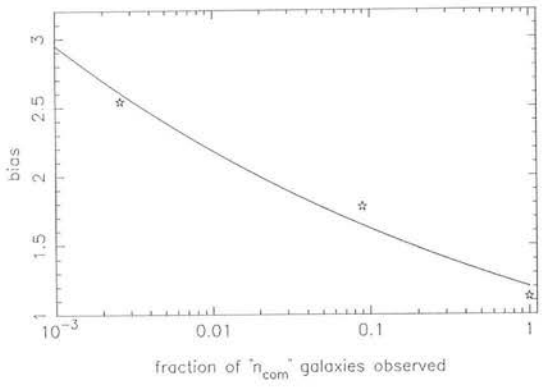

Figure 6.3: The points show average bias computed from photometric data only and SDSS data only for the first three redshift slices against the fraction of galaxies observed in each slice (see text for details). The line is a fit to this data used to infer bias in a redshift slice from a known fraction of observed galaxies.

nous Red Galaxies (LRGs) from SDSS (Blake et al., 2007), which have been corrected for the bias quoted with these results and converted to a $\sigma_8 = 0.75$ cosmology. Figure 6.4 shows that the agreement with these data is good given the slight differences in cosmological model used to deduce the bias and different binning strategies, and reassures us that the model adopted here is reasonable.

The parameters for a $z_m = 0.3$ survey are given in table 6.1 and the corresponding $\Delta\chi^2$ distributions are shown in figure 6.5. The addition of extra redshift slices in this analysis makes it a much more powerful test than those considered above. From figure 6.5 we can see that the additional redshift slices each individually display some ability to discriminate between the hypotheses and this is reflected in the analysis of the dataset as a whole where we now see a large separation between the peaks of the $\Delta\chi^2$ distributions and less overlap between them. We also note that the higher redshift slices have null $\Delta\chi^2$ distributions which are negatively skewed.

Figure 6.6 shows the probabilities of making Type I and II errors as a function of threshold for such a survey and reveals that for a threshold chosen such that the probability of making a Type I error is 5%, the null hypothesis would be rejected assuming that the alternative were true $\sim 30\%$ of the time. The Jeffreys' criterion, with $\Delta\chi^2 > 5$ used to reject the null hypothesis now only has a 9% chance of leading to a Type I error and the Optimal Power of this survey

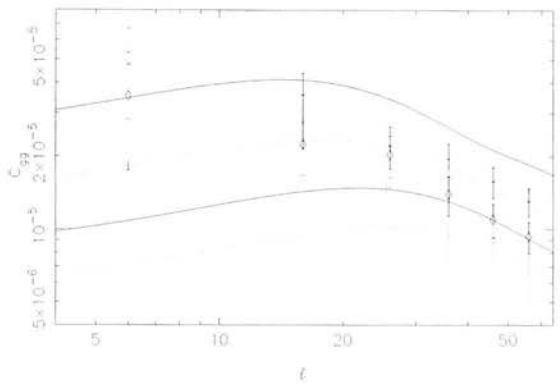

Figure 6.4: Predicted galaxy angular power spectra for galaxies in redshift slices assuming a bias $b = 1$. From top: $0.3 < z < 0.4$ (black), $0.4 < z < 0.5$ (grey), $0.5 < z < 0.6$ (black) and $0.6 < z < 0.7$ (grey). Data points are taken from (Blake et al., 2007) and have been corrected to the bias and value of σ_8 assumed here. Different symbols correspond to different redshift bands: $0.45 < z < 0.5$ (black crosses), $0.5 < z < 0.55$ (grey triangles), $0.55 < z < 0.6$ (black diamonds) and $0.6 < z < 0.65$ (grey stars). Given slight differences in cosmological model and binning, the agreement here is encouraging.

Redshift slice	Number of galaxies	bias	$\bar{z}$	σ
$0.0 < z < 0.1$	4.5×10^5	1.22	n/a	n/a
$0.1 < z < 0.2$	1.9×10^6	1.28	n/a	n/a
$0.2 < z < 0.3$	2.9×10^6	1.36	n/a	n/a
$0.3 < z < 0.4$	3.5×10^6	1.43	0.35	0.0405
$0.4 < z < 0.5$	2.7×10^6	1.56	0.45	0.0435
$0.5 < z < 0.6$	1.8×10^6	1.71	0.55	0.0465
$0.6 < z < 0.7$	1.0×10^6	1.90	0.65	0.0495

Table 6.1: Parameters for a $z_{\rm m} = 0.3$ survey for each redshift slice. For the first 3 redshift slices $z < 0.3$ the measured true redshift distributions from 2MASS are used; at higher redshifts, the true distribution is taken as a Gaussian with mean at the midpoint of the redshift slice and width $\sigma = 0.03(1 + z)$.

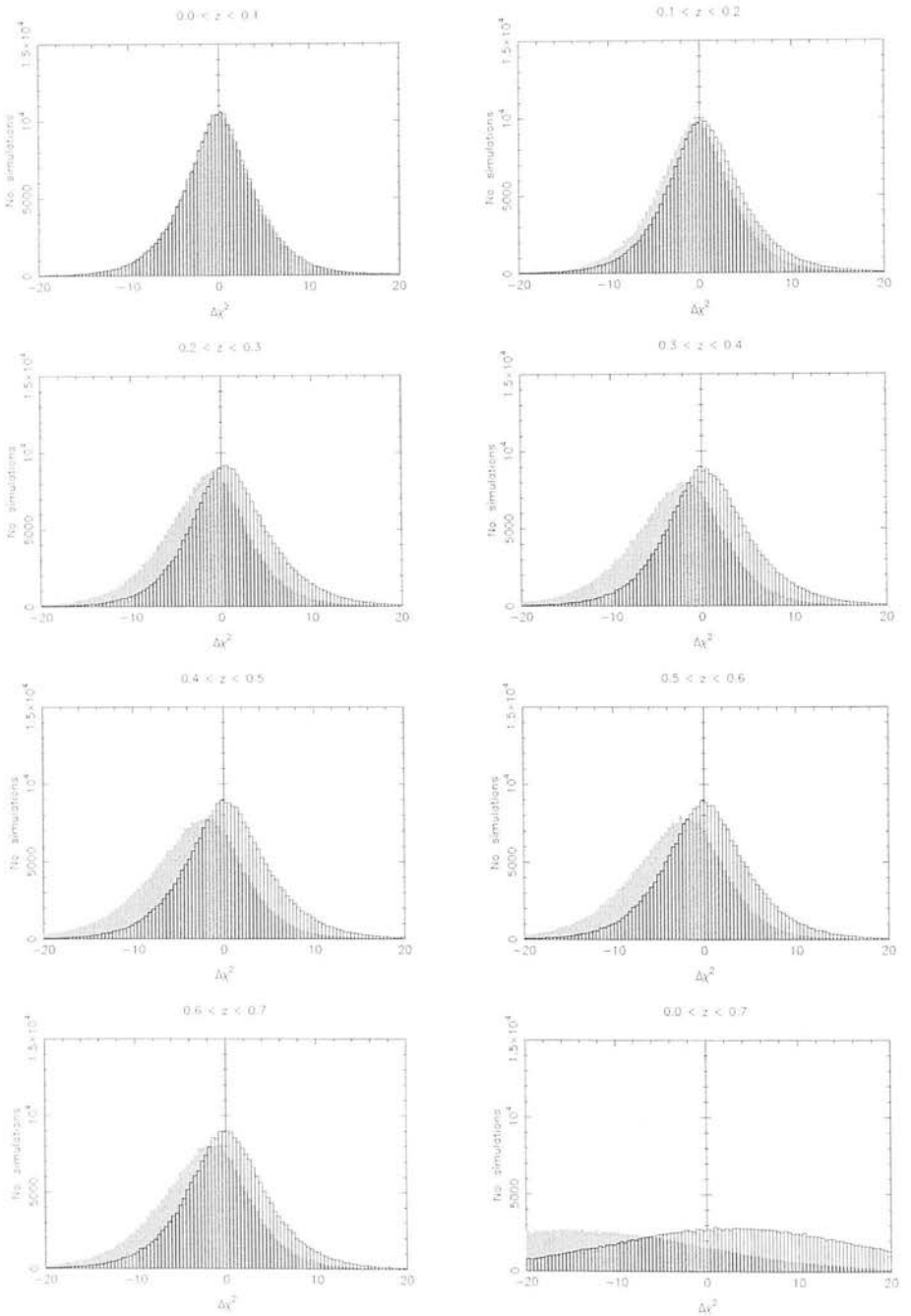

Figure 6.5: Detection prospects for a hypothetical photometric redshift survey with $z_m = 0.3$. The filled histograms show the values of $\Delta\chi^2$ calculated for the null hypothesis; the outline histograms are for the values of $\Delta\chi^2$ for the alternative hypothesis. Comparison of the first three redshift slices with the previous 'data' analysis shows improved detection prospects for these slices and overall.

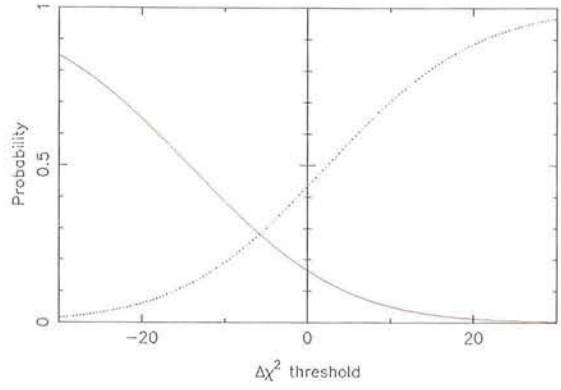

Figure 6.6: The probability of making a Type I error (red solid line) and a Type II error (blue dotted line) as a function of threshold in $\Delta\chi^2$ for an experiment with $z_{\rm m} = 0.3$.

analysed as a whole is $\Upsilon = 0.73$. Figure 6.7 shows how the Optimal Power of this survey increases with depth.

The parameters describing a survey with characteristic redshift $z_m = 0.75$ are given in table 6.2 and otherwise, the method used is exactly the same as above. The results are almost identical to those found for the $z_{\rm m} = 0.3$ survey and are therefore not repeated in full here. The only difference is a small increase in offset between the two $\Delta\chi^2$ histograms in the highest redshift slice, $0.6 < z < 0.7$. The Optimal Power of such an experiment is $\Upsilon = 0.74$ and figure 6.7 again shows how the Optimal Power of this survey increases with depth. The Optimal Powers as a function of depth for all the surveys considered are also given in table 6.3.

The lack of improvement of the $z_{\rm m} = 0.75$ survey over the $z_{\rm m} = 0.3$ survey (when analysed to the same maximum redshift) may seem a little surprising at first. In fact, this is displaying a trend that can also be seen on comparing the results of the deeper surveys with the increased galaxy numbers experiment in Section 6.1.1 out to $z = 0.3$ (see figure 6.7). As long as there are enough galaxies in a redshift slice to keep shot noise to an acceptable level, and the bias within the slice is well understood, then there is nothing gained by observing more galaxies.

6.1.3 Results for the 'Best Possible' Experiment

Another interesting calculation to perform is that of the 'best possible' ISW experiment where one imagines being able to measure directly the ISW temperature fluctuations imprinted in

Redshift slice	Number of galaxies	bias	$\bar{z}$	σ
$0.0 < z < 0.1$	4.5×10^5	1.22	n/a	n/a
$0.1 < z < 0.2$	2.7×10^6	1.22	n/a	n/a
$0.2 < z < 0.3$	5.4×10^6	1.24	n/a	n/a
$0.3 < z < 0.4$	1.0×10^7	1.25	0.35	0.0405
$0.4 < z < 0.5$	1.2×10^7	1.28	0.45	0.0435
$0.5 < z < 0.6$	1.4×10^7	1.31	0.55	0.0465
$0.6 < z < 0.7$	1.6×10^7	1.33	0.65	0.0495

Table 6.2: Parameters for a $z_{\rm m} = 0.75$ survey in each redshift slice. For the first three slices the measured true redshift distributions are used, at higher redshifts the true redshift distribution is taken to be a Gaussian with mean at the midpoint redshift of the slice and width given by $\sigma = 0.03(1 + \bar{z})$

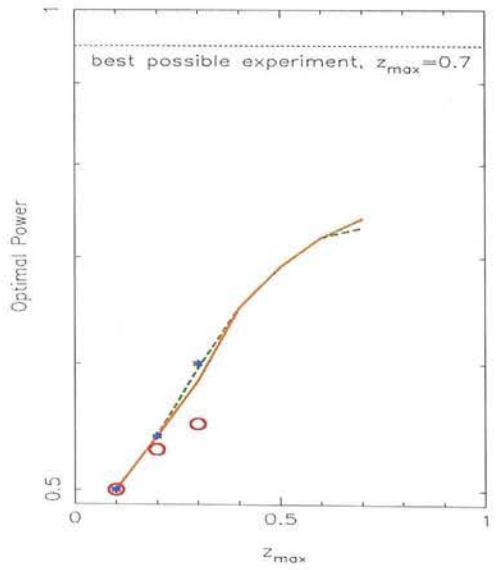

Figure 6.7: The build up of Optimal Power as a function of maximum redshift for the analysis. 2MASS experiment (red), more galaxies (blue), $z_{\rm m} = 0.3$ (green) and $z_{\rm m} = 0.75$ (orange).

z	2MASS	2MASS+	$z_{\rm m} = 0.3$	$z_{\rm m} = 0.75$
$z < 0.1$	0.50	0.50	0.50	0.50
$z < 0.2$	0.53	0.54	0.54	0.54
$z < 0.3$	0.55	0.60	0.60	0.59
$z < 0.4$	n/a	n/a	0.65	0.65
$z < 0.5$	n/a	n/a	0.69	0.69
$z < 0.6$	n/a	n/a	0.72	0.72
$z < 0.7$	n/a	n/a	0.73	0.74

Table 6.3: The Optimal Power for each experiment for different maximum redshifts used in the analysis. We note that all the experiments except 2MASS are almost equally powerful for $z_{\rm max} < 0.3$ and the $z_{\rm m} = 0.75$ experiment only performs better than the $z_{\rm m} = 0.3$ experiment for the highest redshifts considered. Here '2MASS+' refers to the 'galaxy saturation' experiment described in Section 6.1.1.

the CMB over the whole sky (e.g. from precise knowledge of the dark matter density field), rather than using the galaxy distribution. Knowing the power spectrum of ISW signal, random Gaussian realizations of ISW temperature fluctuation maps can be made and used as 'galaxy maps' in the above analysis; the CMB maps remain the same although now no mask is applied.

The $\Delta\chi^2$ distributions for this ideal case are shown in figure 6.8 for an experiment with $z_{\rm max} = 0.7$ and we can see immediately that the overlap between the distributions is smaller than that given by any of the galaxy surveys considered. The histograms are also fairly narrow and the peak of the alternative hypothesis $\Delta\chi^2$ distribution is shifted to a higher value than was observed for any of the galaxy experiments. The Optimal Power of this experiment is $\Upsilon = 0.95$. Interestingly, if $\Delta\chi^2 \geq 5$ constitutes 'strong' evidence for the ISW effect in a ΛCDM universe, then we would expect to fail this criterion $\sim 15\%$ of the time. In a ΛCDM universe, we would expect to prefer the ΛCDM hypothesis 94% of the time with such data, but to strongly prefer the null hypothesis in 1% of cases. The best experiment we could ever hope to perform to detect the ISW effect, would measure the ISW temperature fluctuations back to the surface of last scattering; even in this case, we would not find 'strong' evidence for the ISW effect in 2% of ΛCDM universes. In Section 6.1.4 the consequences of this result with regard to claimed detections of the ISW effect are considered.

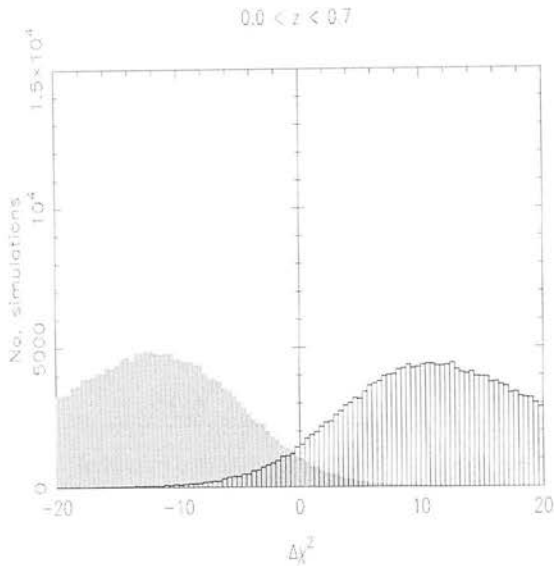

Figure 6.8: The filled histogram shows the $\Delta\chi^2$ values for the null hypothesis of no ISW effect in the 'best possible' case where one can directly measure the ISW temperature fluctuations to $z_{\rm max} = 0.7$. The outline histogram is for the alternative hypothesis of the ISW signal expected in a ΛCDM universe. We see a much diminished overlap between the distributions in this 'best possible' case, although cosmic variance means that there is not complete separation.

6.1.4 ISW Detection Conclusions

The survey considered above with characteristic redshift $z_{\rm m} = 0.3$ has reasonable ISW detection prospects. Shallower surveys like 2MASS with $z_{\rm max} = 0.3$ are not well-suited for ISW detection, even if shot noise in the galaxy distributions is negligible, the increased depth is necessary to adequately distinguish a ΛCDM universe from one with no ISW signal. As long as enough galaxies are observed to keep shot noise at bay, there is little gain in increasing galaxy numbers further as seen on comparison of the $z_{\rm m} = 0.3$ and $z_{\rm m} = 0.7$ surveys. The best 'survey' considered here for ISW detection is therefore that with $z_{\rm m} = 0.3$, the challenge with such a survey will be to produce small enough photometric redshift errors over the full depth of the sample.

Consideration of the 'best possible' ISW experiment out to $z_{\rm max} = 0.7$ reveals that a significant number of ΛCDM universes would not have detectable ISW effects over this redshift range. This is because the intrinsic CMB in these universes happens to be such that the ISW signal which is superimposed on this is effectively 'hidden'. Adding a mask to the analysis

or restricting the redshift range further will only decrease the likelihood of ISW detection. It is therefore intriguing that many groups have claimed detections of the ISW effect using e.g. SDSS galaxies (Scranton et al., 2003; Fosalba et al., 2003; Padmanabhan et al., 2005), NVSS radio galaxies (Vielva et al., 2004; Nolta et al., 2004; Boughn and Crittenden, 2005; Pietrobon et al., 2006; McEwen et al., 2007), SDSS high redshift quasars (Giannantonio et al., 2006) etc. If these claimed detections are correct, then this work implies that we are lucky to live in a universe where such detection is possible.

6.2 SZ Detection Prospects for *Planck*

Following Dolag et al. (2005), the large-scale SZ detection prospects of *Planck* are investigated. Since the SZ effect is frequency dependent and much smaller in amplitude than the primary and ISW temperature anisotropies, it is easier to attempt its detection from difference maps of the CMB which will contain no contribution from either of these two dominating effects. Taking the difference of two CMB maps observed at different frequencies will result in a map which contains an SZ signal, any remaining frequency-dependent foreground signals and noise. A definitive detection of the SZ signal requires evidence of a contribution to the power spectrum of the difference map from this effect.

To investigate whether such a signal is likely to be observed with *Planck* the procedure described in Dolag et al. (2005) is applied with the predicted tSZ field deduced in Chapter 4. The method used to assess the large scale tSZ detection capability of *Planck* proceeds as follows. Firstly, random CMB maps appropriate for *Planck* are produced from Gaussian realizations of the best-fitting WMAP CMB power spectrum and smoothed to the beamwidth anticipated in the different frequency channels[1]. White, non-uniform noise is simulated independently for each channel by making Gaussian realizations of the noise power spectrum

$$C_\ell^{\rm noise} = \Delta_{\rm pix} \left(\frac{\Delta T}{T_{\rm CMB}} \right)^2 \tag{6.3}$$

where $\Delta_{\rm pix}$ is the area over which the noise $\Delta T/T_{\rm CMB}$ is specified. Technical specifications for *Planck* are shown in table 6.4. Finally the appropriate SZ signal for each frequency, computed using the estimate of the local SZ effect found in Section 4.2 is included. The frequencies

[1]Technical specifications for *Planck* are taken from

http://www.rssd.esa.int/index.php?project=PLANCK&page=perf_top

Centre Frequency	Angular Resolution/arcmin	Average $\Delta T/T$ per pixel
70 GHz	14.0	4.7
100 GHz	9.5	2.5
143 GHz	7.1	2.2
217 GHz	5.0	4.8

Table 6.4: Technical specifications for *Planck* used in calculating its large scale tSZ detection prospects. The noise per pixel is given for a square pixel whose side is equal to the FWHM of the beam.

considered here are 70 GHz, 100 GHz, 143 GHz and 217 GHz and difference maps for $217 - 100$ GHz, $143 - 100$ GHz and $143 - 70$ GHz are made. Once constructed, the WMAP Kp0 mask is applied to the difference maps to attempt to eliminate all galactic foregrounds which may interfere with the signal and the power spectrum is computed.

The power spectra for each of the simulated difference maps are corrected for the effect of the mask and the expected noise is removed leaving only any SZ signal and contribution from the cross-correlation of the SZ effect and the noise in the maps, see equation (6.4). This cross-correlation contribution to the power spectrum will differ for each simulation and defines the uncertainty which we can expect at each multipole in the SZ power.

$$\begin{aligned} C_\ell^{\mathrm{A-B}} &= \left(g_\mathrm{A}^2 + g_\mathrm{B}^2 - 2g_\mathrm{A}g_\mathrm{B}\right) C_\ell^{\mathrm{SZ}} + C_\ell^{\mathrm{noise,A}} + C_\ell^{\mathrm{noise,B}} \\ &\quad + \text{SZ-noise cross terms} \end{aligned} \tag{6.4}$$

where g_A describes the frequency dependent term in equation (1.35), evaluated at frequency A and C_ℓ^{SZ} describes the frequency independent part of the SZ power spectrum. Detection of the SZ effect is possible if there is a clear SZ signal from the power spectra even when the uncertainty is accounted for.

Figure 6.9 shows the power spectra for the three difference maps normalised to the SZ signal at 100 GHz together with the 1σ error bars. The normalization is achieved by computing the expected multiple of the SZ power spectrum which will be observed in each difference map and rescaling this to the value observed at 100GHz i.e. the spectra are rescaled by

$$\frac{g_{100}^2}{g_\mathrm{A}^2 + g_\mathrm{B} - 2g_\mathrm{AB}}. \tag{6.5}$$

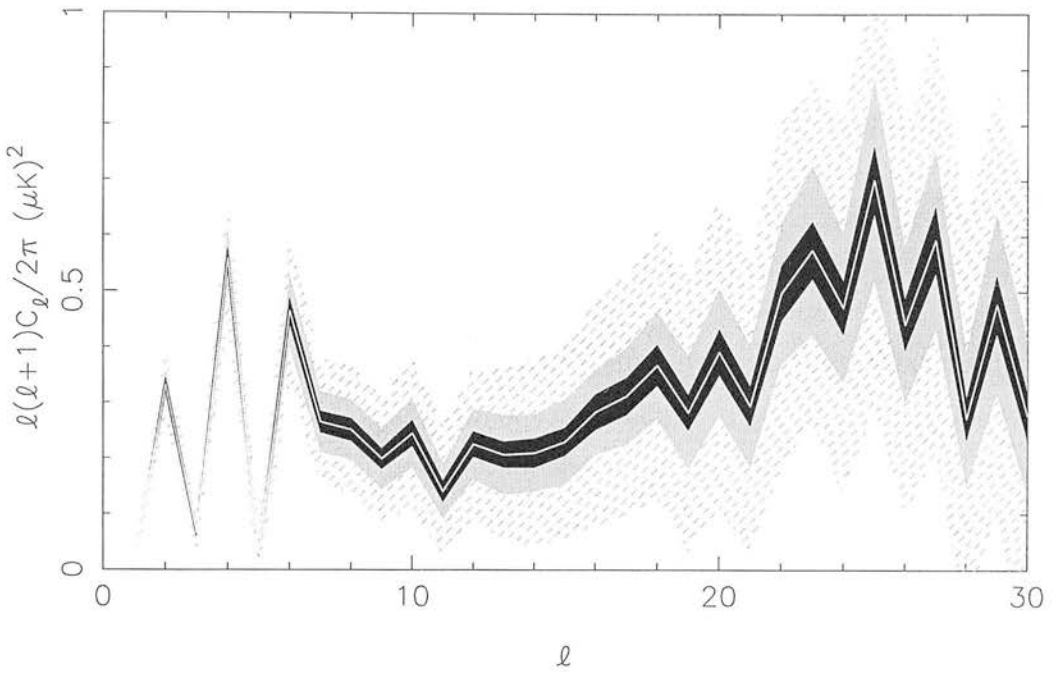

Figure 6.9: The expected large scale SZ power spectrum at 100 GHz (white line) together with the error bars expected for each of the difference maps considered: 217 – 100 GHz (black), 143 – 100 GHz (grey) and 143 – 70 GHz (grey hashed).

We note that for all these maps the signal should be detectable, with the strongest detection coming from the 217 – 100 GHz map. The strength of the detection depends on the noise in the different channels used and the amplitude of SZ signal contained in the map.

These results are encouraging and suggest that *Planck* should indeed be able to detect the large-scale SZ effect where WMAP cannot by virtue of its lower noise and wider frequency range. Dolag et al. (2005) also come to this conclusion using their determination of the local tSZ effect, which is computed from a constrained simulation to $z \lesssim 0.03$. The results of this Section therefore serve to corroborate their result. It should be noted here however, that the above analysis errs on the side of optimism, ignoring the fact that noise in different frequency channels may be correlated and assuming a perfect removal of other frequency dependent foregrounds outside the mask. Should the inclusion of such effects make detection in this manner infeasible, then one could cross-correlate the local SZ map from Section 4.2 with difference maps and attempt to make a detection in this manner. This cross-correlation technique could

also be applied to a map from a single frequency band to attempt a detection in a slightly different manner.

6.3 Investigation of the Cold Region

We noted in Sections 3.4.2 and 5.1.1 a particularly underdense region near the lower edge of the Galactic Plane mask at $l \simeq 330°$ which gives rise to a corresponding cold region in the ISW maps. The region is particularly prominent at the highest redshifts $0.2 \lesssim z \lesssim 0.3$. As a high redshift feature, we might expect this to be less prominent in the ISW signal predicted from the 3D reconstruction when the lack of information towards the redshift limits of the galaxy sample causes the Wiener filter to return a density field which is close to the mean field. Although not so readily identified with an underdense region, there is a similar cold feature at $l \simeq 60°$ which also lies near the lower edge of the mask and again appears in both ISW predictions. This seems associated more with lower redshifts.

Occurring as they do at the edge of the masked region, these underdensities merit further investigation; it is possible that these locations are incomplete, despite escaping the mask. The construction of the mask is motivated by consideration of the 2MASS data alone, but the optical data in this region will be more sensitive to galactic extinction. It is therefore important to investigate the robustness of these features and ascertain whether they are genuine signals.

In order to investigate the robustness, a number of different masks are considered for the galaxy data, ranging from that used throughout this thesis and described in Section 2.1.3, to one which completely obscures the region of interest. These are shown in figure 6.10, applied to the predicted local ISW signal to give an idea of the manner in which they cover the cold/underdense region. The reconstruction algorithm is used together with these masks to produce new 3D reconstructions and then the method of Section 3.1 is used to predict the new ISW signal for $0.0 < z < 0.3$; the results are shown in figure 6.11. We note that as the mask includes more of this area, the cold region in the ISW map diminishes, as one would expect. However, this location remains cold even when the entirety of the region contributing to the original cold section is masked, implying that there exists a large scale trend for this region to be cooler than average.

Figure 6.12 shows the new local ISW quadrupoles and octopoles. There is no significant change to the form of these multipoles although the temperature ranges in general decrease as

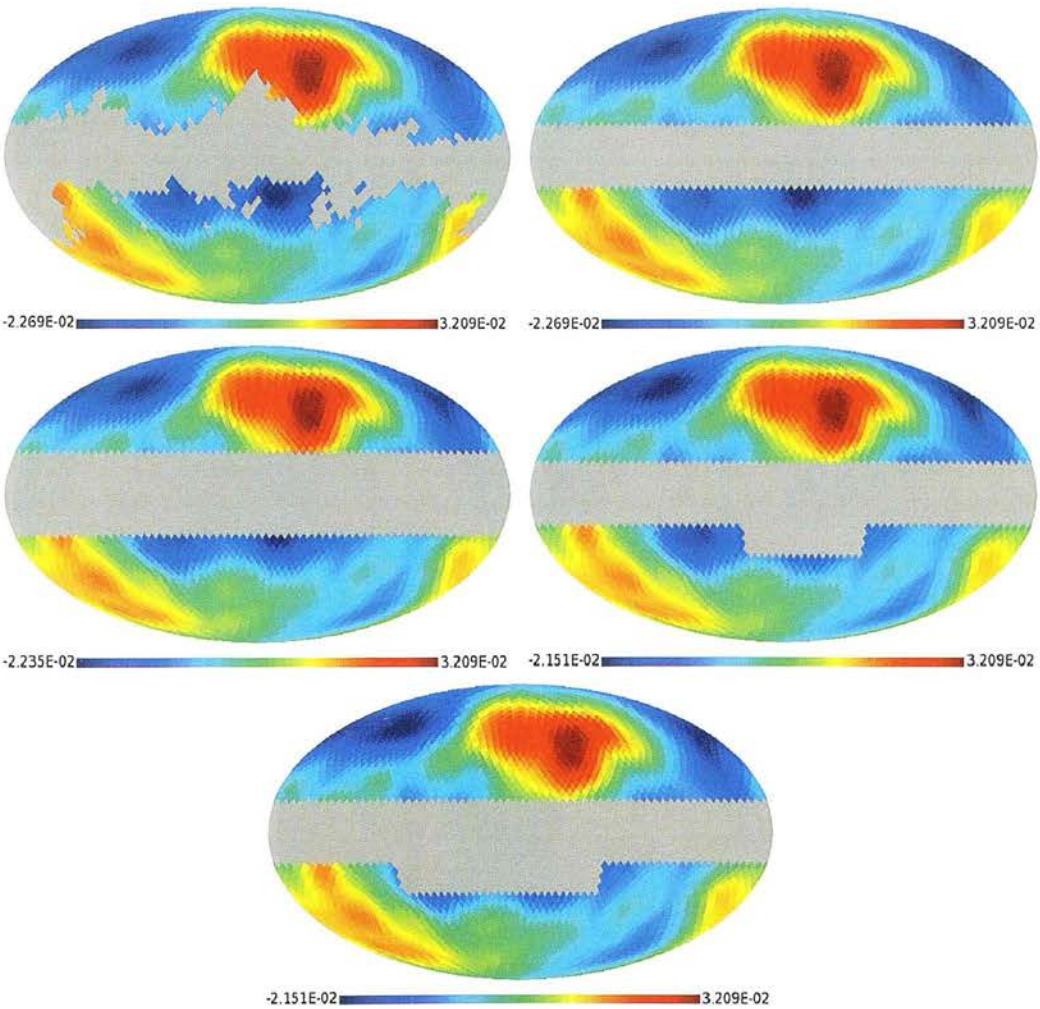

Figure 6.10: The predicted local ISW signal with the series of masks used to investigate the robustness of the cold region close to the Galactic Plane at $l \sim 330°$. (*Top left*) Original mask described in Section 2.1.3, (*Top right*) $|b| \leq 15°$, (*Centre left*) $|b| \leq 20°$, (*Centre right*) $|b| \leq 15°$ and $b \geq -30°$ for $|l - 345°| \leq 45°$, (*Bottom*) $|b| \leq 15°$ and $b \geq -30°$ for $|l - 15°| \leq 75°$.

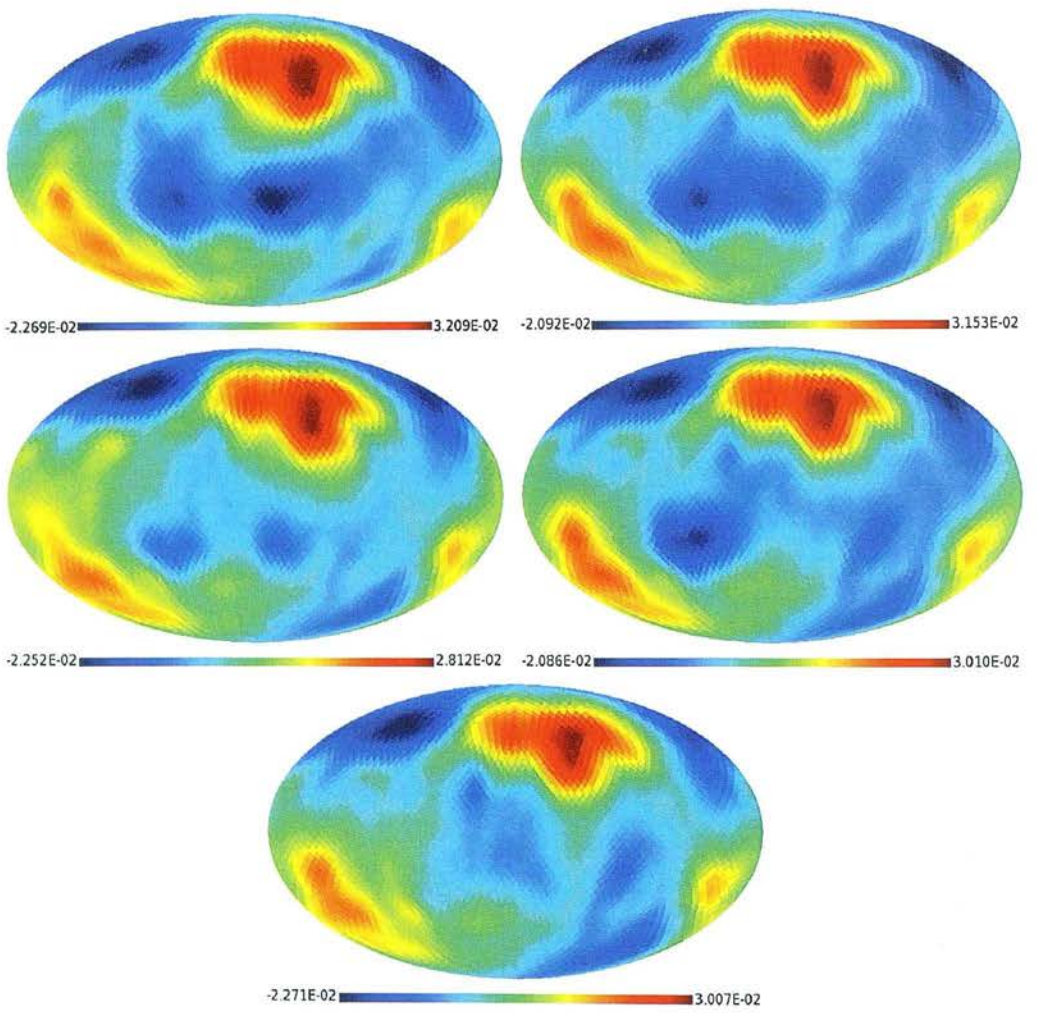

Figure 6.11: The ISW signals for $z < 0.3$ for each of the masks considered: (*Top left*) Original mask, (*Top right*) $|b| \leq 15°$, (*Centre left*) $|b| \leq 20°$, (*Centre right*) $|b| \leq 15°$ and $b \geq -30°$ for $|l - 345°| \leq 45°$, (*Bottom*) $|b| \leq 15°$ and $b \geq -30°$ for $|l - 15°| \leq 75°$. We note that as the severity of the mask increases, the amplitude of the temperature in the cold region decreases.

ISW map	Quadrupole power	p-value
$\|b\| \leq 15°$	587.9	19.0%
$\|b\| \leq 20°$	552.9	17.1%
$b \geq -30°$ for $\|l - 345°\| \leq 45°$	579.7	18.6%
$b \geq -30°$ for $\|l - 15°\| \leq 75°$	541.3	16.4%

Table 6.5: The significance of the CMB quadrupole power after removal of ISW signals computed using different masks. We note that none of the new values are significantly low.

ISW map	$\hat{\mathbf{n}}_2 \cdot \hat{\mathbf{n}}_3$	Separation	Prob.	t	Prob.
$\|b\| \leq 15°$	0.9009	25.7°	9.9%	0.9777	2.5%
$\|b\| \leq 20°$	0.9633	15.6°	3.7%	0.9815	1.9%
$b \geq -30°$ for $\|l - 345°\| \leq 45°$	0.9222	22.8°	7.8%	0.9665	4.8%
$b \geq -30°$ for $\|l - 15°\| \leq 75°$	0.9091	24.6°	9.1%	0.9609	6.0%

Table 6.6: The degree of quadrupole/octopole alignment and octopole planarity in the CMB after removal of ISW signals computed using different masks. The quadrupole and octopole show most alignment in the case of the largest mask considered, in this case the alignment would be expected by chance 4% of the time so is still not particularly significant. The same mask leads to the most planar octopole.

more of the region of interest is masked. The quadrupoles and octopoles for the year-3 WMAP ILC map after each of these ISW predictions have been removed are shown in figure 6.13. Table 6.5 shows the statistics for the quadrupole power, and table 6.6 for the quadrupole and octopole alignments for the year-3 WMAP ILC data after removal of each of the new ISW signals.

The new quadrupole powers become smaller as more of the cold region is masked, but the change is not large enough to make the quadrupole significantly low once again. Comparison of the results in figure 6.13 and those in table 6.6 serves to emphasise the influence of small alterations to the low ℓ multipoles on the alignment statistics. In this case, the alignment between the quadrupole and the octopole is significant for the $|b| \leq 20°$ mask in that it would be expected by chance $\sim 4\%$ of the time. Little hint of either of these results is shown in figure 6.13, where the low ℓ multipoles appear similar in particular to those for the mask which is deliberately chosen to obscure both the cold regions (final panel of this figure), yet the alignment statistics of these two maps are very different. We note however that the ILC3 map has

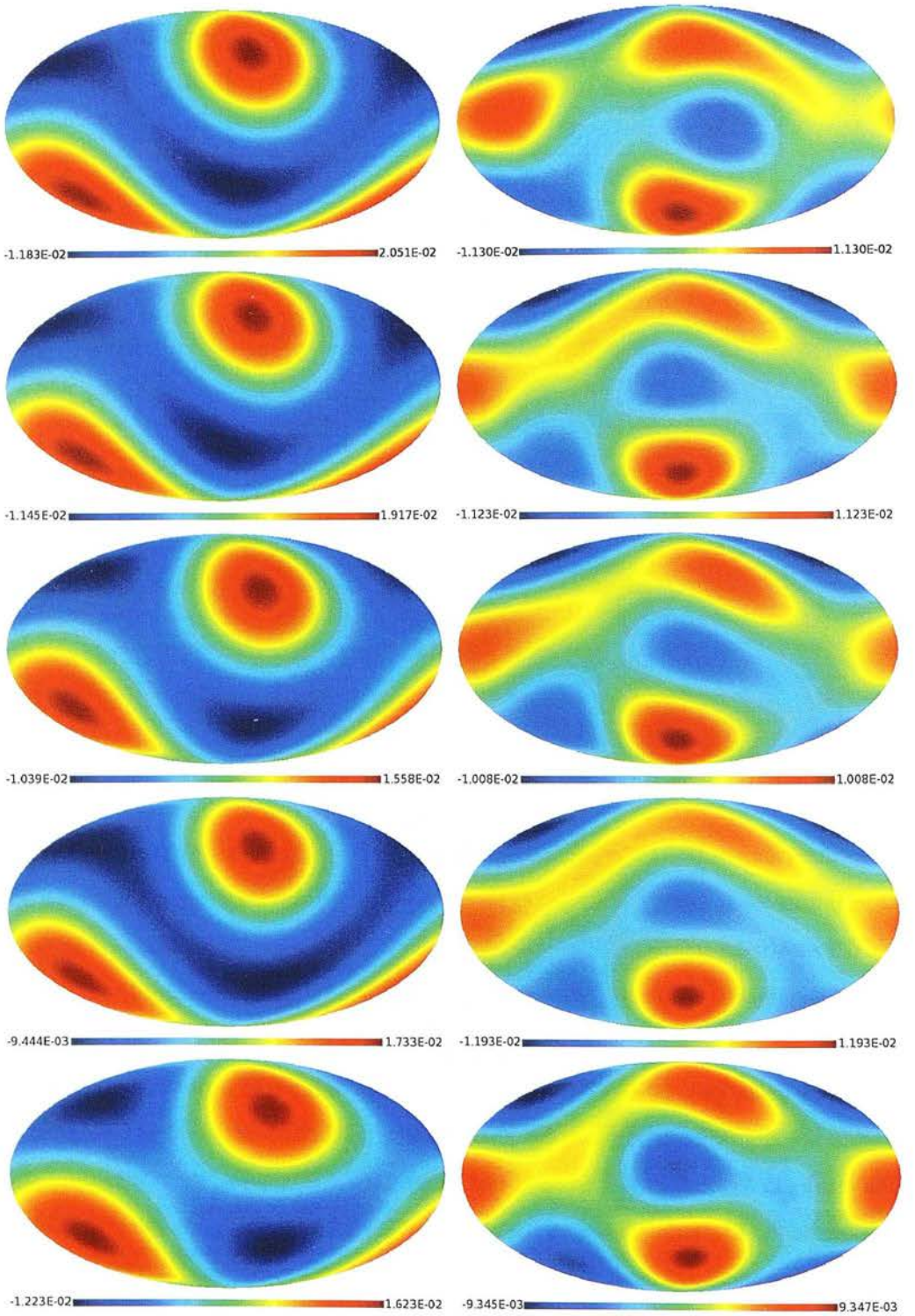

Figure 6.12: (*Left*) The ISW quadrupoles and (*right*) the ISW octopoles for each of the new masks, from top to bottom: original mask, $|b| \leq 15°$, $|b| \leq 20°$, $|b| \leq 15°$ and $b \geq -30°$ for $|l - 345°| \leq 45°$, $|b| \leq 15°$ and $b \geq -30°$ for $|l - 15°| \leq 75°$. The form of these multipoles is largely unchanged as the mask varies, but the amplitudes are affected.

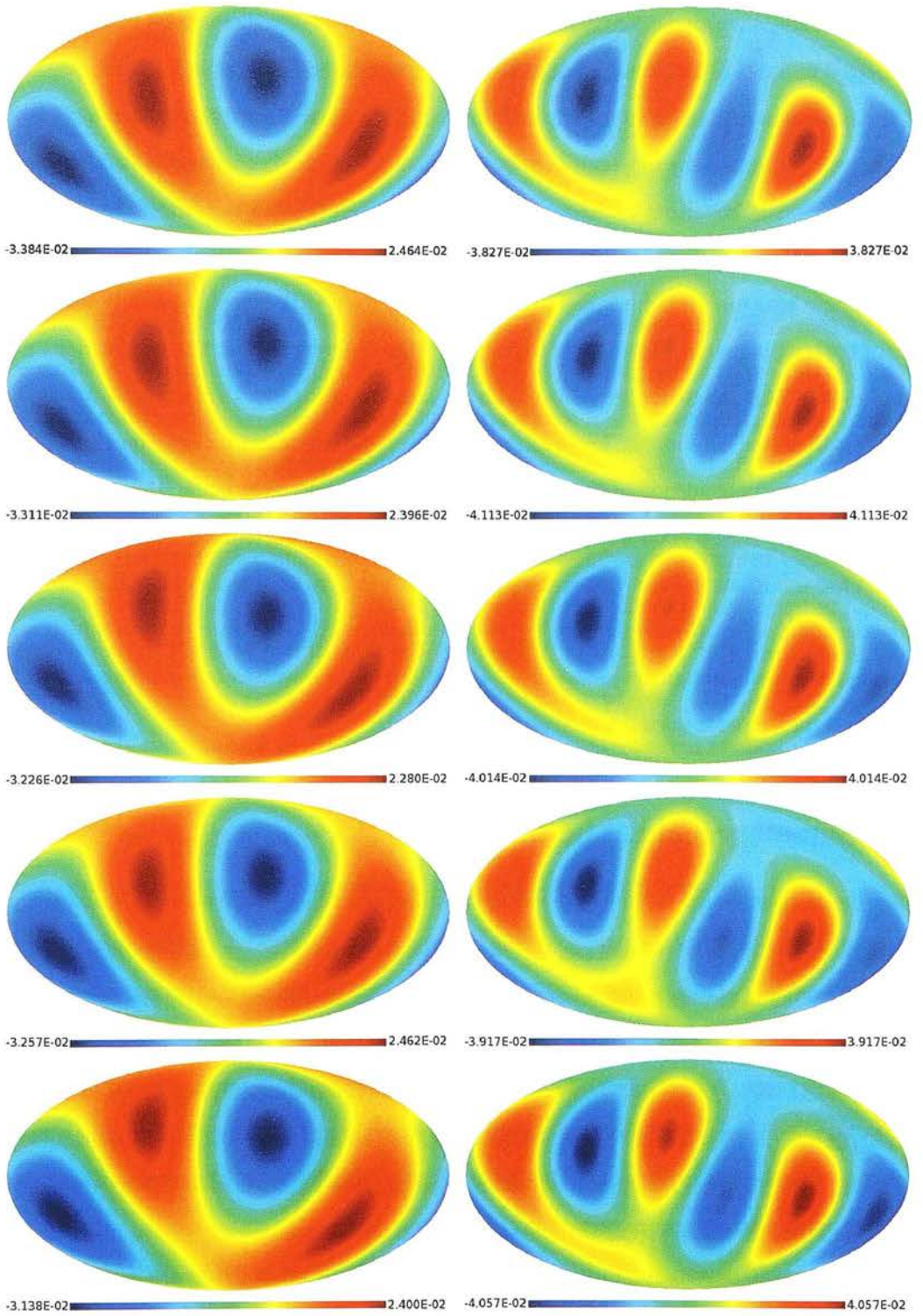

Figure 6.13: The CMB quadrupole after removal of the ISW signal calculated using different masks. (*Top left*) original mask, (*Top right*) $|b| \leq 15°$, (*Centre left*) $|b| \leq 20°$, (*Centre right*) $b \geq -30°$ for $|l - 345°| \leq 45°$, (*Bottom*) $b \geq -30°$ for $|l - 15°| \leq 75°$. The $|b| \leq 20°$ mask gives rise to quadrupole and octopole axes which show the greatest alignment, but even in this case, such alignment would only be expected $\sim 4\%$ of the time.

a separation angle which would only occur by chance $\sim 1\%$ of the time, so the removal of the ISW signal still makes the observed alignment significantly more probable.

In conclusion, the large-scale properties of the ISW signal seem to be robust; even when the entirety of the low density regions near the plane are masked, a reconstruction still leads to an underdensity in this general area. The local ISW signals predicted from reconstructions performed with increasingly severe masks over the affected region have the same quadrupole and octopole structure as the original prediction of the local ISW signal, with only the amplitude of the temperature minima slightly affected by the different masks. The implications with regard to the CMB anomalies are robust, with the removal of the new ISW signals from the observed CMB still alleviating the low quadrupole power, the alignment between quadrupole and octopole and the coincidence of the ecliptic plane with a temperature node. The robustness of the underdensity is also good news for the ISW detection cross-correlation analysis. Although in this case information from within the plane is not used, an artefact existing at the edge of the plane could have affected the results. The fact that the edge of plane features which were identified as possible artefacts have proved robust therefore increases our confidence that the mask used for the cross-correlation analysis is suitable.

6.4 Summary and Evaluation

In this thesis, a smoothed version of the local redshift space density field has been reconstructed from a photometric redshift catalogue derived from the 2MASS XSC. A Wiener filter algorithm modified from that of Fisher et al. (1995) was used to carry out the reconstruction, ensuring that shot noise was suppressed and the signal recovered in a manner which is close to optimal in the least squares sense. A novel method of replacing lost information from the Galactic Plane was developed and the results of this reconstruction were compared to those of other groups and to the galaxy distribution in regions of high spectroscopic completeness. The results of both these analyses reveal that the reconstruction performs well.

The recovered density field is used to predict the ISW signal in the local Universe. Simulations were employed to investigate the consequences of using a reconstruction of this form rather than the true density field to compute the ISW signal, it was found that the difference is almost entirely in the amplitude of the effect. Therefore a rescaling of the spherical harmonic coefficients describing the ISW temperature distribution can be performed to recover an ISW

signal from the reconstruction which is closer to the true signal. Studying the power spectrum of the predicted local ISW effect, it is noted that the power is unusually large at low multipoles. This feature is repeated in a second prediction of the local ISW effect made using a 2D reconstruction of the density field in thick redshift slices. The agreement between the two determinations of the local ISW signal via these independent methods is good and gives us more confidence that the features which are observed in the ISW temperature distribution are real.

In investigating the effect of the local ISW signal on anomalies in the CMB data we want to be certain that the unusually high amplitude of the predicted signal on large scales is not the only factor causing the ISW effect to be of influence on the low ℓ multipoles, and also that the unusually cold region close to the mask mentioned in Sections 3.4.2 and 5.1.1 is robust (see Section 6.3). To allow for the fact that some error may be causing the predicted amplitude on such scales to be too large, both predictions of the local ISW effect and rescaled versions of this chosen to reproduce the expected ΛCDM ISW power are considered with regard to reported anomalies in the WMAP CMB data. The robustness of the cold region is investigated using a number of different masks chosen to obscure underdense regions near the galactic plane. The removal of the resultant ISW signals from the CMB is investigated in Section 6.3 and the resultant maps are still found to be less anomalous than the CMB data alone. Even a severe mask chosen to completely cover the regions of interest leads to an ISW signal which is cold in these locations and we therefore conclude that these features are genuine.

It is found that the majority of the CMB anomalies are alleviated by the removal of the predicted local ISW signal, with the exception of the planarity of the octopole, which actually becomes slightly more planar. This is true of both predictions of the local ISW signal, the rescaled versions of these predictions and the predictions made using more severe masks; the conclusion would therefore seem to be fairly robust. The low quadrupole, any alignment between the preferred axes of the quadrupole and octopole and the coincidence of the ecliptic plane with a node line in the temperature distribution of the $\ell = 2 + 3$ CMB maps are all substantially alleviated or removed altogether. The temperature in the vicinity of the cold spot is also increased by removal of the local ISW signal meaning that this feature could be due to a void at $z \sim 1$ with a smaller size than current estimates suggest. The significance of the planarity of the octopole varies between occurring by chance $\sim 1.6\%$ and $\sim 12\%$ of the time, depending on the ISW map considered. It therefore seems very likely that many of the

anomalies reported in the CMB data can be alleviated by properly accounting for secondary anisotropies on large scales.

In Chapter 4 a method is developed for predicting the large-scale thermal and kinetic SZ effects knowing only properties of the dark matter distribution. This method is applied to the reconstruction of the matter density field recovered in Chapter 2 and a prediction of the local large-scale thermal SZ effect is made. This prediction is in good statistical agreement with previous estimates and shows significant temperature decrements corresponding to the positions of structures such as the Shapley concentration. The large-scale SZ effect is found to have no significant impact on parameter estimation from the WMAP CMB data, low ℓ CMB anomalies or on the temperature in the vicinity of the cold spot. Using this prediction of the local large-scale SZ signal, together with simulations of the CMB as it may be observed in 4 frequency bands, we find that the SZ effect should be detectable with *Planck* data on these scales for the first time. Although this analysis is optimistic in that it assumes perfect foreground subtraction from the region outside the Galactic plane mask, the improved understanding of microwave foregrounds acquired via the WMAP data and the increased frequency range over which the sky is imaged by *Planck*, means that such accuracy should be attainable.

Finally, an attempt has been made to use 2MASS photometric galaxy data to detect the ISW effect. The results show only a weak preference of the data for a ΛCDM universe over one containing no ISW signal, a finding which is not surprising given an analysis which shows the 2MASS experiment to be poor for ISW detection. Investigation of hypothetical photometric redshift surveys shows that a deeper survey with similar photometric redshift accuracy would have much improved detection prospects. Consideration of the 'best possible' ISW experiment, in the light of the number of claimed detections of the ISW effect, reveals that we are relatively fortunate to reside in a universe in which the ISW effect is detectable.

6.5 Possible Extensions of this Work

Having recovered the local density field and used this to predict large-scale secondary anisotropies in the CMB, we can consider possible future applications of this reconstruction:

6.5.1 Local Group Dipole

The Local Group of galaxies is no different to any other structure in the Universe and as such its motion can be determined from theories of structure formation and evolution. As discussed in Chapter 1, the homogeneous background Universe is undergoing uniform expansion where structures move according to the Hubble flow. Perturbations to this smooth background Universe introduce 'peculiar velocities' which are proportional to the gravitational acceleration at any one point, see Section 1.2.4. The motion of the Local Group can therefore be determined in a particular reference frame by calculation of the Hubble flow in its vicinity and the gravitational acceleration field that it is subject to. Within linear theory, the velocity field can be related simply to the density field, and the dipole velocity is therefore described by (Peacock, 1999, p545):

$$\mathbf{u}(\mathbf{0}) = \frac{H_0}{4\pi}\frac{f}{b}\int_0^{2\pi}\int_0^{\pi}\int_0^{\infty}\frac{\delta_{light}(\mathbf{r}')}{|\mathbf{r}'|^2}\,\hat{\mathbf{r}}\;d^3\mathbf{r}' \tag{6.6}$$

where $\mathbf{u}(\mathbf{0})$ is the Local Group dipole, and $f = d\ln g/d\ln a$.

This 'direct' approach to the calculation of the motion of the Local Group (also called the *velocity dipole*) can be compared with a measurement of the Local Group motion with respect to the CMB. The dipole field measured by WMAP shows significantly larger temperature fluctuations than those on other scales (of the order of 10^{-3} compared to 10^{-5}) and it is therefore believed that the bulk of this signal is not primordial in origin, but rather a measure of the motion of the frame in which we measure the CMB relative to its rest frame.

Many groups have used a wide variety of observations to attempt to calculate the gravitational acceleration field in the neighbourhood of the Local Group, and hence the velocity dipole e.g. Lahav (1987); Erdoğdu et al. (2006a), but so far all attempts have shown a discrepancy between the calculated direction of our motion and that inferred from CMB measurements. It is possible that the discrepancy could be caused by a lack of depth in the observations used so far which are therefore missing important contributions to the gravitational field.

An interesting application of the density field reconstruction described in this thesis could therefore be estimation of the Local Group dipole. However, calculation of the dipole would not be as straightforward in this case as it is for spectroscopic reconstructions. Firstly, the effect of the resolution of the density field reconstruction would need to be evaluated – although the velocity field is a larger scale field than the density field, it is still possible that important

contributions to the field would arise from density scales which are unresolved in this reconstruction. Secondly, careful consideration would be needed to ascertain the reference frame with respect to which the velocity field would be found. Whilst spectroscopic redshifts are determined in a heliocentric frame and can therefore easily be corrected to the reference frame of choice, be that the Local Group frame or CMB frame, the use of priors to compute the photometric redshifts means that the frame in question here is not so clear. Simulations could be used to investigate these effects and hence analyse the ability of the reconstruction to robustly determine the Local Group dipole.

6.5.2 Further Incorporation of Spectroscopic Information

There is a wealth of spectroscopic information available for galaxies in the XSC, which has been used in this work only as calibration for the photometric redshifts in the final dataset and to test the quality of the reconstruction. It would be gratifying to be able to make more use of this information, for example to increase the resolution of the recovered density field. At the simplest level, one could imagine creating a reconstruction that merges a spectroscopic determination of the density field at the lowest redshifts where sufficient spectroscopy is available, with the photometric reconstruction described in this thesis at redshifts beyond the scope of the spectroscopic sample. Such a density field could prove useful for dipole estimation where increased accuracy of the density field nearby would undoubtedly be advantageous; but equally knowledge of the higher redshift density field – albeit a low resolution indication of the true field – could at least offer some insight into the importance of contributions to the Local Group dipole beyond the radii currently considered. Additionally, this could prove useful for simulating the local Universe, (see below). The technicalities of combining two such reconstructions are of course non-trivial; there are many ways in which the merging of a spectroscopic and photometric reconstruction could be approached, one would need to determine an optimal method, and indeed whether it is even possible to merge two such fields in a sensible manner. The reward would be a density field combining the advantages of the volume of the photometric reconstruction with the resolution of the spectroscopic field.

Spectroscopic density field reconstructions have been used in the past to constrain the initial conditions of an N-body simulation which will then evolve to reproduce structures in the observed Universe on large scales e.g. Kolatt et al. (1996). Smaller scales are unconstrained

and therefore conform only to the power spectrum of the appropriate cosmological model used for the simulation. With fine enough resolution, such simulations can be used to study galaxy formation in the local Universe (Mathis et al., 2002), although the resolution necessary here means that small simulation boxes are required and a spectroscopic reconstruction of the very local Universe would therefore be a better candidate for such work.

The Millennium simulation is the largest N-body simulation completed to date, containing 1×10^9 dark matter particles, each of mass $8.6 \times 10^8 h^{-1}\mathrm{M}_\odot$ in a box of comoving side length $500\,h^{-1}$Mpc. It has already been used together with semi-analytic galaxy formation codes to produce samples of simulated galaxies which can then be compared to observed galaxy samples as a test of these galaxy formation codes e.g. (Bower et al., 2006; Croton et al., 2006). Assuming that a merged density field as described above could be constructed, a constrained simulation of the local Universe over a reasonably large volume with sufficient resolution to enable the study of local galaxy formation would be interesting to carry out. With the initial conditions of such a simulation chosen to reproduce the local density field as accurately as it is known (very well nearby from spectroscopic data, and at a coarser resolution further away from a photometric reconstruction such as that described in this thesis) galaxy formation could be studied over a cosmologically meaningful volume which approximates the local Universe as well as possible. Direct comparison with galaxy observations would then be possible in addition to the statistical comparisons which are performed at present, paving the way for further testing of our understanding of galaxy formation. An estimate of the non-linear ISW (or Rees-Sciama) effect could also be calculated from such a simulation and the question of whether it has a meaningful effect on the large scale observed CMB could be addressed.

A constrained hydrodynamic simulation similar to the Millennium gas project (Pearce et al., 2007, see Section 4.1.2) could be used to predict the local thermal and kinetic SZ effects directly, rather than using the scaling relations described in Chapter 4. If a spectroscopic reconstruction were indeed used to constrain the nearby density field then an estimate of the SZ effects could be computed on smaller scales than is possible using the method developed in Chapter 4. Even in regions where the photometric reconstruction alone were used as a constraint, the power spectrum of the SZ effect on smaller scales would still be of interest although the density field would remain unconstrained on such scales.

6.5.3 Peculiar Velocities

Within the context of linear theory, knowledge of the density field allows deduction of the velocity field and hence the peculiar velocity field. This is interesting in the context of correcting redshifts to remove the effects of peculiar velocities and therefore give a cleaner representation of the true distance of an object. Such corrections could be applied for example to the supernovae data which are used to construct the Hubble diagram and which provided one of the first lines of evidence for the existence of Dark Energy. The correction for peculiar velocities would reduce the scatter in this diagram (see figure 1.4), and could affect the detection of the acceleration of the expansion of the Universe from this source.

6.5.4 Gamma and Cosmic Ray Cross-Correlation with Large-Scale Structure

There are many situations in which it is of interest to cross-correlate large scale structure with observed phenomena in order to try to determine their origins. Two such examples are the diffuse background of Very High Energy Gamma Rays (VHEGRs) and Ultra-High Energy Cosmic Rays (UHECRs).

The extragalactic diffuse gamma ray background has been detected by EGRET (Energetic Gamma Ray Experiment Telescope) but its origin remains uncertain with possibilities ranging from Active Galactic Nuclei to dark matter annihilation. The energy spectra of different models such as these are too similar to facilitate discrimination between the possible sources, but they have very different large-scale features due to a combination of the existence of a 'cut-off distance' below which VHEGRs can travel to us and the anisotropic distribution of matter around us within a few hundred h^{-1}Mpc (Cuoco et al., 2007). Gamma ray observations are not yet at a stage where such cross-correlations can be performed, but knowledge of the local density field allows the prediction of the gamma ray background under different models. Such calculations have already been performed by Cuoco et al. (2007) for the IRAS PSCz catalogue, smoothed appropriately to suppress shot noise. The majority of the signal is expected to come from $z < 0.1$ and whilst this is within the limits of the IRAS catalogue, coverage at such redshifts is sparse. The spectroscopic accuracy of such a catalogue may be important nearby but equally it is possible that the photometric dataset described in this thesis or the density field we have computed at $z \sim 0.1$ may be useful for such work.

It is uncertain whether UHECRs have their origins in clusters, galaxies or originate entirely

at random. It has been suggested that the large scale UHECR-galaxy angular correlation function could answer this question since galaxies are less strongly clustered than galaxy clusters and therefore give rise to a lower amplitude angular correlation function (Berlind and Farrar, 2007). The use of the large angle correlation function is important since on such scales the uncertainty in the arrival directions of UHECRs due to deflection by magnetic fields are less important. Knowledge of the large scale local density field would again allow the prediction of the UHECR signal from different sources and could possibly allow study of the origins of such phenomena as a function of redshift.

6.5.5 Introduction of New CMB Anomalies

Having in effect created a 'new' map of the CMB after removal of the local ISW signal and in the process alleviated many of the anomalies which have been noted in the CMB data, one can ask whether there is anything anomalous about this new CMB map. We have seen in Chapter 3 that the local ISW effect can have a significant effect on the CMB and therefore it should be borne in mind that the total secondary anisotropy signal has not as yet been estimated. There is further scope for both introduction and removal of any anomalies which exist in the CMB map created by the removal of the predicted ISW signal out to $z = 0.3$. However, one should check that no seriously unexpected features are introduced into the CMB by removal of the predicted local ISW signal.

6.6 Final Remarks

This is an exciting time for Cosmology. On one hand high precision measurements from a wealth of independent sources have lead us to believe that the current concordance cosmology is an excellent descriptor of the Universe which we observe; on the other, $\sim 95\%$ of this Universe is composed of 'dark matter' and 'Dark Energy', neither of which we comprehend. We are poised at the cusp of an era when concerted efforts will be focussed on gaining a greater understanding of Dark Energy – many forthcoming surveys will seek to place tighter constraints on the parameters which describe its behaviour. Although there is some argument about whether this will actually provide insights into the nature of this mysterious component of the Universe, it will certainly enable us to better model its effects. The late ISW signal is one of the key players in understanding Dark Energy; its very existence due to the fact that the

Universe is currently Dark Energy dominated. Detection of this effect is an important verification of our cosmological model, although as we have seen, non-detection of the ISW effect is no indicator that such a model is wrong – even ideal ISW detection experiments have a significant chance of non-detection. Before we can begin to study the intricacies of the behaviour of Dark Energy, it is important that we are confident in the basic tenets of our cosmological model. Further verification of this, for example via detection of the large scale tSZ effect or uncontrived explanation of otherwise anomalous features in the CMB, remains important. The results contained in this thesis, including as they do the first prediction of the ISW and thermal SZ signals out to $z = 0.3$ and a natural explanation for many of the perceived anomalies in the CMB data, should therefore play a small part in the continued quest to understand the Universe which we inhabit.

References

Abramo, L. R., Sodré, L. J., and Wuensche, C. A.: 2006, Phys. Rev. D **74(8)**, 083515

Adelman-McCarthy, J. K. et al.: 2007, ApJS **172**, 634

Afshordi, N., Loh, Y.-S., and Strauss, M. A.: 2004, Phys. Rev. D **69(8)**, 083524

Araújo, H. M., Akimov, D. Y., Alner, G. J., Bewick, A., Bungau, C., Camanzi, B., Carson, M. J., Chepel, V., Chagani, H., Davidge, D., Davies, J. C., Daw, E., Dawson, J., Durkin, T., Edwards, B., Gamble, T., Ghag, C., Hollingworth, R., Howard, A. S., Jones, W. G., Joshi, M., Kirkpatrick, J., Kovalenko, A., Kudryavtsev, V. A., Lebedenko, V. N., Lawson, T., Lewin, J. D., Lightfoot, P., Lindote, A., Liubarsky, I., Lopes, M. I., Lüscher, R., Majewski, P., Mavrokoridis, K., McMillan, J., Morgan, B., Muna, D., Murphy, A. S., Neves, F., Nicklin, G., Paling, S., Pinto da Cunha, J., Plank, S., Preece, R., Quenby, J. J., Robinson, M., Silva, C., Solovov, V. N., Smith, N. J. T., Smith, P. F., Spooner, N. J. C., Stekhanov, V., Sumner, T. J., Tovey, D. R., Thorne, C., Tziaferi, E., and Walker, R. J.: 2006, *Astroparticle Physics* **26**, 140

Bean, R. and Doré, O.: 2004, Phys. Rev. D **69(8)**, 083503

Bekenstein, J. D.: 2004, Phys. Rev. D **70(8)**, 083509

Bell, E. F., McIntosh, D. H., Katz, N., and Weinberg, M. D.: 2003, ApJS **149**, 289

Benítez, N.: 2000, ApJ **536**, 571

Bennett, C. L., Halpern, M., Hinshaw, G., Jarosik, N., Kogut, A., Limon, M., Meyer, S. S., Page, L., Spergel, D. N., Tucker, G. S., Wollack, E., Wright, E. L., Barnes, C., Greason, M. R., Hill, R. S., Komatsu, E., Nolta, M. R., Odegard, N., Peiris, H. V., Verde, L., and Weiland, J. L.: 2003a, ApJS **148**, 1

Bennett, C. L., Halpern, M., Hinshaw, G., Jarosik, N., Kogut, A., Limon, M., Meyer, S. S., Page, L., Spergel, D. N., Tucker, G. S., Wollack, E., Wright, E. L., Barnes, C., Greason, M. R., Hill, R. S., Komatsu, E., Nolta, M. R., Odegard, N., Peiris, H. V., Verde, L., and Weiland, J. L.: 2003b, ApJS **148**, 1

Berlind, A. A. and Farrar, G. R.: 2007, *ArXiv e-prints* 710

Blake, C., Collister, A., Bridle, S., and Lahav, O.: 2007, MNRAS **374**, 1527

Bolzonella, M., Miralles, J.-M., and Pelló, R.: 2000, A&A **363**, 476

Boughn, S. P. and Crittenden, R. G.: 2005, *New Astronomy Review* **49**, 75

Bower, R. G., Benson, A. J., Malbon, R., Helly, J. C., Frenk, C. S., Baugh, C. M., Cole, S., and Lacey, C. G.: 2006, MNRAS **370**, 645

Cabella, P., Hansen, F. K., Liguori, M., Marinucci, D., Matarrese, S., Moscardini, L., and Vittorio, N.: 2006, MNRAS **369**, 819

Carroll, S. M., Press, W. H., and Turner, E. L.: 1992, ARA&A **30**, 499

Chiang, L.-Y., Naselsky, P. D., and Coles, P.: 2007, *ArXiv e-prints* 711

Clowe, D., Randall, S. W., and Markevitch, M.: 2006, *ArXiv Astrophysics e-prints*

Cole, S. and Kaiser, N.: 1989, MNRAS **237**, 1127

Cole, S., Norberg, P., Baugh, C. M., Frenk, C. S., Bland-Hawthorn, J., Bridges, T., Cannon, R., Colless, M., Collins, C., Couch, W., Cross, N., Dalton, G., De Propris, R., Driver, S. P., Efstathiou, G., Ellis, R. S., Glazebrook, K., Jackson, C., Lahav, O., Lewis, I., Lumsden, S., Maddox, S., Madgwick, D., Peacock, J. A., Peterson, B. A., Sutherland, W., and Taylor, K.: 2001, MNRAS **326**, 255

Cole, S., Sanchez, A. G., and Wilkins, S.: 2006, *ArXiv Astrophysics e-prints*

Coles, P. and Jones, B.: 1991, MNRAS **248**, 1

Colless, M., Peterson, B. A., Jackson, C., Peacock, J. A., Cole, S., Norberg, P., Baldry, I. K., Baugh, C. M., Bland-Hawthorn, J., Bridges, T., Cannon, R., Collins, C., Couch, W., Cross,

N., Dalton, G., De Propris, R., Driver, S. P., Efstathiou, G., Ellis, R. S., Frenk, C. S., Glazebrook, K., Lahav, O., Lewis, I., Lumsden, S., Maddox, S., Madgwick, D., Sutherland, W., and Taylor, K.: 2003, *ArXiv Astrophysics e-prints*

Collister, A. A. and Lahav, O.: 2004, PASP **116**, 345

Conway, E., Maddox, S., Wild, V., Peacock, J. A., Hawkins, E., Norberg, P., Madgwick, D. S., Baldry, I. K., Baugh, C. M., Bland-Hawthorn, J., Bridges, T., Cannon, R., Cole, S., Colless, M., Collins, C., Couch, W., Dalton, G., De Propris, R., Driver, S. P., Efstathiou, G., Ellis, R. S., Frenk, C. S., Glazebrook, K., Jackson, C., Jones, B., Lahav, O., Lewis, I., Lumsden, S., Percival, W., Peterson, B. A., Sutherland, W., and Taylor, K.: 2005, MNRAS **356**, 456

Cooray, A. and Sheth, R.: 2002, Phys. Rep. **372**, 1

Copi, C. J., Huterer, D., Schwarz, D. J., and Starkman, G. D.: 2006, MNRAS **367**, 79

Crittenden, R. G. and Turok, N.: 1996, *Physical Review Letters* **76**, 575

Croton, D. J., Springel, V., White, S. D. M., De Lucia, G., Frenk, C. S., Gao, L., Jenkins, A., Kauffmann, G., Navarro, J. F., and Yoshida, N.: 2006, MNRAS **365**, 11

Cruz, M., Cayón, L., Martínez-González, E., Vielva, P., and Jin, J.: 2007, ApJ **655**, 11

Cruz, M., Martínez-González, E., Vielva, P., and Cayón, L.: 2005, MNRAS **356**, 29

Cuoco, A., Hannestad, S., Haugbølle, T., Miele, G., Serpico, P. D., and Tu, H.: 2007, *Journal of Cosmology and Astro-Particle Physics* **4**, 13

Davis, M. and Huchra, J.: 1982, ApJ **254**, 437

de Oliveira-Costa, A. and Tegmark, M.: 2006, Phys. Rev. D **74(2)**, 023005

de Oliveira-Costa, A., Tegmark, M., Zaldarriaga, M., and Hamilton, A.: 2004, Phys. Rev. D **69(6)**, 063516

Dodelson, S.: 2003, *Modern cosmology*, Modern cosmology / Scott Dodelson. Amsterdam (Netherlands): Academic Press. ISBN 0-12-219141-2, 2003, XIII + 440 p.

Dolag, K., Hansen, F. K., Roncarelli, M., and Moscardini, L.: 2005, MNRAS **363**, 29

Efstathiou, G. and Bond, J. R.: 1986, MNRAS **218**, 103

Eisenstein, D. J. and Hu, W.: 1998, ApJ **496**, 605

Eisenstein, D. J. and Hu, W.: 1999, ApJ **511**, 5

Erdoğdu, P., Huchra, J. P., Lahav, O., Colless, M., Cutri, R. M., Falco, E., George, T., Jarrett, T., Jones, D. H., Kochanek, C. S., Macri, L., Mader, J., Martimbeau, N., Pahre, M., Parker, Q., Rassat, A., and Saunders, W.: 2006a, MNRAS **368**, 1515

Erdoğdu, P., Lahav, O., Huchra, J. P., Colless, M., Cutri, R. M., Falco, E., George, T., Jarrett, T., Jones, D. H., Macri, L. M., Mader, J., Martimbeau, N., Pahre, M. A., Parker, Q. A., Rassat, A., and Saunders, W.: 2006b, MNRAS **373**, 45

Eriksen, H. K., Hansen, F. K., Banday, A. J., Górski, K. M., and Lilje, P. B.: 2004, ApJ **605**, 14

Fisher, K. B., Lahav, O., Hoffman, Y., Lynden-Bell, D., and Zaroubi, S.: 1995, MNRAS **272**, 885

Fosalba, P., Gaztañaga, E., and Castander, F. J.: 2003, ApJ **597**, L89

Freedman, W. L., Madore, B. F., Gibson, B. K., Ferrarese, L., Kelson, D. D., Sakai, S., Mould, J. R., Kennicutt, Jr., R. C., Ford, H. C., Graham, J. A., Huchra, J. P., Hughes, S. M. G., Illingworth, G. D., Macri, L. M., and Stetson, P. B.: 2001, ApJ **553**, 47

Giannantonio, T., Crittenden, R. G., Nichol, R. C., Scranton, R., Richards, G. T., Myers, A. D., Brunner, R. J., Gray, A. G., Connolly, A. J., and Schneider, D. P.: 2006, Phys. Rev. D **74(6)**, 063520

Górski, K. M., Hivon, E., Banday, A. J., Wandelt, B. D., Hansen, F. K., Reinecke, M., and Bartelmann, M.: 2005, ApJ **622**, 759

Gould, A.: 1993, ApJ **403**, L51

Hambly, N. C., Davenhall, A. C., Irwin, M. J., and MacGillivray, H. T.: 2001, MNRAS **326**, 1315

Hansen, F. K., Branchini, E., Mazzotta, P., Cabella, P., and Dolag, K.: 2005, MNRAS **361**, 753

Heavens, A. F. and Taylor, A. N.: 1995, MNRAS **275**, 483

Hernández-Monteagudo, C., Genova-Santos, R., and Atrio-Barandela, F.: 2004, ApJ **613**, L89

Hernández-Monteagudo, C., Trac, H., Verde, L., and Jimenez, R.: 2006, ApJ **652**, L1

Hinshaw, G., Branday, A. J., Bennett, C. L., Gorski, K. M., Kogut, A., Lineweaver, C. H., Smoot, G. F., and Wright, E. L.: 1996, ApJ **464**, L25+

Hinshaw, G., Nolta, M. R., Bennett, C. L., Bean, R., Doré, O., Greason, M. R., Halpern, M., Hill, R. S., Jarosik, N., Kogut, A., Komatsu, E., Limon, M., Odegard, N., Meyer, S. S., Page, L., Peiris, H. V., Spergel, D. N., Tucker, G. S., Verde, L., Weiland, J. L., Wollack, E., and Wright, E. L.: 2006, *ArXiv Astrophysics e-prints*

Hu, W. and Dodelson, S.: 2002, ARA&A **40**, 171

Hu, W. and Sugiyama, N.: 1994, Phys. Rev. D **50**, 627

Hu, W. and Sugiyama, N.: 1995, ApJ **444**, 489

Huffenberger, K. M., Seljak, U., and Makarov, A.: 2004, Phys. Rev. D **70(6)**, 063002

Huterer, D.: 2006, *New Astronomy Review* **50**, 868

Inoue, K. T. and Silk, J.: 2006, ApJ **648**, 23

Jackson, J. D.: 1998, *Classical electrodynamics*, New York: Wiley, 1998, 3rd ed.

Jarrett, T.: 2004, *Publications of the Astronomical Society of Australia* **21**, 396

Jones, D. H., Peterson, B. A., Colless, M., and Saunders, W.: 2006, MNRAS **369**, 25

Jones, H., Saunders, W., Colless, M., Read, M., Parker, Q., Watson, F., and Campbell, L.: 2005, in A. P. Fairall and P. A. Woudt (eds.), *Nearby Large-Scale Structures and the Zone of Avoidance*, Vol. 329 of *Astronomical Society of the Pacific Conference Series*, pp 11–+

Kaiser, N.: 1992, ApJ **388**, 272

Kamionkowski, M. and Knox, L.: 2003, Phys. Rev. D **67(6)**, 063001

Kolatt, T., Dekel, A., Ganon, G., and Willick, J. A.: 1996, ApJ **458**, 419

Kolb, E. W. and Turner, M. S.: 1990, *The early universe*, Frontiers in Physics, Reading, MA: Addison-Wesley, 1988, 1990

Lahav, O.: 1987, MNRAS **225**, 213

Lahav, O. et al.: 2002, MNRAS **333**, 961

Lahav, O., Fisher, K. B., Hoffman, Y., Scharf, C. A., and Zaroubi, S.: 1994, ApJ **423**, L93+

Land, K. and Magueijo, J.: 2005, *Physical Review Letters* **95(7)**, 071301

Land, K. and Magueijo, J.: 2007, MNRAS **378**, 153

Lewis, A., Challinor, A., and Lasenby, A.: 2000, ApJ **538**, 473

Loveday, J., Maddox, S. J., Efstathiou, G., and Peterson, B. A.: 1995, ApJ **442**, 457

Luminet, J.-P., Weeks, J. R., Riazuelo, A., Lehoucq, R., and Uzan, J.-P.: 2003, Nature **425**, 593

Magliocchetti, M., Bagla, J. S., Maddox, S. J., and Lahav, O.: 2000, MNRAS **314**, 546

Magueijo, J. and Sorkin, R. D.: 2007, MNRAS **377**, L39

Martinez-Gonzalez, E., Sanz, J. L., and Silk, J.: 1990, ApJ **355**, L5

Mathis, H., Lemson, G., Springel, V., Kauffmann, G., White, S. D. M., Eldar, A., and Dekel, A.: 2002, MNRAS **333**, 739

McEwen, J. D., Vielva, P., Hobson, M. P., Martínez-González, E., and Lasenby, A. N.: 2007, MNRAS **376**, 1211

Milgrom, M.: 1983, ApJ **270**, 365

Mo, H. J. and White, S. D. M.: 1996, MNRAS **282**, 347

Myers, A. D., Shanks, T., Outram, P. J., Frith, W. J., and Wolfendale, A. W.: 2004, MNRAS **347**, L67

Nolta, M. R., Wright, E. L., Page, L., Bennett, C. L., Halpern, M., Hinshaw, G., Jarosik, N., Kogut, A., Limon, M., Meyer, S. S., Spergel, D. N., Tucker, G. S., and Wollack, E.: 2004, ApJ **608**, 10

Norberg, P., Baugh, C. M., Hawkins, E., Maddox, S., Madgwick, D., Lahav, O., Cole, S., Frenk, C. S., Baldry, I., Bland-Hawthorn, J., Bridges, T., Cannon, R., Colless, M., Collins, C., Couch, W., Dalton, G., De Propris, R., Driver, S. P., Efstathiou, G., Ellis, R. S., Glazebrook, K., Jackson, C., Lewis, I., Lumsden, S., Peacock, J. A., Peterson, B. A., Sutherland, W., and Taylor, K.: 2002, MNRAS **332**, 827

Padmanabhan, N., Hirata, C. M., Seljak, U., Schlegel, D. J., Brinkmann, J., and Schneider, D. P.: 2005, Phys. Rev. D **72(4)**, 043525

Padmanabhan, N., Schlegel, D. J., Seljak, U., Makarov, A., Bahcall, N. A., Blanton, M. R., Brinkmann, J., Eisenstein, D. J., Finkbeiner, D. P., Gunn, J. E., Hogg, D. W., Ivezić, Ž., Knapp, G. R., Loveday, J., Lupton, R. H., Nichol, R. C., Schneider, D. P., Strauss, M. A., Tegmark, M., and York, D. G.: 2007, MNRAS **378**, 852

Padmanabhan, T.: 1993, *Structure Formation in the Universe*, Structure Formation in the Universe, by T. Padmanabhan, pp. 499. ISBN 0521424860. Cambridge, UK: Cambridge University Press, June 1993.

Park, C., Vogeley, M. S., Geller, M. J., and Huchra, J. P.: 1994, ApJ **431**, 569

Peacock, J. A.: 1999, *Cosmological Physics*, Cosmological Physics, by John A. Peacock, pp. 704. ISBN 052141072X. Cambridge, UK: Cambridge University Press, January 1999.

Peacock, J. A. and Dodds, S. J.: 1994, MNRAS **267**, 1020

Peacock, J. A. et al.: 2007, *in prep.*

Pearce, F. R. et al.: 2007, MNRAS, *submitted*

Peebles, P. J. E.: 1980, *The large-scale structure of the universe*, Research supported by the National Science Foundation. Princeton, N.J., Princeton University Press, 1980. 435 p.

Penzias, A. A. and Wilson, R. W.: 1965, ApJ **142**, 419

Percival, W. J.: 2005, *astro-ph/0508156*

Perlmutter, S., Aldering, G., Goldhaber, G., Knop, R. A., Nugent, P., Castro, P. G., Deustua, S., Fabbro, S., Goobar, A., Groom, D. E., Hook, I. M., Kim, A. G., Kim, M. Y., Lee, J. C.,

Nunes, N. J., Pain, R., Pennypacker, C. R., Quimby, R., Lidman, C., Ellis, R. S., Irwin, M., McMahon, R. G., Ruiz-Lapuente, P., Walton, N., Schaefer, B., Boyle, B. J., Filippenko, A. V., Matheson, T., Fruchter, A. S., Panagia, N., Newberg, H. J. M., Couch, W. J., and The Supernova Cosmology Project: 1999, ApJ **517**, 565

Pietrobon, D., Balbi, A., and Marinucci, D.: 2006, Phys. Rev. D **74(4)**, 043524

Poggianti, B. M.: 1997, A&AS **122**, 399

Pogosian, L.: 2006, *New Astronomy Review* **50**, 932

Pogosian, L., Corasaniti, P. S., Stephan-Otto, C., Crittenden, R., and Nichol, R.: 2005, *astro-ph/0506396*

Press, W. H. and Schechter, P.: 1974, ApJ **187**, 425

Press, W. H., Teukolsky, S. A., Vetterling, W. T., and Flannery, B. P.: 1992, *Numerical recipes in FORTRAN. The art of scientific computing*, Cambridge: University Press, —c1992, 2nd ed.

Rakic, A., Rasanen, S., and Schwarz, D. J.: 2006, *astro-ph/0609188*

Rassat, A., Land, K., Lahav, O., and Abdalla, F. B.: 2006, *astro-ph/0610911*

Riess, A. G. et al.: 1998, AJ **116**, 1009

Roncarelli, M., Moscardini, L., Borgani, S., and Dolag, K.: 2007, MNRAS **378**, 1259

Rubiño-Martín, J. A., Aliaga, A. M., Barreiro, R. B., Battye, R. A., Carreira, P., Cleary, K., Davies, R. D., Davis, R. J., Dickinson, C., Génova-Santos, R., Grainge, K., Gutiérrez, C. M., Hafez, Y. A., Hobson, M. P., Jones, M. E., Kneissl, R., Lancaster, K., Lasenby, A., Leahy, J. P., Maisinger, K., Martínez-González, E., Pooley, G. G., Rajguru, N., Rebolo, R., Sanz, J. L., Saunders, R. D. E., Savage, R. S., Scaife, A., Scott, P., Slosar, A., Taylor, A. C., Titterington, D., Waldram, E., and Watson, R. A.: 2006, MNRAS **369**, 909

Rudnick, L., Brown, S., and Williams, L. R.: 2007, *arXiv:0704.0908 [astro-ph]*

Saunders, W. et al.: 2000, in S. Courteau and J. Willick (eds.), *Cosmic Flows Workshop*, Vol. 201 of *Astronomical Society of the Pacific Conference Series*, pp 228–+

Sawicki, I. and Carroll, S. M.: 2005, *ArXiv Astrophysics e-prints*

Schäfer, B. M., Pfrommer, C., Bartelmann, M., Springel, V., and Hernquist, L.: 2006, MNRAS **370**, 1309

Schlegel, D. J., Finkbeiner, D. P., and Davis, M.: 1998, ApJ **500**, 525

Schwarz, D. J., Starkman, G. D., Huterer, D., and Copi, C. J.: 2004, *Physical Review Letters* **93(22)**, 221301

Scranton, R. et al.: 2003, *astro-ph/0307335*

Smoot, G. F., Bennett, C. L., Kogut, A., Wright, E. L., Aymon, J., Boggess, N. W., Cheng, E. S., de Amici, G., Gulkis, S., Hauser, M. G., Hinshaw, G., Jackson, P. D., Janssen, M., Kaita, E., Kelsall, T., Keegstra, P., Lineweaver, C., Loewenstein, K., Lubin, P., Mather, J., Meyer, S. S., Moseley, S. H., Murdock, T., Rokke, L., Silverberg, R. F., Tenorio, L., Weiss, R., and Wilkinson, D. T.: 1992, ApJ **396**, L1

Spergel, D. N. et al.: 2006, *astro-ph/0603449*

Spergel, D. N., Verde, L., Peiris, H. V., Komatsu, E., Nolta, M. R., Bennett, C. L., Halpern, M., Hinshaw, G., Jarosik, N., Kogut, A., Limon, M., Meyer, S. S., Page, L., Tucker, G. S., Weiland, J. L., Wollack, E., and Wright, E. L.: 2003, ApJS **148**, 175

Strauss, M. A. and Willick, J. A.: 1995, Phys. Rep. **261**, 271

Sunyaev, R. A. and Zeldovich, Y. B.: 1972, *Comments on Astrophysics and Space Physics* **4**, 173

Tegmark, M., de Oliveira-Costa, A., and Hamilton, A. J.: 2003, Phys. Rev. D **68(12)**, 123523

Trotta, R.: 2007, MNRAS **375**, L26

van Albada, T. S., Bahcall, J. N., Begeman, K., and Sancisi, R.: 1985, ApJ **295**, 305

Verde, L., Heavens, A. F., Percival, W. J., Matarrese, S., Baugh, C. M., Bland-Hawthorn, J., Bridges, T., Cannon, R., Cole, S., Colless, M., Collins, C., Couch, W., Dalton, G., De Propris, R., Driver, S. P., Efstathiou, G., Ellis, R. S., Frenk, C. S., Glazebrook, K., Jackson, C., Lahav, O., Lewis, I., Lumsden, S., Maddox, S., Madgwick, D., Norberg, P., Peacock, J. A., Peterson, B. A., Sutherland, W., and Taylor, K.: 2002, MNRAS **335**, 432

Vielva, P., Martínez-González, E., Barreiro, R. B., Sanz, J. L., and Cayón, L.: 2004, ApJ **609**, 22

Vielva, P., Martinez-Gonzalez, E., and Tucci, M.: 2004, *astro-ph/0408252*

Wandelt, B. D., Larson, D. L., and Lakshminarayanan, A.: 2004, Phys. Rev. D **70(8)**, 083511

White, M., Hernquist, L., and Springel, V.: 2002, ApJ **579**, 16

White, S. D. M., Davis, M., Efstathiou, G., and Frenk, C. S.: 1987, Nature **330**, 451

White, S. D. M. and Rees, M. J.: 1978, MNRAS **183**, 341

Yahil, A., Strauss, M. A., Davis, M., and Huchra, J. P.: 1991, ApJ **372**, 380

Yao, W.-M. et al.: 2006, *Journal of Physics G Nuclear Physics* **33**, 1

Zaroubi, S., Hoffman, Y., Fisher, K. B., and Lahav, O.: 1995, ApJ **449**, 446

APPENDIX A

Derivation of the Equations Describing CMB Anisotropies

A.1 The Boltzmann Equations

To determine the form of the temperature fluctuations in the CMB angular power spectrum it is necessary to consider the evolution of the distribution functions of the different component species of the Universe. Although we ultimately want to investigate the photon distribution function, this cannot be treated in isolation since interactions lead to the evolution of the distribution function of one species being linked to that of another. For example, Compton scattering of photons from electrons leads to a link between the distribution function of photons and that of baryons. In addition to these interactions, the distribution of all the component species is affected by the spacetime metric. The Boltzmann equations express how the distribution functions for the separate species evolve - it is these equations which we need to solve to deduce the form of the anisotropies in the CMB. The Boltzmann equations for the different species are derived below; throughout this Appendix, results are derived following Dodelson (2003).

We work in conformal Newtonian gauge so that the perturbed Friedmann-Robertson-Walker (FRW) metric (see Section 1.1.2) can be expressed as

$$g_{\alpha\beta}\, dx^{\alpha} dx^{\beta} = -(1+2\Psi)\, dt^2 + a^2(1+2\Phi)\, \delta_{ij}\, dx^i\, dx^j \tag{A.1}$$

In this gauge, (including only scalar perturbations since tensor and vector perturbations to the metric are not coupled to the scalar perturbations and do not affect structure formation)[1] the components of the metric are:

$$g_{00}(\mathbf{x}, t) = -(1+2\Psi(\mathbf{x}, t)) \tag{A.2}$$

$$g_{oi} = 0 \tag{A.3}$$

$$g_{ij} = a^2(1+2\Phi(\mathbf{x}, t))\, \delta_{ij} \tag{A.4}$$

where $\Psi(\mathbf{x}, t)$ is the Newtonian potential, $\Phi(\mathbf{x}, t)$ is the spatial curvature perturbation and $|\Psi| \ll 1$, $|\Phi| \ll 1$, in the following we work to $O(|\Psi|^2)$ and $O(|\Phi|^2)$. Note that in previous Chapters, Φ has been used to denote the gravitational potential, whereas Ψ takes this rôle here. Throughout, Greek indices take the values $0, 1, 2, 3$, Roman indices take the values $1, 2, 3$ and the speed of light is set to $c = 1$.

The Boltzmann equation is $df/dt = C[f]$[2] where f is the distribution function of the species in question and the term on the right hand side takes into account interactions with particles of other species. Concentrating on the left hand side of the above, we can re-express this as

$$\begin{aligned} \frac{df}{dt} &= \frac{\partial f}{\partial x^{\mu}} \frac{dx^{\mu}}{dt} + \frac{\partial f}{\partial P^{\mu}} \frac{dP^{\mu}}{dt} \\ &= \frac{\partial f}{\partial t} + \frac{\partial f}{\partial x^i} \frac{dx^i}{dt} + \frac{\partial f}{\partial P^0} \frac{dP^0}{dt} + \frac{\partial f}{\partial P^i} \frac{dP^i}{dt}. \end{aligned} \tag{A.5}$$

We consider now each of the relevant component species in turn and recover the corresponding distribution functions.

[1] Although tensor perturbations do have an effect on the CMB, it is to the polarisation rather than the temperature power spectrum.

[2] The Boltzmann equation is expressed as a derivative with respect to t rather than with respect to the path parameter λ because the collision terms $C[f]$ on the right hand side of the equation turn out to be first order. If we begin with the equation $\frac{df}{d\lambda} = C[f]$ and multiply both sides by $\frac{d\lambda}{dt}$ where $\frac{d\lambda}{dt} = 1$ + first order terms, then we obtain $\frac{df}{dt} = C[f]$ to first order.

A.1.1 Photons

Since photons are massless, the equations of general relativity tell us that $|P|^2 = g_{\mu\nu}P^\mu P^\nu = 0$ where $P^\mu = dx^\mu/d\lambda$ and λ parametrises the path. Hence there are only 3 independent components of the momentum vector instead of the usual 4. If we define $p^2 = g_{ij}P^iP^j$ then:

$$|P|^2 = 0 = g_{00}P^0P^0 + g_{ij}P^iP^j = -(1+2\Psi)(P^0)^2 + p^2 \tag{A.6}$$

$$\begin{aligned} \Rightarrow \quad & (1+2\Psi)(P^0)^2 &&= p^2 \\ \Rightarrow \quad & P^0 = \tfrac{p}{\sqrt{1+2\Psi}} &&= p(1-\Psi) + O(|\Psi|^2) \end{aligned} \tag{A.7}$$

The above relationship allows us to eliminate P^0 in favour of p and Ψ wherever it occurs.

If $\hat{p}^i$ is the unit vector in the direction of P^i then by definition $\delta_{ij}\hat{p}^i\hat{p}^j = 1$ and $P^i = A\hat{p}^i$ where A is some normalization constant. We can find the value of A from the above

$$p^2 = g_{ij}P^iP^j = g_{ij}A^2\hat{p}^i\hat{p}^j = A^2a^2(1+2\Phi) \tag{A.8}$$

$$\Rightarrow A = \sqrt{\frac{p^2}{a^2(1+2\Phi)}} = \frac{p(1-\Phi)}{a} + O(|\Phi|^2). \tag{A.9}$$

Hence $P^i = \frac{p(1-\Phi)}{a}\hat{p}^i$. Returning to our expression for the Boltzmann equation we can now rewrite it in a more useful form since $P^0 = P^0(p)$ and $P^i = P^i(p, \hat{p}^i)$

$$\begin{aligned} \frac{df}{dt} &= \frac{\partial f}{\partial t} + \frac{\partial f}{\partial x^i}\frac{dx^i}{dt} + \frac{\partial f}{\partial P^0}\frac{dP^0}{dt} + \frac{\partial f}{\partial P^i}\frac{dP^i}{dt} \\ &= \frac{\partial f}{\partial t} + \frac{\partial f}{\partial x^i}\frac{P^i}{P^0} + \frac{\partial f}{\partial p}\frac{dp}{dt} + \frac{\partial f}{\partial \hat{p}^i}\frac{d\hat{p}^i}{dt}. \end{aligned} \tag{A.10}$$

The last term of the above equation does not contribute at first order. We can see this since to zero order, the distribution function for photons is the Bose-Einstein distribution $f = (\exp\{p/T\} - 1)^{-1}$ which is independent of $\hat{p}^i$, $\partial f/\partial\hat{p}^i$ is therefore at least a first order term. Similarly, $d\hat{p}^i/dt$ must also be at least a first order term because photon directions only change in the presence of a potential Φ or Ψ, both of which are first order. The final term of equation (A.10) cannot therefore contribute to first order and we can re-express equation (A.10) as

$$\begin{aligned}\frac{df}{dt} &= \frac{\partial f}{\partial t} + \frac{\hat{p}^i(1-\Phi-\Psi)}{a}\frac{\partial f}{\partial x^i} + \frac{\partial f}{\partial p}\frac{dp}{dt} \\ &= \frac{\partial f}{\partial t} + \frac{\hat{p}^i}{a}\frac{\partial f}{\partial x^i} + \frac{\partial f}{\partial p}\frac{dp}{dt}. \end{aligned} \tag{A.11}$$

The second line follows as the zero order Bose-Einstein distribution function for photons does not depend on position and thus $\partial f/\partial x^i$ is a first order term.

Finally, the geodesic equation (A.12) and the relationship between P^0 and p will lead to an expression for dp/dt in terms of Φ and Ψ

$$\frac{d^2x^\mu}{d\lambda^2} + \Gamma^\mu_{\alpha\beta}\frac{dx^\alpha}{d\lambda}\frac{dx^\beta}{d\lambda} = 0. \tag{A.12}$$

Working to first order,

$$\begin{aligned} P^0 = \frac{dx^0}{d\lambda} \Rightarrow \frac{dP^0}{d\lambda} &= P^0\frac{dP^0}{dt} = -\Gamma^0_{\alpha\beta}P^\alpha P^\beta \\ \Rightarrow \frac{d}{dt}[p(1-\Psi)] &= -\Gamma^0_{\alpha\beta}\frac{P^\alpha P^\beta}{p(1-\Psi)} \\ &= -\Gamma^0_{\alpha\beta}\frac{P^\alpha P^\beta}{p}(1+\Psi) \\ \Rightarrow \frac{dp}{dt}(1-\Psi) &= p\left[\frac{\partial\Psi}{\partial t} + \frac{\partial\Psi}{\partial x^i}\frac{dx^i}{dt}\right] - \Gamma^0_{\alpha\beta}\frac{P^\alpha P^\beta}{p}(1+\Psi) \\ \text{Hence, } \frac{dp}{dt} &= p\left[\frac{\partial\Psi}{\partial t} + \frac{\hat{p}^i}{a}\frac{\partial\Psi}{\partial x^i}\right] - \Gamma^0_{\alpha\beta}\frac{P^\alpha P^\beta}{p}(1+2\Psi) \end{aligned} \tag{A.13}$$

Now calculate the Christoffel Symbol $\Gamma^0_{\alpha\beta}$.

$$
\begin{aligned}
\Gamma^0_{\alpha\beta} &= \frac{1}{2}g^{0\delta}\left(g_{\delta\alpha,\beta}+g_{\delta\beta,\alpha}-g_{\alpha\beta,\delta}\right)\\
\Gamma^0_{\alpha\beta}P^\alpha P^\beta &= g^{0\delta}g_{\delta\alpha,\beta}P^\alpha P^\beta-\frac{1}{2}g^{0\delta}g_{\alpha\beta,\delta}P^\alpha P^\beta\\
&= -(1+2\Psi)^{-1}\left[\frac{\partial g_{0\alpha}}{\partial x^\beta}-\frac{1}{2}\frac{\partial g_{\alpha\beta}}{\partial x^0}\right]P^\alpha P^\beta\\
&= -(1-2\Psi)\left[\frac{-\partial(1+2\Psi)}{\partial x^\beta}P^0P^\beta-\frac{1}{2}\frac{\partial g_{\alpha\beta}}{\partial t}P^\alpha P^\beta\right]\\
&= -(1-2\Psi)\left[-2\frac{\partial\Psi}{\partial x^\beta}P^0P^\beta-\frac{1}{2}\frac{\partial g_{00}}{\partial t}P^0P^0-\frac{1}{2}\frac{\partial g_{ij}}{\partial t}P^iP^j\right]\\
&= -(1-2\Psi)\left[-2\frac{\partial\Psi}{\partial x^\beta}P^0P^\beta+\frac{\partial\Psi}{\partial t}P^0P^0-\frac{1}{2}\frac{\partial(a^2(1+2\Phi)\delta_{ij})}{\partial t}P^iP^j\right]\\
&= (1-2\Psi)\left[2\frac{\partial\Psi}{\partial x^\beta}P^0P^\beta-\frac{\partial\Psi}{\partial t}p^2(1-2\Psi)+a\frac{\partial a}{\partial t}(1+2\Phi)\delta_{ij}P^iP^j\right.\\
&\quad \left.+a^2\frac{\partial\Phi}{\partial t}\delta_{ij}P^iP^j\right]\\
&= (1-2\Psi)\left[2\frac{\partial\Psi}{\partial x^i}P^0P^i+\frac{\partial\Psi}{\partial t}p^2(1-2\Psi)+\frac{\partial a}{\partial t}(1+2\Phi)\frac{p^2}{a}(1-2\Phi)\right.\\
&\quad \left.+\frac{\partial\Phi}{\partial t}p^2(1-2\Phi)\right]\\
&= -(1-2\Psi)\left[-2\frac{p^2}{a}\hat{p}^i\frac{\partial\Psi}{\partial x^i}-\frac{\partial\Psi}{\partial t}p^2-Hp^2-\frac{\partial\Phi}{\partial t}p^2\right] \qquad \text{(A.14)}
\end{aligned}
$$

From (A.13) with the expression for $\Gamma^0_{\alpha\beta}$ given in (A.14) we compute dp/dt and arrive at a final expression for the Boltzmann equation for photons.

$$
\begin{aligned}
\frac{dp}{dt} &= p\left[\frac{\partial\Psi}{\partial t}+\frac{\hat{p}^i}{a}\frac{\partial\Psi}{\partial x^i}\right]\\
&\quad -\frac{(1+2\Psi)}{p}\left[-(1-2\Psi)\left\{-2\frac{p^2}{a}\hat{p}^i\frac{\partial\Psi}{\partial x^i}-\frac{\partial\Psi}{\partial t}p^2-Hp^2-\frac{\partial\Phi}{\partial t}p^2\right\}\right]\\
&= p\left[\frac{\partial\Psi}{\partial t}+\frac{\hat{p}^i}{a}\frac{\partial\Psi}{\partial x^i}\right]-\left[2\frac{p}{a}\hat{p}^i\frac{\partial\Psi}{\partial x^i}+\frac{\partial\Psi}{\partial t}p+Hp+\frac{\partial\Phi}{\partial t}p\right]\\
\frac{1}{p}\frac{dp}{dt} &= -H-\frac{\partial\Phi}{\partial t}-\frac{\hat{p}^i}{a}\frac{\partial\Psi}{\partial x^i} \qquad \text{(A.15)}
\end{aligned}
$$

Since $\Phi > 0$ and $\Psi < 0$ in an overdense region, the terms in the above equation state that a photon will lose momentum due to the Hubble expansion (first term), that a photon travelling into a deepening gravitational potential well will lose energy (second term) and that a photon travelling into a gravitational potential well ($\hat{p}^i\frac{\partial\Psi}{\partial x^i} < 0$) will gain energy as it falls in and lose energy as it climbs out.

Putting together equations (A.11) and (A.15) we arrive at an expression for the Boltzmann equation (without collision terms) for photons:

$$\frac{df}{dt} = \frac{\partial f}{\partial t} + \frac{\hat{p}^i}{a}\frac{\partial f}{\partial x^i} - p\frac{\partial f}{\partial p}\left[H + \frac{\partial \Phi}{\partial t} + \frac{\hat{p}^i}{a}\frac{\partial \Psi}{\partial x^i}\right] \tag{A.16}$$

We are interested in the first order Boltzmann equation because our aim is to model the anisotropies in the photon distribution. The perturbed distribution function (A.17) is Bose-Einstein to zero order and to first order contains a perturbation term which depends on $\mathbf{x}$, $\hat{\mathbf{p}}$ and t.

$$\begin{aligned} f(\mathbf{x}, p, \hat{\mathbf{p}}, t) &= \left[\exp\left(\frac{p}{T(t)\left[1+\Theta(\mathbf{x},\hat{\mathbf{p}},t)\right]}\right) - 1\right]^{-1} \text{ where } \Theta = \frac{\delta T}{T} \\ &= \left[\exp\left(\frac{p}{T}\right) - 1\right]^{-1} + \frac{p\,\delta T \exp\left(\frac{p}{T}\right)}{T^2\left[\exp\left(\frac{p}{T}\right) - 1\right]^2} + \text{higher order terms} \\ &= f^{(0)} - \delta T \frac{p}{T}\frac{\partial f^{(0)}}{\partial p} + \text{higher order terms} \\ &= f^{(0)} - p\Theta\frac{\partial f^{(0)}}{\partial p} + \text{higher order terms} \end{aligned} \tag{A.17}$$

The first order Boltzmann equation is:

$$\begin{aligned} \left.\frac{df}{dt}\right|^{(1)} &= \frac{\partial}{\partial t}\left[-p\frac{\partial f^{(0)}}{\partial p}\Theta\right] + \frac{\hat{p}^i}{a}\frac{\partial}{\partial x^i}\left[-p\frac{\partial f^{(0)}}{\partial p}\Theta\right] - \\ &\quad p\frac{\partial}{\partial p}\left[f^{(0)} - p\frac{\partial f^{(0)}}{\partial p}\Theta\right]\left\{H + \frac{\partial \Phi}{\partial t} + \frac{\hat{p}^i}{a}\frac{\partial \Psi}{\partial x^i}\right\}^{(1)} \\ &= -p\Theta\frac{\partial^2 f^{(0)}}{\partial p \partial T}\frac{dT}{dt} - p\frac{\partial f^{(0)}}{\partial p}\frac{\partial \Theta}{\partial t} - \frac{\hat{p}^i p}{a}\frac{\partial f^{(0)}}{\partial p}\frac{\partial \Theta}{\partial x^i} - p\frac{\partial f^{(0)}}{\partial p}\left\{\frac{\partial \Phi}{\partial t} + \frac{\hat{p}^i}{a}\frac{\partial \Psi}{\partial x^i}\right\} \\ &\quad + pH\frac{\partial}{\partial p}\left[p\frac{\partial f^{(0)}}{\partial p}\Theta\right] \\ &= -p\Theta\frac{dT}{dt}\frac{\partial}{\partial p}\left[-\frac{p}{T}\frac{\partial f^{(0)}}{\partial p}\right] - p\frac{\partial f^{(0)}}{\partial p}\frac{\partial \Theta}{\partial t} - \frac{\hat{p}^i p}{a}\frac{\partial f^{(0)}}{\partial p}\frac{\partial \Theta}{\partial x^i} \\ &\quad -p\frac{\partial f^{(0)}}{\partial p}\left\{\frac{\partial \Phi}{\partial t} + \frac{\hat{p}^i}{a}\frac{\partial \Psi}{\partial x^i}\right\} + \frac{p}{a}\frac{da}{dt}\frac{\partial}{\partial p}\left[p\frac{\partial f^{(0)}}{\partial p}\Theta\right] \\ &= -p\frac{\partial f^{(0)}}{\partial p}\left[\frac{\partial \Theta}{\partial t} + \frac{\hat{p}^i}{a}\frac{\partial \Theta}{\partial x^i} + \frac{\partial \Phi}{\partial t} + \frac{\hat{p}^i}{a}\frac{\partial \Psi}{\partial x^i}\right] \text{ since } \frac{da}{a} = -\frac{dT}{T} \end{aligned} \tag{A.18}$$

To complete the equation describing the evolution of the photon distribution function it is necessary to equate the above to the collision term for photons. Thomson scattering is the only

interaction which need to be included here and this leads to a Boltzmann equation for photons of:

$$\begin{aligned} \frac{\partial \Theta}{\partial t} + \frac{\hat{p}^i}{a}\frac{\partial \Theta}{\partial x^i} + \frac{\partial \Phi}{\partial t} + \frac{\hat{p}^i}{a}\frac{\partial \Psi}{\partial x^i} &= n_e \sigma_T \left[\Theta_0 - \Theta(\hat{\mathbf{p}}) + \hat{\mathbf{p}}.\mathbf{v}_b\right] \\ \frac{\partial \Theta}{\partial \eta} + \hat{p}^i\frac{\partial \Theta}{\partial x^i} + \frac{\partial \Phi}{\partial \eta} + \hat{p}^i\frac{\partial \Psi}{\partial x^i} &= n_e \sigma_T a \left[\Theta_0 - \Theta(\hat{\mathbf{p}}) + \hat{\mathbf{p}}.\mathbf{v}_b\right] \end{aligned} \tag{A.19}$$

where n_e is the number density of electrons σ_T is the Thomson scattering coefficient, $\mathbf{v}_b$ is the baryon velocity, $\Theta_0 = \frac{1}{4\pi}\int \Theta \, d\Omega$ and $a d\eta = dt$ i.e. η is conformal time. The spatial Fourier transform of both sides of the equation can then be taken and after defining $\mu = \hat{\mathbf{k}}.\hat{\mathbf{p}}$ and the optical depth $\tau(\eta) = \int_\eta^{\eta_0} n_e \sigma_T a \, d\eta$ we obtain:

$$\frac{\partial \tilde{\Theta}_k}{\partial \eta} + ik\mu\tilde{\Theta}_k + \frac{\partial \tilde{\Phi}_k}{\partial \eta} + ik\mu\tilde{\Psi}_k = -\frac{\partial \tau}{\partial \eta}\left[\tilde{\Theta}_0 - \tilde{\Theta} + \mu\tilde{v_b}\right]_k \tag{A.20}$$

From now on, we will drop the k subscripts and the $\tilde{}$ indicating that equation (A.20) holds in Fourier space independently for all modes k. This is necessary to prevent confusion since we are going to expand the temperature perturbation Θ in terms of Legendre polynomials as:

$$\Theta_\ell = \frac{1}{(-i)^l}\int_{-1}^{1} \mathcal{P}_\ell(\mu)\,\Theta\,\frac{d\mu}{2} \tag{A.21}$$

where $\mathcal{P}_\ell(\mu)$ is the Legendre polynomial of order ℓ and subscripts on Θ will refer to the multipole moment rather than the Fourier mode. This notation has in fact already been employed above as $\mathcal{P}_0 = 1$ and therefore $\Theta_0 = \int_{-1}^{1} \Theta \, \frac{d\mu}{2} = \frac{1}{4\pi}\int \Theta \, d\Omega$.

A.1.2 Cold Dark Matter

Dark matter differs from photons in two key ways which affect the form of its Boltzmann equation i) dark matter particles are non-relativistic and hence have mass and ii) dark matter only interacts via gravity so there is no collision term in this case.

For cold dark matter $g_{\mu\nu}P^\mu P^\nu = -m^2$ and $E = \sqrt{p^2 + m^2}$ where $g_{ij}P^iP^j = p^2$. Hence,

$$
\begin{aligned}
-m^2 &= g_{00}(P^0)^2 + g_{ij}P^iP^j = -(1+2\Psi)(P^0)^2 + p^2 \\
&\Rightarrow (1+2\Psi)(P^0)^2 = E^2 \\
&\Rightarrow P^0 = E(1-\Psi) \text{ to first order} \\
-m^2 &= -(1+2\Psi)E^2(1-\Psi)^2 + a^2(1+2\Phi)\delta_{ij}P^iP^j \\
\delta_{ij}P^iP^j &= \frac{-m^2+E^2}{a^2(1+2\Phi)} \\
\text{Hence, } P^\mu &= \left(E(1-\Psi), \frac{p\hat{p}^i}{a}(1-\Phi)\right)
\end{aligned}
\tag{A.22}
$$

From (A.10) we have

$$
\frac{df}{dt} = \frac{\partial f}{\partial t} + \frac{p\hat{p}^i}{aE}\frac{\partial f}{\partial x^i} + \frac{\partial f}{\partial E}\frac{dE}{dt} + \frac{\partial f}{\partial \hat{p}^i}\frac{d\hat{P}^i}{dt}. \tag{A.23}
$$

Again, the final term in equation (A.23) vanishes as it is the product of two first order terms (distribution function has no directional dependence to zero order and dark matter momentum direction only changes in the presence of the potentials Φ and Ψ). To find an expression for dE/dt, we once again consider the zeroth component of the geodesic equation (A.12).

$$
\begin{aligned}
\frac{dE}{dt} = \frac{d\left(\frac{P^0}{1-\Psi}\right)}{dt} &= (1+\Psi)\frac{dP^0}{dt} + \frac{P^0}{(1-\Psi)^2}\frac{d\Psi}{dt} = (1+\Psi)\frac{dP^0}{dt} + E\frac{d\Psi}{dt} + O(\Psi^2) \\
&= E\frac{d\Psi}{dt} - \frac{(1+\Psi)}{P^0}\Gamma^0_{\alpha\beta}P^\alpha P^\beta \\
&= E\frac{d\Psi}{dt} + \frac{(1+\Psi)}{P^0}(1+2\Psi)^{-1}\left[\frac{\partial g_{0\alpha}}{\partial x^\beta} - \frac{1}{2}\frac{\partial g_{\alpha\beta}}{\partial t}\right]P^\alpha P^\beta \\
&= E\frac{d\Psi}{dt} + \frac{(1-\Psi)}{P^0}\left[-2\frac{\partial\Psi}{\partial x^\beta}P^0P^\beta - \frac{1}{2}\frac{\partial g_{\alpha\beta}}{\partial t}P^\alpha P^\beta\right] \\
&= E\frac{d\Psi}{dt} + \frac{(1-\Psi)}{P^0}\left[-2\frac{\partial\Psi}{\partial x^\beta}P^0P^\beta - \frac{1}{2}\left\{\frac{\partial g_{00}}{\partial t}(P^0)^2 + \frac{\partial g_{ij}}{\partial t}P^iP^j\right\}\right] \\
&= E\frac{d\Psi}{dt} + \frac{(1-\Psi)}{P^0}\left[-2\frac{\partial\Psi}{\partial x^\beta}E(1-\Psi)P^\beta - \frac{1}{2}\left\{-2\frac{\partial\Psi}{\partial t}(P^0)^2\right.\right. \\
&\quad \left.\left. +2a\dot{a}(1+2\Phi)\delta_{ij}P^iP^j + 2a^2\frac{\partial\Phi}{\partial t}\delta_{ij}P^iP^j\right\}\right] \\
&= E\frac{d\Psi}{dt} + \frac{(1-\Psi)}{P^0}\left[-2\frac{\partial\Psi}{\partial x^\beta}E(1-\Psi)P^\beta - \frac{1}{2}\left\{-2E^2\frac{\partial\Psi}{\partial t} + 2Hp^2\right.\right. \\
&\quad \left.\left. +2p^2\frac{\partial\Phi}{\partial t}\right\}\right] \\
&= E\frac{d\Psi}{dt} + \frac{(1-\Psi)}{P^0}\left[-2E^2\frac{\partial\Psi}{\partial t} - 2\frac{Ep\hat{p}^i}{a}\frac{\partial\Psi}{\partial\hat{x}^i} + E^2\frac{\partial\Psi}{\partial t} - Hp^2\right. \\
&\quad \left. -p^2\frac{\partial\Phi}{\partial t}\right] \\
&= E\frac{d\Psi}{dt} - E\frac{\partial\Psi}{\partial t} - 2\frac{p\hat{p}^i}{a}\frac{\partial\Psi}{\partial\hat{x}^i} - \frac{Hp^2}{E} - \frac{p^2}{E}\frac{\partial\Phi}{\partial t} \\
&= -\frac{p\hat{p}^i}{a}\frac{\partial\Psi}{\partial\hat{x}^i} - \frac{Hp^2}{E} - \frac{p^2}{E}\frac{\partial\Phi}{\partial t}
\end{aligned}
\tag{A.24}
$$

As cold dark matter is collisionless, the Boltzmann equation has no collision terms $C[f] = 0$ and hence the Boltzmann equation for cold dark matter is

$$
\frac{df}{dt} = 0 = \frac{\partial f}{\partial t} + \frac{p\hat{p}^i}{aE}\frac{\partial f}{\partial x^i} - \frac{\partial f}{\partial E}\left[\frac{Hp^2}{E} + \frac{p^2}{E}\frac{\partial\Phi}{\partial t} + \frac{p\hat{p}^i}{a}\frac{\partial\Psi}{\partial x^i}\right]. \tag{A.25}
$$

Whereas for photons we knew the form of the zero order distribution function, for dark matter this is no longer the case. We do however know that (by definition) cold dark matter particles are very non-relativistic in the early Universe and hence their thermal motion can be neglected i.e. terms of the order of the square of the velocity, $O\left(\frac{p^2}{E^2}\right)$, can be neglected. Taking moments of the Boltzmann equation for cold dark matter gives:

$$\frac{\partial}{\partial t}\int f\frac{d^3p}{(2\pi)^3} + \frac{1}{a}\frac{\partial}{\partial x^i}\int f\frac{p\hat{p}^i}{E}\frac{d^3p}{(2\pi)^3} - \left[H+\frac{\partial\Phi}{\partial t}\right]\int\frac{p^2}{E}\frac{\partial f}{\partial E}\frac{d^3p}{(2\pi)^3} - \frac{1}{a}\frac{\partial\Psi}{\partial x^i}\int p\hat{p}^i\frac{\partial f}{\partial E}\frac{d^3p}{(2\pi)^3} = 0 \tag{A.26}$$

The final term of this equation is a second order term since $\frac{\partial\Psi}{\partial x^i}$ is first order and the integral over the direction $\hat{p}^i$ can only be non-zero for the perturbed part of the distribution function.

By the definition of the distribution function, the number density and velocity of dark matter particles are given by

$$n = \int f\frac{d^3p}{(2\pi)^3} \qquad v^i = \frac{1}{n}\int f\frac{p\hat{p}^i}{E}\frac{d^3p}{(2\pi)^3}. \tag{A.27}$$

Hence, putting together equations (A.27) and (A.26) gives

$$\begin{aligned}
0 &= \frac{\partial n}{\partial t} + \frac{1}{a}\frac{\partial}{\partial x^i}nv^i - \left[H+\frac{\partial\Phi}{\partial t}\right]\left\{\int\frac{\partial f}{\partial p}\frac{dp}{dE}\frac{p^2}{E}\frac{d^3p}{(2\pi)^3}\right\} \\
&= \frac{\partial n}{\partial t} + \frac{1}{a}\frac{\partial nv^i}{\partial x^i} - \left[H+\frac{\partial\Phi}{\partial t}\right]\left\{\int p\frac{\partial f}{\partial p}\frac{d^3p}{(2\pi)^3}\right\} \\
&= \frac{\partial n}{\partial t} + \frac{1}{a}\frac{\partial nv^i}{\partial x^i} - \left[H+\frac{\partial\Phi}{\partial t}\right]\left\{-\frac{3}{2\pi^2}\int p^2 f dp\right\} \\
&= \frac{\partial n}{\partial t} + \frac{1}{a}\frac{\partial nv^i}{\partial x^i} - \left[H+\frac{\partial\Phi}{\partial t}\right]\left\{-3\int f\frac{d^3p}{(2\pi)^3}\right\} \\
&= \frac{\partial n}{\partial t} + \frac{1}{a}\frac{\partial nv^i}{\partial x^i} + 3n\left[H+\frac{\partial\Phi}{\partial t}\right].
\end{aligned} \tag{A.28}$$

To zero order (v^i is a first order term), equation (A.28) gives

$$0 = \frac{\partial n^{(0)}}{\partial t} + 3Hn^{(0)} \Rightarrow n^{(0)} \propto a^{-3} \tag{A.29}$$

and to first order

$$0 = \frac{\partial n^{(1)}}{\partial t} + \frac{1}{a}\frac{\partial(n^{(0)}v^i)}{\partial x^i} + 3n^{(1)}H + 3n^{(0)}\frac{\partial\Phi}{\partial t}. \tag{A.30}$$

Letting $n^{(1)} = n^{(0)}\delta$ we have

$$\begin{aligned}
0 &= \frac{\partial(n^{(0)}\delta)}{\partial t} + \frac{1}{a}\frac{\partial(n^{(0)}v^i)}{\partial x^i} + 3Hn^{(0)}\delta + 3\frac{\partial\Phi}{\partial t}n^{(0)} \\
&= n^{(0)}\frac{\partial\delta}{\partial t} + \delta\frac{\partial n^{(0)}}{\partial t} + \frac{1}{a}v^i\frac{\partial n^{(0)}}{\partial x^i} + \frac{n^{(0)}}{a}\frac{\partial v^i}{\partial x^i} + 3Hn^{(0)}\delta + 3\frac{\partial\Phi}{\partial t}n^{(0)} \\
&= \delta\left[\frac{\partial n^{(0)}}{\partial t} + 3Hn^{(0)}\right] + n^{(0)}\frac{\partial\delta}{\partial t} + \frac{v^i}{a}\frac{\partial n^{(0)}}{\partial x^i} + \frac{n^{(0)}}{a}\frac{\partial v^i}{\partial x^i} + 3\frac{\partial\Phi}{\partial t}n^{(0)} \qquad \text{(A.31)}
\end{aligned}$$

The terms in the square brackets comprise the zero order equation (A.29) and therefore vanish. The term in equation (A.31) involving the derivative of the zero order number density with respect to position also vanishes. Hence we obtain

$$0 = \frac{\partial\delta}{\partial t} + \frac{1}{a}\frac{\partial v^i}{\partial x^i} + 3\frac{\partial\Phi}{\partial t}. \qquad \text{(A.32)}$$

This is one equation for the two unknowns δ and v^i, we can find another relation by considering the first moment of the distribution function

$$\begin{aligned}
0 &= \frac{\partial}{\partial t}\int f\frac{p\hat{p}^j}{E}\frac{d^3p}{(2\pi)^3} + \frac{1}{a}\frac{\partial}{\partial x^i}\int f\frac{p^2\hat{p}^i\hat{p}^j}{E^2}\frac{d^3p}{(2\pi)^3} - \left[H + \frac{\partial\Phi}{\partial t}\right]\int\frac{\partial f}{\partial E}\frac{p^3\hat{p}^j}{E^2}\frac{d^3p}{(2\pi)^3} \\
&\quad -\frac{1}{a}\frac{\partial\Psi}{\partial x^i}\int\frac{\partial f}{\partial E}\frac{p^2\hat{p}^i\hat{p}^j}{E}\frac{d^3p}{(2\pi)^3} \\
&= \frac{\partial(nv^j)}{\partial t} - \left[H + \frac{\partial\Phi}{\partial t}\right]\int\frac{\partial f}{\partial E}\frac{p^3\hat{p}^j}{E^2}\frac{d^3p}{(2\pi)^3} - \frac{1}{a}\frac{\partial\Psi}{\partial x^i}\int\frac{\partial f}{\partial E}\frac{p^2\hat{p}^i\hat{p}^j}{E}\frac{d^3p}{(2\pi)^3}
\end{aligned}$$

since the other term is $O\left(\frac{p^2}{E^2}\right)$. Hence,

$$\begin{aligned}
0 &= \frac{\partial(nv^j)}{\partial t} - \left[H + \frac{\partial\Phi}{\partial t}\right]\int\frac{\partial f}{\partial p}\frac{p^2\hat{p}^j}{E}\frac{d^3p}{(2\pi)^3} - \frac{1}{a}\frac{\partial\Psi}{\partial x^i}\int\frac{\partial f}{\partial p}p\,\hat{p}^i\hat{p}^j\frac{d^3p}{(2\pi)^3} \\
&= \frac{\partial(nv^j)}{\partial t} - \left[H + \frac{\partial\Phi}{\partial t}\right]\int\frac{\partial f}{\partial p}\frac{p^4}{E}\frac{dp}{(2\pi)^3}\int\hat{p}^j\,d\Omega - \frac{1}{a}\frac{\partial\Psi}{\partial x^i}\int\frac{\partial f}{\partial p}p^3\frac{dp}{(2\pi)^3}\int\hat{p}^i\hat{p}^j\,d\Omega \\
&= \frac{\partial(nv^j)}{\partial t} + \left[H + \frac{\partial\Phi}{\partial t}\right]\int f\left(\frac{4p^3}{E} - \frac{p^5}{E^3}\right)\frac{dp}{(2\pi)^3}\int\hat{p}^j\,d\Omega + \frac{1}{a}\frac{\partial\Psi}{\partial x^i}\int 3fp^2\frac{4\pi}{3}\delta^{ij}\frac{dp}{(2\pi)^3} \\
&= \frac{\partial(nv^j)}{\partial t} + \left[H + \frac{\partial\Phi}{\partial t}\right]\int f\hat{p}^j\left(\frac{4p}{E} - \frac{p^3}{E^3}\right)\frac{d^3p}{(2\pi)^3} + \frac{4\pi}{a}\frac{\partial\Psi}{\partial x^j}\int fp^2\frac{dp}{(2\pi)^3} \\
&= \frac{\partial(nv^j)}{\partial t} + 4nv^j\left[H + \frac{\partial\Phi}{\partial t}\right] + \frac{1}{a}\frac{\partial\Psi}{\partial x^j}n \\
&= \frac{\partial(nv^j)}{\partial t} + 4nv^jH + \frac{1}{a}\frac{\partial\Psi}{\partial x^j}n. \qquad \text{(A.33)}
\end{aligned}$$

Since none of the terms in equation (A.33) are zero order, there is no zero order equation. Consider the first order equation

$$\begin{aligned} 0 &= n^{(0)}\frac{\partial v^j}{\partial t} + v^j\frac{\partial n^{(0)}}{\partial t} + 4n^{(0)}v^j H + \frac{1}{a}\frac{\partial \Psi}{\partial x^i}n^{(0)} \\ &= v^j\left[\frac{\partial n^{(0)}}{\partial t} + 3Hn^{(0)}\right] + n^{(0)}\frac{\partial v^j}{\partial t} + n^{(0)}v^j H + \frac{1}{a}\frac{\partial \Psi}{\partial x^j}n^{(0)} \\ \Rightarrow 0 &= \frac{\partial v^j}{\partial t} + v^j H + \frac{1}{a}\frac{\partial \Psi}{\partial x^j}. \end{aligned} \tag{A.34}$$

Equations (A.32) and (A.34) can be expressed in Fourier space (assuming here that the velocity is irrotational, $\nabla \times \mathbf{v} = 0$) as

$$\frac{\partial \tilde{\delta}_k}{\partial \eta} + ik\tilde{v}_k + 3\frac{\partial \tilde{\Phi}_k}{\partial \eta} = 0 \tag{A.35}$$

$$\frac{\partial \tilde{v}_k}{\partial \eta} + \frac{\tilde{v}_k}{a}\frac{\partial a}{\partial \eta} + ik\tilde{\Psi}_k = 0 \tag{A.36}$$

Again, from now on we will drop the ˜ and subscript k notation which denotes above that the equations hold independently for all Fourier modes k.

A.1.3 Baryons

Ignoring collision terms, the Boltzmann equation for baryons has the same form as that for dark matter. When we include collision terms again we find that there is no resultant collision term on taking the zeroth moment of the Boltzmann equation because the collision processes conserve electron number. When we take the first moment of the Boltzmann equation to find a second equation the collision terms are those describing Coulomb scattering of electrons from protons and vice versa, and Compton scattering for electrons. Hence find that the Boltzmann equations are

$$\frac{\partial \delta_b}{\partial \eta} + ikv_b + 3\frac{\partial \Phi}{\partial \eta} = 0 \tag{A.37}$$

$$\frac{\partial v_b}{\partial \eta} + \frac{v_b}{a}\frac{\partial a}{\partial \eta} + ik\Psi = \dot{\tau}\frac{4\rho_\gamma}{3\rho_b}\left[3i\Theta_1 + v_b\right]. \tag{A.38}$$

A.1.4 Neutrinos

Assuming that neutrinos are massless and that they interact only very weakly we find that the equations describing the evolution of the neutrino distribution are the same as those for photons except that there is no collision term. Hence, if we let $\mathcal{N}$ be defined analogously to Θ for the photon distribution, the Boltzmann equation for neutrinos is:

$$\frac{\partial \mathcal{N}}{\partial \eta} + ik\mu\mathcal{N} + \frac{\partial \Phi}{\partial \eta} + ik\mu\Psi = 0 \tag{A.39}$$

A.2 Solution of the Boltzmann Equations in the Tight Coupling Limit

We can consider what form the equations will take before recombination has occurred when the photons and baryons form a single tightly coupled fluid. In this limit, the differential optical depth $\dot{\tau} = -a\sigma_T n_e$ ($\dot{} = \frac{\partial}{\partial\eta}$) is high and Compton scatterings occur at a high rate, $\tau \gg 1$. By taking moments of both sides of equation (A.20) we can find the evolution of the separate multipole moments with $\ell > 2$, as shown in equation (A.40). It will turn out that in the tightly coupled approximation, only the first two moments are non-negligible.

$$\begin{aligned} \frac{1}{(-i)^\ell}\int_{-1}^{1}\mathcal{P}_\ell\left(\dot{\Theta} + ik\mu\Theta + \dot{\Phi} + ik\mu\Psi\right)\frac{d\mu}{2} &= \frac{-1}{(-i)^\ell}\int_{-1}^{1}\mathcal{P}_\ell\left(\dot{\tau}\left[\Theta_0 - \Theta + \mu v_b\right]\right)\frac{d\mu}{2} \\ \dot{\Theta}_\ell + ik\frac{1}{(-i)^\ell}\int_{-1}^{1}\mu\mathcal{P}_\ell\Theta\frac{d\mu}{2} &= -\dot{\tau}\Theta_\ell \end{aligned} \tag{A.40}$$

since Φ, Ψ etc. have simple μ dependence i.e. only have monopole and dipole terms. Using the Legendre polynomial identity $(\ell+1)\mathcal{P}_{\ell+1}(\mu) = (2\ell+1)\mu\mathcal{P}_\ell(\mu) - \ell\mathcal{P}_{\ell-1}(\mu)$ we see that:

$$\begin{aligned} \dot{\Theta}_\ell + \frac{ik}{2\ell+1}\frac{1}{(-i)^\ell}\int_{-1}^{1}(\ell+1)\mathcal{P}_{\ell+1}(\mu)\Theta + \ell\mathcal{P}_{\ell-1}(\mu)\Theta\frac{d\mu}{2} &= -\dot{\tau}\Theta_\ell \\ \dot{\Theta}_\ell + \frac{ik}{2\ell+1}\left[(\ell+1)\Theta_{\ell+1} + l\Theta_{\ell-1}\right] &= -\dot{\tau}\Theta_\ell. \end{aligned} \tag{A.41}$$

The first term here is $O(\frac{\Theta_\ell}{\eta})$ whereas the term on the RHS is of the order $O(\frac{\tau\Theta_\ell}{\eta})$ which is much larger, hence the first term is negligible. Ignoring the $\Theta_{\ell+1}$ term for the moment we see that for horizon size modes $k\eta \sim 1$, $\Theta_{\ell-1} \gg \Theta_\ell$ (which justifies ignoring the $\Theta_{\ell+1}$ term) and

this relation holds for all modes higher than the dipole, so all such modes are much smaller than the monopole and dipole.

To find the monopole and dipole expressions we take moments again, but this time we cannot ignore the Φ and Ψ terms. We obtain

$$\dot{\Theta}_0 + k\Theta_1 + \dot{\Phi} = 0 \tag{A.42}$$

$$\dot{\Theta}_1 + \frac{2k}{3}\Theta_2 - \frac{k}{3}\Theta_0 = \dot{\tau}\left[v_b - \Theta_1\right]$$

$$\Rightarrow \dot{\Theta}_1 - \frac{k}{3}\Theta_0 = \dot{\tau}\left[v_b - \Theta_1\right] \tag{A.43}$$

since we ignore all modes higher than the dipole.

We also have equations for the baryons (A.37) and (A.38) which apply in this limit. We can rewrite (A.38) as

$$v_b = -3i\Theta_1 + \frac{R}{\dot{\tau}}\left[\frac{\partial v_b}{\partial \eta} + \frac{v_b}{a}\frac{\partial a}{\partial \eta} + ik\Psi\right] \text{ where } R = \frac{3\rho_b}{4\rho_\gamma}. \tag{A.44}$$

To lowest order, as $\tau \gg 1$, we have $v_b = -3i\Theta_1$ and so to first order

$$v_b \simeq -3i\Theta_1 + \frac{R}{\dot{\tau}}\left[-3i\frac{\partial \Theta_1}{\partial \eta} - 3i\frac{\Theta_1}{a}\frac{\partial a}{\partial \eta} + ik\Psi\right]. \tag{A.45}$$

This expression allows us to eliminate v_b in (A.43) and by differentiating (A.42) we can eliminate $\dot{\Theta}_1$. Finally, (A.42) can be used to eliminate Θ_1 and we are left with a second order equation for Θ_0 (Hu and Sugiyama, 1995):

$$\ddot{\Theta}_0 + \frac{\dot{a}}{a}\frac{R}{1+R}\dot{\Theta}_0 + k^2 c_s^2 \Theta_0 = -\ddot{\Phi} - \frac{\dot{a}}{a}\frac{R}{1+R}\dot{\Phi} - \frac{k^2}{3}\Psi \tag{A.46}$$

where c_s is the photon-baryon fluid sound speed. This is an oscillator equation with a forcing term on the right hand side. Ignoring the damping term, which is much smaller than the pressure term for modes that are within the sound horizon at recombination, we see (Dodelson, 2003, p228)

$$\Theta_0(\eta) + \Phi(\eta) = \left[\Theta_0(0) + \Phi(0)\right]\cos(kr_s) + \frac{k}{\sqrt{3}}\int_0^\eta \left[\Phi(\eta') - \Psi(\eta')\right]\sin[k(r_s(\eta) - r_s(\eta'))]\, d\eta', \tag{A.47}$$

where r_s is the sound horizon. The WKB approximation can be used to obtain the full solution, which differs from that given here by a factor $(1+R)^4$ (Dodelson, 2003, p257). We can obtain an expression for the dipole using equations (A.42) and (A.47)

$$\begin{aligned}\Theta_1(\eta) &= \frac{1}{\sqrt{3}}\left[\Theta_0(0)+\Phi(0)\right]\sin(kr_s) \\ &\quad -\frac{k}{3}\int_0^{\eta}\left[\Phi(\eta')-\Psi(\eta')\right]\cos[k(r_s(\eta)-r_s(\eta'))]\,d\eta' \qquad \text{(A.48)}\end{aligned}$$

We see that these two solutions are oscillatory. In fact, they are $\pi/2$ radians out of phase with each other and the amplitude of the dipole is suppressed by a factor of c_s (Hu and Sugiyama, 1995). The $-k^2\Psi$ term in the differential equation causes compression in the fluid but the photon pressure term $k^2c_s^2\Theta_0$ resists this leading ultimately to oscillatory behaviour. Scales which reach a maximum or minimum at last scattering will correspond to a peak in the angular power spectrum and scales which have a zero at last scattering will correspond to troughs in the angular power spectrum.

This solution is very accurate on large scales but on small scales the accuracy suffers because we have assumed that the photons and baryons can be treated as a single fluid, or equivalently that the Thomson scattering rate is infinite, which is only an approximation. However, we can account for this by including a photon diffusion quadrupole term which introduces an exponential damping into the solutions above $\Theta_0+\Psi \rightarrow (\Theta_0+\Psi)\exp-[k/k_D]^2$ where k_D is a damping scale.

A.3 Free Streaming Solution of the Boltzmann Equations

After recombination, the acoustic oscillations which we have described above are 'frozen in' to the distribution of the photons as they free stream through the Universe. To find the form that these fluctuations in the distribution will take for an observer on Earth, we now need to consider again the Boltzmann equation for photons (A.20) where we have dropped the $\tilde{}$ and subscript notation denoting Fourier space. Rearranging puts this in the form:

$$\left(\left[\Theta+\Psi\right]\exp\left\{ik\mu\eta-\int_{\eta}^{\eta_0}\dot{\tau}\,d\eta\right\}\right)^{\cdot}=\left(\dot{\Psi}-\dot{\Phi}-\dot{\tau}\left[\Theta_0+\Psi+\mu v\right]\right)\exp\left\{ik\mu\eta-\int_{\eta}^{\eta_0}\dot{\tau}\,d\eta\right\}$$

where $\dot{} = \frac{\partial}{\partial\eta}$.

We can solve this as follows, defining $\tau(\eta_1, \eta_2) = \int_{\eta_1}^{\eta_2} \dot{\tau}\, d\eta$:

$$
\begin{aligned}
[\Theta + \Psi](\eta_0, \mu) \exp\{ik\mu\eta_0 + \tau(\eta_{dec}, \eta_0)\} - [\Theta + \Psi](\eta_{dec}, \mu) \exp\{ik\mu\eta_{dec}\} = \\
\int_{\eta_{dec}}^{\eta_0} \left(\dot{\Psi} - \dot{\Phi} - \dot{\tau}\left[\Theta_0 + \Psi + \mu v\right]\right) \exp\left\{ik\mu\eta' + \tau(\eta_{dec}, \eta')\right\} d\eta' \\
[\Theta + \Psi](\eta_0, \mu) = [\Theta + \Psi](\eta_{dec}, \mu) \exp\{-\tau(\eta_{dec}, \eta_0)\} \exp\{ik\mu(\eta_{dec} - \eta_0)\} \\
+ \int_{\eta_{dec}}^{\eta_0} \left(\dot{\Psi} - \dot{\Phi} - \dot{\tau}\left[\Theta_0 + \Psi + \mu v\right]\right) \exp\left\{ik\mu(\eta' - \eta_0) - \tau(\eta', \eta_0)\right\} d\eta' \qquad \text{(A.49)}
\end{aligned}
$$

but $\tau(\eta_{dec}, \eta_0) \gg 1$ (Hu and Sugiyama, 1994) and hence we can ignore the first term on the right hand side. Also, $-\dot{\tau}e^{-\tau}$ is the probability that a photon last scattered in the conformal time interval $[\eta, \eta + d\eta]$ and is therefore sharply peaked at the time of last scattering η_*. Using this, we can rewrite equation (A.49) as:

$$
\begin{aligned}
[\Theta + \Psi](\eta_0) = \int_{\eta_{dec}}^{\eta_0} \left(\dot{\Psi} - \dot{\Phi}\right) \exp\left\{ik\mu(\eta' - \eta_0) - \tau(\eta', \eta_0)\right\} d\eta' \\
+ [\Theta_0 + \Psi](\eta_*) \exp\{ik\mu(\eta_* - \eta_0)\} + \left[\frac{v}{ik}\frac{d}{d\eta'} \exp\left\{ik\mu(\eta' - \eta_0)\right\}\right]_{\eta_*} \qquad \text{(A.50)}
\end{aligned}
$$

Taking the ℓth multipole moment of both sides of this equation as defined above (A.21) now gives:

$$
\begin{aligned}
(i)^l \int_{-1}^{1} \mathcal{P}_\ell(\mu) [\Theta + \Psi](\eta_0) \frac{d\mu}{2} = (i)^l \int_{-1}^{1} \mathcal{P}_\ell(\mu) \int_{\eta_{dec}}^{\eta_0} \left(\dot{\Psi} - \dot{\Phi}\right) \exp\left\{ik\mu(\eta' - \eta_0) - \tau(\eta', \eta_0)\right\} d\eta' \\
+ [\Theta_0 + \Psi](\eta_*) \exp\{ik\mu(\eta_* - \eta_0)\} + \left[\frac{v}{ik}\frac{d}{d\eta'} \exp\left\{ik\mu(\eta' - \eta_0)\right\}\right]_{\eta_*} \frac{d\mu}{2}
\end{aligned}
$$

Using the fact that,

$$
\int_{-1}^{1} \mathcal{P}_\ell(\mu) \exp\{ik\mu(\eta - \eta_0)\} \frac{d\mu}{2} = \frac{1}{(-i)^l} j_\ell[k(\eta - \eta_0)]
$$

where j_ℓ is a spherical Bessel function with the properties:

$$
\begin{aligned}
j_\ell(x) &= (-1)^l j_\ell(-x) \\
\frac{dj_\ell}{dx} &= l j_{\ell-1} - \frac{(l+1)}{x} j_\ell
\end{aligned}
$$

Hence:

$$\begin{aligned}
[\Theta_\ell + \Psi](\eta_0) &= (-1)^\ell \int_{\eta_{dec}}^{\eta_0} \exp\left\{-\tau(\eta', \eta_0)\right\} \left(\dot{\Psi} - \dot{\Phi}\right) j_\ell[k(\eta' - \eta_0)]\, d\eta' \\
&\quad + (-1)^l \left[\Theta_0 + \Psi\right](\eta_*)\, j_\ell[k(\eta_* - \eta_0)] + (-1)^l \left[\frac{v}{ik} \frac{d}{d\eta'} j_\ell[k(\eta' - \eta_0)]\right]_{\eta_*} \\
&= \int_{\eta_{dec}}^{\eta_0} \exp\left\{-\tau(\eta', \eta_0)\right\} \left(\dot{\Psi} - \dot{\Phi}\right) j_\ell[k(\eta_0 - \eta')]\, d\eta' \\
&\quad + \left[\Theta_0 + \Psi\right](\eta_*)\, j_\ell[k(\eta_0 - \eta_*)] + \frac{v}{ik} \left[-j_{\ell-1}[k(\eta_0 - \eta_*)] - \frac{l+1}{(\eta_* - \eta_0)} j_\ell[k(\eta_0 - \eta_*)]\right] \\
&= \int_{\eta_{dec}}^{\eta_0} \exp\left\{-\tau(\eta', \eta_0)\right\} \left(\dot{\Psi} - \dot{\Phi}\right) j_\ell[k(\eta_0 - \eta')]\, d\eta' \\
&\quad + \left[\Theta_0 + \Psi\right](\eta_*)\, j_\ell[k(\eta_0 - \eta_*)] + \frac{v}{ik} \left[-j_{\ell-1}[k(\eta_0 - \eta_*)] + \frac{l+1}{(\eta_0 - \eta_*)} j_\ell[k(\eta_0 - \eta_*)]\right]
\end{aligned}$$

At last scattering, $v_b \simeq -3i\Theta_1(\eta_*)$ hence:

$$\begin{aligned}
[\Theta_\ell + \Psi](\eta_0) &= \int_{\eta_{dec}}^{\eta_0} e^{\{-\tau(\eta', \eta_0)\}} \left(\dot{\Psi} - \dot{\Phi}\right) j_\ell[k(\eta_0 - \eta')]\, d\eta' + \left[\Theta_0 + \Psi\right](\eta_*)\, j_\ell[k(\eta_0 - \eta_*)] \\
&\quad + 3\Theta_1(\eta_*) \left[j_{\ell-1}[k(\eta_0 - \eta_*)] - \frac{l+1}{k(\eta_0 - \eta_*)} j_\ell[k(\eta_0 - \eta_*)]\right] \qquad \text{(A.51)}
\end{aligned}$$

We calculate $[\Theta_0 + \Psi](\eta_*)$ and $\Theta_1(\eta_*)$ using the undamped tight coupling solutions (A.47) and (A.48) multiplied by the average damping factor $\mathcal{D}_k$:

$$\mathcal{D}_k = \int_0^{\eta_0} \dot{\tau} \exp\left\{-\tau(\eta, \eta_0)\right\} \exp\left\{-\left[k/k_D(\eta)\right]^2\right\} d\eta \qquad \text{(A.52)}$$

A.4 Potentials

In order to solve the above equations we need expressions for the evolution of the potentials. These can be found by perturbing the Einstein equations of general relativity. The Einstein equations are:

$$G^\mu_\nu = g^{\mu\alpha}\left(R_{\alpha\nu} - \frac{1}{2} g_{\alpha\nu} R\right) = 8\pi G T^\mu_\nu$$

where G^μ_ν is the Einstein tensor, T^μ_ν is the energy-momentum tensor, $R_{\alpha\nu}$ is the Ricci tensor and R is the Ricci scalar. The Ricci tensor and the Ricci scalar are functions of the Christoffel symbols, $\Gamma^\alpha_{\beta\gamma}$, for the metric, which are given by:

$$\Gamma^{\alpha}_{\beta\gamma} = \frac{1}{2} g^{\alpha\delta} \left(g_{\beta\delta,\gamma} + g_{\delta\gamma,\beta} - g_{\beta\gamma,\delta} \right)$$

Hence,to first order,

$$\begin{aligned}
\Gamma^{0}_{00} &= \frac{\partial \Psi}{\partial t} \\
\Gamma^{0}_{0i} &= \frac{\partial \Psi}{\partial x^i} = i k_i \Psi_k \text{ in Fourier space} \\
\Gamma^{0}_{ij} &= \delta_{ij} a^2 \left[H + 2H \left(\Phi - \Psi \right) + \frac{\partial \Phi}{\partial t} \right] \\
\Gamma^{i}_{00} &= \frac{1}{a^2} \frac{\partial \Psi}{\partial x^i} = \frac{i k^i}{a^2} \Psi_k \text{ in Fourier space} \\
\Gamma^{i}_{j0} &= H \delta^i_j + \frac{\partial \Phi}{\partial t} \delta^i_j \\
\Gamma^{i}_{jk} &= \frac{\partial \Phi}{\partial x^k} \delta^i_j + \frac{\partial \Phi}{\partial x^j} \delta^i_k + \frac{\partial \Phi}{\partial x^i} \delta_{jk} \\
&= i \Phi_k \left[\delta_{ij} k_k + \delta_{ik} k_j - \delta_{jk} k_i \right] \text{ in Fourier space}
\end{aligned}$$

The Ricci tensor is given by $R_{\mu\nu} = \Gamma^{\alpha}_{\mu\nu,\alpha} - \Gamma^{\alpha}_{\mu\alpha,\nu} + \Gamma^{\alpha}_{\beta\alpha}\Gamma^{\beta}_{\mu\nu} - \Gamma^{\alpha}_{\beta\nu}\Gamma^{\beta}_{\mu\alpha}$. Evaluating the components of the Ricci tensor using the expressions for the Christoffel symbols above gives, to first order:

$$\begin{aligned}
R_{00} &= \frac{1}{a^2} \frac{\partial^2 \Psi}{\partial x^i \partial x^i} - 3 \frac{\ddot{a}}{a} - 3 \frac{\partial^2 \Phi}{\partial t^2} + 3H \frac{\partial \Psi}{\partial t} - 6H \frac{\partial \Phi}{\partial t} \\
R_{ij} &= \delta_{ij} \left[\left(2\dot{a}^2 + a\ddot{a} \right) \left(1 + 2\Phi - 2\Psi \right) + a^2 H \left(6 \frac{\partial \Phi}{\partial t} - \frac{\partial \Psi}{\partial t} \right) + a^2 \frac{\partial^2 \Phi}{\partial t^2} - \frac{\partial^2 \Phi}{\partial x^k \partial x^k} \right] \\
&\quad - \frac{\partial^2 \left(\Phi + \Psi \right)}{\partial x^i \partial x^j}
\end{aligned}$$

The Ricci scalar is defined by:

$$R = g^{\mu\nu} R_{\mu\nu} = g^{00} R_{00} + g^{ij} R_{ij} \text{ as } g^{0i} = 0$$

Hence in this case:

$$R = 6 \left[H^2 + \frac{\ddot{a}}{a} \right] - 12\Psi \left[H^2 + \frac{\ddot{a}}{a} \right] - \frac{2}{a^2} \frac{\partial^2 \Psi}{\partial x^i \partial x^i} + 6 \frac{\partial^2 \Phi}{\partial t^2} - 6H \left[\frac{\partial \Psi}{\partial t} - 4 \frac{\partial \Phi}{\partial t} \right] - \frac{4}{a^2} \frac{\partial^2 \Phi}{\partial x^i \partial x^i}$$

Substituting these expressions into the Einstein equations gives:

$$\begin{aligned} G_0^0 &= g^{00}\left(R_{00} - \frac{1}{2}g_{00}R\right) \\ &= -\left(1-2\Psi\right)R_{00} - \frac{1}{2}R \\ &= -6H\frac{\partial\Phi}{\partial t} - 3H^2 + 6H^2\Psi + \frac{2}{a^2}\frac{\partial^2\Phi}{\partial x^i \partial x^i} \end{aligned} \tag{A.53}$$

As $G_0^0 = \bar{G}_0^0 + \delta G_0^0$ the first order terms from equation (A.53) give $\delta G_0^0 = -6H\frac{\partial\Phi}{\partial t} + 6H^2\Psi + \frac{2}{a^2}\frac{\partial^2\Phi}{\partial x^i \partial x^i}$. From the Einstein equations, $G_0^0 = 8\pi G T_0^0$ where $-T_0^0$ is the energy density of all the species in the Universe.

$$\begin{aligned} T_0^0 &= -\sum g_i \int \frac{d^3p}{(2\pi)^3} E_i(p) f_i(\mathbf{p}, \mathbf{x}, t) \\ T_{0,photons}^0 &= -2\int \frac{d^3p}{(2\pi)^3} p \left[f^{(0)} - p\frac{\partial f^{(0)}}{\partial p}\Theta\right] \qquad \text{for photons} \\ &= -\rho_\gamma\left[1 + 4\Theta_0\right] \qquad \text{similarly for neutrinos with } \Theta_0 \leftrightarrow \mathcal{N}_0 \\ T_{0,dark\ matter}^0 &= -g_i \int \frac{d^3p}{(2\pi)^3} E_i f_i = -m n_{dark\ matter} \\ &= -m n_{dm}^{(0)}\left(1 + \delta_{dm}\right) \\ &= -\rho\left(1 + \delta_{dm}\right) \qquad \text{similarly for baryons with } \delta_{dm} \leftrightarrow \delta_b \end{aligned}$$

Hence, we obtain $\delta T_0^0 = -4\rho_\gamma\Theta_0 - 4\rho_\nu\mathcal{N}_0 - \rho_{dm}\delta_{dm} - \rho_b\delta_b$ and on moving to Fourier space and letting $\dot{} = \frac{\partial}{\partial\eta}$ we find:

$$-3\frac{da/d\eta}{a}\dot{\Phi} + \frac{3}{a^2}\left(\frac{da}{d\eta}\right)^2\Psi - k^2\Phi = -4\pi G a^2\left[4\rho_\gamma\Theta_0 + 4\rho_\nu\mathcal{N}_0 + \rho_{dm}\delta_{dm} + \rho_b\delta_b\right] \tag{A.54}$$

This is the first of the equations describing the evolution of the potentials, in a non-expanding Universe, it generalises to the Poisson equation.

The spatial part of the Einstein equations is $G_j^i = g^{ik}\left[R_{kj} - \frac{1}{2}g_{kj}R\right]$, substitution of the expressions calculated for the Ricci tensor and the Ricci scalar gives:

$$
\begin{aligned}
G^i_j &= \delta^i_j\left[-H^2 - 2\frac{\ddot{a}}{a} + 2H^2\Psi + 4\frac{\ddot{a}}{a}\Psi - 2\frac{\partial^2\Phi}{\partial t^2} - 6H\frac{\partial\Phi}{\partial t} + 2H\frac{\partial\Psi}{\partial t} + \frac{1}{a^2}\frac{\partial^2(\Phi+\Psi)}{\partial x^k\partial x^k}\right] \\
&\quad - \frac{1}{a^2}\frac{\partial^2(\Phi+\Psi)}{\partial x^i\partial x^j} \\
G^i_j &= \delta^i_j\left[-H^2 - 2\frac{\ddot{a}}{a} + 2H^2\Psi + 4\frac{\ddot{a}}{a}\Psi - 2\frac{\partial^2\Phi}{\partial t^2} - 6H\frac{\partial\Phi}{\partial t} + 2H\frac{\partial\Psi}{\partial t} - \frac{k^2}{a^2}(\Phi+\Psi)\right] \\
&\quad + \frac{k_i k_j}{a^2}(\Phi+\Psi)
\end{aligned}
$$

Contracting the above expression with $\left(\hat{k}_i\hat{k}^j - \frac{1}{3}\delta^j_i\right)$ picks out the longitudinal, traceless part of G^i_j. Performing the same operation on T^i_j and using the Einstein equations gives:

$$
\frac{2k^2}{3a^2}(\Phi+\Psi) = \sum g_i \int \frac{d^3p}{(2\pi)^3}\frac{p^2}{E_i}\left(\mu^2 - \frac{1}{3}\right) f_i
$$

The integrand is proportional to the quadrupole and since the zero order distribution functions have no quadrupole term, the right hand side is first order. Only photons and neutrinos have a non-zero quadrupole term in their distribution functions so we find:

$$
\begin{aligned}
\frac{2k^2}{3a^2}(\Phi+\Psi) &= 8\pi G\left[-\frac{8}{3}\rho^{(0)}_\gamma\Theta_2 - \frac{8}{3}\rho^{(0)}_\nu\mathcal{N}_2\right] \\
\Rightarrow k^2(\Phi+\Psi) &= 32\pi G a^2\left[\rho_\gamma\Theta_2 + \rho_\nu\mathcal{N}_2\right] \qquad \text{(A.55)}
\end{aligned}
$$

The term in brackets in equation (A.55) is proportional to the *anisotropic stress*. In may scenarios this quantity is negligible meaning that we have the useful relationship $\Psi = -\Phi$.

APPENDIX B

Contribution of Sachs-Wolfe Effect to CMB Angular Power Spectrum

We can fairly simply recover the large scale form of the CMB angular power spectrum due to Primary anisotropies. Here the necessary steps are outlined, again following Dodelson (2003). In Appendix A, we found an expression for Θ_ℓ, the moments of the photon distribution, see equation (A.51). This expression involves an integral term which describes gravitational secondary anisotropies and is therefore irrelevant to our quest for an expression for primary anisotropies. Ignoring this, we find

$$\begin{aligned}[\Theta_\ell + \Psi](\eta_0) &= [\Theta_0 + \Psi](\eta_*) j_\ell [k(\eta_0 - \eta_*)] \\ &\quad + 3\Theta_1(\eta_*) \left[j_{\ell-1}[k(\eta_0 - \eta_*)] - \frac{\ell+1}{k(\eta_0 - \eta_*)} j_\ell [k(\eta_0 - \eta_*)] \right] \end{aligned} \quad \text{(B.1)}$$

$\Theta_0(\eta_*)$ and $\Theta_1(\eta_*)$ are evaluated under the tight coupling limit using equations (A.47) and (A.48). On large scales, where k is small we can neglect the dipole term and

$$[\Theta_\ell + \Psi](\eta_0) = [\Theta_0 + \Psi](\eta_*) j_\ell [k(\eta_0 - \eta_*)] \quad \text{(B.2)}$$

where once again η_* refers to the epoch of recombination when the tight coupling approximation holds.

Considering this tight coupling limit, we find that only the monopole and dipole moments of the photon distribution are significant, this leads to equations (A.42) and (A.43). Evaluating these in the large scale (small k) limit, together with the Boltzmann equations for dark matter and baryons we obtain

$$\dot{\Theta}_{r,0} = -\dot{\Phi} \tag{B.3}$$

$$\dot{\Theta}_{r,1} = 0 \tag{B.4}$$

$$\dot{\delta} = -3\dot{\Phi} \tag{B.5}$$

$$\dot{v} + \frac{\dot{a}}{a} v = 0 \tag{B.6}$$

and from the Einstein equation (A.54)

$$3\frac{\dot{a}}{a}\left(\dot{\Phi} - \frac{\dot{a}}{a}\Psi\right) = 4\pi G a^2 \left[\rho_{dm}\delta + 4\rho_r \Theta_{r,0}\right]. \tag{B.7}$$

Here, the subscript r refers to both neutrinos and photons since in the tight-coupling, large scale limit, these species follow the same evolution equations. From (B.3) and (B.5) we see

$$\delta - 3\Theta_{r,0} = \text{const.} \tag{B.8}$$

For adiabatic perturbations (see section 1.2.1), this constant is 0 and $\delta = 3\Theta_{r,0}$.

Consider the large scale form of the Einstein equation (B.7) at early times when the Universe was radiation dominated and $a \propto \eta$, $\dot{a}/a = 1/\eta$. Then,

$$\begin{aligned}
\frac{\dot{\Phi}}{\eta} - \frac{\Psi}{\eta^2} &= \frac{16\pi G a^2 \rho}{3}\left(\frac{\rho_\gamma}{\rho}\Theta_0 + \frac{\rho_\nu}{\rho}\mathcal{N}_0\right) \\
\Rightarrow \frac{\dot{\Phi}}{\eta} - \frac{\Psi}{\eta^2} &= \frac{2}{\eta^2}\left(\frac{\rho_\gamma}{\rho}\Theta_0 + \frac{\rho_\nu}{\rho}\mathcal{N}_0\right) \\
\Rightarrow \eta\dot{\Phi} - \Psi &= 2\left(\frac{\rho_\gamma}{\rho}\Theta_0 + \frac{\rho_\nu}{\rho}\mathcal{N}_0\right) \\
\Rightarrow \eta\ddot{\Phi} + \dot{\Phi} - \dot{\Psi} &= 2\left(\frac{\rho_\gamma}{\rho}\dot{\Theta}_0 + \frac{\rho_\nu}{\rho}\dot{\mathcal{N}}_0\right) = -2\dot{\Phi}
\end{aligned} \tag{B.9}$$

from equation (B.3) which holds for both photon (Θ_0) and neutrinos ($\mathcal{N}_0$). Since the photon and neutrino quadrupoles are negligible in this regime, we can take $\Phi = -\Psi$, see equation (A.55) and therefore (B.9) becomes

$$\ddot{\Phi}\eta + 4\dot{\Phi} = 0 \Rightarrow \Phi = A\eta^{-3} + B \tag{B.10}$$

where A and B are both constants. The first term of the solution is the decaying mode which will rapidly become negligible as time passes; the solution of interest is therefore $\Phi = \text{constant}$. Returning to equation (B.9) we have

$$\Phi = 2\left(\frac{\rho_\gamma}{\rho}\Theta_0 + \frac{\rho_\nu}{\rho}\mathcal{N}_0\right) \tag{B.11}$$

Since most structure formation models do not distinguish between photons and neutrinos we can set $\Theta_0 = \mathcal{N}_0$ initially and see that $\Phi(0) = 2\Theta_0(0)$.

Now, equation (B.3) gives $\Theta_0 + \Phi = \text{const}$, and with the initial conditions, this constant is $3\Phi(0)/2$, therefore

$$\left[\Theta_0 + \Phi\right](\eta) = \frac{3\Phi(0)}{2}. \tag{B.12}$$

and

$$\left[\Theta_0 + \Psi\right](\eta_*) = \Theta_0(\eta_*) - \Phi(\eta_*) = \frac{3\Phi(0)}{2} - 2\Phi(\eta_*). \tag{B.13}$$

Returning to equations (B.3), (B.5) and (B.7), we can deduce a form for the super-horizon potential Φ in terms of it's initial value $\Phi(0)$, which can then be replaced in the above equation. Recalling (B.8), and substituting for $\Theta_{r,0}$ in equation (B.7) gives:

$$3\frac{\dot{a}}{a}\left(\dot{\Phi} - \frac{\dot{a}}{a}\Psi\right) = 4\pi G a^2 \rho_{dm}\delta\left[1 + \frac{4}{3}\frac{\rho_r}{\rho_{dm}}\right]. \tag{B.14}$$

Defining $y = a/a_{\text{eq}} = \rho_{dm}/\rho_r$, and re-expressing equation (B.14) in terms of y alone, one finds

$$y\Phi' + \Phi = \frac{3y+4}{6(y+1)}\delta \tag{B.15}$$

where $' = \frac{\partial}{\partial y}$. Re-expressing this in terms of δ, differentiating with respect to y and using equation (B.5) to set $\delta' = -3\Phi'$ gives

$$\Phi'' + \frac{21y^2 + 54y + 32}{2y(y+1)(3y+4)}\Phi' + \frac{\Phi}{y(y+1)(3y+4)} = 0 \tag{B.16}$$

which has solution (obtained by introducing $u = y^3\Phi/\sqrt{1+y}$)

$$\Phi = \frac{\Phi(0)}{10}\frac{1}{y^3}\left[16\sqrt{1+y} + 9y^3 + 2y^2 - 8y - 16\right] \tag{B.17}$$

For small y ($a \ll a_{\rm eq}$ i.e. radiation dominated regime), $\Phi = \Phi(0)$; for large y ($a \gg a_{\rm eq}$ i.e. matter dominated regime), $\Phi = \frac{9}{10}\Phi(0)$. If recombination occurs long after matter-radiation equality, equation (B.13) becomes

$$\left[\Theta_0 + \Psi\right](\eta_*) = -\frac{1}{3}\Phi = \frac{1}{3}\Psi. \tag{B.18}$$

Now we have the large scale form of Θ_ℓ, it remains only to compute the power spectrum. Using the growth function to relate the potential today to its form at recombination (which we assume occurs much latter than matter-radiation equality), we see

$$\left[\Theta_0 + \Psi\right](\eta_*) = \frac{1}{3}\Psi \simeq -\frac{\Omega_{m0}H_0^2}{2k^2}\left(\frac{g(\eta_*)}{a(\eta_*)}\right)\delta(\eta_0) \tag{B.19}$$

The spherical harmonic coefficients $a_{\ell m}$ are given by

$$a_{\ell m}(\mathbf{x},\eta) = \int \frac{d^3k}{(2\pi)^3}\, e^{i\mathbf{k}.\mathbf{x}} \int d\Omega\; Y^*_{\ell m}(\hat{\mathbf{p}})\,\Theta(\mathbf{k},\hat{\mathbf{p}},\eta), \tag{B.20}$$

and the angular power spectrum C_ℓ by

$$C_\ell\, \delta^{\rm K}_{\ell\ell'}\, \delta^{\rm K}_{mm'} = \langle a_{\ell m}\, a^*_{\ell' m'}\rangle\,. \tag{B.21}$$

Putting all this together and evaluating the integral gives the expression quoted in equation (1.32),

$$\ell(\ell+1)C_\ell^{\rm SW} = \frac{\pi}{2}\left(\frac{\Omega_{m0}g(\eta_*)}{a(\eta_*)}\right)^2 \delta_{\rm H}^2 \tag{B.22}$$

where $\delta_{\rm H}$ is the amplitude of the fluctuations at Horizon crossing ($k = H_0/c$) as predicted by inflation.